Topological electronic phases in graphene

a dissertation presented
by

Jose Luis Lado Villanueva

to
the Department of Physics
in partial fulfillment of the requirements
for the degree of
Doctor of Philosophy
in the subject of

Physics

University of Santiago de Compostela
Spain
April 2016

Topological electronic phases in graphene

Abstract

Graphene is a two dimensional material made of single layer of carbon atoms arranging into a honeycomb lattice. It can be synthesized by variety of methods as exfoliation, chemical vapor deposition or organic polymerization. Its electronic properties are not the ones of an insulator nor a metal, being usually known as a zero gap semiconductor. Electrons in graphene behave as massless Dirac fermions, having a zero effective mass. The Dirac equation that governs electrons turns graphene into a material that can easily develop topological states due to Berry phase effects of the Dirac points. Such topological states of matter are characterized for having properties which are independent on the defects and imperfections that the material might have. In addition, the two dimensional nature of graphene makes it specially suitable to inherit properties from other materials by proximity effect, as superconductivity or magnetism. In this thesis we will explore by means of theoretical techniques how graphene can show topological insulating states by combination of magnetic fields, electron-electron interaction, spin orbit coupling, exchange and superconducting proximity effects.

Author
Jose Luis Lado Villanueva

Thesis advisor
Joaquín Fernández Rossier

University advisor
Víctor Pardo Castro

Contents

Chapter 1

Introduction

Starting around the middle of the XX century, one of the biggest technological revolutions was achieved by the electronic industry. Born and grown for less than 100 years[1], in its brief life has changed the way humanity carry out their lives. Instant communications between people thousands of kilometers away, computational power not ever dreamt before and even the redefinition of human relations. All these phenomena were possible only by systematic optimization and price reduction of the semiconductor industry. The improvement has been so incredibly huge, that a single smartphone that you can wear in your pocket has more computational power that the whole NASA back in 1969, when they placed two astronauts in the moon[2]. It is fair to say that nowadays, you can have the computational power needed to land in the moon, for the same price than a bicycle.

But this technological revolution did not come out of nowhere. The birth and development of quantum mechanics at the beginning of the XX century marked the point where the physical foundations of microscopic matter were discovered. It was with the understanding of unsolved physical phenomena, the development of advanced mathematical formalism and high precision measurement techniques, that the world changed in just one hundred years. Nobody would image back then that in three generations humans would have the capability to explore the outer space[3], instruments able to precisely imaging our bodies on the inside[4], a network connecting the most distant parts of the world in less than a second[5] and even the power to manipulate matter at the very atomic level[6]. It was the discovery of new physics, new mathematics and new science what gave us computers, what changed the global economy, our jobs and our lives.

The transistor is the basic building block in the electronic technology, and its continuous improvement has been driven by a very simple idea: the smaller the circuit, the more you can have in a fixed surface. Such simple motivation has proven to give remarkable results, and has given engineers a clear objective for decades[7]. However, physics will not allow this idea to work forever, a circuit cannot

be made smaller than the size of the atom. The physics of the current logical circuits is not in the deep the quantum limit, but more in the semiclassical limit, where electrons show semiclassical dynamics but the phase space effects are determined by quantum mechanics. Electrons behave as particles with a Fermi-Dirac distribution, that populate the valence band due to thermal excitations. Doping with P or N impurities allows to tune the concentration of electrons in the conduction band or holes in the valence band. They suffer scattering with defects, having an effective mean free path and mobility. These parameters are system dependent, and they are strongly tuned by the quality of the sample. Sample quality has been one of the most important concerns from the engineering point of view. Quantum phenomena plays essentially a phase space role, determining which transitions are allowed and which ones are not. However, it is another quantum phenomena one of the potential threats for engineers: the tunnel current does not allow to build an arbitrarily small circuit that has a small enough offset current. The question is, could we do better than this? Could we take quantum effects not as an enemy, but as our most powerful ally? The answer is yes.

There are two remarkable quantum phenomena which show the emergence of the quantum world into the macroscopic scale: superconductivity[8] and quantum Hall effect[9]. Superconductivity is a collective electronic state in which the electrons with opposite momentum pair and form a macroscopic wavefunction, conserving coherence along large distances. This long range coherence also manifest into a zero resistance state, so that no heat losses appear in the system. Such zero resistance state can be easily understood in the terms of the excitation spectra of the system. Bogoliubov quasiparticles have a band gap in their spectrum, so that a finite amount of energy has to be given to the system to change its quantum state. A unique feature of the superconducting state is also the Meissner effect, which can be understood as the photon gaining a mass term in the superconductor, derived first by Anderson[10], which also found a direct application in high energy physics as the Higgs mechanism[11]. The latter effect creates an effective mass for the photon inside the superconductor, killing incoming magnetic fields into the superconductor, turning them into perfect diamagnets. The sad news is that superconductors only have been found at low temperatures. In particular, conventional superconductors driven by phonon interactions show critical temperatures smaller than 40 K[12], whereas high temperature superconductors, driven by spin fluctuations, can reach up to 130 K[13]. Still, the state of the art is far from room temperature.

The second remarkable macroscopic quantum state is the so called quantum Hall effect. This electronic state shows up when a large magnetic field is applied to a system with high mobility. In this quantum state, the bulk electronic state becomes insulating, whereas the edges of the system develop chiral conducting states, so that electrons move in a particular direction in a given edge. The consequences of such

phase transition are dramatic: the Hall conductance σ_{xy} becomes quantized in terms of fundamental quantities, the Planck constant $\hbar$ and the charge of the electron e. The chiral nature of the edge states turns the electronic state totally immune towards any kind of perturbation. Electrons cannot back scatter because there is no counter-propagating state, no matter if the perturbation is an impurity, an electric field or electron-electron interaction: the conductance is perfect. Actually, it is this robustness the reason why Quantum Hall measurements are used as the ultimate technique in metrology to determine the charge of the electron[14, 15]. Quantum Hall effect is an electronic state without electrical losses, and therefore also no heat losses. The sad news are that very high magnetic fields are needed to observe the quantum Hall state, in particular for GaAs heterostructures, fields on the order of 10 T are needed. With the discovery of graphene the conditions of quantum Hall effect have drastically softened[16], making possible to observe quantum Hall effect even at room temperature[17]. Although magnetic field seems a mandatory ingredient, there is a a class of materials that can also show perfect conductance, the so called topological insulators. Actually, these materials are classified not with the usual Landau theory of broken symmetry states and order parameters[18], but by the topological nature of the electronic structure[19]. In particular, the perfect conductance of the quantum Hall state can be simply understood as a topological invariant[20], the Chern number, of the bulk electronic state. It is this topological nature the ultimate responsible of the perfect quantization [20, 21]. Among the family of topological insulators, quantum anomalous Hall insulators will realize exactly the same physics as the quantum Hall state, but without magnetic field. The finding of such materials[22] will give rise to perfect conductors, that do not show any heat loss, even at room temperature, with their obvious technological implications.

Most electronics are based on a single property of electrons, its electric charge. Nevertheless, additional degrees of freedom can be exploited, some of them material dependent such as the valley in graphene[23, 24]. However, the material independent degree of freedom that electrons show is spin, giving rise to the whole area of spintronics[25, 26, 27, 28, 29, 30]. One of the simplest physical phenomena that arises when the spin degree of freedom is taken into account is spin dependent transport, whose iconic realization is the giant magnetoresistance[31]. The technological implications of such discovery were totally ground breaking: it settled the basis for non-volatile hard disk drives, MRAM and magnetic sensors. But even more interesting physical effects appear when the spin degree of freedom is considered: spin not only acts as filter, but can also introduce topological effects in the charge transport similar to the Aharonov–Bohm effect[32] when electrons interact with non-collinear textures known as skyrmions [33].

A more active role of spin[34] is not to act as passive effect, but as an active one, so that the transport phenomena is not the charge but the spin itself. One of the

most remarkable examples of systems that show spin transport is the quantum spin Hall effect[35, 36, 37], a topological state of matter where pure spin currents without charge flow, and therefore no Joule losses, are protected by time reversal symmetry. An even more radical example is spin transport in electronic insulators, where the spin flows not by the movement of electrons but by spin wave excitations[38]. If these possibilities work out, the compatibility with conventional electronic devices is key. The later is realized by charge to spin conversion using the spin Hall effect[39, 40, 41, 42, 43], and spin to charge using the inverse spin Hall effect. Combination of spin dependent transport, spin orbit effects, spin wave transport, topology and even superconductivity will give rise to unknown emergent phenomena. The goal of this thesis is to show how such interplay can give rise to unconventional phenomena in very particular class of systems: two dimensional materials, and in particular graphene.

The rise of graphene[44] was a game changer event. Not only from the theoretical point of view, where it was believed that the Mermin-Wagner theorem[45, 46] did not allow the existence of two-dimensional materials, but also from the experimental point of view. Synthesis of graphene can be realized in nearly any lab in the world by exfoliation[47, 48]. High quality can synthesized by chemical vapor deposition[49], and even nanostructures can be created by organic chemistry methods[50, 51]. Moreover, it shows a remarkably high electrical conductivity, very large mobility and even ballistic transport[52, 53, 54, 55, 56, 57, 58, 59, 60, 61, 59, 62, 63]. The latter arises due to the unconventional electronic structure: in comparison with normal materials in which the electrons show classical dynamics with an effective mass, electrons in graphene are governed by a Dirac equation with zero effective mass[44]. In turn this gives rise to electronic properties totally different to either normal metals, semiconductors or insulators. Moreover, its two dimensional nature allows a huge tunability by proximity effect, the whole graphene system is surface, the proximity effect is maximal. By putting graphene in contact with other systems, electrons will gain exchange[64, 65], superconducting[66], band-gap[67, 68], spin orbit coupling[69] and doping by field effect[70].

The appearance of two dimensional materials boosts even further the tuning possibilities of graphene, van der Waals heterostructures can be made up to introduce those effects into a graphene sheet, using MoS_2 to induce spin orbit coupling[69], $NbSe_2$ to induce superconductivity[71] or BN to induce a low gap semiconducting state [68, 72]. But the usefulness of the new family of two dimensional materials goes way beyond tuning graphene. Dichalcogenides as MoS_2 find applications for solar cells[73], spintronics due to its large spin-orbit coupling [74] and even transistors[75]. The family of two dimensional materials grows every day with the isolation of new materials, turning the possibilities bigger and bigger.

However, the discovery of new materials will only postpone the unavoidable

frontier that we will encounter for conventional electronics. With no need to enter into technical details, there is a clear hard limit in miniaturization in transistors: a circuit cannot be smaller than an atom. Therefore, there seems to be a limit to the computational power that we can achieve in an smartphone, or even in a supercomputer. At first sight it might seem fine, the computational resources that we already have are more than enough for the tasks we have. Moreover, the optimization continues, maybe at a slower pace, but still goes on. Therefore, do we really need to worry about getting more powerful resources? The answer is yes, there are several taks that we would not do otherwise.

Even if better materials are found for act as semiconductors, even if better contacts without heat losses are developed, some tasks will still be un-doable due to the miniaturization limitation. This limitation comes from the mathematical nature of conventional computational logic, the complexity of such tasks grows too fast to be doable within the current computational framework. Among these intractable problems we have, breaking of cryptography algorithms, large scale materials modeling, deep software testing, complex disease modeling and even computational design of drugs. All these tasks require computational resources that are still far from our possibilities, and will ever be if we do not change the way we understand computing. However, there is a way around: quantum computing[76] provides a framework where new algorithms can be implemented, which do not have analogous counterpart in conventional computation. As an example, Shor's algorithm[77] allows to factorize large numbers in polynomial time, in comparison with the exponential time needed by classical approaches, changing the playground of many of the current cryptography techniques.

Among the physical systems that have proposed to use as qubits there are localized electronic states[78, 79], Josephson junctions, fractional Hall states and Majorana bound states. The tunability of two dimensional materials yields a huge freedom to tailor their electronic properties, and reach a state with a suitable electronic state to be used as qubit building block. Moreover, topological electronic states can systematically be used to create Majorana bound states[80], anyonic states[81] that can used to perform quantum operations. We are still far from being able to systematically develop quantum computers, but the possibilities are encouraging[82] and the prize is totally worth the effort.

Graphene marked the beginning of the rise of the two dimensional electronic world. Its huge tunability, together with its proximity to topological quantum phase transitions due to its Dirac spectrum yields a exciting zoo of possibilities. Experimental realizations of quantum spin Hall effect[83] and anomalous Hall effect[64] confirm the previous theoretical excitement that started with the observation of quantum Hall effect. Topological effects provided a playground to observe new physics yet unexplored, with the potential to break the mold of current computa-

tional power, and explore particles with mathematical properties not yet achieved in high energy physics[84]. Finally, atomic scale manipulation[85], which turns Feynmann's dream[86] into a reality, makes possible atomic tailoring of electronic properties, in materials with tunable electronic orders, made of a simple element as carbon. Landau order parameters are no longer alone, topology is the new game in town.

Chapter 2

About this thesis

This thesis resulted from the work carried out within the Marie Curie International Training Network SPINOGRAPH[87], supported by an Early Stage Researcher Fellowship of the same project. In particular, my specific project intended to study spin related phenomena in graphene and other 2D materials by means of theoretical techniques. The project was carried out under the supervision of Joaquín Fernández Rossier, at the Iberian Nanotechnology Laboratory in Braga, Portugal. This thesis will be presented in the university of Santiago de Compostela (USC), Spain, within the PhD program in Material Science, with Joaquín Fernández Rossier as PhD advisor and Víctor Pardo as local tutor at USC.

This thesis is organized as follows. First, a comprehensive introduction of the different topological states in graphene is presented 3, intended to act as an introductory tutorial. Afterwards, the interplay between interactions, magnetism and intrinsic quantum spin Hall effect in graphene is discussed 4. The thesis continues with magnetism in the quantum Hall state 5, focusing on the interplay between magnetic structure and electronic properties, to end up studying spin wave properties. The next chapters focus on two new different mechanisms to generate a quantum anomalous Hall state in graphene 67. The first one taking advantage of topological imprinting between skyrmions and graphene 6. The second anomalous mechanism presents a exploit to drive antiferromagnetic honeycomb lattices into quantum anomalous Hall insulators 7. The next chapters jump to the interplay between magnetism and superconductivity. First we focus of the simplest effect that manifests as Shiba bound states 8, which in graphene show a totally unconventional behavior. We continue showing a new topological state on the interplay between magnetism and superconductivity, topological superconductivity. We focus on how by combination of quantum Hall effects, ferromagnetism and even antiferromagnetism, Majorana bound states can be created in graphene 9. The next chapter 10 is devoted to the study of quantum Hall effects and topological insulating states in other 2D materials by using a combination of first principles and tight binding,

using the Wannierization technique. We continue detailing a special technique to calculate numerically the spectrum of single impurities in infinite systems, the embedding method 11. The next chapter is devoted to explaining how to use a user friendly software 12[88, 89] that I have developed that allows non-experts to reproduce many of the results presented. Next, we detail other additional techniques 13 used through this thesis. And finally, we summarize our main conclusions 14.

The main publications that form the basis of the work presented in this thesis are the following

- Edge states in graphene-like systems
  J. L. Lado, N. Garcia-Martinez, J Fernandez-Rossier
  Synthetic Metals 210, 56-67 (2015)

- Magnetic Edge Anisotropy in Graphene-like Honeycomb Crystals
  J. L. Lado, J. Fernández-Rossier
  Physical Review Letters 113 (2), 027203 (2014)

- Noncollinear magnetic phases and edge states in graphene quantum Hall bars
  J. L. Lado, J. Fernandez-Rossier
  Physical Review B 90 (16), 165429 (2014)

- Quantum Anomalous Hall effect in graphene coupled to skyrmions
  J. L. Lado, J. Fernandez-Rossier
  Physical Review B 92 (11), 115433 (2015)

- Unconventional Yu-Shiba-Rusinov states in hydrogenated graphene
  J. L. Lado, J. Fernandez-Rossier
  2D Materials 3 (2), 025001 (2016)

- Majorana Zero Modes in Graphene
  P. San-Jose, J.L. Lado, R. Aguado, F. Guinea, J. Fernandez-Rossier
  Physical Review X 5 (4), 041042 (2015)

This thesis also includes results appart from the ones contained in the previous publication list, giving further details for all the works, and presenting unpublished ones.

Below it is the list of side works

- Noncollinear versus collinear description of the Ir-based one-t_2g-hole perovskite-related compounds: $SrIrO_3$ and Sr_2IrO_4
  JL Lado, V Pardo
  Physical Review B 92 (15), 155151 (2015)

- Controlled Complete Suppression of Single-Atom Inelastic Spin and Orbital Cotunneling
  B Bryant, R Toskovic, A Ferron, JL Lado, A Spinelli, J Fernandez-Rossier, Alexander F Otte
  Nano Letters 15 (10), 6542-6546 (2015)

- Electronic properties of transition metal atoms on Cu_2N/Cu (100)
  A Ferron, JL Lado, J Fernandez-Rossier
  Physical Review B 92 (17), 174407 (2015)

- Design and Synthesis of Highly Active Al–Ni–P Foam Electrode for Hydrogen Evolution Reaction
  Jose Luis Lado, Xiaoguang Wang, Elvira Paz, Enrique Carbo-Argibay, Noelia Guldris, Carlos Rodríguez-Abreu, Lifeng Liu, Kirill Kovnir, Yury V Kolen'ko
  ACS Catalysis 5 (11), 6503-6508 (2015)

- Centimeter-scale synthesis of ultrathin layered MoO_3 by van der Waals epitaxy
  Aday J Molina-Mendoza, Jose Luis Lado, Joshua Island, Miguel Angel Niño, Lucia Aballe, Michael Foerster, Flavio Y Bruno, Herre SJ van der Zant, Gabino Rubio-Bollinger, Nicolas Agrait, Emilio Perez, Joaquin Fernandez-Rossier, Andres Castellanos-Gomez
  arXiv:1512.04355 (2015)

- Topological features of hydrogenated graphene
  LA Gonzalez-Arraga, JL Lado, F Guinea
  arXiv:1507.07714 (2015)

- Quantum spin Hall phase in multilayer graphene
  NA Garcia-Martínez, JL Lado, J Fernandez-Rossier
  Physical Review B 91 (23), 235451 (2015)

- A kilobyte rewritable atomic memory
  F. E. Kalff, M. P. Rebergen, E. Fahrenfort, J. Girovsky , R. Toskovic, J. L. Lado, J. Fernandez-Rossier and A. F. Otte
  arXiv:1604.02265 (2016)

In addition, the material covered in chapters 10 and 11 form the basis for two more papers to be submitted in the incoming months.

Chapter 3

An overview on edge states and topology in graphene [1]

Edge states can appear in graphene for two main reasons: effects which depend on specific details of the edge, and states whose origin is topological and do not depend on edge details. In this introductory chapter we will review the different mechanisms by which edge states can appear in graphene. In particular, we present simple examples of the different topological electronic phases.

3.1 Introduction

Graphene has been the most studied material of the last decade. Its extraordinary electronic and mechanical properties came as a great surprise: the existence of stable two dimensional crystals was customarily dismissed, and surfaces had been identified as the source of reduction of electronic mobility, due to defects and adsorbate trapping. The age of graphene was initiated by the observation of the field effect transistors[90], and more strikingly the quantum Hall effect[91, 92], a phenomena that had only been observed in high mobility semiconductor heterostructures[93].

Graphene is a two dimensional lattice of carbon atoms that form a honeycomb lattice, that can also be described as a triangular lattice with a two atom basis, displayed with different colors in Fig 3.1. This makes of the graphene honeycomb lattice a bipartite lattice, a fact that strongly influences its electronic properties.

The electronic properties of graphene can be described in terms of a very elegant and simple picture[94, 95] by means of the Dirac equation. Close to the Fermi energy, electrons in graphene behave as two dimensional relativistic massless particles, the so called Dirac electrons. The energy bands are linear, $E_{\pm} = \pm\hbar v_F|\vec{k}|$, so that the three dimensional plot of these two dimensional bands produces the so called

[1] some parts of this chapter are taken from the paper Synthetic Metals 210, 56-67 (2015)

Dirac cones. The Brillouin zone associated to the honeycomb lattice is also hexagonal, and has a copy of these Dirac bands, located at the corners of the hexagon. Only two of these so called valleys are actually non-equivalent. As a result, electrons in graphene have an additional isospin, the valley.

All these properties are also expected for a wider class of material systems, the graphene-like materials, that can also be described in terms of electrons moving in a honeycomb lattice with just one orbital per site. An incomplete list of graphene-like materials includes Silicene[96], Germanene[97], Stanene[98], Metallic organic framework[99], hydrogenated Bi(111)[100], and artificial graphene lattices[101].

The purpose of this chapter is to review what is known about the fate of the Dirac electrons at the edges, the boundaries of these otherwise endless two dimensional crystals. In some instances Dirac electrons simply scatter at the edges but, very often, graphene hosts edge states, *i.e.*, states whose wave function are evanescent in the direction perpendicular to the edge, and itinerant in the parallel direction. Their energies are at, or close to, the Dirac point, and very often their wave functions have peculiar properties, such as sublattice polarization, spin polarization or net spin current, just to mention a few.

Edge states are particularly important when graphene is driven into what nowadays are known as topological insulator phases[102]. Historically, the first example of this phase is associated to the Quantum Hall Effect (QHE)[93], observed in high mobility two dimensional electron gases in semiconductor heterostructures. In these systems, application of a sufficiently large magnetic field produces a discrete spectrum of Landau levels (LL) in the bulk states. This leads to an insulating state when the Fermi energy lies in between the LL. Importantly, in that situation the edges host chiral (or unidirectional) states that are ideal quantum conductors [103, 104], and are responsible of the perfect quantization of the Hall conductance[93].

Soon after the discovery of the QHE, it was shown by Thouless and coworkers (TKNN[20]) that the Hall conductance could be expressed, using the conventional linear response theory, in terms of a topological invariant[20, 21], the so called Chern number $\mathcal{C}$, associated to the Berry curvature of wave functions of the bulk states.

The prediction of other insulating phases with quantized edge transport due to topological order without a net magnetic field is one of the greatest successes of modern condensed matter theory. This includes the quantum spin Hall (QSH)[105, 106], and the quantum Anomalous Hall (QAH) phases, proposed in a seminal paper by Haldane[107] where he showed how spinless fermions moving in a honeycomb lattice exposed to a periodic magnetic field with no net flux would display quantized Hall conductance, with topologically protected edge states.

The QSH phase was proposed by Kane and Mele[105, 106]. They found that intrinsic spin-orbit coupling would open a gap in graphene with non-trivial topological order that would come accompanied by spin filtered[105] edge states robust with re-

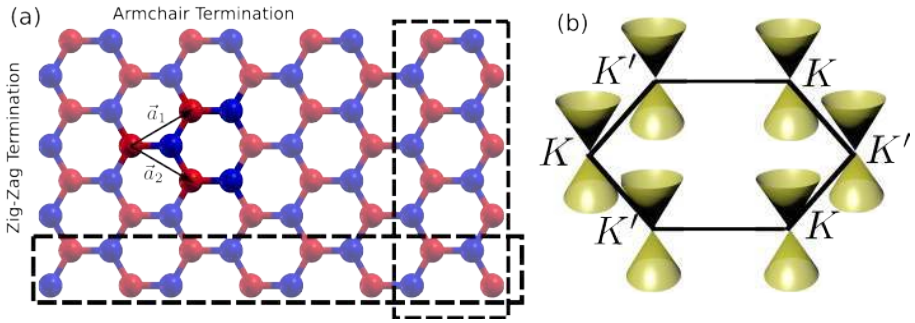

Figure 3.1: (a) Honeycomb lattice showing two types of edge, zigzag and armchair. The two triangular sublattices, A and B, are displayed with fake color, red and blue. The vectors of the Bravais lattice are also shown. (b) Brillouin zone associated to the honeycomb lattice, including the plot of the two energy bands forming Dirac cones in the neighborhood of K and K' points (see text)

spect to time reversal perturbations. Interestingly, the description of electrons with spin-orbit coupling in graphene was mathematically identical to two independent copies of the Haldane model, one per spin. They also introduced a Z_2 topological classification[106] of time-reversal invariant two dimensional systems, analogous to the TKNN classification of quantum Hall states.

Subsequent computational work[108, 109] showed that the magnitude of the intrinsic spin-orbit coupling in graphene was so small that would render the observation of the QSH phase almost impossible. However, there are graphene-like materials, such as Silicene and other group IV honeycomb crystals, for which the Kane Mele model applies[110] and for which these predictions are relevant. More importantly, there is quite strong experimental evidence that the QSH phase has been observed both in HgTe quantum wells[111] and inverted InAs/GaSb quantum wells [112], both theoretically predicted to be QSH insulators[113, 114]

The role of Coulomb interactions can also affect dramatically the properties of some of these edge states, in particular, whenever edge states produce a large density of states at the Fermi energy, that makes them prone to Stoner instabilities. This is the case of zigzag edge states for which ferromagnetic order is expected[115, 116, 117, 118, 118, 119, 120, 121, 122, 123, 124, 125]. The interplay between this magnetism, spin-orbit interactions[126, 127, 128, 129] and the Quantum Hall phases[130] is a very fascinating area of research that we also review here.

Apart from the previous examples, interfacial effects can also create topologically protected states. Some examples are driven by domain boundaries between gapped graphene[131, 132], local electric edge fields[133, 134] or interfaces between antiferromagnetic graphene and a superconductor.[135]

The basic real space model to study graphene consists on a single p_z orbital

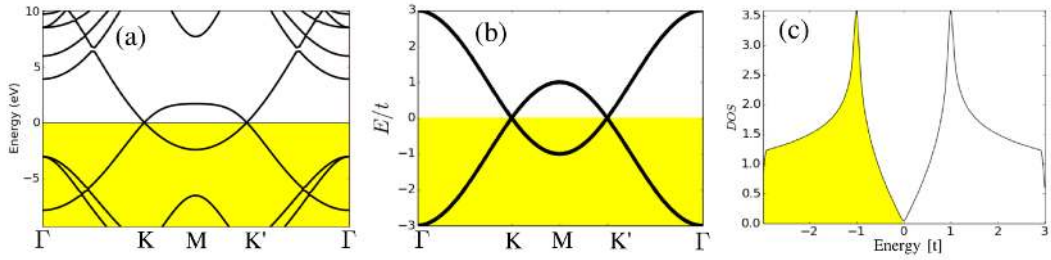

Figure 3.2: Band structure obtained by all-electron (Elk) first principles calculation of graphene (a), and band structure with a nearest neighbor tight binding model (b). Both electronic structures show the Dirac-like spectrum in the K and K' valleys. Panel (c) shows the calculation of the density of states, showing the zero DOS at Fermi level.

in a honeycomb lattice, having a honeycomb lattice. This tight binding model is able to reproduce the low energy band structure obtained in first principles density functional theory calculation Fig. 3.2. The Dirac like spectrum yields a zero density of states at the Fermi level, at the same time as a linearly dependent DOS with the energy. Within the tight binding model, the effective Dirac equation can be easily derived by Taylor expansion around the two valleys

$$H = t \begin{pmatrix} 0 & f(k) \\ f^*(k) & 0 \end{pmatrix} = \hbar v_f \begin{pmatrix} 0 & k_x + i\kappa k_y \\ k_x - i\kappa k_y & 0 \end{pmatrix} \tag{3.1}$$

In the upcoming section we will show different electronic properties that arise from the unconventional Dirac electronic spectrum. We will also show how new terms in the Hamiltonian lead to topological electronic states which show protected charge transport. These together drives our motivation in Dirac like spectrum, and will serve as a route map for oncoming chapters.

3.2 Tight binding model for graphene and graphene-like materials

A material is said to be graphene-like if its quantum states can be described in terms of a tight-binding model that describes electrons hopping in a honeycomb lattice with a single state per site. In the case of graphene, Silicene, etc, the site would be a group IV atom, and the state would be p_z orbital. Within this model, electrons can hop to their first neighbor atoms, with a hopping amplitude t, that takes a value of $t \simeq 2.7$eV[94] in the case of graphene. The tight-binding approach can also include the effect of magnetic fields by means of the so called Peierls substitution.

Basically, the effect of the magnetic field consists on multiplying by a phase the hopping integrals $t_{\alpha,\beta} \rightarrow t_{\alpha,\beta} e^{i\phi_{\alpha,\beta}}$ where

$$\phi_{\alpha,\beta} = \frac{e}{\hbar} \int_{\alpha}^{\beta} \vec{A} \cdot d\vec{r} \tag{3.2}$$

and $\vec{A}$ is the vector potential applied to the system.

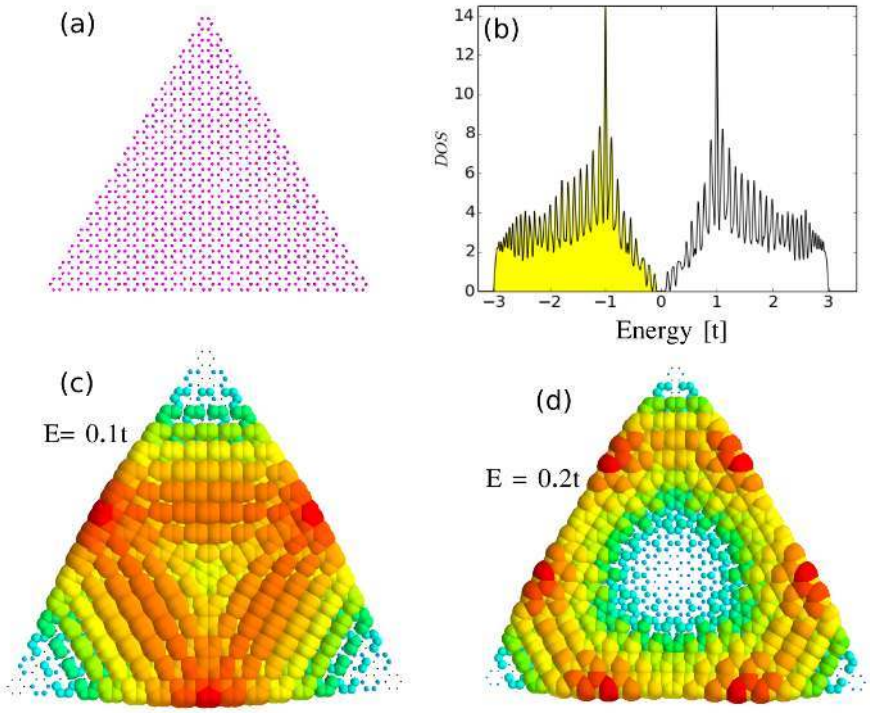

Figure 3.3: Structure of a triangular graphene island with armchair edges (a), and density of states obtained with a tight binding model (b). Due to finite size effects, the spectrum is made of confined modes that have site dependent spectral densities depending on their energy (c,d)

Within the tight binding framework it is simple to study the electronic spectrum finite size systems as well as two dimensional graphene. As an example we shown in Fig.3.3 a triangular armchair graphene island and its density of states. Due to finite size effect, the spectrum is not continuous in energy, but it resembles the DOS of bulk pristine graphene. A effect that will show up in finite systems are that the density of states is site dependent, which can be understood in terms of the normal modes of the system. This last effect will be crucial when dealing with zigzag ribbons, that have strongly localized states at zero energy. In the particular

case of this island the effect is way smother, and it appears as different spectral densities depending on the energy chosen (Fig.3.3)

3.2.1 Bloch and Dirac Hamiltonians

The honeycomb lattice of bulk graphene can be treated as two interpenetrating triangular lattices, that we label as A and B and assign them the red and blue color in Fig. 3.1. Thus, the honeycomb lattice is a triangular lattice with two atoms per unit cell that naturally leads, within the simple TB model, to a Bloch Hamiltonian of dimension two:

$$\mathcal{H}_0(\vec{k}) = \begin{pmatrix} \frac{\Delta}{2} & tf(\vec{k}) \\ tf^*(\vec{k}) & -\frac{\Delta}{2} \end{pmatrix} \tag{3.3}$$

where t is the first neighbor hopping, Δ is the so called mass term that is present whenever there is a sublattice symmetry breaking perturbation and it is assumed to vanish in the case of freestanding graphene, $f(\vec{k}) = 1+e^{i\vec{k}\cdot\vec{a}_1}+e^{i\vec{k}\cdot\vec{a}_2}$ is the form factor associated to first neighbor hopping in the honeycomb lattice, and $\vec{a}_1 = \frac{a}{2}\left(\sqrt{3}, 1\right)$, $\vec{a}_2 = \frac{a}{2}\left(\sqrt{3}, -1\right)$ where a is the unit cell spacing, which coincides with the second neighbor distance and it satisfies the relation $a = \sqrt{3}a_{CC}$ with the first neighbor distance. The resulting energy bands, $\epsilon_{\pm}(\vec{k}) = \pm\sqrt{|\frac{\Delta}{2}|^2 + |tf(\vec{k}|^2}$ are shown in Fig. 3.1b for the $\Delta = 0$ case relevant for graphene , and feature the so called Dirac cones at the corners of the hexagonal Brillouin Zone. Valence and conduction band meet at the so called Dirac point, which coincides with the Fermi energy at half filling. At this point we introduce the concept of sublattice as a pseudo spin degree of freedom. For that matter, we can write down the Bloch Hamiltonian in terms of the Pauli matrices $\sigma_x, \sigma_y, \sigma_z$:

$$\mathcal{H}_0(\vec{k}) = t\left[Re(f(\vec{k}))\sigma_x + Im(f(\vec{k}))\sigma_y\right] + \frac{\Delta}{2}\sigma_z = \vec{h}\cdot\vec{\sigma} \tag{3.4}$$

This notation makes it apparent that the Bloch states of graphene, that we can describe as two component spinors $\begin{pmatrix} \phi_A \\ \phi_B \end{pmatrix}$. Actually, for $\Delta = 0$, those states are analogous to the eigenstates of a pseudo spin under the influence of an in-plane magnetic field.

As a result, the projection of their wave functions over the two sublattices have the same weight $|\phi_A| = |\phi_B|$. In other words, the *bulk* states of graphene are sublattice unpolarized.

In the neighborhood of the K and K' points, denoted by the label $\tau_z = \pm 1$, it is convenient to Taylor expand the Bloch Hamiltonian to obtain the so called Dirac

Hamiltonian:

$$\mathcal{H}_0(\vec{q}) = \hbar v_F \left(q_x\sigma_x + \tau_z q_y \sigma_y\right) + \frac{\Delta}{2}\sigma_z \tag{3.5}$$

where $\vec{q} \equiv \vec{k} - \vec{K}_\tau$ and $v_F = 3ta_{CC}/2\hbar$, Many of the low energy properties of graphene can be understood in terms of the previous continuous model.

3.2.2 Spin dependent terms

The spin plays a crucial role in most of the edge state physics in graphene and graphene-like systems. The Hamiltonian of electrons in graphene can have up to three different spin-dependent terms. At finite field, the Zeeman term

$$\mathcal{H}_Z = \frac{1}{2} g\mu_B \vec{B}\cdot\vec{\sigma} \tag{3.6}$$

where $g \simeq 2$.

The other term is spin orbit coupling (SOC). The original atomic spin-orbit term, $\lambda\vec{S}\cdot\vec{L}$, has a vanishing value on the p_z. However, higher order processes involving orbitals from the p_x and p_y manifold, or even from the d manifold,[136] will add an effective SOC term to the Hamiltonian.

Whereas a constructive procedure has not been derived in general, the following Hamiltonian postulated by Kane and Mele, reproduces all the important properties that the actual SOC brings in more realistic calculations[105, 106]:

$$H_{KM} = \sum_{\langle\langle\alpha,\beta\rangle\rangle,\sigma} i t_{KM}\sigma\nu_{\alpha,\beta} c^\dagger_{\alpha\sigma} c_{\beta\sigma} \tag{3.7}$$

double angle brackets denote second neighbors summation, $\sigma = \pm 1$ are the spin projections (along the axis perpendicular to the crystal plane) and $\nu_{\alpha\beta} = +(-)1$ for clockwise (anticlockwise) second neighbor hopping.

When added to the first-neighbor hopping Hamiltonian, the Kane-Mele term opens a band-gap $\Delta_{SOC} = 6\sqrt{3}t_{KM}$ at the Dirac points. Thus, SOC would turn graphene into a gapped material and, as it was also found out by Kane and Mele, of a very special nature. In contrast with most of the band insulators, graphene was predicted to be a quantum Spin Hall insulator, i.e., topologically different from vacuum. A dramatic consequence of the topological non-triviality of the QSH phase is the existence of chiral edge states in graphene.

At first sight, it is somewhat surprising that in the Kane-Mele spin-orbit coupling Hamiltonian, S_z is a good quantum number, $[\mathcal{H}_{KM}, S_z] = 0$. Mirror symmetry is the ultimate cause of this conservation law, which can also be understood as follows. Spin-flip terms $S^+L^- + S^-L^+$ connect the π orbitals with the $p_{x,y}$ orbitals. Thus,

the effective Hamiltonian has to include these processes in couples, so that the π electron with spin $\uparrow$ couples to a state $p_x + ip_y$ with spin $\downarrow$ and then return to the original state, preserving the spin thereby. In addition, density function theory calculations shows[136] that even though the low energy properties are dominated by the p_z orbitals, the SOC contribution comes also from the d manifold. Actually, this contribution turns out to be even bigger than the one from the p manifold.

Whenever mirror symmetry is broken, due to application of an external off-plane electric field, or due to interaction with the substrate, another spin orbit coupling arises known as the Rashba Hamiltonian[105, 108]:

$$\mathcal{H}_R = it_R \sum_{i,j,s,s'} \vec{E} \cdot (\vec{r}_{ij} \times \vec{\sigma})_{s,s'} c_{is}^\dagger c_{js'} \tag{3.8}$$

where $\vec{r}_{ij}$ is unit vector along the bond between the carbon sites i and j, $\vec{\sigma}$ are the spin Pauli matrices and $\vec{E}$ is a vector related to inversion symmetry breaking of the graphene lattice, such as an off-plane electric field[108]. The Rashba spin orbit coupling does not commute with S_z.

3.2.3 Coulomb interaction

In general, electron-electron interactions play a secondary role in the electronic properties of graphene and graphene-like systems[137], whose defining properties are captured by the tight-binding model presented above. However, in those instances where the single-particle spectrum has a large degeneracy, such as the case of zigzag edge states as well as the bulk LL, interactions can have a strong effect. In order to model electron-electron interactions, two approximations are often employed. First, only the intra-atomic part of the interaction is considered. This is the so called Hubbard approximation:

$$\mathcal{H}_U = U \sum_i n_{i\uparrow} n_{i\downarrow} \tag{3.9}$$

where the sum runs over the sites i of the lattice. The resulting Hubbard model can not be solved exactly, except in a monostrand one dimensional chain. Thus, very often the model is treated at the mean field approximation, where the exact Hamiltonian is replaced by an effective Hamiltonian

$$\mathcal{H}_{MF} = \mathcal{H}_{\text{Hartree}} + \mathcal{H}_{\text{Fock}} \tag{3.10}$$

where

$$\mathcal{H}_{\text{Hartree}} = U \left(n_{i,\uparrow} \langle n_{i,\downarrow} \rangle + n_{i,\downarrow} \langle n_{i,\uparrow} \rangle \right) \tag{3.11}$$

$$\mathcal{H}_{\text{Fock}} = -U \left(c_{i,\downarrow}^\dagger c_{i,\uparrow} \langle c_{i,\uparrow}^\dagger c_{i,\downarrow} \rangle + c_{i,\uparrow}^\dagger c_{i,\downarrow} \langle c_{i,\downarrow}^\dagger c_{i,\uparrow} \rangle \right) \tag{3.12}$$

so that electrons interact with an external field that is self-consistently calculated. In most of papers[115, 116, 120, 122, 138, 124, 125, 127, 139] an additional approximation has been used, that assumes a collinear magnetization so that the Fock term vanishes. However, instances in which this is not the case are very interesting and also reviewed here[130].

3.2.4 Calculation method for edge states

Two methods are normally used to compute edge states starting from a tight-binding Hamiltonian. In most instances we compute the energy bands of a so called graphene ribbon, a one dimensional crystal with two edges [140]. When the width of the ribbon is sufficiently large, compared to the penetration length of the edge states, the interactions between the edges are negligible, allowing to study the properties of the edge states. Graphene ribbons are interesting by their own sake, and there has been enormous progress in the fabrication of ribbons with smooth edges[141, 142, 143, 144, 145], so that inter-edge coupling is also an interesting topic[146, 116, 117, 119, 122, 138, 124, 125, 127, 129, 145].

A second strategy to calculate edge states is to calculate the Green's function of a semi-infinite two dimensional crystal using the recursion method. Using the translation invariance along the direction parallel to the edge, it is possible to write the Hamiltonian of the semi-infinite crystal as a one dimensional semi-infinite crystal whose effective Hamiltonian depends on the transverse wave vector k. By so doing, the conventional Green's function techniques[147] normally used to deal with 1D problems can be used. In particular, the Green's function of the unit cell in the semi-infinite crystal reads:

$$G(k,E) = \left(E - h_0(k) - \Sigma(k,E) + i\epsilon\right)^{-1} \tag{3.13}$$

where $\Sigma(k)$ is the self-energy induced by the coupling to the rest of the crystal:

$$\Sigma(k,E) = t(k)G(k,E)t^{\dagger}(k) \tag{3.14}$$

where $h_0(k)$ and $t(k)$ are the intracell and intercell matrices of the Block Hamiltonian. Equations (3.13) and (3.14) define a set of non-linear coupled matrix equations that is solved by numerical iteration. Once the surface Green's function is derived, the density of states can be obtained through $\rho(k,E) = -\frac{1}{\pi}\mathrm{Im}\left(G(k,E)\right)$. Contour plots in the k, E plane can reveal the existence of in-gap edge states, as shown below.

Most of the results presented in this chapter reproduce existing results of the literature. However, we have re-computed most of them using a home-made code, Quantum Honeycomp (see chapter 12) a package that computes the electronic properties of honeycomb tight-binding models in one dimension, including the couplings to the magnetic field (eqs. (3.2,3.6), the spin-orbit couplings (eqs. (3.7,3.8))

as well as the mean field Hubbard terms in the non-collinear approximation (eqs. (3.11,3.12)). The code is available online[89] and has a graphical user interface that permits a simple use by non-experts.

3.3 Zigzag edge states

We now review the properties of the simplest type of edge state in graphene, the so called zigzag edge states. Figure 3.1a shows the two simplest types of edges in graphene, the so called armchair and zigzag. Of course, other terminations are possible in principle[139], but we shall not discuss them here. As we show now, the zigzag terminations host $E = 0$ energy states, whereas the armchair terminations do not. The ultimate reason for these states is sublattice polarization. Firstly, the zigzag edges present a very strong sublattice imbalance. Secondly all the atoms of a given zigzag edge belong to the same sublattice. This turns out to be a very important property that leads to the existence of $E = 0$ evanescent states. This can be seen in several ways.

3.3.1 Effective mass description of Zigzag edge states

A quick and simple argument for the existence of mid-gap $E = 0$ edge states in graphene can be obtained using the effective mass Hamiltonian from eq. (3.19) taking $E = 0$ and $B = 0$ and proposing the antsaz $e^{iqy}\begin{pmatrix}\phi_0(x)\\0\end{pmatrix}$ in which the wave function lives only in one sublattice. It is apparent that $\phi_0(x) = e^{-qx}$ satisfies the Dirac equation. Therefore, the localization length can be written as $\lambda = q^{-1}$, is maximal for the Dirac point, $q = 0$, and decreases (the state becomes more localized) as q increases. A more complete analysis along this line, including the calculation of the inter edge coupling in the case of graphene ribbons, can be found in the seminal work of Brey and Fertig[146]. The validity of the effective mass approximation to describe states abrupt perturbations, such as an edge, is questionable a priori. However the results of this approximation compare well with the tight-binding results[146].

3.3.2 Tight-binding description of Zigzag edge states

The existence of an $E = 0$ edge state was first inferred from the calculation of the energy bands of a zigzag graphene ribbon in the early work of Nakada and coworkers[140]. Direct diagonalization of the TB Hamiltonian yields the energy bands that we show in figure (3.4b). Two types of bands are seen: confined bulk modes, that have a gap, and two flat bands with $E \simeq 0$ corresponding to states localized at the two edges of the ribbon. Small departures of their energy from

$E = 0$ are related to inter edge hybridization. This occurs because the edge wave function associated to a given edge lives in the opposite sublattice than the edge state coming from the opposite edge. An important property of the electronic states of zigzag ribbons is that they do not mix valleys[146]. Actually, the confined bulk modes are cuts of the two Dirac cones, whereas the $E \simeq 0$ flat bands join the otherwise disconnected valleys.

The $E = 0$ wave function of a single edge can be worked out analytically[140]. If the edge atoms belong to the A sublattice, they found that $\phi_B = 0$ and $\phi_A(m) = \left(2cos\left(\frac{ka}{2}\right)\right)^{2m}$ where $m = 1, 2, ..$ labels the A atoms starting from the edge along an armchair row. This wave function is only normalized if $ka > \frac{2\pi}{3}$, i.e., between the Dirac points and the Γ point, which naturally explains the results of figure 3.4b. An expansion of the wave function coefficient around the Dirac point gives an exponential decay, similar to the one obtained using the Dirac Hamiltonian.

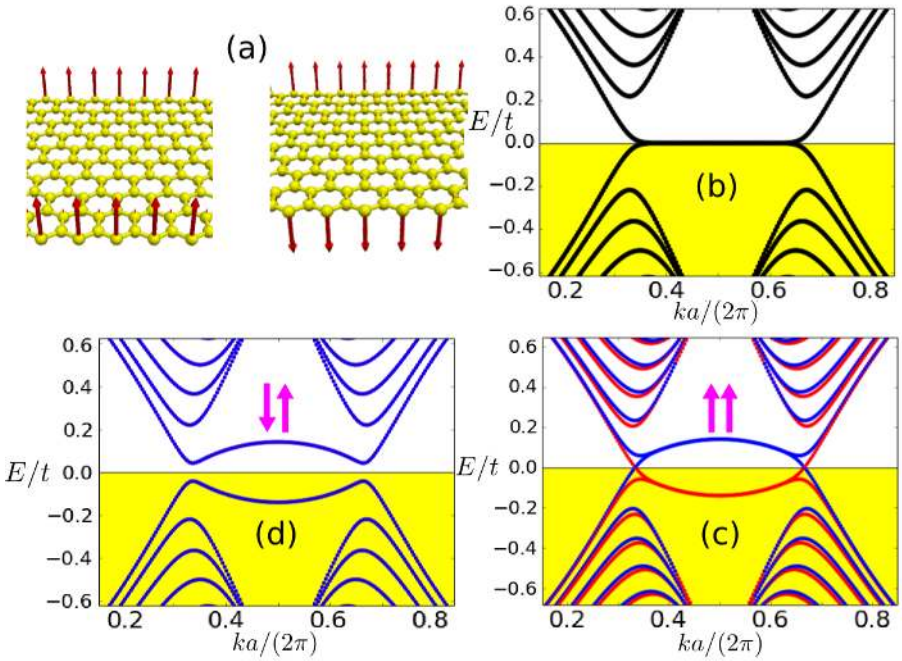

Figure 3.4: (a) Calculated magnetic moments Zigzag edge states for a graphene ribbon with $N = 20$ atoms in the unit cell, both in the AF and FM configurations, using the meant field Hubbard model with $U = t$. Energy bands for the non-interacting (b), and the AF (c) and FM (d) solutions for a ribbon with $N = 40$ atoms in the unit cell. The color red (blue) denotes spin up (down), notice that in figure (a) only one of the spins are visible but the degeneracy is two for the whole spectrum.

3.3.3 Zero modes in bipartite lattices

The zero modes of the zigzag edge can be understood in a broader context. A one orbital tight-binding Hamiltonian defined on any bipartite lattice, with a number of atoms in one lattice larger than in the other ($N_A > N_B$), has least

$$N_Z = |N_A - N_B| \tag{3.15}$$

states with zero energy whose wave function is localized in the A (majority) sublattice[148]. Three standard examples of systems with sublattice imbalance would be graphene with a vacancy[149], semi-infinite graphene with a zigzag edge and a triangular graphene island with zigzag edges[120].

The proof of this theorem goes as follows. For a bipartite lattice, the Schrodinger equation can be written as two linear systems:

$$\begin{aligned} \sum_b H_{ab}\Phi_b &= E\Phi_a \\ \sum_a H_{ba}\Phi_a &= E\Phi_b \end{aligned} \tag{3.16}$$

In order to verify the theorem, we take $E = 0$ and $\phi_b = 0$ for the N_B sites of the lattice, so that we are left with an undetermined linear homogeneous system of equations, $\sum_a H_{ba}\Phi_a = 0$, with N_A variables, the components of the wave function on the majority sublattice, but only N_B equations. There are an infinity of such solutions, which form a vector space, whose dimension is the difference between the number of unknowns N_A and the rank of the matrix of the system, N_B. This vector space is the one of the $E = 0$ modes enunciated in the theorem.

In the case of a bipartite lattice with a constant staggered potential, such that all A (B) atoms have an on-site energy $\frac{\Delta}{2}$ ($\frac{-\Delta}{2}$) the theorem can be also applied, but now the "zero modes' have energy $\pm\frac{\Delta}{2}$, depending on which one is the majority sublattice[150], and they are still entirely localized on a single sublattice.

A dramatic example of $E = 0$ edge states is provided by triangular graphene nano islands with zigzag edges[120], shown in figure 3.5. A remarkable feature of this class of systems is that their sublattice imbalance scales with size, and so it does the number of $E = 0$ states. So, the triangular islands can have strict $E = 0$ states, even for small systems. The smallest of such systems has an odd number of $N = 13$ atoms, so that it has to have a sublattice imbalance, $N_A - N_B = 1$. But the second of such structures has an even number of atoms, $N = 22$, which would permit to build many structures with $N_A = N_B$ such as pentancene , yet the triangulate has $N_A - N_B = 2$ and, thereby two mid-gap $E = 0$ states. Inspection of the wave function reveal that their wave functions have more weight on the edges[120]. Another example of $E = 0$ edge state is provided by the minimal edge that can be devised, the one created by a single vacancy. The theorem warrants the existence

of a $E = 0$ state. The lack of a gap in graphene turns this $E = 0$ state into a resonance[] whose amplitude decays . In the case the quantum spin Hall phase, where a non-trivial gap is open, the vacancy creates a real mid-gap state with a normalizable wave function[151]. In both cases, the vacancy localizes an electron

It must be stressed that the theorem of eq. (3.15) gives the minimal number of zero modes of a given structure. As discussed by Koshino and coworkers[152], the presence of symmetries in the Hamiltonian that commute with the chiral symmetry, the one responsible of the electron-hole symmetry and other features of bipartite Hamiltonians, can increase the number of zero modes if the invariant subspaces associated to that symmetry have their own sublattice imbalance. As a result, structures with a global null sublattice imbalance still have zero energy states[153].

3.3.4 Edge magnetism: mean field Hubbard model

The $E = 0$ states discussed in the previous subsection play a very important role in graphene because, at half filling, the Fermi energy lies exactly at $E = 0$. Actually, in a system with $N_A + N_B$ atoms at half filling, with $N_A > N_B$, the number of bound states with $E < 0$ is N_B, so that the valence band hosts $2N_B$. If we write the number of electrons $N = N_A + N_B = N_Z + 2N_B$, it is apparent that the in-gap $E = 0$ states are half-full. Given that the wave functions of the $E = 0$ states overlap in space, the Coulomb interactions are expected to favor ferromagnetic spin correlations, very much like in open shell atoms. In a solid state physics parlance, the presence of edge states creates a large density of states at the Fermi energy. Therefore, Coulomb interactions could result in a Stoner instability that produces ferromagnetic order.

These hand-waving arguments can be put on a very firm basis. Density functional theory (DFT) calculations have shown that zigzag edges are indeed ferromagnetic[117, 119, 120]. In the case of graphene ribbons, the magnetization of the edges affects the otherwise flat edge bands, which become dispersive. When the magnetization of the edges is (anti)parallel, the so called (anti)ferromagnetic configuration, the ribbon is (non) conducting. The change of the conduction properties of a zigzag graphene ribbon with the relative orientation of the edge magnetization inspired the proposal of a graphene based spin valve[123, 124] as well as a Silicene spin valve[154].

Interestingly, the description of the magnetic order in graphene ribbon using the mean field approximation of the Hubbard model[122, 138] gave results very similar to those of DFT and, in addition, provided analytic insight on origin of the magnetization induced dispersion as well as a treatable description of the evolution of magnetism away from half filling[155] . The difference between the $U = 0$ bands (fig. (3.4b)) and the $U \neq 0$ bands (fig. (3.4c,d)) is known as the interaction self-energy. In the case of the AF configuration, the self-energy is non zero only for

the two edge bands, so that it can be calculated analytically[122]. In that case the self-energy is a dimension two matrix and it has both intra-edge and inter-edge contributions. The former gives rise to the spin splitting of the band states close to the Γ point $k = \pi$ and is thereby identical for the AF and FM solutions. As we move away from the Γ point towards the valleys, the wave functions become more dellocalized and the inter-edge contribution to the self-energy takes over and, depending on the relative orientation of the edge magnetic moments a gap opens (AF) or a spin polarized conducting channel remains open at each valley (FM).

The results of the mean field Hubbard model calculations for the ferromagnetic (FM) and antiferromagnetic (FM) for a graphene ribbon are shown in figure (3.4), taking $U = t$ for a ribbon with $N = 40$ atoms. For this value of $U/t = 1$ the magnetization of the edge atoms is $0.15\mu_B$, three times smaller than the magnetic moment of Nickel atoms in ferromagnetic Nickel. The magnetization of non-edge atoms is much smaller and decays exponentially as a function to the distance to the edge. Within the same mean field Hubbard model, it would take a value of U larger than $2.2t$, to produce magnetic order in the bulk honeycomb lattice, which would be antiferromagnetic (AF). More sophisticated approximations, such as quantum Monte Carlo, push the critical value of U to even higher values[156]. In the case of edge atoms, the mean field magnetization is non-zero for any positive value of U[115].

In the case of triangular graphene islands, both density functional calculations and mean field Hubbard model calculations yield very similar results[120]. Triangular islands whose single particle spectrum has N_Z zero energy states develop edge magnetism with $S_Z = \frac{N_Z}{2}$, as if these systems were following the atomic Hund rule[120]. Actually, in the case of the Hubbard model, Lieb demonstrated the following theorem[157]: the spin S of the ground state of a Hubbard model defined in a bipartite lattice, at half filling, is given by $S = \frac{N_A - N_B}{2}$. Thus, the mean field approximation is, in some sense, compatible with the Lieb theorem, but it is important to keep in mind the differences between the broken symmetry mean field solutions and the exact solutions. In the case of graphene ribbons, the AF configuration has lower energy than the FM solution, which very often is said to be in agreement with the Lieb theorem, but the exact solution with $S = 0$ would have a vanishing magnetic moment at each edge, whereas the mean field AF solution the net magnetization vanishes, but not the local magnetization.

A last interesting effect in graphene islands is when spin orbit coupling effects are turned on. In the case of graphene, a Rashba-like spin orbit coupling can be tuned by applying an off-plane electric field so it will be the one we will consider. In this situation, the spin mixing effect of SOC can favor a non-collinear configuration of the edge moments as shown in Fig. 3.5c,d. The reason for this behavior is simply that Rashba coupling favors magnetization in-plane and perpendicular to the edge.

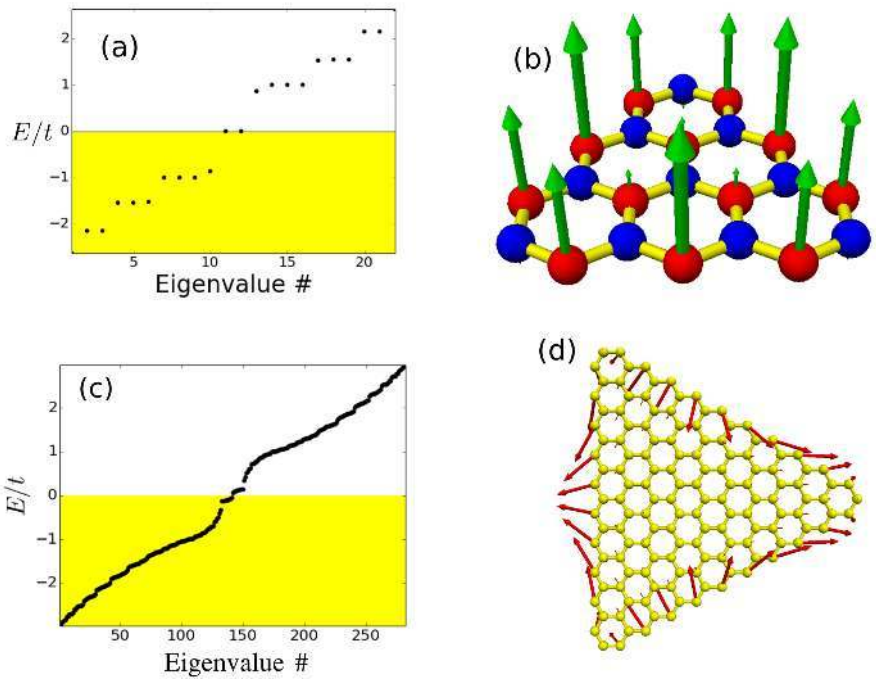

Figure 3.5: (a) Non-interacting ($U = 0$) energy levels for the $N = 22$ triangulene, Notice the two states with $E = 0$. (b) Calculated magnetization, within the mean field Hubbard model with $U = t$. The self-consistent solution has two unpaired electrons ($S_z = 2$) whose magnetization goes predominantly to the majority sublattice atoms (shown in red) at the edges. Moving now to a bigger triangular island, when SOC are turned on in the form of Rashba coupling, selfconsistent spectrum still yields spin splitting (c), but the edge magnetic can no longer be collinear, forming a spiral along the edge (d).

Since the in-plane normal to the edge changes in the different edges, the magnetic moments tend to form a spiral.

3.3.5 Beyond the mean field Hubbard model

The mean field theory of the Hubbard model provides a handy first description of the magnetic properties of the edges of graphene and graphene-like materials. However, this approach has several well known shortcomings. For instance, the long-range tail of Coulomb interactions in graphene should be poorly screened. Therefore, non-local exchange effects are missed both by mean field Hubbard approximation and DFT calculations based on local density approximations. A proper treatment of non-local exchange[158] shows that magnetic features are further stabilized, both for intra-edge and inter edge exchange.

Both local and non-local mean field approximations ignore spin dynamics and the fact that long-range order is not possible in one dimension. The spin waves of the magnetically ordered zigzag ribbon were calculated within the RPA approximation for the Hubbard model by Wakabayashi and coworkers[116] who found gap-less Goldstone modes, as expected. In consequence, long-range order should be suppressed. Therefore, at finite temperature intra-edge spins correlations are expected to survive up to a temperature dependent spin correlation length that was computed by Yazyev and Katsnelson[159]. At room temperature the magnetic correlation length was estimated to be $1nm$.

Within the mean field approximation the Fermi liquid picture of quasiparticles remains intact. However, in one dimension, interactions are expected to fully renormalize the one-particle bands, and strongly correlated phenomena such as spin-charge separation are expected to occur. This scenario has been considered for the case of quantum Hall edge states[160], as well as the quantum Spin Hall edge states[126] and more recently for the case of ferromagnetic zigzag edges as well[161].

3.4 Quantum Hall phase

In this section we discuss a totally different type of edge states. They arise in graphene when a magnetic field is applied perpendicular to its surface, they are extended much more than a few unit cells, and they can live in all types of edges, not only at zigzag boundaries. These edge states are associated to the so called Quantum Hall state, which shows a bulk insulating behavior together with perfectly conducting edge transport. In a classical naive picture, bulk insulating behavior is associated to electrons performing closed orbits, whereas the edge electrons are able to move forward in the so called skipping orbits by bouncing on the interface.

Nevertheless, the quantum mechanical treatment gives a much richer understanding of QHE. Bulk localization is associated to the emergence of the so called Landau levels (LL), with a discrete spectrum that replaces the energy bands and localized wave functions. The perfectly quantized edge conductance can be understood by taking into account the non-trivial topology of the bulk states as well as the bulk to edge correspondence.

The role of topology can be seen as follows. Both vacuum, or of that matter any trivial insulator, and the quantum Hall state are insulators. However, there is no way to change the parameters in their Hamiltonians to turn one into the other without closing the band gap. Therefore, the space of Hamiltonians generated by changing parameters in the trivial and quantum Hall insulators, without closing the gap, gives rise to (at least) two disconnected classes of insulating Hamiltonians that can not be deformed one into each other without passing through a gapless state. As a consequence, at the physical interface between two materials described with

Hamiltonians that belong to these two different classes there must be a conducting state. The general argument does not only apply to the quantum Hall state, but also to a large amount of different systems known as topological insulators. In the next sections of this review, we shall discuss also some of them in the context of graphene.

3.4.1 Electronic states

The description of the electronic states of graphene in a constant magnetic field starts with the choice of a vector potential $\vec{A} = B(-y, 0, 0)$ to be inserted in eq. (3.2), so that the original periodicity of the crystal is only preserved along the x direction. As a result, the TB description of graphene under a magnetic field is very often restricted to one dimensional stripes which permits to study the bulk and edge states on equal footing. In a tight binding model this minimal coupling is realized via Peierls substitution. The magnetic field introduces a new length scale in the problem:

$$l_B = \sqrt{\frac{\hbar}{eB}}. \tag{3.17}$$

which is $l_B = 25.7nm$ for $B = 1T$. For a sufficiently high magnetic field the magnetic length is much smaller than the width of the system W. In that situation, the bulk quantum states become localized, giving rise to LL, but the edge states are dispersive, as shown in figure (3.6) obtained by numerical diagonalization of the TB Hamiltonian for a 1D stripe with zigzag edges (3.6a) and armchair edges (3.6b).

Although pristine graphene does not show a band gap, it is interesting to note the different effects that two masses have on the Landau spectra. For the sake of simplicity will focus on the spinless case. In such situation, the two different masses that can be induced in the honeycomb lattice are a sublattice imbalance, and a Haldane mass by second neighbor imaginary hopping. The first case opens up a trivial gap, whereas the second one opens up a topological gap. In the Landau spectrum, the two different mechanisms create different splittings in the zero Landau level. In particular, sublattice imbalance creates a valley dependent splitting of the zero Landau level, whereas the Haldane mass creates a splitting with the same sign on both valleys. This can be clearly seen in Figs.3.6c,d, where it is shown the spectral function projected on the bulk of a wide Quantum Hall bar, calculated using the Kernel polynomial method. The mathematical reason for this tow different splittings of the mass will be easily understood in terms of the analytic model.

The spread of the edge wave functions depends on their energy with respect to their reference Landau level[132], scales with l_B and is thereby much larger than the spread of the $B = 0$ zigzag edge states discussed in the previous section. Importantly, in the case of zigzag edges, both the magnetic edge states and the $E = 0$ edge states

coexist. Actually, inspection of the wave functions show that, at a given valley, the two bands with $E = 0$ bands shown in fig.(3.6a) correspond both to the $n = 0$ Landau level in that valley and the edge state.

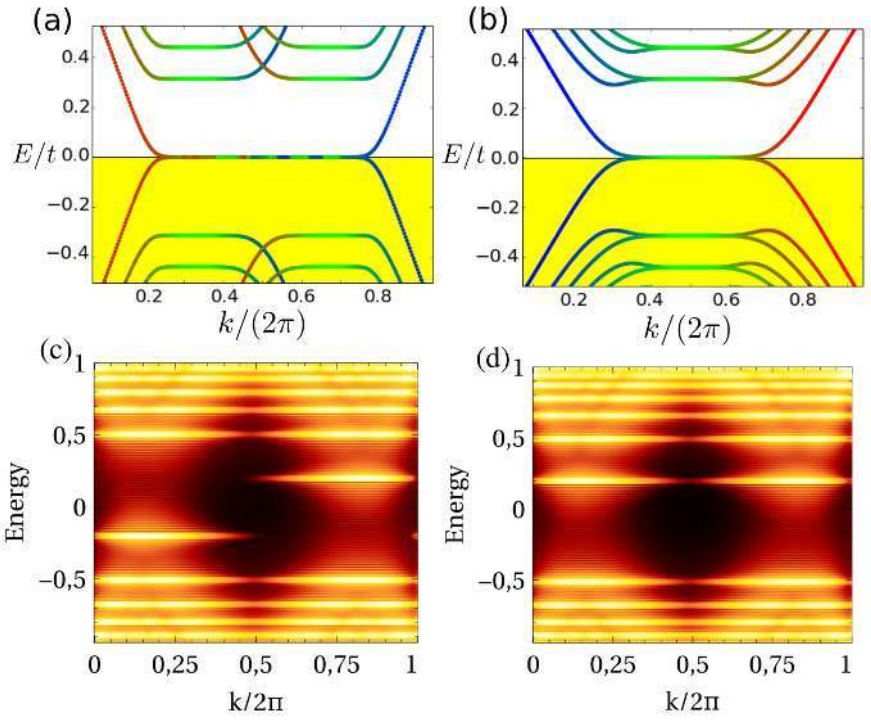

Figure 3.6: LL for zigzag (a) and armchair (b) ribbons. Band structure for a graphene ribbon with orbital magnetic field. The color code means red and blue for the edges and green denotes the bulk states. Bulk spectral function for gapped graphene (c,d), for two different gaps: sublattice imbalance (c), and Haldane gap (d), showing the different sign of splitting of the 0LL depending on the mass type. Panels (c,d) are calculated by applying the kernel polynomial method (see 13), calculating the k-resolved DOS on the bulk of a ribbon.

Further insight of these results can be obtained within the so called effective mass description, that can be formally derived from the kp theory of the energy bands. This technique had tremendous importance in the description of semiconductors[162]. In practical matters, it amounts to replace $\vec{q}$ in equation (3.5) by the momentum operator. By so doing, we obtain an effective mass Hamiltonian isomorphic to the Dirac Hamiltonian at each valley:[163]

$$H_\tau = v_F \left(\Pi_x \sigma_x + \tau \Pi_y \sigma_y\right) + \Delta \sigma_z, \tag{3.18}$$

where $\vec{\Pi} \equiv \vec{p} - e\vec{A}$ is the canonical momentum operator, $v_F = 3ta_{CC}/2\hbar$, $\vec{\sigma}$ are the

Pauli matrices describing the graphene sublattice degree of freedom and $\tau = \pm 1$ describes the valley index.

In the case of constant magnetic field perpendicular to the plane this Hamiltonian can be solved exactly. Using the transnational invariance along the x direction, we can assume its eigenfunctions are products $e^{ik_x x}\vec{\phi}_n(k_x, y)$ which permits replacing the operator p_x by the quantum number $\hbar k_x$ in Eq. (3.18). The Schrodinger equation becomes then a problem of two first order differential equations in one dimension:

$$H_\tau = v_F(\hbar k_x - eBy)\sigma_x + \tau v_F p_y \sigma_y) + \frac{\Delta}{2}\sigma_z \tag{3.19}$$

The solution of the problem is facilitated by introducing the dimensionless operators: $Q(k_x) \equiv \left(\frac{y}{l_B} - k_x l_B\right)$ and $P \equiv \frac{l_B}{\hbar} p_y$, and the ladder operators

$$\alpha(k_x) = \frac{1}{\sqrt{2}}\left(Q(k_x) + iP\right), \tag{3.20}$$

which satisfy bosonic commutation relations $[\alpha(k_x), \alpha(k_x)^\dagger] = 1$. Using these operators, the Hamiltonian (3.19) for valley $\tau = -1$ can be written as:

$$H = \frac{\Delta}{2}\sigma_z - \frac{\hbar\omega_0}{2\sqrt{2}}\left(\sigma^+\alpha + \sigma^-\alpha^\dagger\right) \tag{3.21}$$

where $\sigma^\pm = \sigma_x \pm i\sigma_y$ where we have defined $\frac{\hbar\omega_0}{2} \equiv \frac{\hbar v_F}{l_B}$. For $\tau = +1$ we have to exchange α and $\alpha^\dagger$. This model is mathematically equivalent to the Jaynes-Cummings model in quantum optics describing a two level system coupled to a bosonic mode. The resulting eigenfunctions and eigenvalues have the following properties [164, 165, 132]. First, there is a spectrum of states with wave functions with non-zero ϕ_A and ϕ_B, with energies:

$$E_N = \pm\sqrt{\Delta^2 + \frac{1}{2}\left(\hbar\omega_0\right)^2 N} \tag{3.22}$$

with N a strictly positive integer. This spectrum comes with a twofold valley degeneracy, in addition to the twofold spin degeneracy. Notice, that for $\Delta = 0$ the Landau level spectrum for Dirac particles scales with $\sqrt{NB}$, in contrast to the linear scaling of Schrodinger particles, that can be retrieved in the limit of very large Δ.

In addition to the states described with eq. (3.22), there is one *zero mode* per valley, with energy $E_0 = \tau\frac{\Delta}{2}$ and with wave function fully sublattice polarized:

$$\phi_{\tau=+1} = \begin{pmatrix} \phi_0 \\ 0 \end{pmatrix}, \quad \phi_{\tau=-1} = \begin{pmatrix} 0 \\ \phi_0 \end{pmatrix}. \tag{3.23}$$

For $\Delta = 0$, these zero mode would be degenerate at $E = 0$. Importantly, the bulk Dirac-Landau levels obtained analytically from the effective mass approach are in very good agreement with the tight-binding calculation. For the edge states it is also possible to work out the kp theory[166], but this goes beyond the scope of this review.

3.4.2 Topological origin of the edge states

As we anticipated at the beginning of this section, in the context of the non trivial topology of the band structure, the edge currents are just protected interface states in a boundary between two insulators with topologically inequivalent ground states. Moreover, the perfect conductance of this state, is a result of the relation between the quantum Hall conductance and the so called Chern number

$$\sigma_{xy} = \frac{e^2}{\hbar}\mathcal{C} \tag{3.24}$$

where $\mathcal{C}$ is the flux over Brillouin zone

$$\mathcal{C} = \frac{1}{2\pi}\int \Omega d^2k \tag{3.25}$$

of the Berry curvature Ω

$$\Omega = i\left(\partial_{k_x}\langle\Psi|\partial_{k_y}|\Psi\rangle - \partial_{k_y}\langle\Psi|\partial_{k_x}|\Psi\rangle\right) \tag{3.26}$$

which acts as an anomalous term in the velocity.

The Chern number of normal insulators is $\mathcal{C} = 0$. In contrast, the Chern number of the quantum Hall state is an integer different from zero[167], which results in the quantization of the Hall conductance.

In the case of interfaces between two different quantum Hall states, the previous interpretation gives a simple way to predict the number of edge states. For an interface between a first system with Chern number $\mathcal{C}_1$ and a second system with Chern number $\mathcal{C}_2$, the number of protected edge states is simply $|\mathcal{C}_1 - \mathcal{C}_2|$.

In the quantum Hall regime, the lack of edge states when a sublattice imbalance mass gap opens at half-filling[168, 160, 130], accounts for $\mathcal{C} = 0$ and can be rationalized in terms of adiabatic evolution of the massive Dirac Hamiltonian from $B = 0$. Taking the half-filled case as a reference, the total Chern number away from half filling can be calculated by adding one unit for each Dirac Landau level crossed by the Fermi energy as we move it up, including the valley and spin degeneracy. Conversely, if we consider hole doping, the Chern number becomes negative as we move the Fermi energy down in energy. For example, starting from half filling filling the electron $n = 0$ Landau level gives $\mathcal{C} = 1$ per spin channel, as can be observed in Fig. 4. Analogously, un-filling the hole $n = 0$ level gives a total $\mathcal{C} = -1$, per spin channel. This will lead to remarkable phenomena when dealing with spin polarized systems. As we discuss below, different fillings for the up and down channels, can give rise to a very special type of quantum spin Hall effect[168].

A final remark is that vacancies in a system with the Quantum Hall state can be understood as tiny boundaries. In the case of a graphene lattice which has a single missing atom, the spectral function close to the missing site shows additional peaks

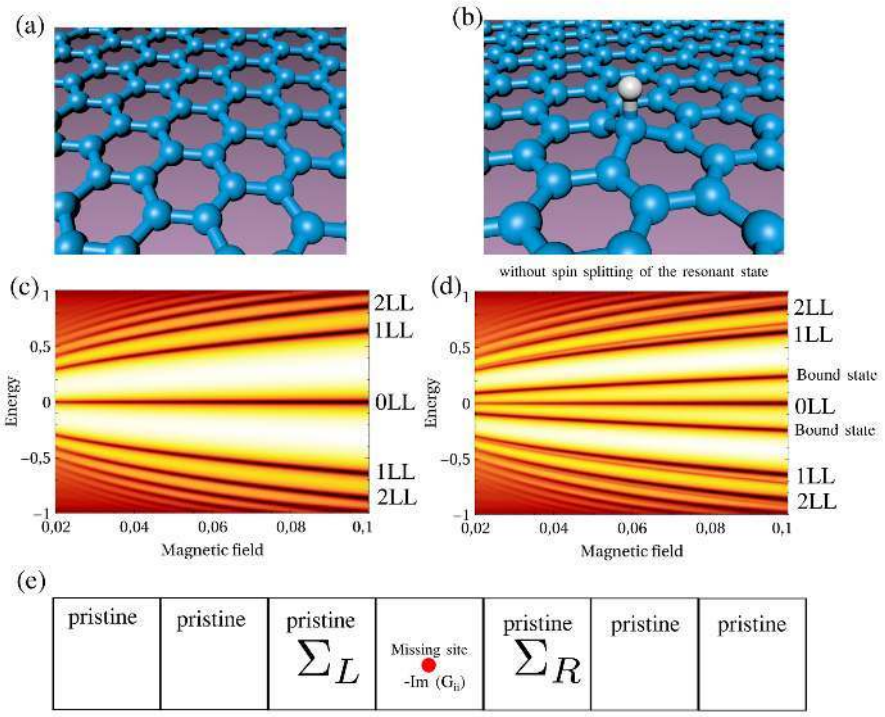

Figure 3.7: Sketch of pristine (a) and single hydrogenated graphene (b), the later being equivalent to a missing atom in the honeycomb lattice. When magnetic field is applied, calculation of the spectral function shows that a set of Landau levels shown up (c), and bound states close to the vacancy (d). Panel (e) shows the partition of the lattice considered in the computational method to study the vacancy in quantum Hall regime.

Apart from the one that arise due to Landau quantization. This can be seen clearly in Fig. 3.7 where the spectral function in the bulk of graphene bar is shown. In the first case (Fig. 3.7a,c) the bulk is pristine graphene, and therefore shows poles that evolve with the magnetic field as $\sqrt{(Bn)}$. In comparison, when a single atom is introduced, an additional set of poles appear (Fig. 3.7b,d), located between the ones of the bulks Landau levels. Those states correspond to bound states of the defect, and when the hole becomes bigger will turn into the dispersive edge band. The method to get the spectrum of this system relies on solving the Dyson equation for a single impurity in an infinite ribbon $G = (E - H_0 - \Sigma_R - \Sigma_L)^{-1}$ (Fig. 3.7e), where the two leads are pristine. Afterwards, the Green function is projected onto the proximity of the vacancy to avoid the edge states contribution.

3.5 Quantum Anomalous Hall phase

Another kind of topologically non-trivial quantized phase is the so called Quantum Anomalous Hall (QAH) phase. This topologically insulating phase has properties analogous to those of the quantum Hall phase, including chiral edge states for which backscattering is impossible, and breaking of time reversal symmetry. However, the QAH phase is driven by internal degrees of freedom and interactions, such as spin-orbit coupling and exchange, rather than by the application of an external magnetic field. The fabrication of materials showing this phase has enormous potential since they are expected to show a perfect edge conductance as the quantum Hall state, but without the drawback of having to apply large magnetic fields[].

Two important graphene related models present the QAH phase. First, the Haldane model for spinless fermions moving in a honeycomb lattice[107]. Second, graphene perturbed both with a Rashba spin-orbit interaction and subject to an exchange field that couples to the off-plane spin component [169, 170].

3.5.1 Haldane model for QAH

The toy model proposed by Haldane[107] consists of a honeycomb lattice in which there are local magnetic fields of different sign within the hexagon, but whose flux over it is zero. This gives rise to an imaginary second neighbor hopping, which accounts for the local magnetic fields:

$$\mathcal{H}_{QAH1} = \mathcal{H}_0 + t_2 \sum_{\langle\langle i,j\rangle\rangle} i\nu_{ij} c_i^\dagger c_j \tag{3.27}$$

where $\nu_{ij} = \left(\vec{d}_1 \times \vec{d}_2\right) \cdot \hat{z}$ is the chirality of the path of the second neighbor hopping, where $\vec{d}_{1,2}$ are defined as follows: for a given pair of second neighbor atoms i and j, with a common first neighbor k, $\vec{d}_{1,2}$ are the unit vectors along the bonds ik, kj, respectively.

In this model, the bulk is characterized by a gapped spectrum as shown in (Fig.3.8a). A kp expansion of the t_2 term around the Dirac point would yield the following extra term in the Dirac Hamiltonian:

$$\delta H = \frac{3}{2}\sqrt{3} t_2 \tau_z \sigma_z \tag{3.28}$$

where the *mass* can be written as a valley dependent object, $\Delta_{QAH1} = 3\sqrt{3}\tau_z$, in contrast with eq. (3.5). This has a very important consequence. The Chern number associated to Hamiltonian (3.5) reads[171]:

$$\mathcal{C}(\Delta, \tau_z) = \frac{1}{2}\tau_z \frac{\Delta}{|\Delta|} \tag{3.29}$$

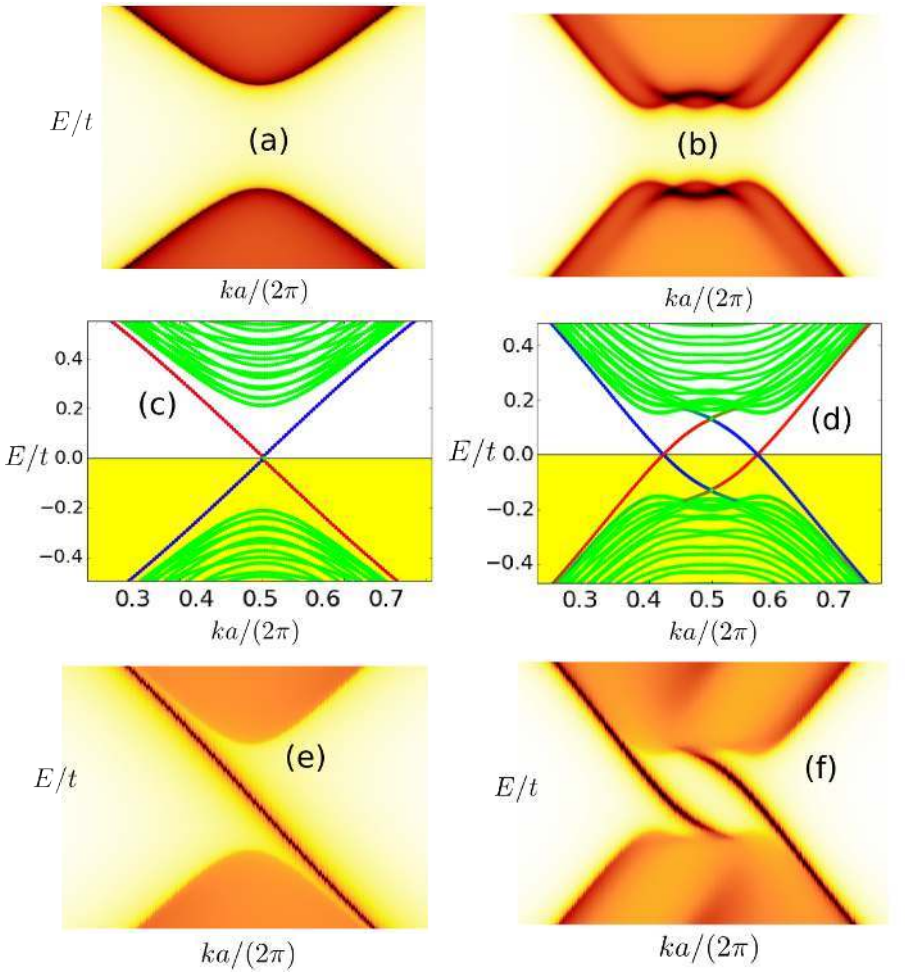

Figure 3.8: Quantum Anomalous Hall phase in two toy models. Left panels: Haldane model[107]. Right panels: model proposed by Qiao and coworkers[169]. Panels (a,b): Bulk density of states showing a gapped spectrum resolved in the k_x Panels (c,d): band structure of an armchair ribbon system for the same two models, showing that in addition to the gapped bulk states, gap-less edge states show up. Panels (e,f): density of states in the armchair edge of a semi-infinite plane, showing a coexistence of bulk and one-way edge modes, calculated using the Green's function approach.

Therefore, in the Haldane model both valleys contribute with a Chern number with the same sign that sum $\mathcal{C} = 1$, whereas in graphene with a trivial gap, opened with a term that breaks sublattice symmetry, the two valleys contribute with a Chern number with opposite sign, that give $\mathcal{C} = 0$.

From the $\mathcal{C} = 1$ for the Haldane model we expect the existence of a chiral edge

band. This is seen in the spectrum of a ribbon with armchair edges as in-gap chiral state in (Fig.3.8c), together with the confined modes (in green). The chiral character of the edge states prevents backscattering. Therefore, the Haldane model describes a phenomenology identical to the quantum Hall phase, but without the presence of flat Landau levels in the bulk. In addition, a generalization of the Haldane model played a crucial role in the proposal in the proposal of the quantum Spin Hall phase[105, 106], as we discuss below.

3.5.2 Exchange plus Rashba model for QAH

A more realistic model describing another realization of the quantum anomalous Hall state in graphene was proposed by Qiao and coworkers[169, 170]. In their model they describe electrons in graphene including both the Rashba spin-orbit term (eq. (3.8)) and exchange fields that splits the spin along the off-plane direction:

$$\mathcal{H}_{QAH2} = \mathcal{H}_0 + \mathcal{H}_R + \lambda \sum_{i,s} c^\dagger_{is} s_z c_{is} \tag{3.30}$$

A qualitative understanding of how these two terms open a gap in the bulk structure, can be gained from the following argument. The off-plane exchange field will split the Dirac cones[169, 170], so that the $\uparrow$ and $\downarrow$ cones are degenerate on a circle in momentum space that, at half filling, corresponds to the Fermi circle. The Rashba term couples $\uparrow$ and $\downarrow$, opening a band gap in the Fermi circle.

The k_x resolved bulk DOS shows again a gapped spectrum (Fig.3.8b). However for a finite ribbon, several bands crossing the Fermi energy appear (Fig.3.8d). From those four bands that appear in the ribbon, two of them are located in one edge of the ribbon and two in the other. This becomes clear calculating the DOS on the edges, showing also that the two bands present are co-propagating, thus yielding a protection against back-scattering as in the Haldane model. The Chern number of this is system is $\mathcal{C} = 2$,[172] in agreement with the two states per edge observed in Fig. 3.8d.

There are several proposals to modify graphene so that it is described by Hamiltonian (eq. (3.30)), including the use of ferromagnetic substrates,[173] magnetic ad-atoms,[174] and even antiferromagnetic substrates[175]. Finally, a similar QAH can be obtained in graphene [176] by replacing the Rashba-like term by a topological spin texture known as skyrmion.

3.6 Quantum Spin Hall phase

The prediction[105, 106, 113] and discovery[111] of the Quantum Spin Hall phase boosted the research field of topological insulators. Very much like the QH and QAH

phases, the QSH phase has an insulating bulk and conducting chiral edge states which, in contrast with the QH and QAH case, have well defined spin chirality: a given edge hosts two counter-propagating states with opposite spin projection, which has potential for spin electronics applications[177, 178]. Here we discuss two of the pioneer proposals for the QSH, both of them based on graphene. In the first one, Kane and Mele proposed[105, 106] that intrinsic spin-orbit coupling would turn graphene into QSH. Unlike the QH and QAH, this system would be time reversal invariant. The second proposal, by Abanin and coworkers[168] is rather special: ferromagnetic order of the QH phase in graphene at half filling, for which $\mathcal{C} = 0$, would results in a QSH phase, with $\mathcal{C}_\uparrow = -\mathcal{C}_\downarrow = +1$, but with time reversal symmetry clearly broken. We now review the most remarkable features of the edge states of these two fascinating QSH states.

3.6.1 QSH driven by spin-orbit

The influence of atomic spin-orbit coupling on the Dirac bands, formed by $L_z = 0$ atomic orbitals, is subtle: to lowest order, the atomic spin orbit coupling $\lambda \vec{L} \cdot \vec{S}$ within the p-manifold has no effect at all. Second order interband scattering gives the first non-zero contribution but it is not obvious how to include it in the Hamiltonian. Further work,[136] showed that inclusion of $d-channels$ lead to a first order contribution in SOC. In their seminal work, based on symmetry considerations, Kane and Mele postulated that the effective Hamiltonian for SOC in the subspace of the π orbitals would be given by a spin dependent second neighbor hopping, eq. (3.7), which turns out to be mathematically identical to the Haldane term that, as discussed in the previous section, turns spinless fermions into the QAH phase. Thus, the Kane-Mele Hamiltonian $\mathcal{H}_0 + \mathcal{H}_{KM}$ for graphene with SOC is made of two decoupled copies of the Haldane model, one per spin, with opposite sign of the gap-opening term. Thus, the QSH phase described by the Kane-Mele model can be thought of as two QAH, one per spin, with opposite magnetization.

In the neighborhood of the Dirac points, the KM model would give the following Hamiltonian:

$$\mathcal{H}_{KM}(\vec{q}) = \mathcal{H}_0(\vec{q}) + \frac{3}{2}\sqrt{3}t_{KM}\tau s_z \sigma_z S_z \tag{3.31}$$

where $\mathcal{H}_0(\vec{q})$ is given by eq. (3.5). Thus, the Kane-Mele gap-opening term respects both time-reversal symmetry and inversion symmetry, in contrast with eq. (3.28).

The fact that the Kane-Mele model consists of two copies of the Haldane model permits to anticipate its most salient electronic properties: bulk states present a gap while the edges host one chiral conducting states per spin channel. Since the sign of the gap is given by the projection of the spin S_z, spin $\uparrow$ and $\downarrow$ edge states propagate in opposite directions, i.e., they have a well defined spin chirality. As a result, the

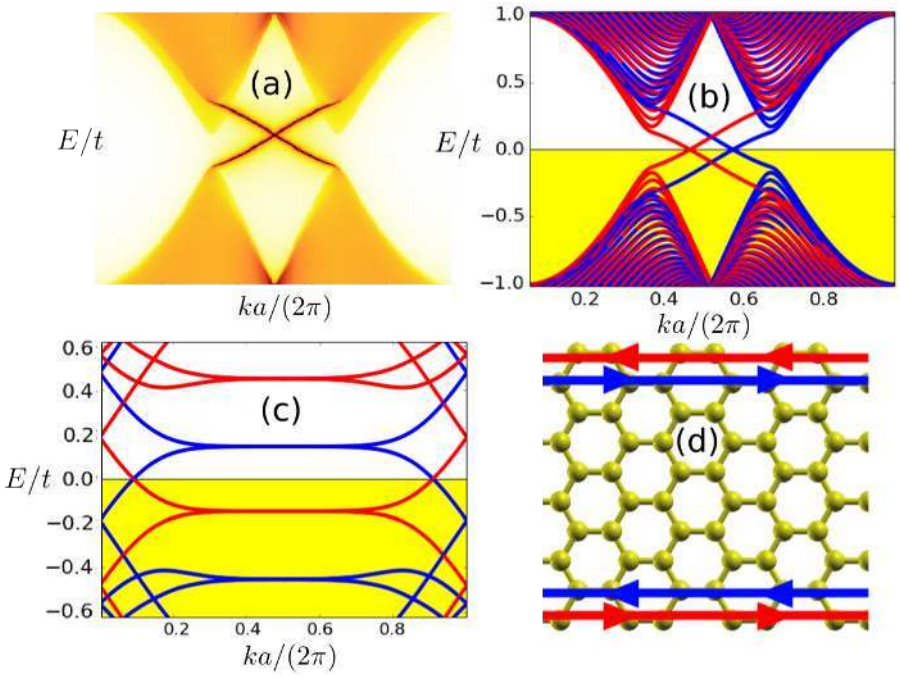

Figure 3.9: Top panels: Electronic band structure of a graphene zig-zag ribbon with a small staggered potential and an external magnetic field (off-plane) to resolve the degeneracies. Panel (a) shows the density of states at the edge of a semi-infinite plane with zig-zag termination. Panel (b) corresponds to the band structure of a zig-zag ribbon, the color represents spin polarization. Panel (c): the band structure for a ribbon in the presence of an off-plane Zeeman magnetic field and an orbital magnetic flux leading to the appearance of LL. In panel (d) a scheme of the QSH effect, where two spin polarized conducting states are present in each edge.

edge states carry an equilibrium spin current, in contrast with the QH and QAH phases for which edge states carry a net charge current (see figs. 3.9(a,b,d)).

Trivially, the Chern number of each spin channel is $\mathcal{C}_{S_z} = sgn(S_z)$, so that the spin Chern number $\mathcal{C}_\uparrow - \mathcal{C}_\downarrow = 2$ would be finite but the the total Chern number would vanish. So, it would seem that the addition of spin-flip perturbations, such as the Rashba Hamiltonian, would result in intra-edge backscattering. However, this is not the case and it turns out that the Spin Hall phase is topologically different from the normal phase, even when S_z is not conserved. To show this, Kane and Mele introduced another topological invariant[106] in order to classify these systems, the Z_2 invariant. The Z_2 group consists only of two elements, say, $\{0, 1\}$ and according to Kane and Mele's classification, all non-trivial insulators would have a Z_2 index equal to 1 while trivial insulator would have Z_2 index equal to 0. When $Z_2 = 1$ the edge states are counterpropataging Kramers pairs, so that only perturbations

that break time reversal symmetry can produce backscattering. Importantly, Kane and Mele showed that the addition of a small Rashba term to their Hamiltonian would keep $Z_2 = 1$, and only when the Rashba term is large enough as to close the bulk gap would the system turn into a $Z_2 = 0$ trivial phase without topologically protected edge states.

Whereas the observation of the spin-orbit coupling driven QSH phase in graphene is very difficult due to the small size of the spin-orbit gap (smaller than 0.1 meV[108]), the observation of the Quantum Spin Hall phase HgTe/CdTe quantum wells [179] as well as in $InAs/GaSb$ inverted quantum wells[112] has confirmed the existence of this fascinating class of materials.

3.6.2 Quantum spin Hall effect without spin-orbit coupling

Even if spin-orbit coupling can not drive graphene into the QSH phase, there is a different mechanism that can do the trick and, contrary to other proposals[105, 106, 113], it does not require spin-orbit coupling[168]. This mechanism relies instead on the very special Landau level structure that emerges upon application of a magnetic field.

Lets take graphene under the influence of an off-plane magnetic field. At half filling, the Chern number of all the occupied bands is zero and two of the four $n = 0$ LL, *valence* and *conduction* with spin degeneracy. Due to the four $n = 0$ are degenerate, there are several alternative filling patterns. At half filling, all possible combinations give $\mathcal{C} = 0$, but it is possible to have $\mathcal{C}_S = 2$ if we fill the two LL with the same spin, and leave empty the other two. Interestingly, this spin-polarized filling can be driven by Coulomb interactions[168, 160, 180, 181] and also by intrinsic spin-orbit coupling[182].

Thus, at half-filling, the spin-polarized quantum Hall phase has $\mathcal{C} = 0$ and $\mathcal{C}_\mathcal{S} = \pm 2$, so that it has the same topological properties than the QSH phase described by the Kane-Mele model. The energy bands corresponding to the addition of a large Zeeman splitting are shown in figure 3.9(c). They feature a gapped bulk together with counter-propagating spin-filtered in-gap edge states. Similar results can be obtained[130] using a self-consistent calculation of the mean field Hubbard model, including an in-plane Zeeman field that favors ferromagnetic order.

Unlike the QSH phase driven by spin-orbit coupling, spin-flip perturbations give rise to spin-flip edge backscattering and, because time reversal symmetry is broken, it is not possible to accommodate this QSH system into the Z_2 classification of Kane and Mele. Interestingly, there is very strong experimental evidence that this interaction driven QSH phase has been observed in the experiments, where the ferromagnetic order is favored by applying a quite large in-plane magnetic field[183]. At half filling, the experiments show how two terminal conductance of graphene is tuned from 0, corresponding to a gapped quantum Hall phase to $1.8\frac{e^2}{h}$, that most

likely is the QSH phase predicted[168] by Abanin and coworkers.

3.7 Coulomb driven breakdown of the edge conduction in the QSH phase

The gapless edge states in the quantum spin Hall states are protected by the spin Chern number in the case of magnetic field driven phase,[168] and by the Z_2 invariant in the case of the SOC driven.[106] These topological invariants are well defined as long as S_z is a good quantum number (Spin Chern) and time reversal symmetry is present (Z_2). In the case spontaneous magnetism shows up, such conditions no longer apply, so the gap-less edge states are no longer guaranteed.

In this section we show two examples of how Coulomb interactions can lead to the disappearance of spin chiral edge states due to the emergence of spontaneous edge magnetization. Following the structure of the previous section, we consider both the SOC driven, and the quantum Hall ferromagnet QSH phases.

3.7.1 Kane-Mele-Hubbard model

In order to study the interplay between edge magnetism and topologically protected edge states we use the so called Kane-Mele-Hubbard model[184, 127, 185, 186, 187, 188, 129] Although the gapless edge states are protected against time reversal perturbations, an important issue is whether electron-electron interactions are able to drive the system into a symmetry breaking state. The study of the bulk properties of the Kane-Mele-Hubbard model has attracted considerable attention[185, 186, 187, 188]. Here we focus on the competition between SOC and magnetic order at the edges[127, 189, 129].

Edge magnetic order would break time reversal symmetry and could gap out those edge states. Early work assumed that magnetic order would be off-plane[127, 189]. In this situation, the gapless edge states survive (Fig.3.10c), at least for small U and large SOC[127]. In general, magnetic order in a topological insulator protected by time reversal symmetry should destroy the gapless edge states. This case is exceptional because in addition to being protected by time reversal symmetry, the Kane-Mele model shows a well defined spin Chern number, which relies only in conservation of S_z, preserved by the off-plane magnetic order.

The situation changes radically when the edge magnetic moments lie in-plane.[190, 129] Then, S_z is no longer a good quantum number, and thus the protection that remained in the off-plane magnetic case no longer holds. Now, the in-plane magnetism opens up a spin mixing channel, driving the system into an edge insulator, as shown in Fig.3.10d.

Interestingly, spin orbit coupling produces magnetic anisotropy, so that both configurations are not expected to be energetically equivalent. Actually, the ground state of the mean field Hubbard model is in fact the in-plane magnetic state.[129] However, the disappearance of the chiral edge states can be restored, by overcoming the magnetic anisotropy of the system, and forcing the states to lie off-plane. This could be achieved by a magnetic substrate, which if made switchable, would allow to control the flow of the spin channels along the edge at will.

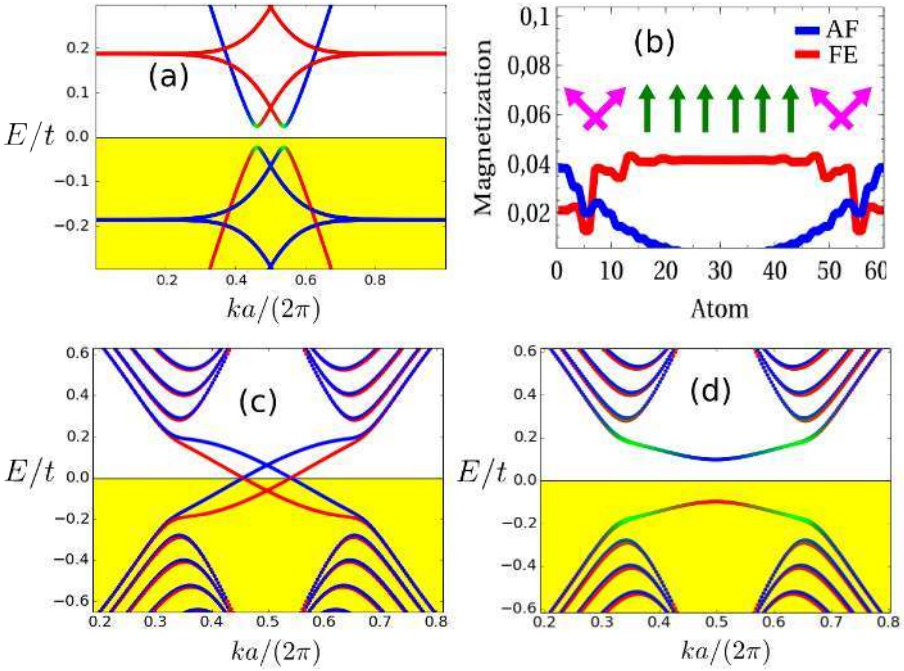

Figure 3.10: Band structure (a) and local magnetization (b) of the ferromagnetic quantum Hall state with interaction driven edge canted antiferromagnetism. The local edge antiferromagnetism, gapes out the original counter propagating spin filtered edge state. Band structure of a zigzag ribbon with spin orbit, whose edge magnetic moments driven by interaction are of plane (c) and in-plane (d). The in-plane magnetization destroys the gapless states due to breaking of TR and spin mixing, whereas the off-plane does not because s_z is still conserved.

3.7.2 Magnetic field driven QSH phase

In this situation, the shifting between the LL driven by the magnetic field yields the effective Quantum Spin Hall state.

The state arises when the in-plane field is large enough to overcome the possible antiferromagnetic state.[191] However two situations of edge states are possible. On

one hand, at weak interactions the edge becomes ferromagnetic at the same time as the bulk. On the other hand, when interactions are stronger, the edge of the system is able to develop a canted magnetic order, even though the bulk remains ferromagnetic.

Experimentally, it was observed that in order to reach the QSH in graphene, a large magnetic field of 20 T had to be applied.[183] Two different scenarios are possible to understand the large field needed to overcome a the fully gapped phase. The first one consists on having an AF ground state at zero in-plane field, turning it into ferromagnetic above the critical field.[191] In this situation, the edge does not play a key role, and the conductance only depends on the bulk magnetic order. A second scenario appears when considering that, according to theoretical predictions,[180, 181] the order in the bulk is actually ferromagnetic due to the long range Coulomb interaction. Starting in this situation, two counter-propagating spin polarized states appear on the edge of the system.[168] Those states, can be highly vulnerable to the local electron-electron interactions, and a local canted antiferromagnetic gap can be opened, gaping out the states and destroying the quantum Hall state. Thus, the critical field needed to reach the QSH is the one needed to recover ferromagnetism on the edge. In the context of the Hubbard model, it is found that at medium interactions ($U = 2t$), even in the presence of an exchange field, the bulk of the system can be in a ferromagnetic state, at the same time the edge remains a canted antiferromagnet, as shown in Fig.3.10b.

3.8 Experimental evidence

All the previous discussion was focused on our theoretical understanding of a variety of different edge states in graphene and graphene like systems. Here we briefly touch upon the experimental evidence that has been obtained so far.

3.8.1 Zigzag Edge states and edge magnetism

We first discuss the observation of zigzag edge states and edge magnetism. Scanning tunneling microscopy (STM) had permitted early on to identity zigzag and armchair edges in graphite[192]. A fairly convincing evidence[144] of the existence of localized edge states at chiral edges of ultrahigh quality graphene ribbons obtained by unzipping carbon nanotubes[141] was obtained by means of scanning tunneling microscopy. The same group also showed the capability to engineer the edges by means of plasma etching[193] of graphene nanoribbons (GNR). They found that hydrogen-plasma-etched GNRs are generally flat, free of structural reconstructions, and terminated by hydrogen atoms with no re-hybridization of the outermost carbon edge atoms. Both zigzag and chiral edges show the presence of edge states.

Edge states at the interface between graphene and h-BN have also been imaged with STM[194].

The direct evidence for edge magnetism is less abundant, and most of the claims are based on indirect evidence. Part of the problem is that conventional magnetic probes, such as SQUID and EPR, have a resolution limit in the range of $10^{12}\,\mu_B$ that would require graphene flakes beyond current capabilities[195]. Therefore, such measurements are performed on solutions of graphene processed by various techniques, including unzipping carbon nanotubes whose grow very often requires ferromagnetic catalyst. Therefore, the observation of room temperature ferromagnetism in graphene ribbons[196] should be revised under the light of the recently work [197] discussing artifacts for analogous claims for highly oriented pyrolitic graphite[198].

These shortcomings highlight the need to study edge magnetism in graphene using some sort of local probe, preferably spin polarized STM[199], or some type of nanomagnetometry technique, such as NV center detectors, that can be used to probe local moments on a surface[200]. A non-magnetic local probe was used by Tau and coworkers[144] who compared their fairly extensive STM spectroscopy, both along the edge of the ribbon and in the direction perpendicular to the edge with mean field Hubbard model calculations where edge magnetism was included. The good agreement between theory and experiment is certainly a hint that edge magnetism was present. Further computational work using density functional calculations have confirmed[201] the presence of edge magnetism in hydrogenated graphene ribbons deposited on Au(111). However, they also showed edge magnetism would not survive on other substrates, such as Cu(111) and Ag(111).

The claims of room temperature edge ferromagnetism in graphene ribbons[145] are also based on STM spectroscopy and comparison of the data to well established theoretical results. Unlike the work of Tau et al[144], a detailed evolution of the $I(V)$ curves along the ribbons is not provided. In addition, edge magnetism is definitely not expected to survive up to room temperature[159], although the effect of long-range order depletion due to quantum and thermal fluctuations on the spectral function of the quasiparticles has not been studied. A local probe of magnetism would be desirable in order to back up these extraordinary claims.

The recent report[202] of ballistic transport with a conductance of $G = \frac{e^2}{h}$ in epitaxial graphene nanoribbons would imply time reversal symmetry breaking compatible with edge magnetism. Great care was taken by the authors of this paper to rule out a great number of possible experimental artifacts and the understanding of their data remains a very interesting challenge for theory.

Finally, recent experimental breakthrough showed the synthesis of high quality graphene islands and ribbons by means of organic chemistry methods[203]. The method consists on cyclohydrogenation of specific precursor monomers.

The finite spin of small triangulate molecules, with $S = \frac{1}{2}$ and $S = 1$ has been

observed experimentally[204], in macroscopic samples, using electron paramagnetic resonance techniques.

3.8.2 Edge transport in topological phases in graphene like systems

The observation of the quantum Hall effect in graphene with perfect quantization of the Hall conductance provides an extremely convincing, albeit indirect, evidence of the existence of Quantum Hall edge states. The Quantum Spin Hall predicted by Abanin *et al.*[168] has been recently found experimentally[183] by A. Young and coworkers. They verified, by means of local capacitance measurements, the opening of a band-gap in bulk and the edge nature of the transport by means of a floating gate technique[183]. The edge conductance in the QSH-like phase was $G = 1.8G_0$, below the ideal case of $G = 2G_0$ which suggest that some sort of spin-flip backscattering mechanism is present in the sample. Moreover, a quantum spin Hall state in twisted bilayer graphene has also been reported[205], whose origin can be rationalized as two decoupled quantum Hall states for each monolayer.

3.9 Summary

We have provided an overview of the electronic properties of edge states in graphene, and related materials, using as a guideline the standard tight-binding model for electrons in a honeycomb lattice. Remarkably, small additions on the same model that describes the main properties of graphene, including the observed quantum Hall phase, have led to the prediction of the Quantum Spin Hall and Quantum Anomalous Hall phases, inspiring the search of graphene based topological phases. Therefore, small modifications of graphene, via proximity or functionalization, are expected to drive graphene into these exciting topological phases.

Edge states play an important role in the study of some of the most fascinating electronic properties of graphene and graphene like materials. The study of graphene edge states has ramifications in many branches of modern material science, including graphene spintronics[30], organic chemistry[203], quantum topological phases[183], and metrology[206], just to mention a few.

Combined with the discovery of new graphene-like materials, and the construction of artificial structures where different two dimensional crystals are stacked and put in close proximity to materials with various types of electronic order, such as ferromagnetism and superconductivity, we can expect that the study of the electronic properties of edge states will bring many exciting results in the years to come.

Chapter 4

Magnetic anisotropy in graphene-like crystals[1]

Graphene zigzag edges show strongly localized edge states that can show magnetic order. In addition, spin orbit coupling creates topological spin polarized edge states, which are potentially gapped out by magnetism. In this chapter we will show the interplay these two phenomena, and unveil how the direction of the magnetization dramatically changes the transport properties.

4.1 Introduction

The independent predictions of edge ferromagnetism and the Quantum Spin Hall phase in graphene have inspired the quest of other two dimensional honeycomb systems, such as silicene, germanene, stanene, iridiates, and organometallic lattices, as well as artificial superlattices, all of them with electronic properties analogous to those of graphene, but much larger spin-orbit coupling. Here we study the interplay of ferromagnetic order and spin-orbit interactions at the zigzag edges of these graphene-like systems. We find an in-plane magnetic anisotropy that opens a gap in the otherwise conducting edge channels, that should result in large changes of electronic properties upon rotation of the magnetization.

Magnetic anisotropy, a technologically crucial property, is driven by spin-orbit interaction, which is normally the underdog in the competition with the other two terms that control ferromagnetism, namely, kinetic and Coulomb energy[207]. As a result, magnetic anisotropy energy in conventional ferromagnets is at least 2 orders of magnitude smaller than the Curie temperature and the Fermi energies (or the band-gap, in the case of insulators). For the same reason, transport properties in

[1]Sections 4.1 to 4.4 of this chapter are based on the publicaiton Physical Review Letters 113 (2), 027203 (2014)

ferromagnetic metals are only weakly dependent on the magnetic orientation, and typical values for the anisotropic magnetoresistance (AMR) are below 3 percent[207].

Here we study magnetic anisotropy in a class of systems for which the balance between these three energy scales is very different from the usual, which leads to two dramatic consequences, very different from conventional ferromagnetism. First, the conducting properties change from metal to insulator, depending on the magnetization orientation, an effect that, to the best of our knowledge, has never been reported. Second, the magnetic moment magnitude depends strongly on the magnetic orientation, and it can change even vanish in some directions, a phenomenon dubbed colossal magnetic anisotropy[208, 209]. The class of systems in question are the zigzag edges of two dimensional honeycomb crystals[210] whose electronic properties can be described with a tight-binding model with a single orbital per site and Kane-Mele spin-orbit interactions[211]. This includes several materials, such as group IV two dimensional crystals (graphene[211], as silicene[212, 213, 214], germanene[215], and stanene[216]), the double layer perovskite iridates [217, 218], and metal organic frameworks (MOF) [219]. In addition, given that the existence of non-dispersive edge states occurs at the zigzag edge of any system described with the Dirac equation[220], the results discussed here should also be valid for the so-called designer Dirac fermions formed in "artificial graphene" formed by decoration of two dimensional electron gases with honeycomb arrangements[221, 222].

Ignoring spin-orbit and Coulomb interactions altogether, these 2D crystals are zero band-gap semiconductors with Dirac-like dispersion close to the Fermi energy. Zigzag edges in these systems are known to host localized edge states that, when both Coulomb and spin-orbit coupling are neglected, are non-dispersive, sub lattice polarized, and lie precisely at the Fermi energy, at half-filling[210]. The ensuing large density of states results in a Stoner instability that leads to ferromagnetic order at the edge[223, 117, 120, 122].

On the other hand, Kane-Mele spin-orbit interaction, a second-neighbor spin dependent hopping that conserves the spin component s_z perpendicular to the two dimensional crystal[211], has dramatic consequences in these honeycomb crystals. It opens a topologically non-trivial gap in bulk and the emergence of in-gap spin-filtered dispersive edge states: for a given spin projection s_z, electrons propagate along one direction only, preventing back-scattering even in the presence of time-reversal symmetric disorder. Importantly, the slope of the edge bands is proportional to the Kane-Mele spin-orbit coupling, which controls thereby the density of states at the Fermi energy. The interplay of spin-orbit and Coulomb repulsion on the otherwise non-dispersive edge states leads to the strong magnetic anisotropy effects anticipated above.

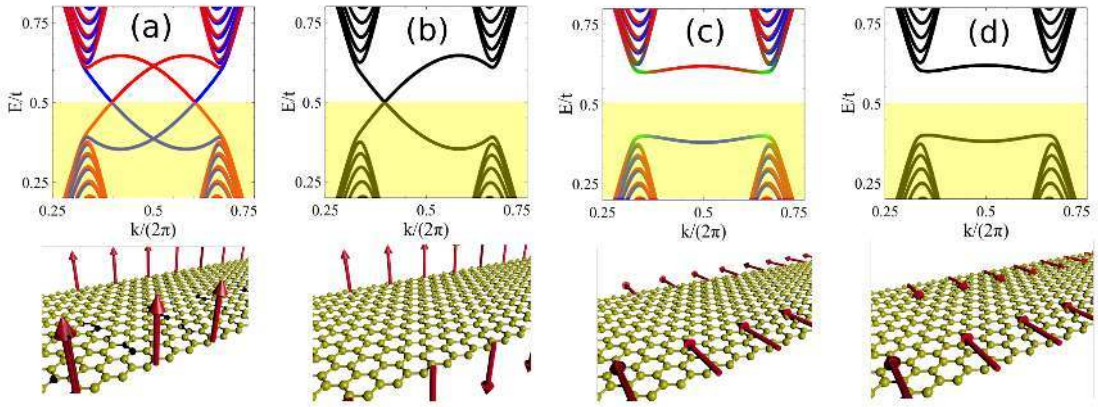

Figure 4.1: Four different ferromagnetic configurations, either in and off-plane and parallel (FM) and anti-parallel (AF) edge magnetization, together with their band structures calculated within the mean field Kane-Mele-Hubbard model. (a,b) Off plane and conducting (both for FM and AF arrangements). (c,d) In-plane and insulating parallel (both FM and AF) magnetizations. Calculations done with $U = t$ and $t_{SO} = 0.02t$

4.2 Model

Before entering the results, we present briefly the computational method to study anisotropy in graphene-like systems

4.2.1 Collinear mean field Hubbard model

To model this kind of systems, we use the so called Kane-Mele-Hubbard Hamiltonian[224, 225], which provides a minimal model to study the effect of the Coulomb interactions on the topologically protected edge states:

$$H = \sum_{\langle ij\rangle,\sigma} t c^{\dagger}_{i\sigma} c_{j\sigma} + \sum_{\langle\langle ij\rangle\rangle,\sigma} i t_{SO} \sigma \nu_{ij} c^{\dagger}_{i\sigma} c_{j\sigma} + H_{\text{int}} \tag{4.1}$$

where $\sigma = \pm 1$ are the spin projections of the spin along the axis perpendicular to the to the two dimensional crystal, $\langle\rangle$ stands for first neighbor and $\langle\langle\rangle\rangle$ for second, $\nu_{ij} = \pm 1$ for clockwise or anti-clockwise second neighbor hopping [226, 211].

For simplicity, we neglect the Rashba coupling,[227, 228]. In the case of planar honeycomb systems, such as graphene, the Rashba term is null. For buckled group IV crystals, such as silicene, germanene and stanene, the magnitude of the Rashba is one order of magnitude lower than the pure spin-orbit.[229]

The Hubbard term reads:

$$H_{int} = U \sum_i n_{i\uparrow} n_{i\downarrow} \tag{4.2}$$

where $n_{i\uparrow} = c^\dagger_{i\uparrow} c_{i\uparrow}$ denotes the occupation operator of site i with spin $\uparrow$ along an arbitrary quantization axis. We treat the Hubbard interaction in the collinear mean field approximation, enforcing the magnetization to lie along the axis $\vec{\Omega} = (sin\alpha, 0, cos\alpha)$, that we take as the quantization axis (see Fig.4.4a). This approach permits to study solutions with different α and compare their properties. Rotations in the xy plane leave the results invariant, due to the symmetry of the Kane-Mele spin-orbit coupling. In general, the Coulomb interaction term evaluated in the mean field approximation leads to two self-consistent potentials terms, direct and exchange. In the case of the Hubbard model in the collinear approximation, only the direct term survives:

$$H_{MF} = U[\langle n_{i\uparrow(\alpha)}\rangle n_{i\downarrow(\alpha)} + n_{i\uparrow(\alpha)}\langle n_{i\downarrow(\alpha)}\rangle - \langle n_{i\uparrow(\alpha)}\rangle\langle n_{i\downarrow(\alpha)}\rangle] \tag{4.3}$$

where the notation explicitly shows the spin quantization axis is taken along $\vec{\Omega}(\alpha)$ and $\langle n_{i\uparrow(\alpha)}\rangle$ stand for the average of the occupation operator calculated within the ground state of the mean field Hamiltonian:

$$H = H_0 + H_{MF} \tag{4.4}$$

As usual, this defines a self-consistent problem that we solve by iteration. Because of the spin-orbit Kane-Mele term in H_0, mean field solutions with different α are not equivalent. Notice as well that the H_{MF} term is non-diagonal when represented in the basis of eigenstates of S_z and $\alpha \neq 0$.

We pay special attention to the atomic magnetization, along the $\vec{\Omega}(\alpha)$ in site i:

$$m_{i(\alpha)} = g\mu_B \frac{[\langle n_{i\uparrow(\alpha)}\rangle - \langle n_{i\downarrow(\alpha)}\rangle]}{2} \tag{4.5}$$

and we take $g = 2$.

4.2.2 Density operators for arbitrary quantization axis

Upon a rotation of angle α of the spin quantization axis in the xz plane, the rotated of up and down density operators take the following form in the basis of the z-axis eigenstates.

$$n_{\uparrow(\alpha)} = \begin{pmatrix} \cos^2\frac{\alpha}{2} & \cos\frac{\alpha}{2}\sin\frac{\alpha}{2} \\ \cos\frac{\alpha}{2}\sin\frac{\alpha}{2} & \sin^2\frac{\alpha}{2} \end{pmatrix} \tag{4.6}$$

$$n_{\downarrow(\alpha)} = \begin{pmatrix} \sin^2\frac{\alpha}{2} & -\cos\frac{\alpha}{2}\sin\frac{\alpha}{2} \\ -\cos\frac{\alpha}{2}\sin\frac{\alpha}{2} & \cos^2\frac{\alpha}{2} \end{pmatrix} \tag{4.7}$$

Thus, these are the local mean field operators in a collineal calculation only allowing the development of magnetism along this particular quantization axis. This choice of mean field operators restricts the available Hilbert space to the collinear solutions, whereas the inclusion of the exchange term will lead to the full non-collinear solutions.

4.3 Anisotropy effects in zigzag ribbons

In order to study the zigzag edges it is convenient to study ribbons, that define a one dimensional crystal (see Fig. 4.1) with two edges. A given unit cell of the one dimensional crystal is formed by N units of 4 atoms. In the following we characterize the width of the ribbons by N. For finite U, and as long as t_{SO}/U is not too large, we find solutions with ferromagnetic order at the edges. The magnetic moment calculated self-consistently is non-negligible only at the edge atoms. Attending to their mutual magnetization orientation, ribbons yield two types of solutions with ferromagnetic edges: parallel (FM) and anti-parallel (AF). For sufficiently wide ribbons the inter-edge coupling is negligible and both solutions have identical properties.

4.3.1 Angle dependent electronic structure

The first important result of the chapter is shown in figure 4.2. Whereas off-plane magnetization ($\alpha = 0$) leads to a conducting solution, found in previous works[225], the in-plane magnetization opens a gap. Therefore, transport properties of zigzag edges will change dramatically[230] upon rotation of the magnetization direction, in contrast with conventional metallic ferromagnets. This metal-insulator transition will is developed as well in chiral edge ribbons, which have been widely reported [231, 232].

4.3.2 Anisotropy energy

The second important result of the chapter is shown in Fig.4.2b. The ground state energy $E(\alpha)$ is minimal for $\alpha = \frac{\pi}{2}$, i.e., for in-plane magnetization, which means that spontaneous magnetic order in this system leads to insulating behavior.

The results of figure 4.2 can be understood as follows. In the absence of magnetic order, two spin-filtered in-gap edge states with opposite velocities exist at each edge[211], resulting in a two-fold degeneracy (not shown). Ferromagnetic order with $\vec{\Omega} = \hat{z}$ breaks time reversal symmetry but does not mix spins. Thus, magnetic order

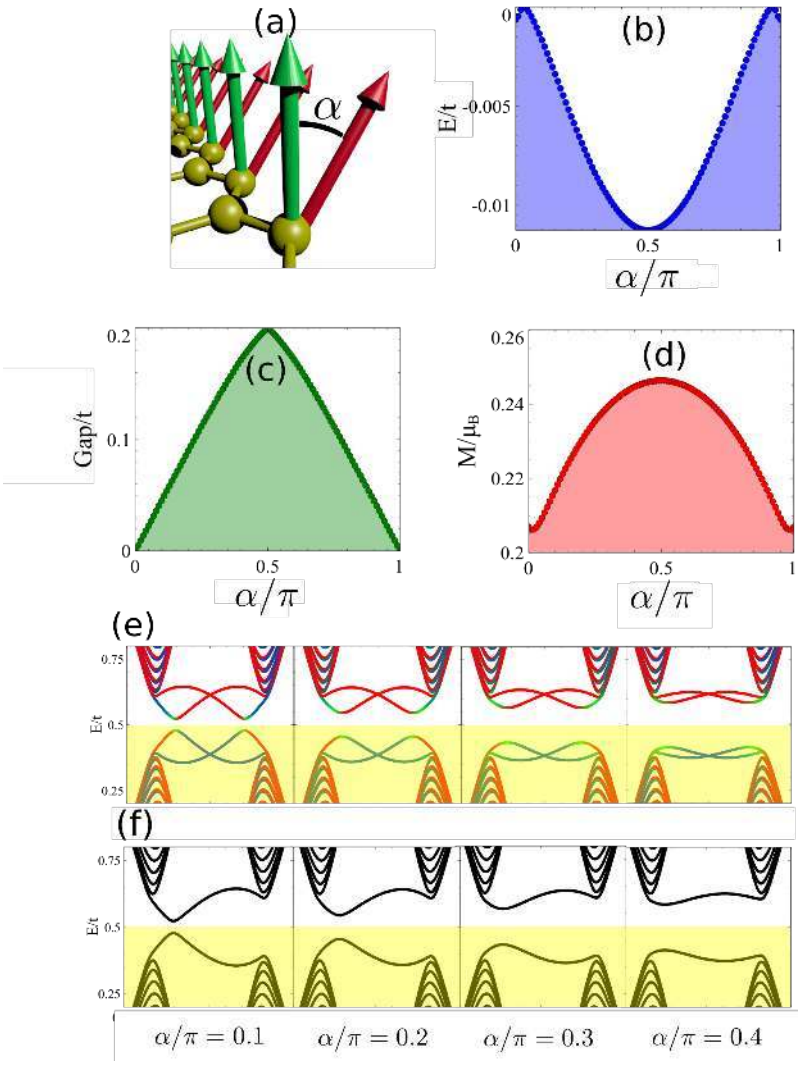

Figure 4.2: Evolution of electronic properties for the FM ribbon as a function of the magnetization direction $\vec{\Omega} = (sin\alpha, 0, cos\alpha)$. (a) Scheme of the edge magnetization for two different angles 0 and α. Ground state total energy (per unit cell, with 2 magnetic atoms per cell) (b), gap(c) and magnetization (d) as a function of α. (e) and (f) Evolution of the band structure for different values of α for the FM (e) and AF(f) configurations. $N = 30$, U=t, $t_{SO} = 0.02t$.

merely yields a spin-dependent shift that breaks the two-fold degeneracy, as seen in Fig.4.1a, for the FM case. For the AF configuration, there is an extra symmetry that restores the double degeneracy: the combined action of spatial inversion, that results in a exchange of the atoms of the two interpenetrating triangular sub lattices A and B that form the honeycomb, and time reversal, that exchange $\uparrow$ and $\downarrow$, leave

Material	t_{SO}	t	**Reference**
Graphene	0.1-5.0 μeV	2.7 eV	[234, 235, 236]
Silicene	0.16 meV	1.5 eV	[229, 237]
Germanene	2.5 meV	1.4 eV	[229, 237]
Stanene	8-30 meV	1.3 eV	[229, 216]
MOF	1 meV	0.3 eV	[219]
Double perovskyte	1 meV	0.1 eV	[218]

Table 4.1: Energy scales for different graphene-like honeycomb materials.

the system invariant. Thus the spin $\uparrow$ band localized at the at the A type edge is degenerate with the spin $\downarrow$ band localized in the opposite edge.

The situation is radically different when the magnetization lies in plane. Representing the self-content potential in the basis of the $U = 0$ spin filtered edge states, with spin quantized along the $\hat{z}$ axis, the effect of the in-plane magnetization is to mix bands with opposite spins. As a result, a band gap opens at the k point where the non-interacting edge bands cross. The evolution of the bands as the magnetization is rotated from almost off-plane (left) to almost in-plane (right) is shown if Fig. 4.4)(e,f). It is apparent that the band gap (Fig. 4.4)(c)) is maximal for in-plane magnetization ($\alpha = \frac{\pi}{2}$) and null for off-plane $\alpha = 0$. The preference for in-plane magnetization can also be connected with the variation of the magnitude of the edge magnetic moment with α (Fig.4.4d). These two results naturally explain the fact that the ground state energy is minimal for in-plane magnetization. At half-filling, all the valence bands are occupied and the conduction bands are empty. Therefore, increasing the band-gap decreases the total energy.

The gap opening as long as magnetization is not off-plane will certainly have dramatic consequences on the transport properties along the edges. A result similar to this has been obtained recently[233], using a Kane-Mele model where magnetic order is externally driven, and modeled by a magnetic exchange potential that arises from proximity rather than spontaneously, as discussed here.

The results of figures 4.2 and 2 are for a specific choice of $U/t = 1$ and $t_{SO}/t = 0.02$, and for a ribbon with $N = 30$ sites, wide enough to decouple the two edges. We now discuss how the results depend, quantitatively, on the specific values of the spin-orbit coupling, ribbon width and U. The evolution of several energy differences between AF/FM and in-plane off-plane configurations, as a function of the ribbon width N is shown in Fig.4.3a . For large N it is apparent that FM and AF have the same ground state and anisotropy energy. In addition, the edge gap (4.3b) also becomes independent on the magnetic configuration at large width.

4.3.3 Dependence of anisotropy on λ_{KM} and U

In figure (Fig.4.3(c)(e))) we plot the dependence of the magnetic anisotropy and magnetic moment (both in and off-plane) on the magnitude of the spin-orbit coupling t_{SO}/t, for two different values of U . Attending to the difference between the magnitude of the magnetic moment in the off-plane and in-plane cases (Fig.4.3(e)), three different regions are found. For very small t_{SO}/t the magnetic moment is the same for out of plane and in-plane magnetization and the magnetic anisotropy energy depends quadratically on t_{SO}/t . From this standpoint, the behavior of the zigzag edge is similar to conventional magnets, although a small gap, open for in-plane magnetization. For wide enough ribbons, the value of this gap is given by $min\,(\Delta_{\mathrm{2D}}, Um_{\mathrm{edge}})$ where $\Delta_{\mathrm{2D}} = 6\sqrt{3}t_{SO}$ is the bulk gap opened by spin-orbit interaction and Um_{edge} is the exchange splitting gap, which is a decreasing function of t_{SO}, giving rise to the curve seen in figure 4.3(d).

For intermediate values of t_{SO}/t it is apparent that the magnetic moment magnitude is different for in-plane and off-plane orientations, but in both cases finite. In this region the anisotropy energy scales approximately linear with t_{SO}/t, and the band-gap of in-plane magnetization is still a linear function of t_{SO}/t. Finally, above a given critical value $t_{SO} \simeq 0.02t$ $(0.04t)$ for $U = 0.5t$ $(U = t)$, the system enters in the so-called colossal[208, 209] magnetic anisotropy regime, for which magnetic order is only possible in-plane, and the magnetic solutions off-plane do not exist. Increasing spin-orbit coupling beyond this point starts to reduce the band-gap and the magnetic order altogether, which leads to a reduction of the magnetic anisotropy energy (Fig.4.3(e))

We thereby expect that graphene, silicene and germanene are in the small t_{SO}/t region, MOF is in the intermediate region and the stanene zigzag edge could show the colossal magnetic anisotropy effect. Notice that in the intermediate region the magnetic anisotropy energy per magnetic atom can be extremely large. For instance, for stanene, taking $U = t$, intermediate $t_{SO} \simeq 8$meV and $t \simeq 1.3eV$, we obtain of $\Delta E \simeq 4$meV, significantly larger than record materials such as YCo_5[207]. Na_2IrO_3 and related systems[217, 218] offer also a fascinating possibility of real tuning of the effective t_{SO} by strain,[218], which would make it possible to build devices with strain-tunable anisotropy.

Given the spread of estimates of the actual values of U for a given material, as well as the fact that it different substrates can result in different values of U, we address the question of how the results above depend on the strength of the on-site Coulomb repulsion U. At finite t_{SO} there is a critical U_{c1} below which the edges are non-magnetic[225], and a second U_{c2} above which the entire honeycomb lattice becomes antiferromagnetic[223]. For $U_{c1} < U < U_{c2}$ only the edge is magnetic, and its magnetic anisotropy energy is a non-monotonic function of U. It increases first, reflecting the increase of the magnetic moment, and then it decreases slightly,

reflecting the reduction of the ratio t_{SO}/U. As U approaches $U \simeq 2.2t$ the magnetic anisotropy overshoots because the bulk becomes magnetic as well.

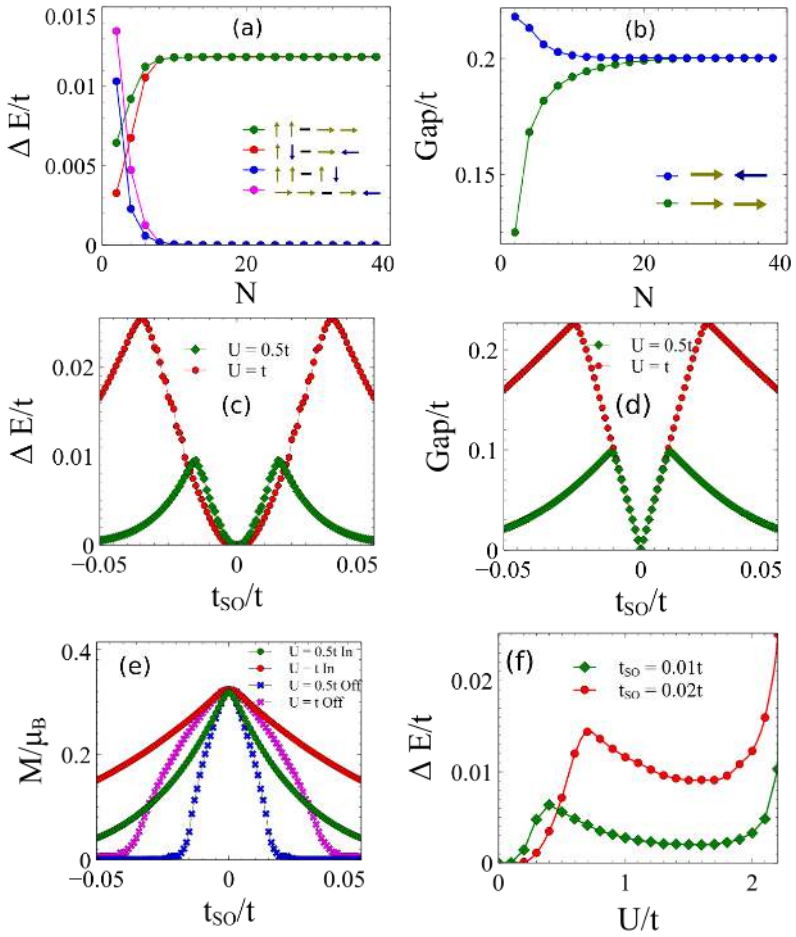

Figure 4.3: (a) Evolution of the energy differences between the in-plane vs off-plane as well as the FM vs AF configurations (4 cases) as a function of ribbon width N. (b) Gap, for in-plane magnetization solution, for FM and AF solutions, as a function of N. (c,d,e) Evolution with the strength of the spin-orbit coupling t_{SO} : anisotropy energy (c), gap (d) and edge magnetization (e). (f) Evolution of the gap with the on-site Hubbard interaction. In (a-b) $U = t$ and $t_{SO} = 0.02t$. In (c-d) $N = 30$.

We now discuss the physical effects not covered within our two main approximations, namely, treating the interactions at the mean field level and ignoring the Rashba spin-orbit term. In one dimension, collective spin fluctuations are expected to destroy the infinitely long-range order described by mean field theory. Still, for ribbons shorter than the spin correlation length $\xi(T)$ the mean field theory provides

a fair description, very much like density functional theory describes properly the magnetization of clusters and nanomagnets. The spin correlation length $\xi(T)$ in graphene edges, calculated within the spin wave approximation and ignoring spin-orbit coupling[159], is $\xi \simeq 40\mathring{A}$ for $T = 75K$. The magnetic anisotropy barrier to rotate the spins out of plane for the approximately 15 tin atoms of a zigzag stanene edge that long would be $\Delta \simeq 60$ meV.

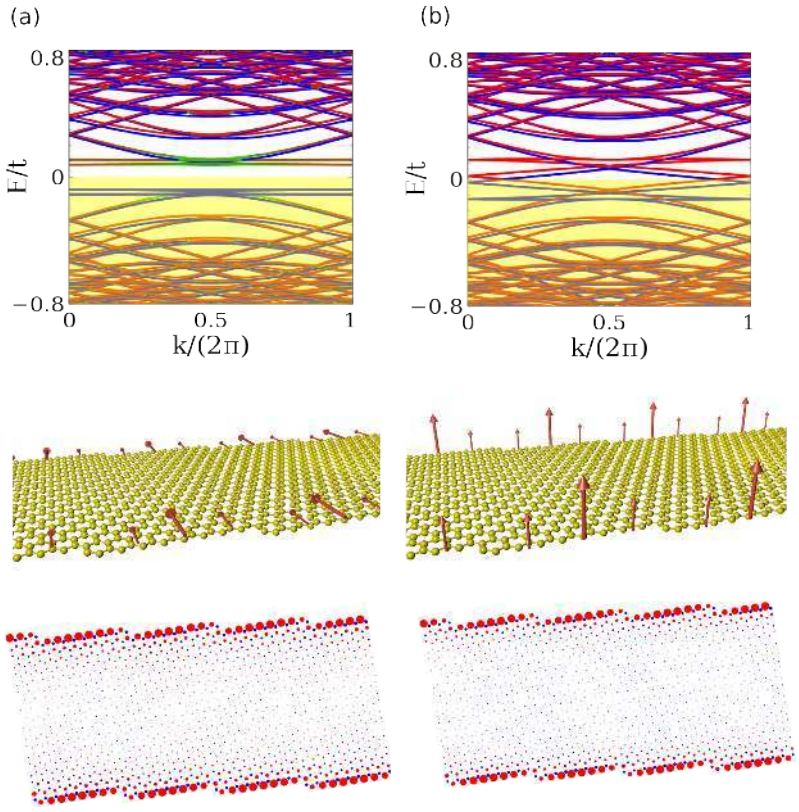

Figure 4.4: Band structures, scheme and calculated spatial distribution of the magnetic state in a chiral (8,1) ribbon in edge ferromagnetic configuration for in-plane (a) and off-plane (b) solutions. In the same fashion as in the perfect zigzag edge case, the in-plane magnetism opens up a gap whereas the off-plane one remains gapless.

4.4 Anisotropy in chiral ribbons

Even though the anisotropy calculations were performed on a zigzag edge, localized edge states also appear on chiral nanoribbons [231, 232]. Thus, this anisotropy effect will appear as well in chiral (n,m) nanoribbons due to the local lattice imbalance.

As a particular example, we show the selfconsistent band structure for in-plane and off-plane edge ferromagnetic configurations for a (8,1) chiral ribbon, as reported in [231, 232]. It is observed that, in the same fashion as in the zigzag ribbon, the off-plane magnetic solution host gapless edge states whereas the in-plane solution opens up a gap in the topological edge states, being this last one the lowest energy configuration of the system. For the limiting case of pure armchair edges, magnetism is not developed and the edge states remain gapless.

4.5 First principles calculations

In the previous sections we have seen that the value of the anisotropy energy depends quadratically on the spin orbit coupling gap. In the case of graphene its effect is negligible, however other graphene-like materials can have to a significantly larger value. In the following we will try unveil what is the actual value of the SOC gap for two graphene-like materials, focusing on the ultimate responsible of the gap opening, the d levels.

4.5.1 Other graphene-like materials

Silicene[238] and germanene[239] are two dimensional crystals with a buckled honeycomb lattice and a small gap opened by spin-orbit interactions that make them quantum Spin Hall insulators. Very much like in graphene, the low energy bands are made of p and s orbitals, and the d bands lie 10eV above the Fermi energy. Thereby, tight-binding models normally ignore d bands and assume that the spin-orbit coupling responsible of the band-gap is operating on the p shell only. By means of all-electron density functional calculations, we show that this assumption is incorrect and the contribution of the d orbitals is indeed dominant, which was shown to be the case in graphene as well.

The figure of merit in order to determine the robustness of the non-trivial properties of a quantum Spin Hall insulator is the band-gap energy. In the case of graphene the consensus is that this gap is very small, below 0.1meV and therefore very hard to observe experimentally. The predicted values for the band-gaps of silicene and germanene are 1.5 and 14 meV, respectively. Since the conduction and valence bands of graphene, silicene and germanene are made of s and p orbitals, the description of these materials in terms of tight-binding models very often ignores the d orbitals, that lie 10 eV above in energy. By so doing, the only contribution to the spin-orbit coupling in these models comes from the p shell. However, it was shown that, in the case of graphene, the contribution of the d orbitals is essential. In this paper we address the same problem in the case of silicene and germanene and we explore the relative contribution of the d orbitals to their band-gap. Our

all electron density functional calculations show that, very much like in the case of graphene, the contribution of the d orbitals is essential.

4.5.2 Density functional methodology

The calculations were performed using the density functional packages Quantum Espresso[240] and Elk[241].

Full relaxations were carried out by Quantum Espresso using projected augmented plane wave pseudopotentials with the PBEsol exchange-correlation functional.

With the relaxed structures, all-electron calculation were carried out using the Elk package with the same exchange-correlation functional. DFT+U were performed in the fully localized limit, within the non-collinear framework including spin orbit coupling.

4.5.3 Channels of spin-orbit coupling

Very much like in graphene[242], the main contribution to the spin orbit coupling gap comes from the d orbitals[243], which are usually neglected in tight binding calculations. This unintuitive behavior arises due to the different orders in the spin orbit coupling strength which involves transitions in between the low energy p_z orbitals and far energy states.

Starting with the planar case, the processes which involve spin flipping transitions within the sp2 manifold are second order due to symmetry considerations[244]. In comparison, transitions involving the d manifold are non vanishing even in at first order in the spin orbit coupling[242]. Even though for bucked structure new first order channels are opened in the p manifold, the contribution of d-orbital remains dominant up to physical achievable buckling[242].

By modifying the Kohn-Shan hamiltonian according to

$$H = H_0 + \lambda_{SOC} H_{SOC} \tag{4.8}$$

where H_0 is the usual non relativistic part and H_{SOC} the relativistic term. The parameter λ_{SOC} allows to perform an interpolation between the non relativistic and relativistic cases in order to unveil the evolution of the system.

From the previous equation, the topological gap at the k-point is expected to have the following form

$$\Delta_{SOC} = \lambda_{SOC}\alpha_{pd} + \lambda_{SOC}^2 \beta_{pp} + O(\lambda_{SOC}^3) \tag{4.9}$$

where α_{pd} the first order contribution to the gap and β_{pp} the second order contribution. As limiting cases of the previous equation, we would have the non relativistic

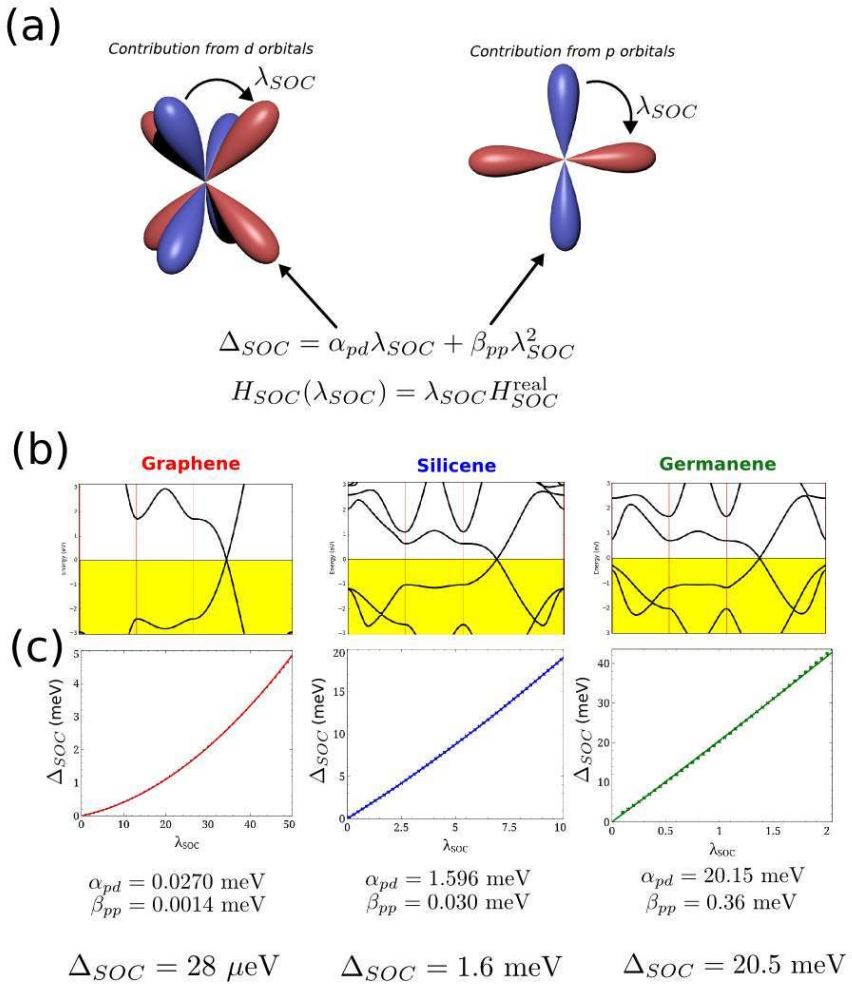

Figure 4.5: (a) Scheme of the two contributions, the one involving p orbitals and d orbitals. (b) Band structure of the three monolayers and (c) evolution of the topological gap with increasing SOC strength.

case as $\lambda_{SOC} = 0$ and the realistic case $\lambda = 1$. For the real SOC, the gap turns out to be

$$\Delta^{real}_{SOC} = \alpha_{pd} + \beta_{pp} \tag{4.10}$$

In Fig. 2(c) we show the evolution of the gap at the k-point as a function of the SOC strength. It is observed a nearly linear behavior at low λ_{SOC} values, which turns out to be a clear clue that the main contribution in first order. In order to perform a more quantitative proof of the previous argument, we fitted the previous

curves to a function of the form of Eq.4.9. The results are shown in Table 1. For the three systems, the main contribution is linear, being most dominant one for germanene. In the case of buckled systems (silicene and germanene), the linear contribution comes in part for the spin mixing channels which open the buckling in the p-manifold[245, 246, 247, 248, 249], and the spin mixing which involves high energy d-levels.[250] In comparison, the linear behavior in graphene comes strictly from d-level contributions.[250]

Once has been shown that the main contribution is first order in λ_{SOC}, we will show how increasing of the d-orbital contribution indeed increases the SOC gap in the three systems. To do so, we consider the effect of interactions within the p-manifold using a DFT+U scheme. This approach can be understood as an effective energy-independent GW correction, giving an insight of the importance of the many-body corrections to the Khon-Shan spectrum.

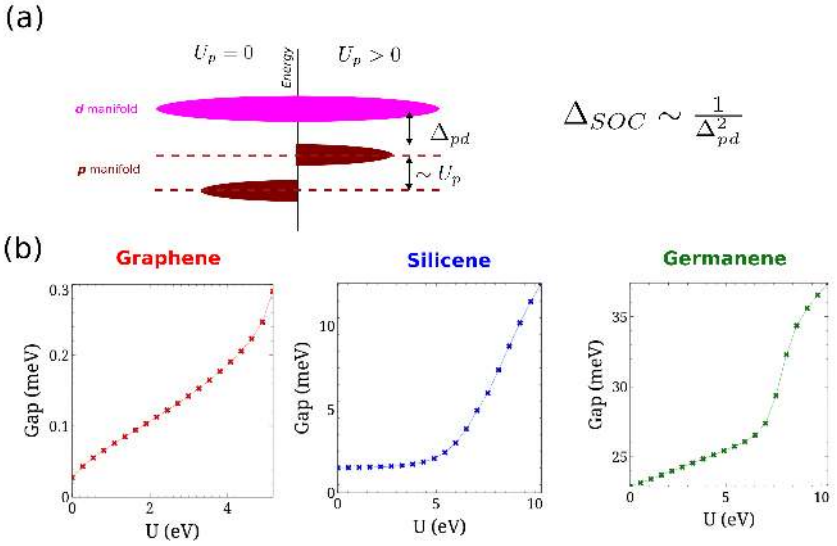

Figure 4.6: (color online) (a) Scheme of the relative position of p and d manifolds as the electron-electron interaction is increased in the p manifold. (b) Evolution of the gap for graphene silicene and germanene.

Furthermore, a simple mean field picture can be given to the behavior of the system within the DFT+U scheme. Upon increasing of U, the energy of the p-manifold becomes closer to the high energy d-manifold. Taking into account that due to perturbation theory consideration, the contribution is expected to have the form

$$\Delta_{SOC} \sim \frac{1}{\Delta_{pd}} \tag{4.11}$$

System	Graphene	Silicene	Germanene
Gap (Δ_{SOC})	28 μeV	1.6 meV	20.5 meV
α_{pd}	27 μeV	1.596 meV	20.15 meV
β_{pp}	1.4 μeV	0.03 meV	0.36 meV
α_{pd}/β_{pp}	19.3	53.2	55.97

Table 4.2: Gap, linear and quadratic contributions in λ_{SOC} and quotient of contributions for the three different materials. The linear contribution is the most dominant in the three cases, being the highest in germanene.

where Δ_{pd} is the energy difference between the center of the p-manifold and the center of the d-manifold as shown in Fig 2(a).

Upon increasing of electron-electron interaction, the gap increases for three systems (Fig. 2(B)). Its worth noting, that the gap remains topological, so gapless edge states are expected to be developed in finite samples. Thus, interactions turn the topological state stronger, as has been argued to happen in some other systems.

Whereas in the three systems the gap develops a monotonically increasing evolution, the strongest dependence is observed in graphene. Local electronic interactions in graphene can be important in very clean samples, being mandatory to being included in theoretical calculations in order to take into account several experimental results. Taking the previous fact into account, that would mean that its consideration in the topological gap of graphene can be non negligible, Assuming a realistic value of U = 4 eV, it turns out that the gap expected is around $\Delta_{SOC} = 150\mu eV$, in comparison with the vanishing U value of $\Delta_{SOC} = 28\mu eV$. Although the present DFT+U scheme is far from being strict, it highlights the possible importance of taking into consideration the interplay between interactions and SOC corrections to the Kohn-Shan spectrum.

4.6 Summary

In conclusion, we have studied the magnetic anisotropy of the ferromagnetic phase of the zigzag edges of graphene and graphene-like systems, that can be described with a single orbital Hubbard model model on a honeycomb lattice with spin-orbit coupling described with the Kane-Mele Hamiltonian. This includes a large class of two dimensional crystals, such as silicene[212, 213, 214], germanene[215], stanene[216], iridates[217, 218] and metal organic frameworks[219]. Since the electronic dispersion of the non-interacting edge states is fully determined by the spin-orbit coupling, the resulting magnetic anisotropy effects, computed within a mean field approximation, turn out to be very strong: the system undergoes a metal to insulator transition when the magnetization is rotated out of the normal and for large values of t_{SO}

the magnetic solutions are only stable for in-plane magnetization. For all values of the spin-orbit interaction we find that the ground state energy occurs for in-plane magnetization and the edge states are gapped. Finally, we also showed the different contribution to the SOC gap in several honeycomb systems, remarking the origin of the topological gap as a phenomena involving d-robitals and its strong dependence with interactions.

Chapter 5

Magnetically ordered phases in quantum Hall graphene[1]

Application of a perpendicular magnetic field to charge neutral graphene is expected to result in a variety of broken symmetry phases, including antiferromagnetic , canted and ferromagnetic. All these phases open a gap in bulk but have very different edge states and non-collinear spin order, recently confirmed experimentally. Here we provide an integrated description of both edge and bulk for the various magnetic phases of graphene Hall bars making use of a non-collinear mean field Hubbard model. Our calculations show that, at the edges, the three types of magnetic order are either enhanced (zigzag) or suppressed (armchair). Interestingly, we find that preformed local moments in zigzag edges interact with the quantum Spin Hall like edge states of the ferromagnetic phase and can induce back-scattering.

5.1 Introduction

The remarkably perfect[93] quantization of conductance in quantum Hall systems, that provides our standard of resistance for h/e^2 , arises from the combined opening of a gap in the bulk of the sample, topologically different from vacuum, that implies the existence of chiral edge states for which back-scattering is impossible[103, 104]. In graphene, quantum Hall effect [251, 92] also shows perfect quantization, but it has its own peculiarities[252, 253], as a result of the relativistic-like nature of the graphene electron dispersion, with two non-equivalent valleys with Dirac-like bands. In a honeycomb lattice, each valley hosts two sets of unevenly spaced Landau levels (LL), for electrons $n > 0$ and holes $n < 0$, plus a special $n = 0$ LL, at the Dirac energy. Whereas all graphene LL have fourfold degeneracy, coming from the spin

[1]some parts of this chapter are taken from Physical Review B 90 (16), 165429 (2014)

and valley, the $n = 0$ is different from the rest: for a given spin and a given edge, it has only one electron-like and hole like dispersing edge states.

It was found[254] early on that perturbations could open a gap in the $n = 0$ LL in two fundamentally different ways, either by splitting the levels according to their spin, or to the valley (which is completely correlated to the sub lattice for the $n = 0$ LL), resulting in very different edge states. Whereas breaking the sub lattice symmetry would give gaped edge states (leftmost panel of figure 5.1d), the spin-polarized state would have counter propagating edge states inside the gap (rightmost panel of figure 5.1d). In this sense, the spectrum of spin-polarized graphene in the quantum Hall regime, would be identical to the acclaimed quantized Spin Hall phase proposed by Kane and Mele[211].

A generic feature of quantum Hall systems, is that when the Fermi energy lies at the middle of a Landau level, interactions can open a gap and break the spin symmetry. In the case of spin-degenerate LL, this leads to the quantum Hall ferromagnetism. In the case of the $n = 0$ graphene quartet, several types of electronic order have been studied[255, 256, 257, 258, 259, 260, 261, 262, 263, 264, 265, 266, 267, 268]. Three obvious candidates come to mind: a charge density wave (CDW), a spin density wave resulting in antiferromagnetic (AF) order, both breaking valley symmetry, and ferromagnetic order (FM). Only the latter is expected to have gap-less spin-filtered edge states [254, 266].

Different experiments have provided strong evidence of interaction driven band gap opening in the $n = 0$ quartet in graphene at half filling[269, 270, 271]. In a recent experimental breakthrough[272], the combined application of an in-plane B_x and off-plane B_z fields, have made it possible to observe the controlled transition between different electronically ordered phases at half filling. Thus, as B_x is ramped up, the system goes from an insulating phase, most likely AF, to a phase with thermally activated edge transport, presumably a canted AF (CAF) phase with gapped edge states, and at higher in-plane field to a phase with G slightly below $2G_0$ (where $G_0 = e^2/h$) , as expected from the FM phase with quantum spin Hall like spectrum. Upon gating, all these phases merge into a phase with $G = G_0$.

These recent experimental results[272] highlight the interplay between non-collinear bulk electronic order and the emergence of spin-filtered edge states that, in contrast with the $n \neq 0$ states that are topologically protected, are the consequence of an interaction driven electronic phase transition in bulk. This motivates the interacting theory presented here, that describes on equal footing the non-collinear spin order of both bulk and edge states, going beyond previous theory work [255, 256, 257, 258, 259, 260, 261, 262, 263, 264, 265, 266, 267, 268]. In particular, a previously overlooked but important aspect of this problem is the fact that the magnetic order is different at the edges and bulk. Our non-collinear mean field Hubbard model calculations show that zigzag and armchair edges enhance and suppress, respectively,

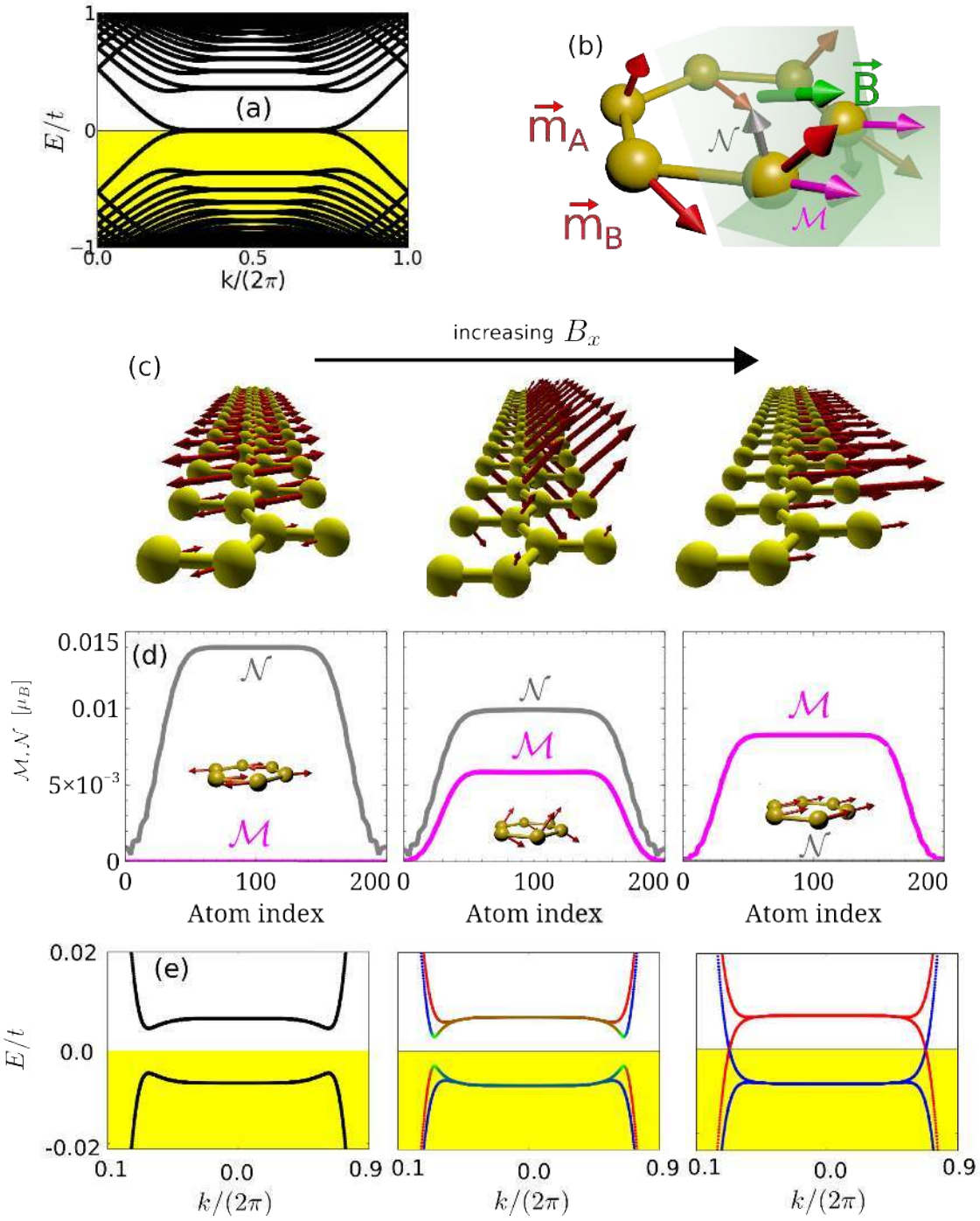

Figure 5.1: (a) Non interacting spectrum of a quantum Hall armchair ribbon, and (b) scheme of the magnetism developed when interactions, off-plane and in-plane fields are present. (c) Magnetism in the ribbon, (d) magnetic order parameters and (e) band structures as the in-plane field increases, showing a pure edge insulator to metal transition.

the magnetic order associated to the bulk Landau levels. In the case of the recently observed Quantum Spin Hall like phase, the coexistence of spin filtered edge states with local magnetic moments at zigzag terminations is likely to play a role in the observation[272] of a conductance smaller than $2G_0$ that is expected from these states in the absence of spin flip interactions[254].

5.2 Modeling and non-collinear formalism

We model graphene quantum Hall bars with a Hubbard model for a honeycomb lattice stripe:

$$\mathcal{H} = \mathcal{H}_0(B_z) + g\mu_B \vec{B} \cdot \vec{S} + U \sum_i n_{i,\uparrow} n_{i,\downarrow} \tag{5.1}$$

The first term describes electrons in a honeycomb lattice and the effect of the perpendicular magnetic field B_z on the orbital motion is included by means of the standard Peierls substitution in the tight binding model. The second term is the Zeeman coupling and the third is the Hubbard term, where $n_{i\sigma} = c^\dagger_{i\sigma} c_{i\sigma}$ is the occupation number for spin σ at site i. Our gauge choice preserves translational invariance along the transport direction, so that k is a good quantum number. The spectrum of $\mathcal{H}_0(B_z)$ is shown in figure 5.1a for a stripe with armchair terminations, and features both the bulk Landau levels and the dispersive edge states.

The effect of interactions is treated at the unrestricted Hartree-Fock approximation with a variational wave function $|\Omega\rangle = \prod_i \left(u_i c^\dagger_{i\uparrow} + v_i c^\dagger_{i\downarrow}\right)|0\rangle$. This naturally leads to write the Hubbard part of the Hamiltonian as a one-body mean field Hamiltonian:

$$H^{MF} = H_0 + g\mu_B \vec{B} \cdot \vec{S} + H_H + H_F + E_{DC} \tag{5.2}$$

where $H_H = U \sum_\sigma n_{i\sigma} \langle n_{i\overline{\sigma}} \rangle$ is the Hartree term, $H_F = -U \sum_\sigma c^\dagger_{i\sigma} c_{i\overline{\sigma}} \langle c^\dagger_{i\overline{\sigma}} c_{i\sigma} \rangle$ is the Fock term, $E_{DC} = -U[\langle n_{i\uparrow}\rangle\langle n_{i\downarrow}\rangle - \langle c^\dagger_{i\uparrow} c_{i\downarrow}\rangle\langle c^\dagger_{i\downarrow} c_{i\uparrow}\rangle]$ is a constant, $\overline{\sigma} = -\sigma$ and $\langle O \rangle = \langle \Omega | O | \Omega \rangle$. The variational coefficients v_i and u_i are determined by iteration, starting from a trial solution, until a self-consistent solution is found. Solutions for bulk graphene, ignoring boundaries, can be found analytically[262] and are consistent with our numerical results. For strips, a numerical implementation of this procedure yields, in general, solutions with non-collinear magnetization[273, 274, 275, 276, 277] whose magnitude and orientation vary from bulk to edge. Since a numerical calculation of the actual stripes, with one micron width, is beyond reach of our computational resources, we consider narrower stripes with W =10 nm, with larger B_z, so that the magnetic length $\ell_B = \sqrt{\frac{\hbar}{eB_z}}$ that controls inter edge coupling is still much smaller than W.

The magnetic order of a given self-consistent solution is completely characterized by the average spin moment in every atom of the ribbon unit cell, $\vec{m}_i = \langle \Omega | \vec{S}_i | \Omega \rangle$. It is convenient to introduce to two fields that measure the degree of ferromagnetic

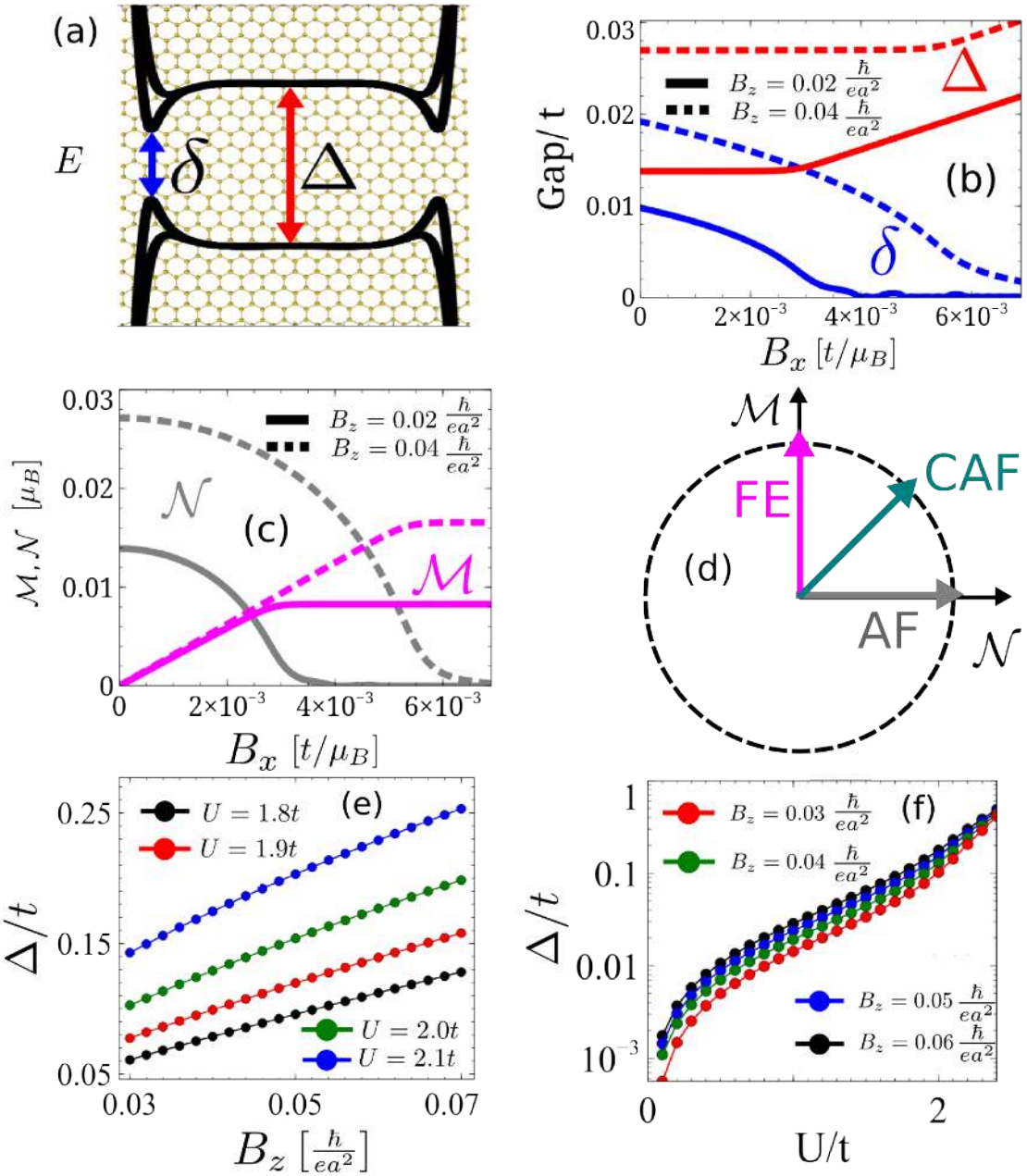

Figure 5.2: (a) Scheme of the two different gaps (edge and bulk) observed in the band structure for an armchair ribbon, and (b) their evolution with an increasing in-plane field. (c) Bulk magnetic order parameters obtained in the calculation, and (d) scheme representing the phase transition in the order parameter space. (e) Dependence of the AF gap in absence of in-plane field in a quantum Hall armchair bar as a function of the off-plane field, and (f) the electron-electron interaction.

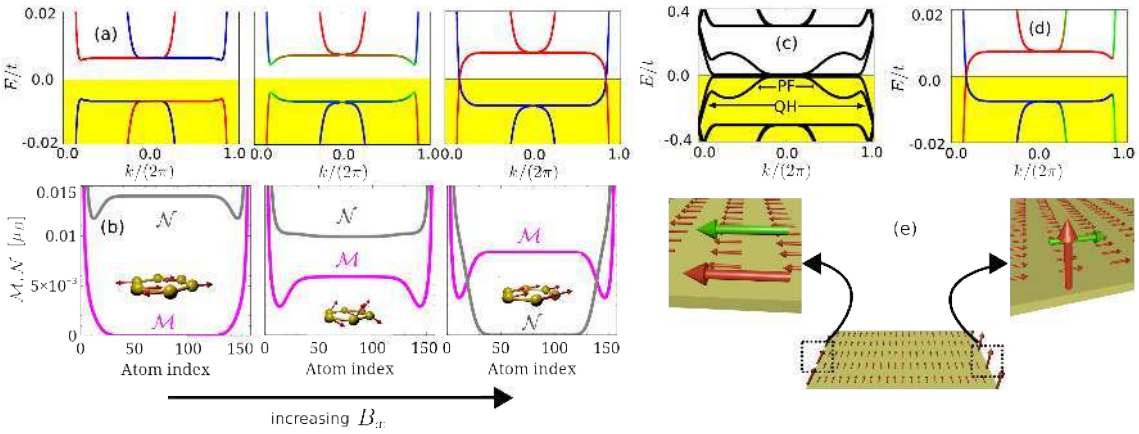

Figure 5.3: (a) Energy bands for the AF, CAF and FM in a zigzag ribbon and (b) magnetic order parameters across the width. (c) Band structure of a zigzag ribbon marking the two different kinds of edge states. (d) Band structure and (e) scheme of a zigzag ribbon in the ferromagnetic regime with an excited magnetic moment on one edge.

(FM) and antiferromagnetic (AF) order of a given solution. For each pair of adjacent atoms, A and B, we define:

$$\vec{M} = \frac{\vec{m}_A + \vec{m}_B}{2}, \qquad \vec{N} = \frac{\vec{m}_A - \vec{m}_B}{2} \tag{5.3}$$

5.3 Phase transition in quantum Hall bars

At half filling we find that $|\vec{m}_A| = |\vec{m}_B|$ which implies that $\vec{N}$ and $\vec{M}$ are orthogonal. We also find that $\vec{N}$ and $\vec{M}$ points always perpendicular and parallel, respectively, to the applied magnetic field, in order to minimize the Zeeman energy. The mean field Hamiltonian is invariant to rotations of $\vec{N}$ in the plane perpendicular to the applied field. Therefore, at half filling is enough to refer to $\mathcal{N} = |\vec{N}|$ and $\mathcal{M} = |\vec{M}|$

5.3.1 Bulk properties at half filling

Both the evolution of the magnetic order parameters from edge to edge [Figs. 1(d) and 3(b)], as well as the band dispersion [Figs. 1(e) and 3(a)], make it clear that edges and bulk are very different. We first discuss the calculated properties of the bulk region, which are in line with previous theory work[262, 266]. At half filling we find three different phases, depending on the value of B_x. In the limits $B_x = 0$ and $B_x \to \infty$, the Hubbard interaction yields bulk in-plane antiferromagnetic order ($\mathcal{M} = 0$) and in-plane ferromagnetic order ($\mathcal{N} = 0$), respectively. As B_x is ramped

between these two extremes, both the $\mathcal{N}$ and $\mathcal{M}$ components survive, in the so called canted AF (CAF) phase[266, 262].

The three magnetically ordered phases, FM, AF or CAF, open a bulk gap Δ in the $n = 0$ quartet. In Fig. 5.2(b) and 2(c) we show how the magnitude of the bulk gap Δ remains initially constant as a function of B_x, whereas the $\mathcal{M}$ increases linearly and $\mathcal{N}$ is depleted according to a $\sqrt{1 - \left(\frac{B_x}{B_0}\right)^2}$ law. Since $\mathcal{M}$ scales linearly with B_x this results shows that $\Delta \propto \sqrt{\mathcal{M}^2 + \lambda^2 \mathcal{N}^2}$, and B_x is actually driving a rotation of the $(\mathcal{N}, \mathcal{M}) \propto (cos\theta, \lambda sin\theta)$ vector[262]. Thus, the FM, AF and CAF phases can be interpreted as different realizations of a common multidimensional order parameter, rather than phases with different order parameters[262, 266].

An important test for the model is the dependence of the bulk gap Δ on the off-plane magnetic field B_z. In the experiments, a roughly linear dependence[278] $\Delta \propto B_z$ was found, in contrast with the expected[265, 264] from the HF theory for long-range Coulomb interaction, in which $\Delta \simeq \frac{e^2}{\ell_B} \propto \sqrt{B}$.

Within the mean field Hubbard model, the origin of the linear scaling is the following. First, the gap scales linearly with the atomic magnetic moment. Secondly, the magnetic moment scales linearly with the number of electrons in the zero Landau level, which are the ones that are unpaired. This number of electrons is given by the ratio of the area of sample and the square of the magnetic length A_{sample}/l_B^2. This ratio is proportional to B_z, yielding the linear scaling of the gap.

The magnitude of the mean field gap depends strongly on U. In order to account for the experimentally observed magnitude of $\Delta/(eBa^2/\hbar) = 40eV$, we would need to assume $U/t \simeq 2-2.5$, within the limits considered in the literature[279]. However, in order to calculated Δ it is probably more realistic to assume a smaller value for U and to include the effect of long range Coulomb interaction as well [265, 264].

5.3.2 Edge properties at half filling

We now discuss the electronic properties of the edges. We consider both zigzag and armchair terminations. In both cases $\mathcal{N}$ and $\mathcal{M}$ are modulated as the edge is approached, but in a different way: they are depleted at the armchair edges [Fig. 5.1(c,d)] and enhanced at the zigzag terminations [Fig. 5.3(b)]. We start the discussion with the evolution of the edge states as a function of B_x for the simpler case of armchair edges. As B_x is ramped up, $\mathcal{N}$ is depleted in bulk, so it does the edge gap, δ [Fig. 5.2(b)]. Thus, in the AF phase, with $\delta \simeq \Delta >> k_B T$ edges are insulating, but in the CAF phase, when $\mathcal{N}$ and δ are close to zero, thermally activated edge transport is possible, as reported experimentally[272]. In the ferromagnetic phase, with $\mathcal{N} = 0$, the edge gap closes, $\delta = 0$, and our calculated spectrum is identical to that of a Quantum Spin Hall insulator[211], with a finite gap Δ in the bulk spectrum and spin-polarized counter propagating gap-less edge

states.

The existence of the quantum spin Hall like spectrum in the FM phase is true both for zigzag and armchair terminations, confirming the prediction based in a model that ignored the modulation of the order parameter at the edge[254]. However, in the zigzag edges the enhancement of the magnetic moment at the edges has non-trivial and important consequences. Two types of edge states exist at the zigzag terminations in the Quantum Hall regime: the topologically protected current carrying states, present in any Quantum Hall bar (QH), and the preformed (PF) non-dispersive mid gap edge states[140], present already at $B_z = 0$, that host magnetic moments when Hubbard interactions are turned on[115, 122]. These two types of edge states, QH and PF, are marked in Fig. 5.3(c). Inspection of their wave function confirms that the PF edge states are mostly localized in last atomic row of the stripe, in contrast with the QH states, that are extended over a distance of order ℓ_B[280] . The enhancement of the magnetic order at the zigzag edges comes from the interaction driven ferromagnetic order associated to the PF edge states. The calculations yield edge magnetic moments lying parallel to the applied magnetic field, i.e., mostly in-plane.

An important question is to which point the edge magnetic moments associated to the PF states are coupled to the QH edge states. To address this question we perform a mean field calculation for the FM phase (with $B_x >> B_z$) where we constraint the magnetic moment of one of the edges to lie perpendicular to the plane [Fig. 5.3(e)]. The resulting self-consistent solution still has in-plane magnetization for bulk and for the free edge. The calculated energy bands are shown in Fig. 5.3(d). It is apparent that at the edge where the PF magnetic moments are forced to lie off plane, a gap opens in the QH edge states.

Our calculation clearly shows that spin-filtered QH edge states are sensitive to the spin orientation of the PF edge moments. This provides a natural scenario to account for the experimentally observed value [272] of the zero bias conductance $G = 1.8G_0$, rather than $G = 2G_0$, the conductance expected if no spin-flip interactions occur. In a micron size flake there will be several patches with zigzag terminations and PF edge states. There, spin fluctuations of the edge moments will induce spin mixing and back-scattering of the spin-filtered QH edge states. A second mechanism that would induce spin back-scattering combines spin-orbit coupling and disorder.

5.3.3 Ferromagnetic bulk and antiferromagnetic edge

In the half filled case, we observed that the electronic structure of the edge was determined by the electronic order in bulk. That interesting behavior holds as long as the electronic order both in bulk and edge are equivalent. According to that, it may seem that an insulating edge implies a canted or antiferromagnetic bulk order. In the following we will see that this is not completely true: close to the magnetic

transition, edge and bulk can host different magnetic orders.

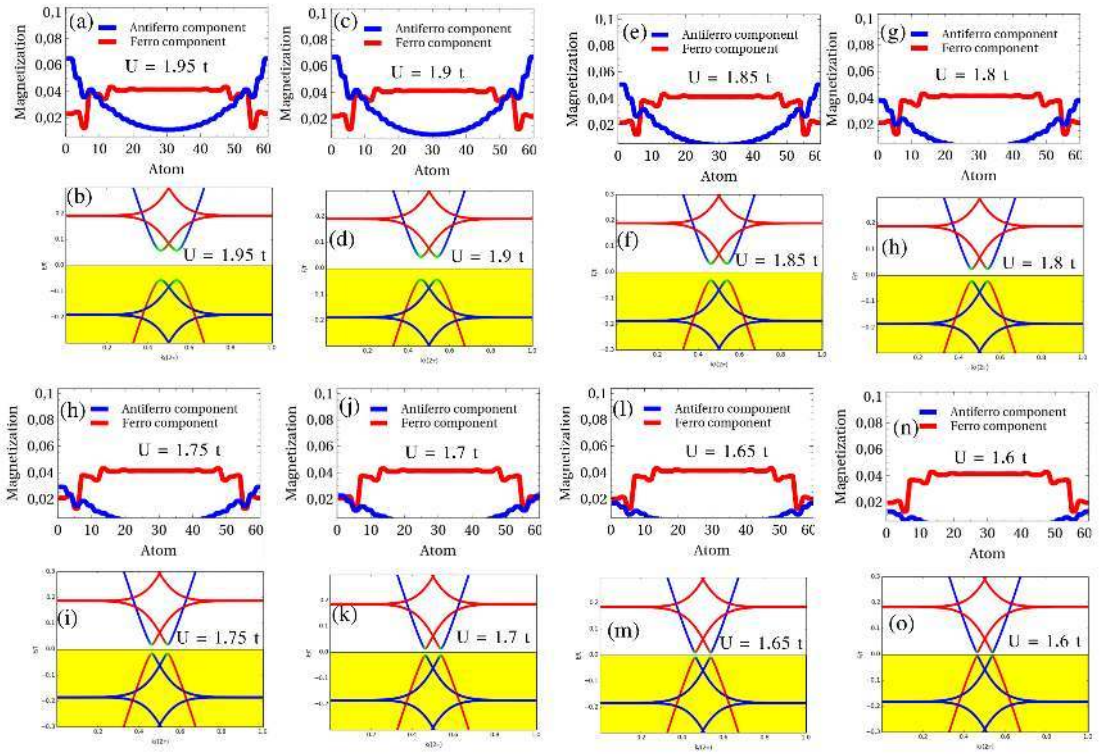

Figure 5.4: Evolution of the band structures and magnetic order as the U value approaches the transition point. It is observed that the antiferromagnetic order starts at the edges, and propagates towards the bulk. In this situation, electronic order in bulk does not determine the electronic properties of the edge.

At large enough interactions, a situation can arise where the bulk sustains the ferromagnetic phase at the same time as the edge sustains the canted antiferromagnetic phase. This situation can be understood as if the electronic interactions had a bigger effect on the edge, due to a quenching of the kinetic energy due to the presence of the boundary.

We show in Fig. 5.4 how the magnetic structure of an armchair ribbon evolves as the interaction is increased, starting close to the transition value between ferromagnetic to canted. The canting of the moments starts to take place in the edge of the system, and starts propagating towards the bulk. It is interesting to note, that if an actual sample of graphene is in a situation close to this one, the actual bulk of graphene can be ferromagnetic, but the edge states will be gapped due to the spin mixing in the edge, taking place due to the canting order. Therefore, the magnetic order in the bulk does not determine the electronic properties in the edge, if the

system is close to the transition.

5.3.4 Ferrimagnetic $\nu = 1$ phase away from half filling

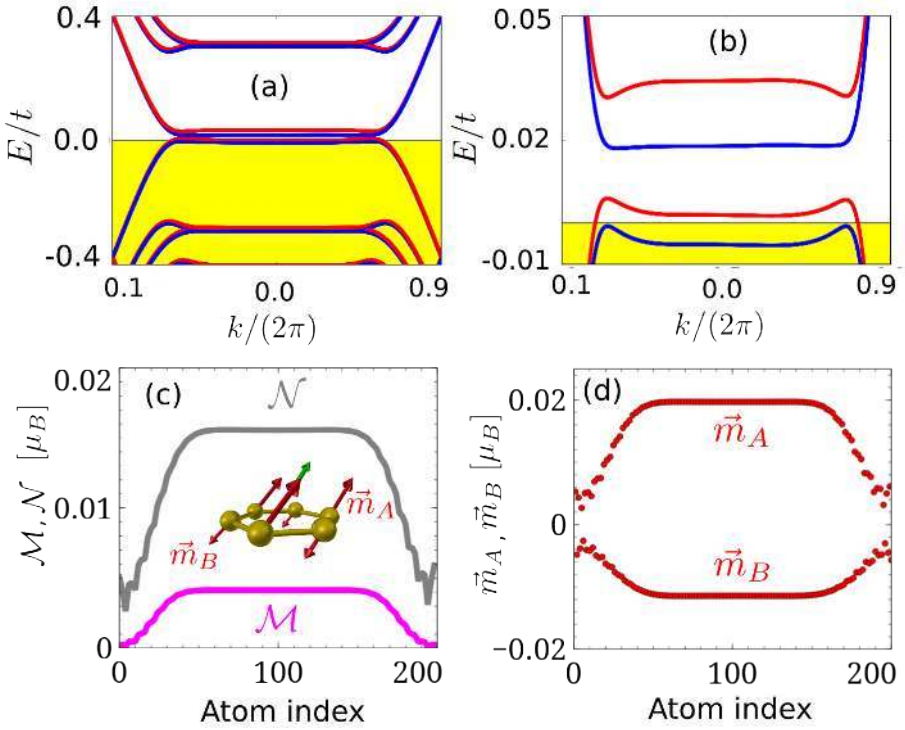

Figure 5.5: Quarter filling phase. (a,b) Energy bands, (c) magnetic order parameters, $\mathcal{N}$ and $\mathcal{M}$ as a function of position and (d) sublattice resolved magnetic moments.

As a final test for the model, we now discuss our results [Fig. 5.5] for the system away from half-filling. Experiments[272] indicate that, upon gating up to quarter filling the three magnetic phases merge into a unique phase with edge conductance $G = G_0$ which means that both spin and valley degeneracy have to be broken. Our calculations, show that at quarter filling [Figs. (a) and (b)], the system develops a ferrimagnetic phase [Fig. 5.5(c)]. Unlike the case of half-filling, we have now $|\vec{m}_A| \neq |\vec{m}_B|$ and the magnetic moments of both sub lattices are parallel to the total applied field. The different magnitude of the sub lattice magnetizations m_A and m_B, shown in Fig. 5.5(d), is a clear indication of the valley symmetry breaking.

The occupation of a unique LL, possible due to the valley and spin symmetry breaking, automatically implies that a single spin-polarized dispersive edge state, accounting for the observation[272] of the $G = G_0$ plateau. Importantly, both the

bulk magnetization and the number of edge channels in this ferrimagnetic phase are insensitive to the magnitude of the in plane magnetic field, in agreement with the experiment [272]. Moreover, the bulk gap is found to increase with the in-plane field as observed in experiments.

5.4 Spin-waves

5.4.1 General considerations of spin waves

As shown previously, electronic interactions are able to turn an initially metallic system into an insulator. At very strong interactions, these systems reach the Mott insulating limit, in which the charge is frozen in each atom. However, a degree of freedom remains free, and able to create transport phenomena. This degree of freedom is the spin of the electrons.

In fact, the magnetic order is one of the simplest examples of spontaneous symmetry breaking. In the absence of spin-orbit coupling, the Hamiltonian electronic system has a continuous degree of freedom which is the spin rotation, which is broken in the ground state. However, this (broken) continuous symmetry has an important consequence, it guarantees the existence of gapless bosonic excitations, the so called Goldstone modes[281, 282, 10]. In comparison, for discrete broken symmetries, gapless excitations are no longer guaranteed, as will be the case of a system with uni-axial anisotropy.

The gapless excitations in the case of symmetry breaking by magnetic order are called magnons. Their large lifetime allows to existence of spin transport in insulators, as confirmed with many recent experiments[283, 284]. The amazing fate of spin transport without charge transport suggests their potential application in spintronics.

Apart from spin transport, the effect of spin waves has more mundane implication in materials. The temperature dependence of the magnetization of conventional materials as iron, is governed by the increasing population of spin waves at high temperature[285]. Therefore, in the former case they are the responsible of phase transition between ferromagnetic to non magnetic at high temperatures. Moving to the spintronics world, in ferromagnets spin waves carry the missing spin angular momentum in a spin non-conserving scattering event.

In the following we will deal with how to calculate spin wave properties, mainly focusing on its spectrum, starting from an electronic Hamiltonian. We will show how spin waves show up as an emergent property of the excitations of the ground state[286]. The calculations will be done in several steps (Fig. 5.6). First, usual mean field calculation will deal with the ground state Hartree-Fock wavefunction. Then, the spin response is calculated and finally many body perturbation theory

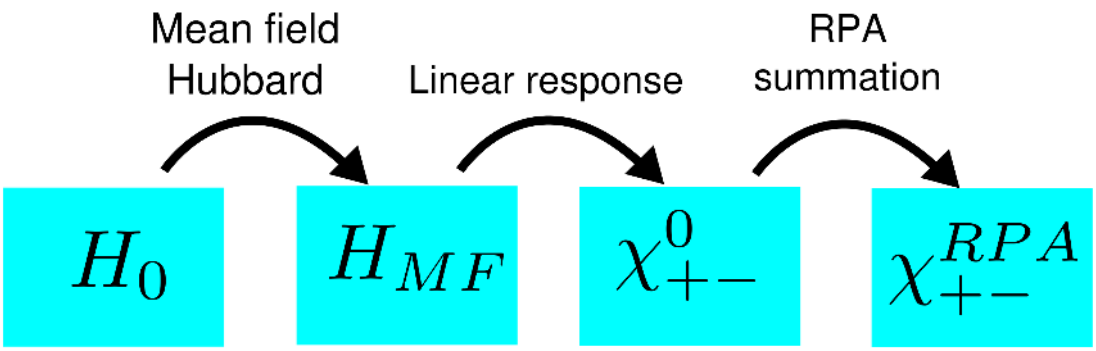

Figure 5.6: Sketch on how the spin wave spectrum is calculated. First a free Hamiltonian is set up, interactions are introduced and solved in a mean field approximation. Then the spin response is calculated, and finally the RPA summation is performed.

within the random phase approximation (RPA) will allow to calculate the dressed spin-spin correlation function.

5.4.2 Spin-spin response by RPA re-summation

We use the standard tight binding model with first neighbors hopping between localized p_z orbitals. Orbital magnetic field is introduced by the usual Peierls substitution and in-plane magnetic fields by a Zeeman coupling.

To model electronic interaction which will give rise to magnetic order, we use a phenomenological Hubbard model

$$H = \sum_{<i,j>} t_{ij} c_i^\dagger c_j + U c_{i,s}^\dagger c_{i,s} c_{i,s'}^\dagger c_{i,s'} \tag{5.4}$$

The ground state of the previous model turns out to be a antiferromagnetic trivial Quantum Hall insulator at low in-plane fields and a topological ferromagnetic Quantum Hall insulator at large in-plane fields. The previous behavior, reproduces the experimentally observed transition between a Quantum Hall insulator and a Quantum spin Hall with the in-plane field.

The previous Hamiltonian is solved self-consistently. Once the ground state is obtained, the ladder spin-spin response is calculated by linear response theory as

$$\chi^0_{+-(i,j)}(\omega, q) = \sum_{l,m} \frac{a_{l,m,i,j,k,q}}{E_{l,k} - E_{m,k+q} - \omega + i\epsilon}(n_l - n_m) \tag{5.5}$$

$$a_{l,m,i,j,k,q} = \langle \Psi_{l,k} | S_+(i) \Psi_{m,k+q} \rangle \langle \Psi_{m,k+q} | S_-(j) \Psi_{l,k} \rangle \tag{5.6}$$

With the previous linear spin response, we compute the interacting spin correlation function χ_{+-} by means of the random phase approximation

$$\chi_{+-} = \chi^{RPA}_{+-} = \chi^{0}_{+-} \left(I - U\chi^{0}_{+-} \right)^{-1} \tag{5.7}$$

The poles of the imaginary part of the response function give the spin wave excitations[287]. It worth to remark that for a gapped spectrum, Eq.5.5 doesn't show poles at $\omega = 0$, whereas the many body Eq.5.7 is able provided that $\det(I - U\chi^{0}_{+-}) = 0$. For gapped electronic spectrum, the previous condition is enough to guarantee a gapless spin many-body excitation, however for gapless electronic calculations the full Eq.5.7 has to be considered. In order to simplify the discussion, we will look in all the cases at the poles of the full spin response, both in the insulating and gapless cases.

5.4.3 First steps: the linear chain

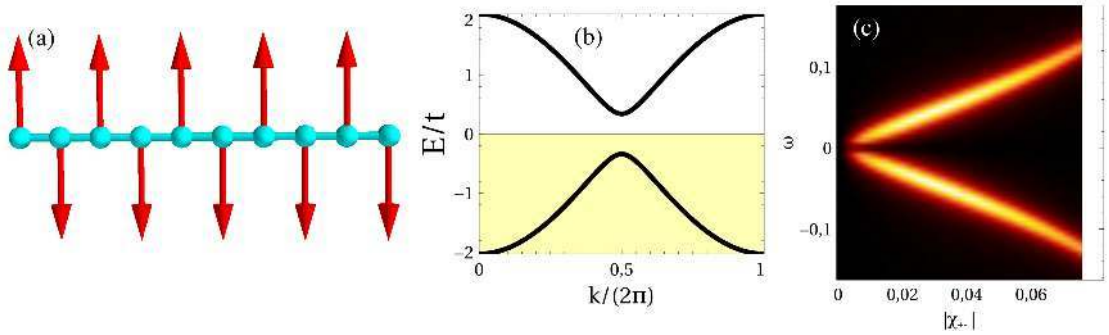

Figure 5.7: (a) Magnetic order and (b) band structure of a linear chain at half filling. Although the electronic structure is gapped (b), the spin wave spectrum (c) is gapless, developing a linear dispersion relation as expected from antiferromagnetic spin waves.

Antiferromagnetic chain

The ultimate goal of the RPA method is to calculate the effect of spin waves in the electronic spectrum of Quantum Hall bars. Nevertheless, lets start with a first minimal example. A way more simple model than the Quantum Hall graphene is a linear chain at half filling. In this simple case, nesting of the wavefunction at $k = \pi$ already indicates that the system will tend to form antiferromagnet order[288]. Moreover, the same conclusion can be reached by applying Lieb theorem, provided a lineal chain is also a bipartite lattice. In Fig. 5.7 we show the simplest

situation, a calculation with two atoms per unit cell to accommodate the antiferromagnet order. At the mean field level, interactions open up a gap in the electronic spectrum. In comparison, spin waves remain gapless, showing a linear dispersion relation characteristic of antiferromagnetic systems.

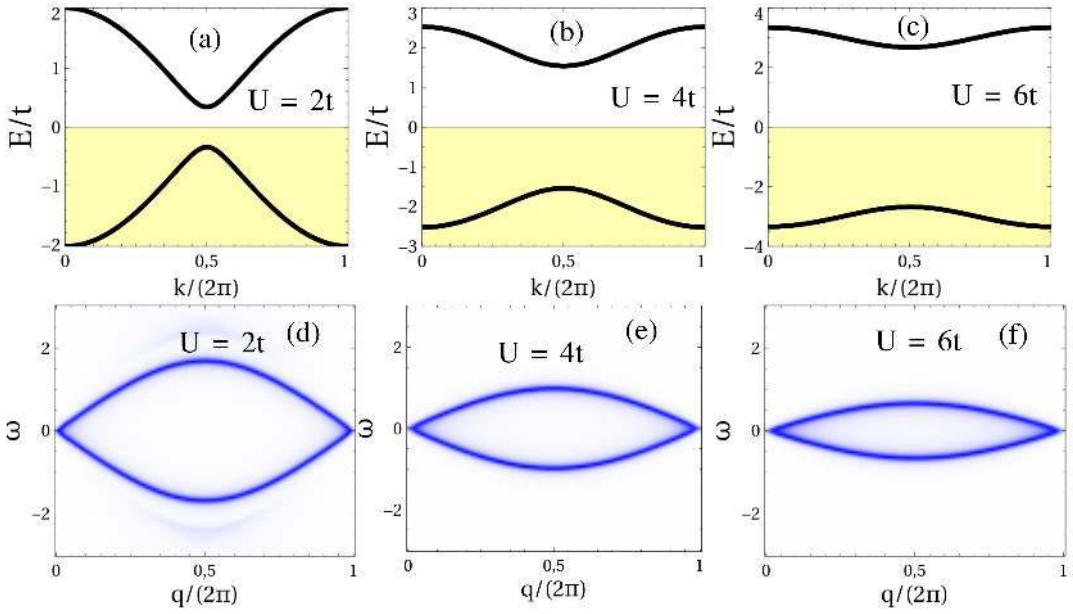

Figure 5.8: Band structures (a,b,c) at different U, and corresponding spin wave dispersions (d,e,f). As can be observed, the slope of the dispersion becomes smaller for larger U, which implies that the group velocity of the spin waves also becomes smaller.

The dispersion relation of the spin waves will determine their transport behavior due to the relation with the group velocity. In the limit of infinite interaction, the spin is completely frozen and the spin waves do not propagate. This can be easily understood in terms of an effective Heisenberg Hamiltonian for the Mott insulating phase

$$H = J\vec{S}_i \cdot \vec{S}_j \tag{5.8}$$

where $\vec{S}$ is the spin operator. Since J is the only energy scale in the previous Hamiltonian, the group velocity will proportional to J. For an electronic system in the large U limit, second order perturbation theory[289, 290] in the hopping give an effective J of the form

$$J \propto \frac{t^2}{U} \tag{5.9}$$

which for infinite U limit becomes zero. Therefore, as long as the localized limit is good starting point for a perturbative argument, bigger interactions will yield smaller spin wave dispersions, but always gapless.

The previous basic phenomenology is correctly captured by the RPA formalism for the spin wave spectrum. We show in Fig. 5.8 how the band structure and spin-spin response evolve as the interaction becomes bigger. It is worth to note, that only at large U, the slope of the linear dispersion will follow Eq. 5.9. At low U electrons are not in the Mott insulating regime, which in particular implies that the expectation value of the spin operator in every site will be 1/2.

Ferromagnetic chain

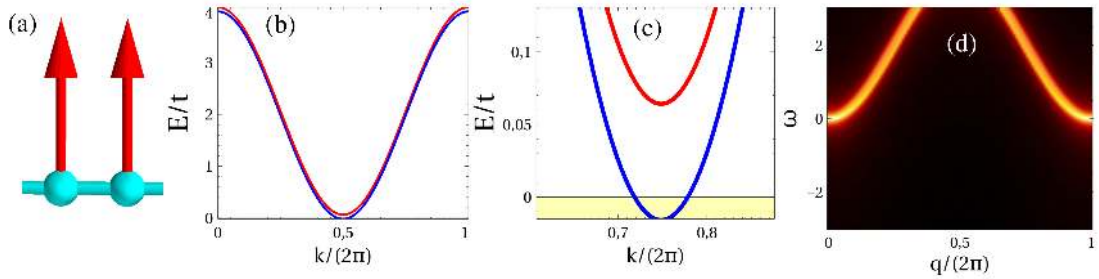

Figure 5.9: (a) Sketch of ferromagnetic order in a linear chain. Band structure (b,c) of the ferromagnetic chain at low filling factor (0.02). At this filling factor, the spin waves (d) develop a quadratic behavior at low q, in comparison with the linear dependence in antiferromagnetic systems. For this calculations $U = 2t$.

Another text-book example of spin waves are the ones found in a ferromagnet. In that case the spin wave spectrum is known to develop a quadratic behavior at low q, $\omega = Dq^2$. Within a tight binding model, the simplest case that shows ferromagnetic order is a linear chain at very low (or very large) filling. In that case, interactions create a Stoner instability in a non-magnetic ground state of the system, driving the system towards an ordered phase, creating a spin splitting in the band structure. The Stoner criteria states that the system will become ordered when the condition $\rho J > 1$ holds, where ρ is the density of states at the Fermi energy and U the relevant electronic interaction, relation that can be easily derived for a free electron gap taking interactions at the mean field level. It is worth to note that the previous criteria is derived for itinerant electrons, and therefore is expected to hold specially for not too large interactions, the limit of itinerant magnetism. This situation is the one that holds in ferromagnetic bulk iron.

Intermediate filling, chiral magnet

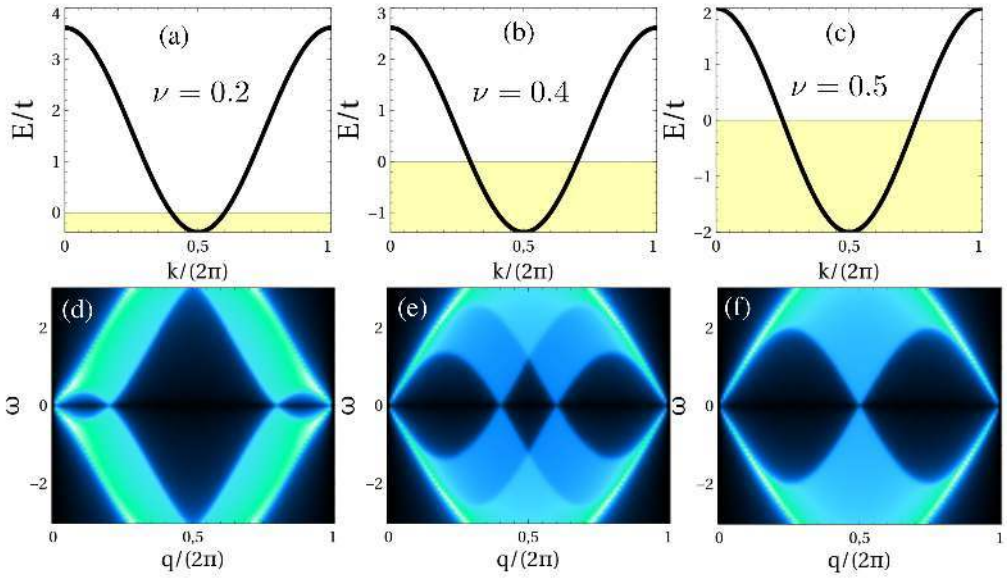

Figure 5.10: Non magnetic chain at different filling factors (a,b,c). For every filling, the Fermi surface is nested at a different q-vector. The spin-spin response for the previous fillings (d,e,f) show a poles at $\omega = 0$ and $q = 0$ and further poles for $q \neq$. Those q_N are precisely the nesting vectors, and indicate that a spin excitation at that energy will be gapless. In particular, they will be unstable, so that the system will be driven towards a different ground state, the chiral magnetic state.

Due to the perfect nesting of the band structure in one dimensional systems, ground states with chiral order are trivial to obtain in a linear chain. Given a particular band structure, the nesting vector can be tuned by changing the electronic doping of the system. For one atom per unit cell, the dispersion relation follows $E = 2\cos(k)$. In particular, as we presented in the first case, for half filling this leads to a nesting vector $q_N = \pi$, which is precisely an antiferromagnetic order. For very low filling, the nesting vector becomes arbitrarily small $q_N \to 0$, which corresponds with an asymptotically ferromagnetic order. Nevertheless, in the intermediate regime, a finite nesting vector will give rise to a finite nesting vector, which indicates a transition towards a chiral magnetic order.

Finally, it is worth to remark that the chiral order can be anticipated from an anomalous spin wave spectrum, even in the case they are calculate with "wrong" ground state. The features that indicate an instability towards chiral order are zero spin wave modes, at $q \neq 0$.

5.4.4 Spin waves in quantum Hall regime

After having shown the basic phenomenology of spin waves, in the following we will apply the same technique to study the spin wave spectrum in a graphene[286] Quantum Hall bar. In comparison with the linear chain, the quantum Hall bar we will be interested in the spatial variation of the spin wave spectral function. In the fashion as zigzag boundaries bound electronic states, we will see that the localized magnetic moments of the zigzag edges create specific spin wave branches, Apart from the conventional bulk spin waves. In the following we will focus on the antiferromagnetic[286] Quantum Hall state, i.e. the situation when only off-plane magnetic field is applied.

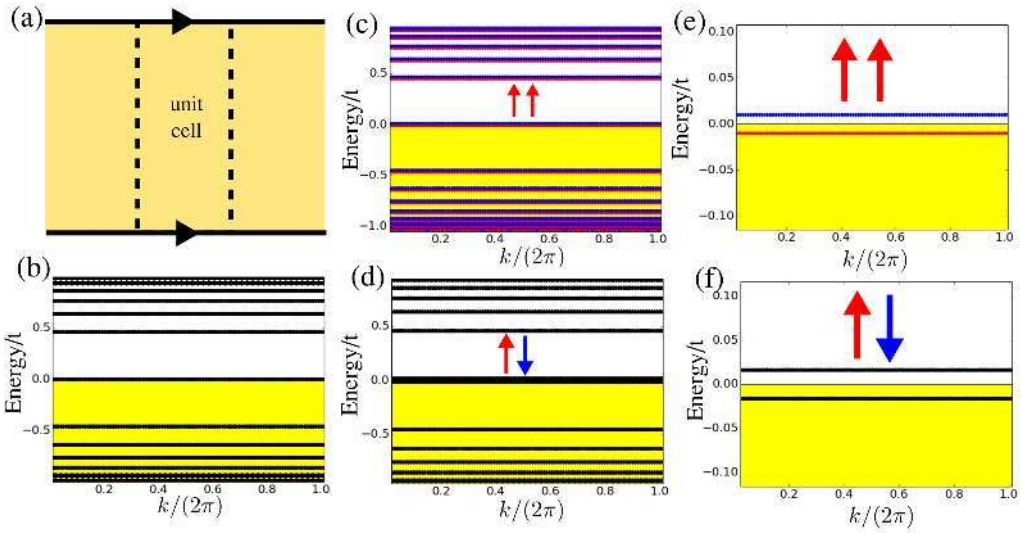

Figure 5.11: Sketch of a periodic unit cell (a), where the magnetic field has been chosen so that the upper and lower edges have the same Peierls phase, showing a flat band Landau band structure (b). Band structure in ferromagnetic (c,d) and antiferromagnetic (e,f) cases, showing the two different splitting of the Landau levels.

In first case, we consider a system with periodic boundary conditions in also in the direction y. In that situation, edge states do not appear, provided a commensurate magnetic field with the lattice is chosen. The condition that the magnetic field has to fulfill is that the Peierls phase is the same in the lower and upper edge of the ribbon

$$2\pi n = BW\Delta x \tag{5.10}$$

where W is the width of the ribbon. In order to maintain the calculations as efficient as possible, we will choose $m = 1$. It is worth to note that the periodic

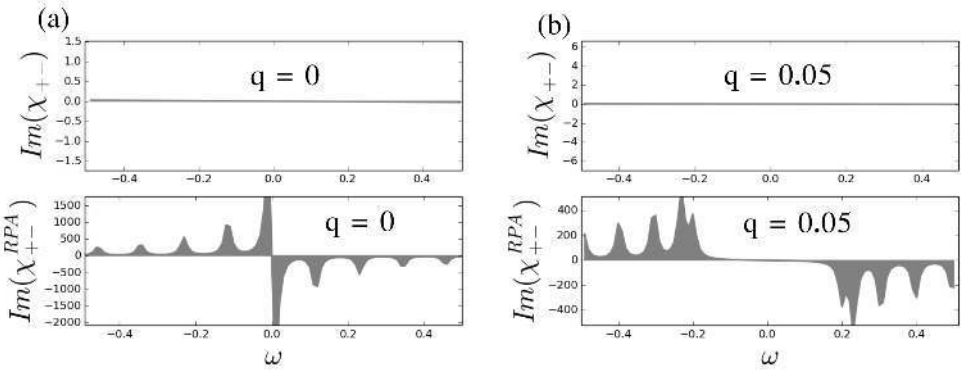

Figure 5.12: Spin-spin response at two different qvectors for antiferromagnetic Quantum Hall graphene. For the free response $\chi^0_\pm$, no imaginary part is present due to the electronic band gap. In comparison, the RPA re-summation $\chi_\pm$ shows poles at the spin wave modes, including the Goldstone mode at $\omega = q = 0$. The finite width of the peaks arises due to the finite analytic continuation δ.

boundary conditions impose a quantization on the magnetic field, which translates into the fact that we will not be able to change it continuously. This is in comparison with the conventional ribbons studied previously, where the magnetic field was a continuous parameter.

The spectrum in that situation5.11 consists of only Landau levels. This geometry allows to study the spin waves of the pure bulk system and compare it with the case in which both bulk and edge states are present.

The antiferromagnetic case shows a symmetry for negative and positive frequencies, which is yield by the combination of the product of time reversal and inversion symmetry. The interacting response shows poles at $\omega = 0$ as well as different poles at different energies, which is a mark of the linear dispersion relation expected for an antiferromagnet.

The different branches observed in Fig. 5.13 correspond to the different spin wave modes that can be observed in the confined ribbon. It is clearly seen that they follow a Dirac like spectrum, which arises naturally from a linear dispersion for two dimensional spin waves of the form

$$\omega = D|q| = D\sqrt{q_x^2 + q_y^2} \tag{5.11}$$

Such dispersion relation, gives in the finite geometry of the ribbon confined modes. The quantization is the spin modes yields a dispersion of the form

$$\omega_n = D|q| = D\sqrt{q_x^2 + \left(\frac{2\pi n}{W}\right)^2} \tag{5.12}$$

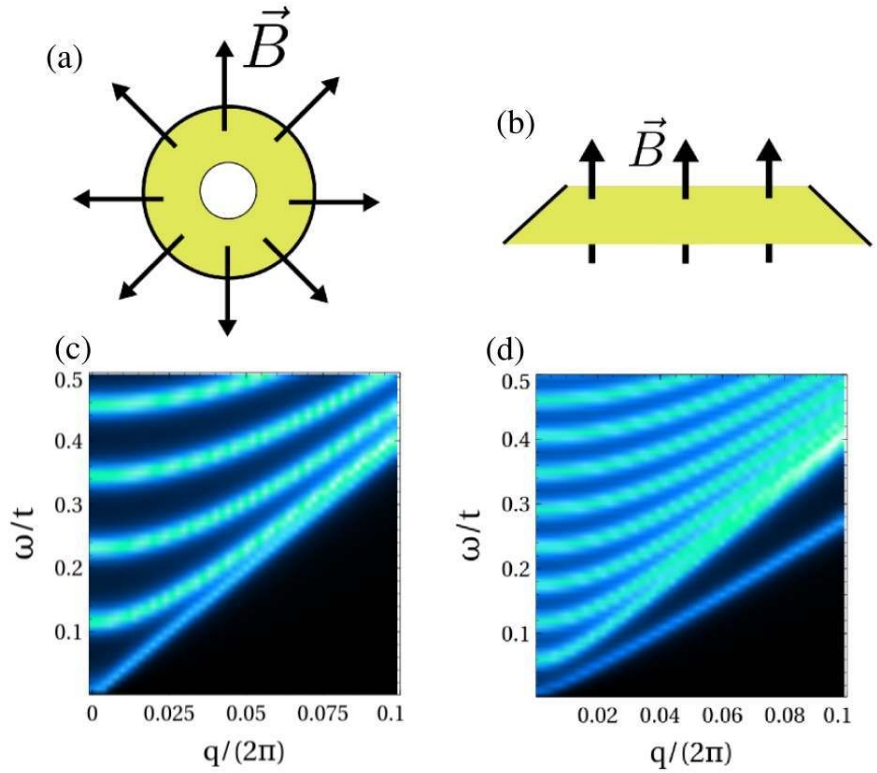

Figure 5.13: Scheme of the geometry of the magnetic flux in the nanoribbons for th compactified (a) and edge (b) configurations. (c,d) Spin wave spectrum for the two previous configurations. The system with edge (c) which shows localized moments, develops a branch with different stiffness. Response at q=0 for the edges system (e), and local density of states of the lowest excitation, showing a coupling between bulk and edge spin waves.

where W is the width of the ribbon. In particular, for $q_x = 0$ the frequencies of the spin-waves are spaced by a quantity $D2\pi/W$

$$\omega_n(q_x = 0) = D\frac{2\pi n}{W} \tag{5.13}$$

Fig. 5.13 shows the spin wave excitation for a zigzag edged antiferromagnetic quantum Hall ribbon. Bulk spin wave branches become quantized due to finite size effects, and in comparison with the edge-less system, a new branch shows up. This new branch becomes decoupled from the other ones at high q. Inspection of its LDOS, reveals that the decoupled branch corresponds to excitations which live on the edge. Nevertheless, low q LDOS are no longer pure edge states, but a combination of bulk and edge and spin waves. This is easily rationalized taking into

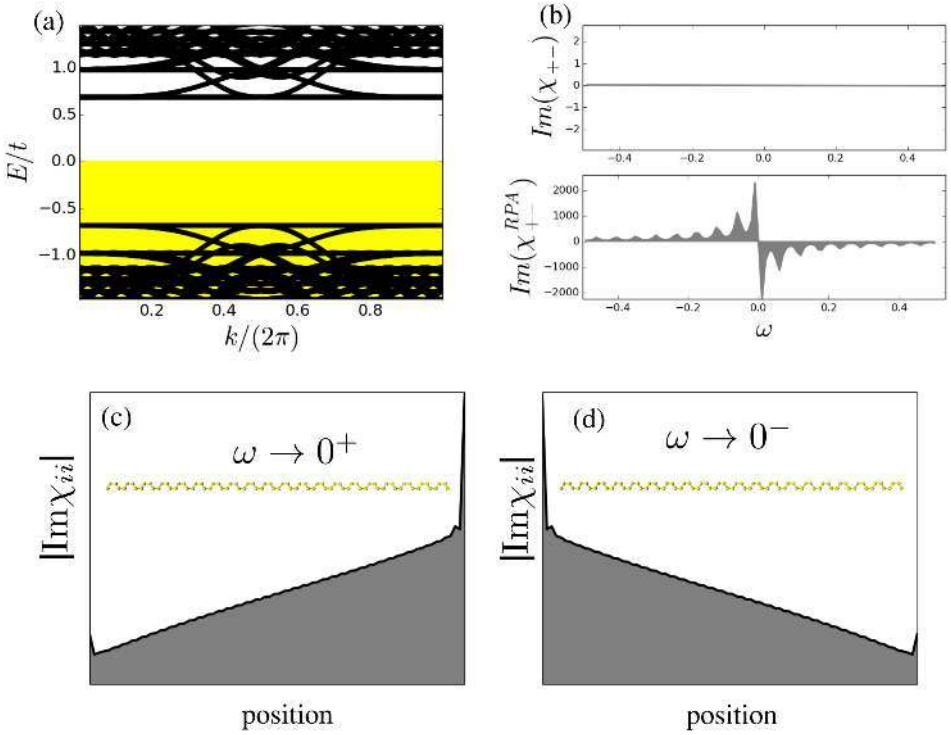

Figure 5.14: (a) Band structure of an antiferromagnetic zigzag ribbon in the quantum Hall regime. (b) Imaginary part of the spin-spin response of the system, showing poles only when RPA is considered. The diagonal terms of the imaginary part of the response can be understood as the spectral function of the spin waves. In this fashion, the pole at $\omega = 0$ (c,d) is associated with collective spin excitations, whose weight is mainly edge modes.

account that a gapless spin wave excitation is expected to appear, which corresponds to the magnetic Goldstone mode. This mode lives everywhere there is a magnetic moment, where the spin symmetry has been broken, thus having weight in the bulk as well as in the edge.

So far the spin dispersion where shown for the bulk spectrum, which electronically consist only in pure bulk Landau levels. In the following, we consider the simultaneous interplay between the bulk and edge spin waves, by performing the calculation in a system with an edge. For the case of a zigzag edged ribbon, the spin wave spectrum show new spin wave branches which are associated with the edge magnetic moments. Again, the spin response shows poles associated to the different spin waves of the system. Focusing first in the dispersion for $q \to 0$, it is observed that the system shows the Goldstone modes expected. However, as can be

seem from the diagonal terms of the response, the zero energy spin excitations are strongly localized in the edge. It is important to realize that in the antiferromagnetic quantum Hall state, in the zigzag ribbon the localized magnetic moments of the edges are also in an antiferromagnetic configuration. This fact allows to understand the strong transition between Fig. 5.14c,d. For positive frequencies, the spin-wave tries to flip the edge in the up configuration. The result for negative frequency holds due to the special symmetry of the antiferromagnetic configuration, which allows to relate negative frequency to the time reversal and spatially inverted system.

The other peaks observed in Fig. 5.14 correspond to the different modes that the finite ribbon can sustain. They are a combination between bulk and edge excitations, and in comparison with the $n = 0$ mode, the show a stronger weight on the bulk part. As the index of the peak increases, the spin wave shows more maximums, which are associated with the mode number n.

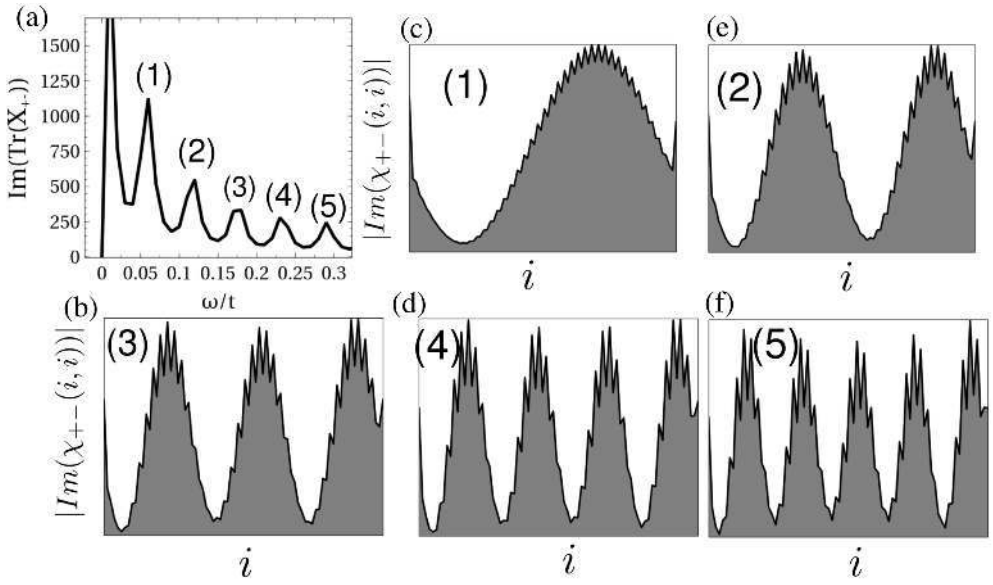

Figure 5.15: Spin-spin response for $q \to 0$ (a) in a zigzag ribbon. The space-resolved local spectral function for each peak in (a) shows the structure of typical confined modes, as shown in panels (b,c,d,e,f). It is seen that although the spatial distribution resembles normal modes in confined cavity, there is a strong coupling with the localized edge mode.

5.4.5 Spin wave stiffness of the antiferromagnetic state

For the antiferromagnetic state, the slope of the spin wave dispersion is controlled by the spin wave stiffness. In here we will focus on characterizing the stiffness of

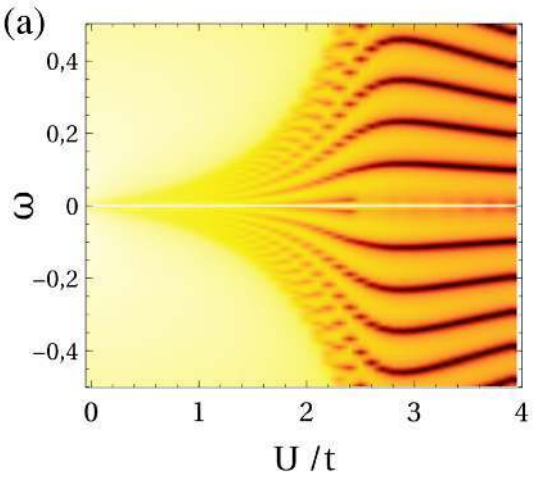

Figure 5.16: Evolution of the RPA spin response with the interaction U, whose splitting are proportional to the spin stiffness of the spin waves.

the quantum Hall antiferromagnet.

First, it worth to note that in comparison with usual antiferromagnetic insulators, the insulating state of the QHAF, arises due to the Landau level localization. In particular, the Landau level structure causes that an arbitrary small interaction U is able to open up a gap.

In the following, we will assume that a certain Heisenberg model can be associated with the magnetic state

$$H = JS_i \cdot S_j \tag{5.14}$$

We will focus first on the high U limit. In this situation, the system can be described as lattice of localized electrons. The local spin are coupled one to each other by virtual processes which involved second order processes in which an electron hops t a neighboring site and comes back. This gives rise to an effective Heisenberg model with coupling

$$J_{U\to\infty} = t'^2/U \tag{5.15}$$

In the low U limit, the magnitude of the local magnetization is dominated by the interaction U. The gap opening will increase with U, and will provoke different filling of the up and down, increasing the local magnetization. Furthermore, and in comparison with usual antiferromagnets, the QHAF shows a very strong scaling of the local magnetization, leading to nearly dependent magnetic order as a function of the off-plane magnetic field. Assuming a linear scaling of the local magnetization

with U, and taking into account the scaling with the magnetic field, the renormalized Heisenberg coupling will take the form

$$J_{U\to 0} = B^2 U^2 \tag{5.16}$$

As shown in Fig.3, numerical calculations show a trend compatible with the previous waving hand arguments.

5.5 Summary

We have presented a comprehensive study of magnetic order in graphene stripes in the Quantum Hall regime, mostly at half filling, based on a non-collinear mean field Hubbard model that treats both edge and bulk on equal footing. The interplay between bulk magnetism and the type of edge state, confirmed in recent experimental results[272], motivates the present work where the modulation of the magnetic order at the edges is taken into account. The model captures the main experimental observations including the linear scaling between the bulk gap Δ and the off-plane magnetic field B_z. Our calculations reveal the coupling between the quantum spin Hall like edge states and preformed local moments at zigzag edges, that provides a natural scenario for the spin back-scattering observed experimentally. This scenario is similar to recent proposals[291, 292] where spin-Hall edge states interact with magnetic impurities. The last but not the least, at quarter filling the model predicts the existence of a previously overlooked ferrimagnetic phase with spin polarized edge states with $G = G_0$.

Finally, we have shown that spin waves naturally arise in the antiferromagnetic case, showing the conventional linear dispersion relation. Importantly, the localized edge moments create a specific branch of edge sin waves, that become decoupled from the bulk al large k. The spin stiffness determines the group velocity of the spin waves, and it has been unveiled its dependence with the interaction strength.

Chapter 6

Quantum anomalous Hall effect in graphene driven by skyrmions[1]

One of the obstacles to get quantum anomalous Hall effect in graphene is that usually the topological gap involves spin orbit coupling. Since carbon is a light atom, the topological gap opened is very small. In this chapter we show how a quantum anomalous Hall state can be induced in graphene without any spin orbit coupling in carbon, simply by exchange effects of the conduction electrons. This mechanism takes advantage of topological magnetic structures in real space, known as skyrmions, imprinting the topological properties from the magnetic structure into the graphene electrons.

6.1 Introduction

Electronic Chern insulators usually show up by an interplay of spin orbit coupling and magnetism. For instance, a "constructive" way to create Chern insulators consist on taking a Z_2 non magnetic topological insulator, and dope it with magnetic impurities. If the gap closes and reopens, and you are "lucky", you might obtain a Chern insulator. Another constructive way is to take a magnetic system and add spin orbit coupling, if a gap opens up, another Chern insulator might have been obtained. Of course both of this recipes are not going to yield always Chern insulators, but have been proven to be good routes towards it. The simplest way to check whether they are topological is to calculate their Chern number. Therefore, put as ingredients magnetism and spin orbit coupling, turn on the blender, and Chern insulators can show up.

The quest with getting Chern insulators with light materials struggles with the fact that spin orbit coupling in light atoms is fairly weak. Magnetism in principle

[1] some parts of this chapter are taken from Physical Review B 92 (11), 115433 (2015)

is not a problem, light atoms can become magnetic, for example, the molecular oxygen O_2 that we breathe is ferromagnetic, has spin $S = 1$. At this point it seems meaningful to ask whether spin orbit coupling is necessary to have Chern insulators. The answer is no, spin orbit coupling is not necessary at all. This will be clear shortly by examining the symmetry properties of the Chern number.

The Chern number C is an integer number which is directly related with the Quantum Hall conductivity

$$\sigma_{xy} = \frac{e^2}{h} C \tag{6.1}$$

The Hall conductivity is odd with respect to time reversal, and also by the application of complex conjugation. The same symmetry affects the Chern number upon complex conjugation

$$C \to -C \tag{6.2}$$

therefore, only ground states that break time reversal and conjugation symmetry can lead to Chern insulators. Ferromagnetic order by itself still has conjugation symmetry (magnetic order in z direction only involve the real matrix s_z), so it is not enough to create a topological state. Spin orbit coupling alone has time reversal symmetry, so it is also un-capable. The simplest way to break both symmetries simultaneously is by a combination of ferromagnetic order (which breaks time reversal) plus spin orbit coupling (whose inclusion also breaks spinless time reversal, i.e. complex conjugation).

Importantly, a magnetic order that involves a complex spin matrix as s_y will break conjugation symmetry. The bottom-line is that, if magnetic terms in the Hamiltonian are complex, conjugation symmetry might be broken. Of course collinear magnetization in y direction is not enough, since a spin rotation will turn it real (to the x or z axis). Only a magnetic order that involves the three Pauli matrices, so that no global rotation can make the magnetization lie in the real xz axis, is able to create a Chern insulator. To summarize, non-coplanar magnetic textures are another recipe to get a Chern insulator.

6.2 Graphene as a Chern insulator

Graphene is a zero gap semiconductor in the brink of becoming a topological insulator. It is no coincidence that several predictions of topological phases in two dimensional systems are based on some small modification of the model that actually describes graphene, namely, a tight-binding Hamiltonian for electrons in a honeycomb lattice at half filling. In a seminal paper[107], Haldane proposed that

a honeycomb crystal with a suitable magnetic flux decoration would become insulator with a quantized Hall response, without Landau levels. The ground-breaking proposal of the quantum Spin Hall phase by Kane and Mele[105, 106] is also based on graphene with spin-orbit coupling, that is mathematically related to the Haldane model. A QSH-like phase was also predicted for graphene under the influence of a perpendicular magnetic field and ferromagnetic order[168]. In addition, the quantum Hall effect has been observed in graphene at a relatively low magnetic field at low temperatures[183], and even at room temperature[293] at high fields. Furthermore, the combination of exchange interaction and spin-orbit coupling has been predicted to give rise to the QAH phase[169]. Here we propose a topological phase that, unlike all of the above, requires no spin-orbit coupling and no applied magnetic field.

Topological insulating phases in two dimensions attract interest because of the very special transport properties, such as the perfect conductance quantization of the quantum Hall phase[93]. These special transport properties arise from the fact that topological phases have a gapped bulk and conducting edge states. Interestingly, QAH phases have chiral edge states for which intraedge backscattering is impossible. Thus, quantization of conductance of the QAH phase should be as perfect as the one observed in the quantum Hall effect. This contrasts with QSH edge states, for which only the total absence of time-reversal symmetry breaking impurities, such as nuclear spins or local moments, prevents backscattering. As a result, the quantization of conductance in QSH and QSH-like phases is far[111, 183] from the perfection observed in graphene QH systems[293, 93].

The notion that exchange interaction with the local moments with non-collinear spin textures affects severely the kinetic energy of itinerant electrons, goes back to the proposal of the double-exchange mechanism[294]. Later, the role of non trivial effects on the Berry phase was recognized[295, 296], and the notion that non-collinear spin textures induce an effective orbital magnetic field that would lead to an anomalous Hall term was put forward[297, 298, 299, 300, 301, 302, 303, 304]. It was also shown by Ohgushi *et al.*[305] that the double exchange model on a two dimensional Kagome lattice with non-collinear classical spins led to a quantum anomalous Hall phase with quantized Hall conductance. Recent experiments have demonstrated the possibility of growing graphene islands on top of a two dimensional skyrmion lattice hosted by a single atomic layer of Fe deposited on an Ir(111) substrate[306]. This experiment, together with the notion that non-collinear spin textures induce very interesting effects on conduction electrons, [296, 297, 302, 303, 305], motivate our study of graphene electrons coupled to a skyrmion lattice. Interestingly, we find that this system can exhibit the Quantum Anomalous Hall effect (Fig. 6.1e,f), a topological phase of matter that is being actively pursued in condensed matter physics[307]

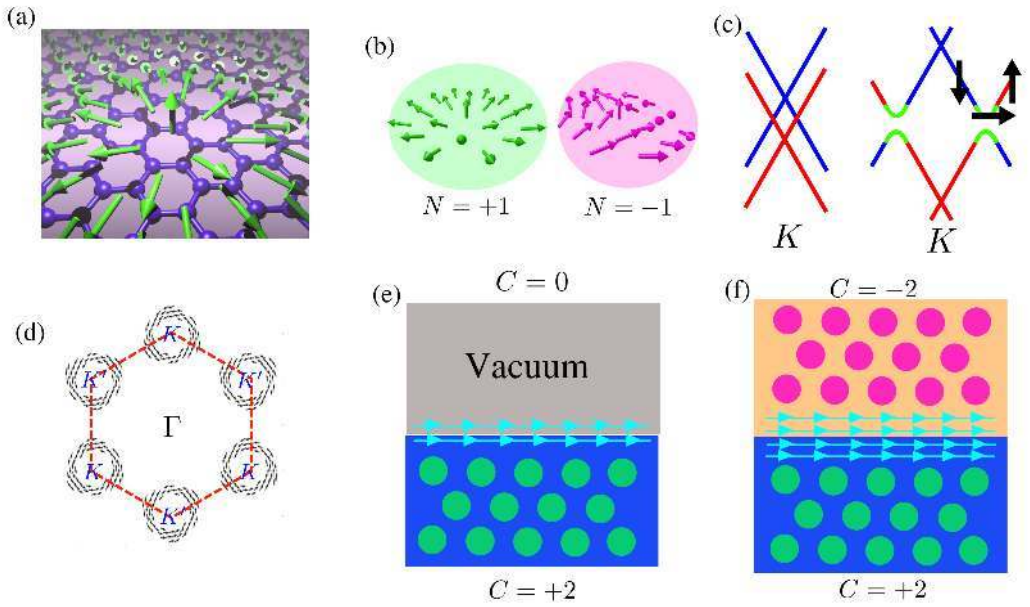

Figure 6.1: (a) Scheme of a graphene layer deposited on a skyrmion lattice (only the skyrmion cores are shown). (b) Skyrmions with $N = \pm 1$, that trigger a QAH. (c) Influence of the exchange to the skyrmions on the Dirac cones: spin splitting and band-gap opening (d) Spin texture induced in the reciprocal space by the Skyrmion driven gap opening. Edge states between vacuum and 2d Skyrmion crystal (e), and between two skyrmionic crystals with different chirality (f).

6.3 Model

Skyrmions are non-collinear spin textures (Fig. 6.1a and b) characterized by a topological number[308]

$$N = \frac{1}{4\pi} \int \vec{n} \cdot \left(\frac{\partial \vec{n}}{\partial x} \times \frac{\partial \vec{n}}{\partial y} \right) dA \tag{6.3}$$

where $\vec{n} = \frac{\vec{M}}{|\vec{M}|}$ is the unit vector associated to the skyrmion magnetization. Skyrmions are being very actively studied in the context of spintronics[308, 309], and they have been found both in bulk compounds[308] and two dimensional systems [310]. Here we propose a mechanism to induce the QAH phase in graphene, fully independent of the spin-orbit coupling of carbon. Namely, it is based on exchange interaction with a magnetically ordered surface that hosts a skyrmion lattice (Fig. 6.1a).

Our starting point is the tight-binding model for electrons in graphene $\mathcal{H}_0 = \sum_{ij\sigma} c^\dagger_{j\sigma} c_{i\sigma}$ plus their exchange to an arbitrary magnetization field, that is treated

classically:

$$\mathcal{H} = \mathcal{H}_0 + J \sum_i \vec{S}_i \cdot \vec{M}_i \tag{6.4}$$

Here i labels the sites of the honeycomb lattice, J is the short-range exchange interaction constant, $\vec{S}_i$ and $\vec{M}_i = M_0 \vec{n}_i$ are the electronic spin density operator and classical magnetization, respectively, evaluated at site i. The length of the magnetization field M_0 is assumed to be the same for all sites. Unlike most of previous work[311], we focus on the weak coupling limit $J << t$, adequate for proximity induced magnetism. Therefore, the exchange field act as a perturbation on the Dirac spectrum.

The magnetization of a single skyrmion can be expressed as a map from the plane described in polar coordinates r, ϕ to the unit sphere, described in spherical coordinates Θ, Φ,

$$\vec{n} = (\sin\Theta(r)\cos\Phi(\phi), \sin\Theta(r)\sin\Phi(\phi), \cos\Theta(r)) \tag{6.5}$$

where $\Theta(r)$ is such that $\Theta(r = 0) = 0$ and $\Theta(r > R_{Sky}) = \pi$, where R_{Sky} is the skyrmion radius. $\Phi(\phi) = N\phi + \gamma$, where N is the skyrmion number that accounts for its vorticity[308] and γ is a phase that determines the helicity of the skyrmion. Since γ can be gauged by a rotation along the z-axis, we take $\gamma = 0$ without loss of generality. For the sake of simplicity, in the following we will assume a step-wise profile for the magnetization

$$\Theta^{\text{hard}}(r) = \begin{cases} 0 & r = 0 \\ \pi/2 & 0 < r < R_{Sky} \\ \pi & r > R_{Sky} \end{cases} \tag{6.6}$$

We have verified that the results do not change qualitatively if we use a smooth parametrization of the azimuthal angle.

6.4 Quantum anomalous phase at weak coupling

In this section we present the result for the weak exchange limit ($J << t$). This situation is the one to be realistically obtained for graphene on top of a skyrmion lattice. We show that a topological gap opens for arbitrarily small exchange coupling and independently on the type of skyrmion lattice, triangular or rectangular.

6.4.1 Triangular skyrmion lattice

We now consider the properties of graphene interacting with a triangular crystal of skyrmions. In Fig 2b we show the energy bands for a 5x5 supercell with one

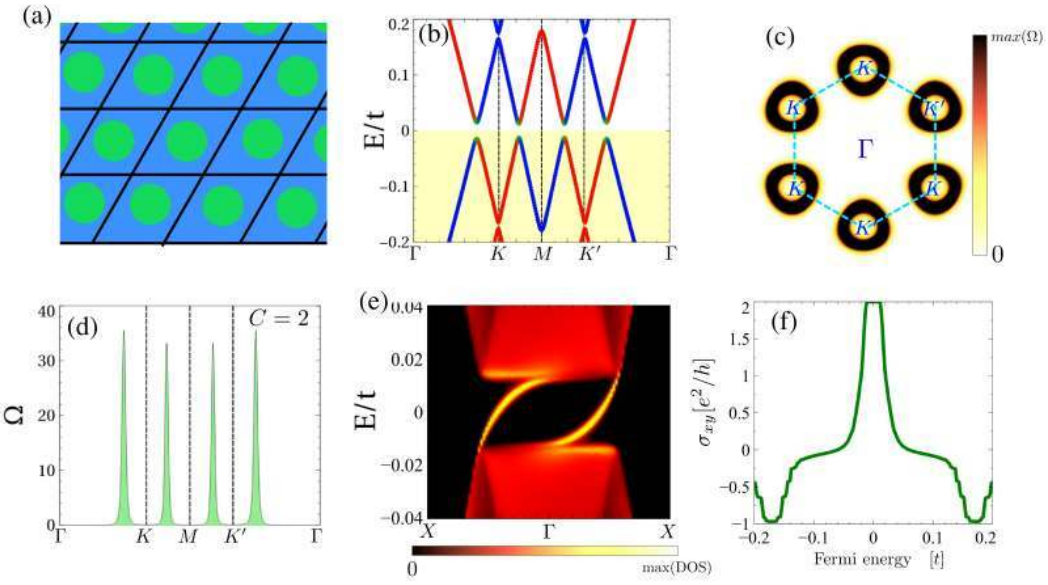

Figure 6.2: (a) Scheme of a triangular arrangement of skyrmions and (b) band structure of a 5x5 honeycomb supercell with a skyrmion with winding number equal to 1 and $J = 0.3t$. (c) Contour plot of the Berry curvature, with a small trigonal warping around the corners of the hexagonal Brillouin zone. (d) Positive Berry curvature localized at the region of band-gap opening. (e) Surface density of states on the termination of a semi-infinite graphene plane, showing two in-gap chiral states. (f) Anomalous Hall conductivity as a function of Fermi energy

skyrmion. It is apparent that exchange interaction with the skyrmions opens up a gap in graphene. This can be understood as follows. We write the exchange part of the Hamiltonian as

$$\mathcal{V} = +J \sum_I \vec{S}_I \cdot \left(\langle \vec{M} \rangle + \delta \vec{M}_I \right) \tag{6.7}$$

where $\langle \vec{M} \rangle = \frac{1}{N} \sum_I \vec{M}_I$ is the average magnetization, and $\delta \vec{M}_I = \vec{M}_i - \langle \vec{M} \rangle$ are the fluctuations. Ignoring the fluctuation term, the average magnetization induces a spin-splitting, shown in figure 1b, where the bands have a well defined spin along the average magnetization. The resulting conduction band of one spin projection is degenerate with the valence band of the opposite spin projection, defining a circle of degenerate points that, at half filling, happens to be the Fermi surface (see Fig. 6.1c). For non-collinear spin textures, $\delta \vec{M}$ has terms orthogonal to $\langle \vec{M} \rangle$, $\delta \vec{M}_\perp$, that open up the gap at the degeneracy circle, and creates a spin vorticity in the reciprocal space (see Fig. 6.1d). A similar argument has been used by Qiao and coworkers in their proposal[169] for QAH in graphene with Rashba spin-orbit coupling and a exchange field. In our system the $\delta \vec{M}_\perp$ part of the Hamiltonian plays the same role

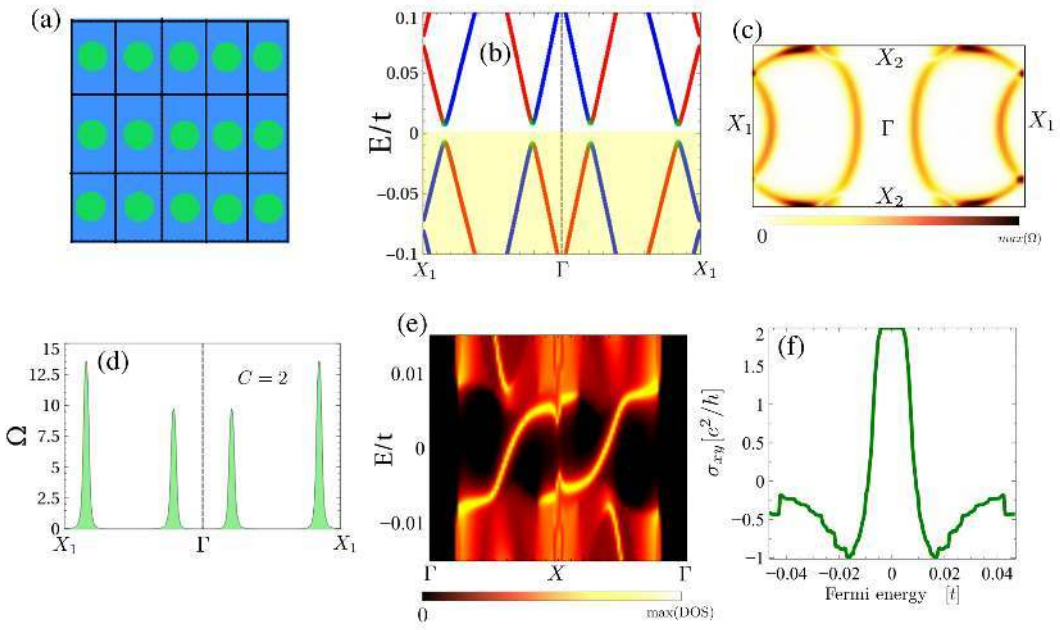

Figure 6.3: (a) Scheme of a rectangular skyrmion crystal. (b) Band structure of half filled graphene with a rectangular unit cell, coupled to the rectangular skyrmion lattice with $J = 0.3t$. (c) Berry curvature in the whole Brillouin zone, showing a same sign behavior which sums up to a $\mathcal{C} = +2$ total Chern number. (d) Berry curvature along the k path shown in the band structure, showing a non-vanishing contribution in the anti-crossings points. (e) Surface DOS in a seminfinite geometry showing two chiral states. (f) Anomalous Hall conductivity as a function of Fermi energy

as the Rashba coupling in their model. However, we found that only skyrmions with topological charge $N = \pm 1$ are able to open a topological gap.

The non-trivial nature of the gap of Fig. 6.2b can be anticipated from the Berry curvature[171] profile shown in Fig 2d. A non vanishing Berry curvature arises at the crossing circle of the spin-split Dirac points (see Fig. 6.2c), where the spin-flip terms open-up a gap.

The Hall conductivity can be be expressed as an integral of the Berry curvature[107, 303, 20]:

$$\sigma_{xy}(E_F) = \frac{1}{2\pi}\frac{e^2}{h}\sum_n \int f(\epsilon_n(\vec{k}), E_F)\Omega_n(\vec{k})d^2k \tag{6.8}$$

where $f(\epsilon_n(\vec{k}))$ is the Fermi occupation function, and n labels the bands. When the Fermi energy, E_F, lies inside a gap, the Hall conductivity is proportional to a

Chern number $\mathcal{C}$[20], which is an integer number $\mathcal{C}$, resulting in a quantized Hall conductivity $\sigma_{xy} = \mathcal{C}e^2/h$. Our calculations show that when E_F lies in the gap opened by the coupling to the $N = \pm 1$ skyrmions, the Chern number is given by.

$$\mathcal{C} = 2N \tag{6.9}$$

This is the central result of this work: the topological winding number of the skyrmions is imprinted into the Dirac electrons. Several consequences follow. First, two chiral edge states are expected to occur at the boundaries of the crystal. This is confirmed by our calculations, using a recursive Green function method[312] to calculate the surface states, as shown in Fig. 6.2e. Second, an interface between two skyrmion lattices, with opposite skyrmion numbers $N = 1$ and $N = -1$, is expected to show 4 interface states according to the index theorem (see fig. 6.1f). Third, when E_F lies inside the gap, the Hall conductance is quantized [20, 303] $\sigma_{xy} = \mathcal{C}\frac{e^2}{h}$. Importantly, the Hall conductivity also takes large, but not-quantized values, when effect Fermi energy lies close to, but outside, the gap (see Figs. 2f, 3f), on account of the finite Berry curvature integrated over the occupied states[313].

6.4.2 Square skyrmion lattice

We now address the question of the influence of the type of skyrmion lattice on the existence of the QAH phase. In particular, motivated by experimental results[306], we consider a rectangular skyrmionic crystal, commensurate with the graphene lattice (see figure 6.3a). We find that the topological character of such system strongly depends on whether the valley mixing is an important effect.

The topological phase is observed for those unit cells in which the two valleys fold to different points in the Brillouin zone, which avoid intervalley mixing. As in the triangular case, the in-plane components open up a gap in the exchange split bands (Fig. 6.3b), which leads to a finite non-vanishing Berry curvature localized in the band crossing points (Fig. 6.3d). The Fermi surface in this case can be more complex than in the triangular skyrmion lattice due to the large folding of the reciprocal space, which is also reflected in Berry curvature Fig. 6.3c. The calculated Chern number is also $C = 2N$, as in the triangular lattice, which in a semi-infinite geometry gives rise to two copropagating edge branches (Fig. 6.3e).

Away from half filling, when the Fermi energy no longer lies within the gap, the anomalous response is still non-vanishing up to energies 4 times the gap (Fig. 6.3f). The sign of the anomalous response is again the same for electrons and holes as in the triangular case. In comparison, upon entering the conduction (valence) band, the response can rapidly become negative and with a value close to 1, due to the presence of an edge branch located in the valence (conduction) band (see Fig. 6.3e), that coexist with normal valence (conduction) states.

6.4.3 Experimental verification

The experimental verification of our proposal is not far from the state of the art. The optimal conditions to detect perfect edge transport associated to the QAH phase is induced by a skyrmion lattice hosted by an insulating magnetic material that couples to the graphene electrons. Three ingredients have been demonstrated in different systems. First, recent experimental results showing the possibility of growing graphene on the surface of Fe/Ir, a surface that hosts a skyrmion lattice[306]. Second, and independent from the first, recent experiments show that non-quantized anomalous Hall is induced in graphene by proximity to a ferromagnetic insulating substrate [314]. Finally, skyrmion lattices have been observed in insulating chiral-lattice magnet Cu_2OSeO_3[315].

The critical figure of merit to realize our proposal is the magnitude of the skyrmion induced gap. This is controlled by the strength of the exchange field of the underlying magnetic state. To gain some insight of the gap opening mechanism, it is convenient to change independently the off-plane (exchange shift) and in-plane (spin mixing) components of the skyrmion texture. Our numerical calculations (see Fig. 6.4b) for the triangular lattice of hard core skyrmions ($n_z(r < R_{Sky}) = 0$) show that the gap satisfies $\Delta \propto J_{in}J_{off}/t$ where J_{in} and J_{off} are the magnitude of the in-plane and off-plane components of the exchange field (see Fig. 6.4bcd). In the case of constant exchange strength, a quadratic exchange dependence is obtained $\Delta \propto J^2/t$.

For reference, and given that there are no measurements of J, we take it from DFT calculations for graphene on top of $BiFeO_3$ [316] that give $J = 70$ meV, and $t = 2.6$ eV. With the previous parameters, the topological gap would get a value of $\Delta \simeq 0.4$ meV, within reach of transport spectroscopy. Taking these numbers, the window of E_F within which the non-quantized intrinsic Hall effect would be sizable extends in a window of $1-3$ meV around the Dirac energy. Our calculations indicate that the non-quantized Hall conductivity would be larger in the case of the square lattice (Fig. 6.3f). We also note that the sign of the skyrmion-induced Hall contribution would be the same for electrons and holes, in contrast with the conventional Hall effect.

6.5 Strong coupling limit

We discuss here the behavior of the system in the large J limit, where $J >> t$ and the spin-splitting of the bands is much larger than the bandwidth. This strong coupling limit has been considered in previous works[305], but is not realistic in the case of graphene. In the strong coupling limit at half filling, the system behaves as a topologically trivial magnetic insulator, where both valence and conduction states

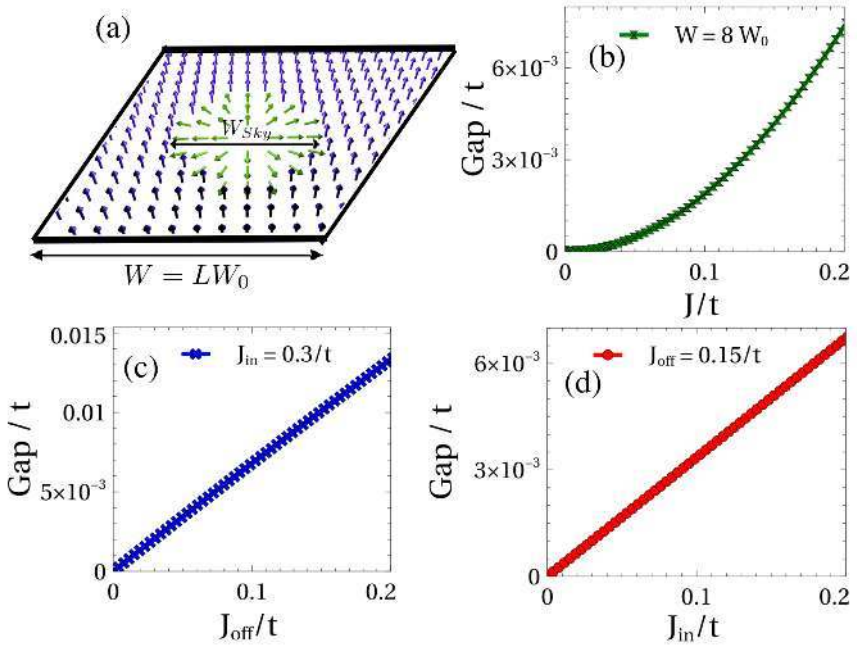

Figure 6.4: (a) Scheme of a hard core skyrmion, showing an in-plane radial magnetic profile and an out-core off-plane magnetism. Evolution of the topological gap at half filling with the global exchange (b), only the out core exchange (c) and the core exchange (d).

of the majority spin are completely full. Since spin degeneracy is completely lifted in this case, the Fermi energy lies at the Dirac point at quarter filling. In this case (Figs. 6.5), the low energy states are described by a gaped Dirac like spectrum and our calculations in this limit give $\mathcal{C} = 1$, for $N = 1$. Therefore, this is topologically different to the weak-coupling case discussed in the main text, and much closer to the original QAH phase proposed by Haldane [107].

The physical origin of this topological phase can be understood as follows. The standard[297, 303, 302, 305] spin rotation is performed, so that the exchange term is always diagonal[296, 297]. The local nature of this transformation generates a coupling to a gauge field in the hopping operator[297, 303, 302, 305] that describes an effective inhomogeneous magnetic field, that is responsible of the band-gap opening in this limit. In that limit, a skyrmion with topological number N creates an effective field equal to $N\Phi_0$, where $\Phi_0 = e/h$ is the magnetic flux quantum [308].

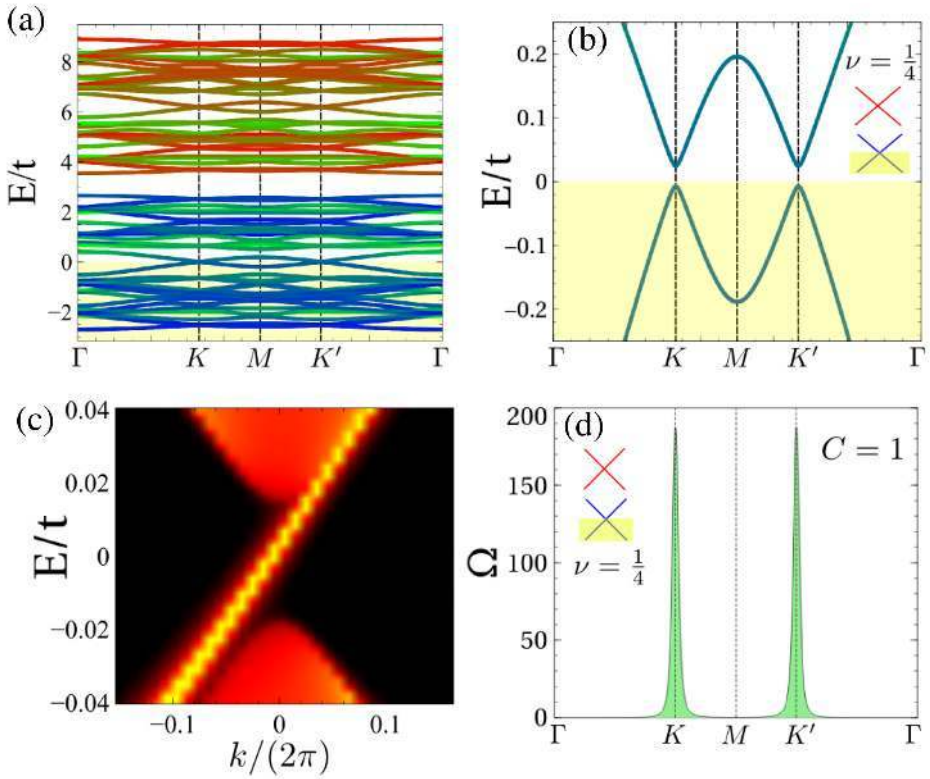

Figure 6.5: Graphene supercell over a triangular skyrmion crystal. Band structure (a,b) at filling 1/4 in the large exchange limit (J=3t). As shown by the surface density of states (c) and the Berry curvature (d), the system develops a quantum anomalous Hall state with a total Chern number $\mathcal{C} = 1$ At large exchange, the half filling state becomes trivial, whereas the filling 1/4 becomes topological resembling the Haldane model.

6.6 Perturbations to the QAH phase

6.6.1 Trivial gap opening

In this section we will discuss some of the situations in which a skyrmion texture will not give rise to a topological gap. First we emphasize that strong defects or inhomogeneities both in graphene, the underlying skyrmion lattice or the exchange coupling can give rise to a phase transition between the topological state to a trivial state. This problem is common to any engineered topological state, and its study relies on the particular features of the microscopic models, which depend on the underlying material that hosts the skyrmions.

In the following we focus on homogeneous effects well captured by our phe-

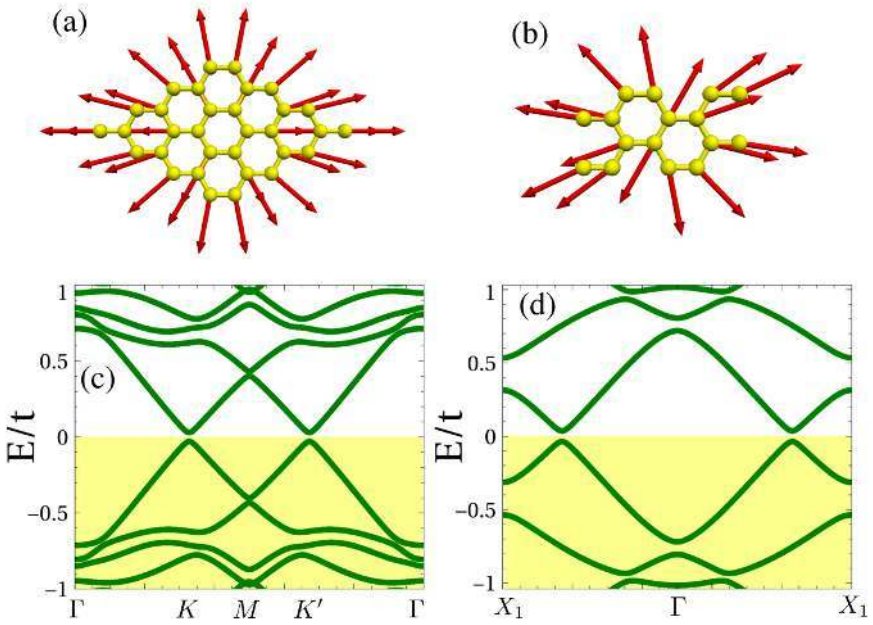

Figure 6.6: Unit cells (a,b) and band structures (c,d) for graphene over a fully in-plane triangular (a,c) and rectangular (b,d) skyrmion lattice. A gap is opened in the band structure, but the Chern number is identically zero, yielding a trivial insulator.

nomenological model that can ruin the perfect $\mathcal{C} = 2$ state. We will discuss two situation, the case of a pure coplanar spin texture, and situations with strong inter-valley mixing.

Coplanar spin textures

Here we consider the case of graphene coupled to coplanar non-collinear spin textures, shown in Fig. 6.6. We address the weak coupling limit ($J << t$) at half filling. In the case of a purely in-plane exchange field, the Hamiltonian can be made real by a rotation onto the Pauli matrices σ_x, σ_z, leading to a vanishing Hall response. We show in Fig. 6.6 examples of band structures of triangular and rectangular graphene unit cells subjected to fully in-plane exchange field. Although a band-gap opens, the calculated Berry curvature, and thereby the Chern number vanish in both cases.

The necessity of a non-coplanar spin texture can be easily understood in terms of the symmetry properties of the Chern number. Without loss of generality, the exchange field of a coplanar spin texture can be expressed in terms of the Pauli matrices σ_x and σ_z, provided the exchange field is rotated to lie in the xz plane

$$\vec{M} \cdot \vec{\sigma} = M_x \sigma_x + M_z \sigma_z \tag{6.10}$$

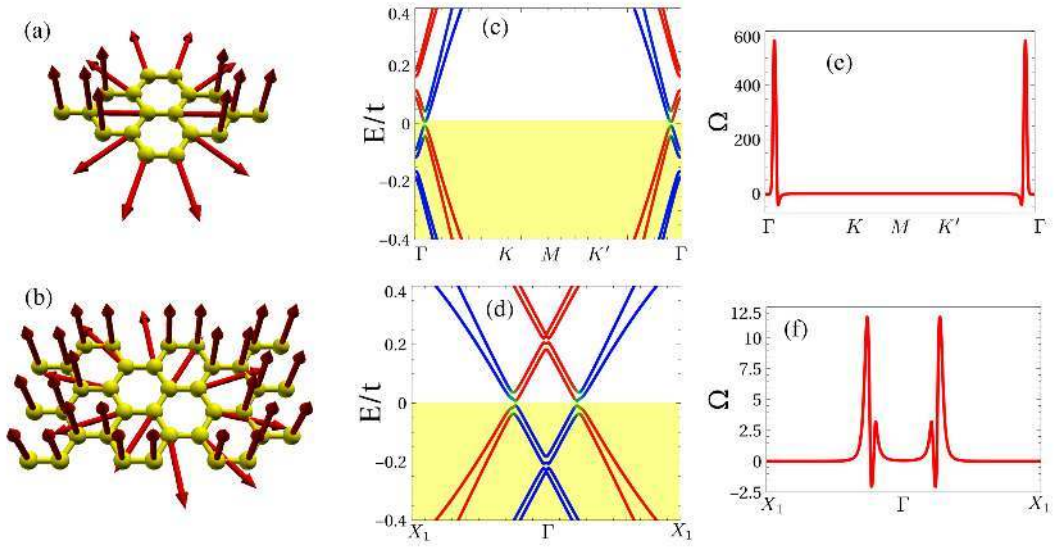

Figure 6.7: Unit cells (a,b), band structures (c,d) and Berry curvatures (e,f) for graphene over a triangular (a,c) and rectangular (b,d) skyrmion lattice. The commesuration of graphene with the skyrmion lattice make that both valleys are folded onto the Γ point. Even though a gap with non vanishing Berry curvature opens up, the sign changes along the Brillouin zone, and summing up all the contributions gives a vanishing Chern number. In the present situation, the gap is dominated by intervalley mixing.

turning the exchange term of the Hamiltonian purely real, and therefore also the full Hamiltonian. Since the Chern number is odd under conjugation

$$K : \mathcal{C} \to -\mathcal{C} \tag{6.11}$$

and a purely real Hamiltonian is invariant under conjugation

$$K : \mathcal{H} \to \mathcal{H}^* = \mathcal{H} \tag{6.12}$$

the Chern number is identically zero ($\mathcal{C} = 0$) for a co-planar spin texture. Thus, non-coplanar spin arrangements are necessary to induce the anomalous Hall phase.

Intervalley mixing

In some instances the skyrmion lattice will be commensurate with the carbon honeycomb lattice, the two valleys in band structure of graphene could be folded to a single point, allowing to intervalley mixing. In particular, for the triangular lattice, the folding of the two valleys onto the Γ point takes place for $3n \times 3n$ unit cells.

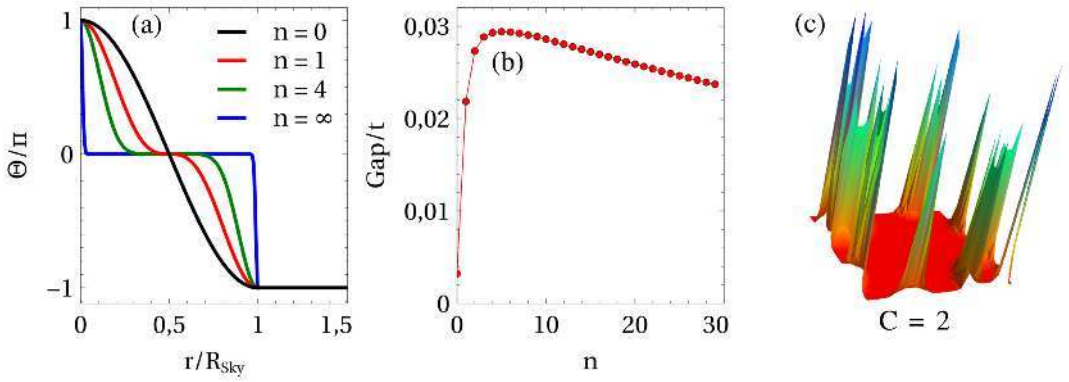

Figure 6.8: (a) Example of the radial Θ dependencies that the parametrization Eq. yields. The limiting case of hard core skyrmions used in the main analysis corresponds to the limiting case $n = \infty$. The gap as function of n, shows an always different that zero gap, indication that the system is always topological as show by the Berry curvature (c) of the $n = \infty$ case. Calculations correspond to 5x5 supercell with $J = 0.3t$.

For a rectangular unit cell, the folding takes place for a supercell $3n$ in the zigzag direction. In these situations, intervalley scattering can open a trivial gap, as shown in Fig.6.7 of such behavior. Interestingly, the Berry curvature can be non zero, but the Chern number vanishes. Importantly, this situation requires a fine-tuning of the skyrmion and carbon lattices. In general, this is not the case, and non-trivial gaps are to be expected.

6.6.2 Profile smoothness

So far, for the sake of simplicity we assumed a step-wise profile for the magnetization, a core region in-plane and an outer region off-plane. From the point of view of the symmetry of the electronic Hamiltonian, the previous assumption captures the only critical ingredient: non-coplanarity and finite spin chirality. Realistic systems are expected to show a smoother behavior in the magnetic profile. Actually, it is that smooth behavior the feature that allows to define a topological invariant associated with the real space structure of the skyrmion.

In this section we show that the precise spatial profile of the skyrmion is not critical for the topological properties induced over the electrons in graphene. We will take take the again parametrization for the magnetic profile Eq. 6.5

$$\vec{n} = (\sin\Theta(r)\cos\Phi(\phi), \sin\Theta(r)\sin\Phi(\phi), \cos\Theta(r)) \tag{6.13}$$

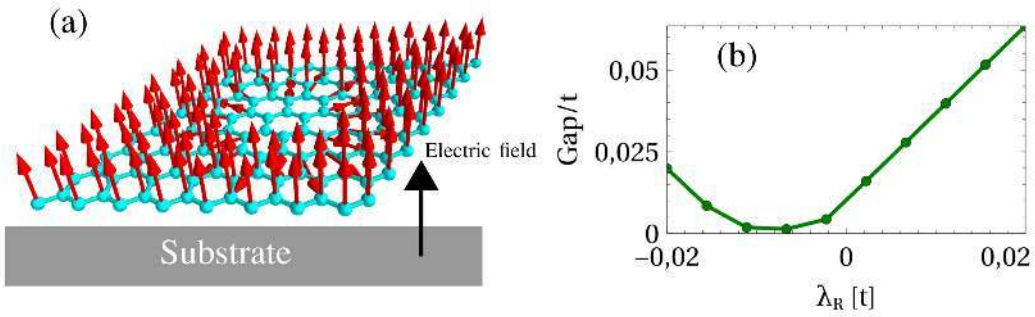

Figure 6.9: (a) Sketch of skyrmionic graphene over a substrate, showing the induced perpendicular electric field. The band gap (b) as a function of the Rashba coupling shows an asymmetric behavior, reflecting the competition between spin chirality and the spin orbit coupling chirality.

with the following parametrization for Θ and Φ

$$\cos\Theta = \left(\cos\pi\frac{r}{R_{Sky}}\right)^{2n+1} \tag{6.14}$$

The previous parametrization has simple behavior as shown in Fig. 6.8a. For low n, the profile has a smooth evolution from the center until the skyrmion radius. For $n = \infty$, a step profile is recovered, which corresponds to the hard skyrmion case.

6.6.3 Effect of Rashba coupling

Relativistic effects in conduction electrons were ignored so far (except for their implicit participation in the formation of the skyrmion) , all the anomalous effect came from interaction with the magnetic structure. Nevertheless, the setup of graphene over a surface breaks mirror symmetry with respect to the $z - axis$, so that Rashba couplings are expected to appear. In comparison, electric field does not affect the kinetic part of the electrons, due to the planar structure of graphene. The strength of the Rashba coupling will depend on the perpendicular electric field felt, and on a combination of the spin orbit couplings of carbon and the underlying material. In general, the net effect on the graphene electrons can be minimally captured by the following term in the Hamiltonian

$$H_R = \lambda_R \sum_{\langle i,j\rangle} \hat{z}\cdot(\vec{r}_{ij}\times\vec{s}) \tag{6.15}$$

within the previous model, the gap of a certain unit cell changes as shown in Fig. 6.9

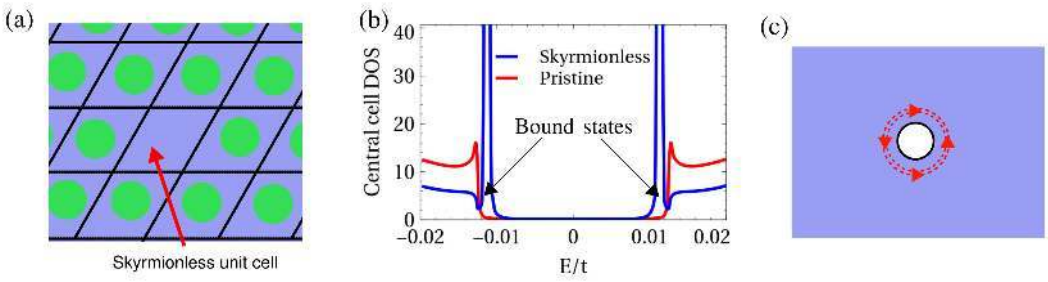

Figure 6.10: (a) Sketch of a system with a single skyrmion missing in a unit cell, coupled to a pristine infinite skyrmionic graphene. The DOS (b) in the skyrmionless cell shows two a peaks below the skyrmionic graphene gap, which correspond to states bound states to the skyrmions-less defect (c).

6.6.4 Skyrmion defects

In this section we will focus on the effect of different defects in the skyrmion lattice. We will consider a single missing skyrmion in the lattice, a single skyrmion with different chirality and a missing atom.

In this section, we will deal with a system in which the defect is located in a central unit cell, coupled to an infinite pristine graphene skyrmion lattice. The method used to calculate the Green function of the defect is the embedding method, explained in detail in Chapter 11.

Missing skyrmion

The first impurity we will consider is a central central cell whose skyrmion is missing and remains non-magnetic. This situation corresponds to a missing skyrmion in the underlying system that hosts the skyrmions. The outer system remains a pristine graphene skyrmion lattice, having a topological gap at half filling.

In the case of a hole in a topological insulator, it is expected that an in-gap state is trapped by the impurity. This can be understood thinking about the hole as a limiting case of a boundary between vacuum and the QAH. For very large holes, several in-gap states show up creating a band whose states are localized in the boundary, in particular there will be a state a zero energy. For a tiny hole, a zero energy state is no longer guaranteed, but it is expected that some remaining bound state survives.

The present situation is more complicated, since it is not clear whether the inner non-magnetic part will give rise to the same behavior. However, it is obtained that this defect also traps a in-gap state, as shown in Fig. 6.10. The two peaks located below the gap of the pristine case are precisely these two bound states. It is worth to note, that when the part with missing skyrmions becomes larger, these states will

not be bounded to the boundary. The inner part will recover the gapless graphene spectrum, which will allow the in-gap states to the delocalize.

6.7 Summary

We have shown that, at half filling, graphene with a weak exchange coupling to a skyrmion lattice develops a quantum anomalous Hall phase, with gapped bulk and chiral edge states that should have perfect quantization. This occurs at least for two different skyrmion lattices, rectangular and triangular, and seems a generic feature as long as the skyrmion lattice does not produce valley mixing. The Chern invariant $\mathcal{C}$ that characterizes the QAH phase is given by the topological invariant that describes the individual skyrmions N, through the remarkable relation $\mathcal{C} = 2N$, valid for $N = \pm 1$. Thus, graphene edges will have 2 chiral edge states, and graphene on top of an interface between two skyrmions lattices with opposite skyrmion number $N = +1$ and $N = -1$ will have 4 chiral edge states. Importantly, the topological state of the system does not rely on whether the skyrmion texture is sharp or smooth. Our proposal has the advantage with respect of any previous QAH phase in graphene because it requires no spin-orbit coupling and no magnetic field acting on the graphene electrons.

Chapter 7

Quantum anomalous Hall effect in honeycomb antiferromagnets

The quantum anomalous Hall state is topologically order state of matter characterized by a perfect quantum Hall conductance, usually driven by a combination of ferromagnetism and spin orbit coupling. Here we show, that such state can be realized in the presence of antiferromagnetic order, without net magnetization. In particular, we show that an antiferromagnetic buckled monolayer can be electrically driven into a quantum anomalous Hall state. Furthermore, a similar mechanism can be used to drive a bilayer antiferromagnetic into the quantum anomalous Hall phase. Our findings show that ferromagnetism is not mandatory to realize this state, in comparison with previous proposals who relied on a non vanishing net exchange field.

7.1 Introduction

The interest for topological states has increased dramatically in the last years. The interest has been boosted by the experimental observation have of quantum spin Hall effect[272], quantum anomalous Hall effect[317, 22] and Majorana bound states[318].

Perfect electric conduction in materials is a long standing goal. Both superconductors and the quantum Hall state can be considered as perfect conductors. Starting with quantum Hall effect found in graphene, two dimensional materials have been shown to be potential candidates for Quantum Hall effects. Their perfect quantization is a consequence of the non-trivial topology of the Landau levels, which give rise to an integer topological invariant known as the Chern number, which is proportional to the perfect Hall quantization σ_{xy}. Within the topological classification, the QH state is known as a Chern insulator.

The quantum anomalous Hall state[319, 320] is an example of Chern insulator,

in which there is no net magnetic field but a locally broken time reversal symmetry. Starting with the original Haldane model, different mechanisms have been proposed to create this remarkable electronic state. Many of the mechanisms consisted on non coplanar spin textures[321, 322, 323], or a combination of collinear exchange fields and Rashba-like spin orbit coupling (SOC)[324, 317]. Focusing on the SOC driven mechanism, different proposals rely on a net exchange field whose effect is to polarize the system, plus a SOC field which opens a gap by spin mixing.

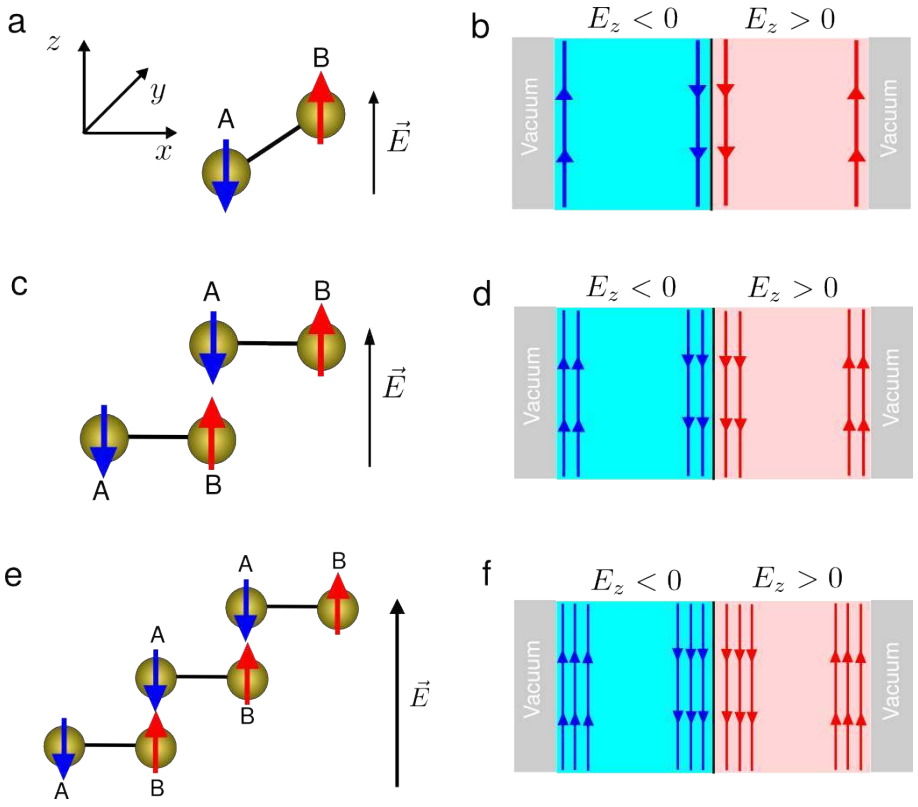

Figure 7.1: (a,c,e) Scheme of the different multilayered honeycomb lattices and (b,d,f) edge states developed. Two regions with opposite electric field create interface states due to the opposite Chern number of the regions. The number of states is proportional to the number of layers for monolayer, bilayer and trilayer graphene.

Two dimensional materials are specially suitable to be tuned by substrate due to their almost pure surface behavior. For example, spin orbit coupling and exchange fields an be induced by growing 2D materials over substrates with heavy atoms or magnetic ordering[325]. Furthermore, if the substrate is also insulating, the electronic transport takes place purely on the original 2D material, with a extrinsically modified SOC or exchange. Regarding induced QAH, several proposals[324, 317] showed that a combination of exchange fields and SOC are able to generate the

topological state, however the low amount of ferromagnetic insulators makes those proposals challenging from material science point of view. Moreover, ferromagnetic substrates might create in addition an additional Hall response due to a net magnetic field, which has to be decoupled from the intrinsic anomalous contribution.

Proposals which involve antiferromagnetic insulators usually rely on proximity effect to only one of the sublattices, thus yielding an effective net exchange field[317, 326]. In comparison, we will show that an intrinsic antiferromagnetic order is able to drive quantum anomalous state in multilayered honeycomb systems. The antiferromagnetic order naturally arises in a bipartite system at strong interactions, and thus represents an intrinsic mechanism to drive the QAH. In particular, antiferromagnetic states in honeycomb systems are strong candidates insulating states experimentally observed in monolayer[327, 83], bilayer[328, 329, 330, 331] and trilayer[332, 333, 334] graphene, and in the same fashion, they are expected to be realized in other graphene-like systems. Among the systems that will fit in the previous proposals are silicene[335] , germanene[336, 337], stanene[338] or functionalized bismuth[339]. Our results show that electrical gating yields a simple way to tune the gap in this systems.

7.2 Minimal model of a QAH antiferromagnet

We will show that the QAH state can be systematically induced in an antiferromagnet lattice, whose exchange field can be intrinsic or substrate induced.

The general Hamiltonian that we will use reads as

$$H = H_{NN} + H_{AF} + H_{SOC} + H_V \tag{7.1}$$

where H_{NN} is the nearest neighbor hopping in the honeycomb lattice

$$H_{NN} = \sum_{\mathrm{NN}} t c^\dagger_{j,l} c_{i,l} \tag{7.2}$$

H_{AF} is a spin dependent potential that describes the antiferromagnetic order

$$H_{AF} = m_{AF} \sum_i \sigma_z s_z c^\dagger_i c_i \tag{7.3}$$

H_{SOC} is the intrinsic spin orbit coupling[36].

$$H_{SOC} = \lambda_{SOC} \sum_{\mathrm{NNN}} s_z \hat{z} \cdot (\vec{r}_{ik} \times \vec{r}_{kj}) c^\dagger_{j,s} c_{i,s} \tag{7.4}$$

The term H_V is the one responsible for opening a gap with opposite Berry curvature in different valleys, breaking inversion symmetry but maintaining time

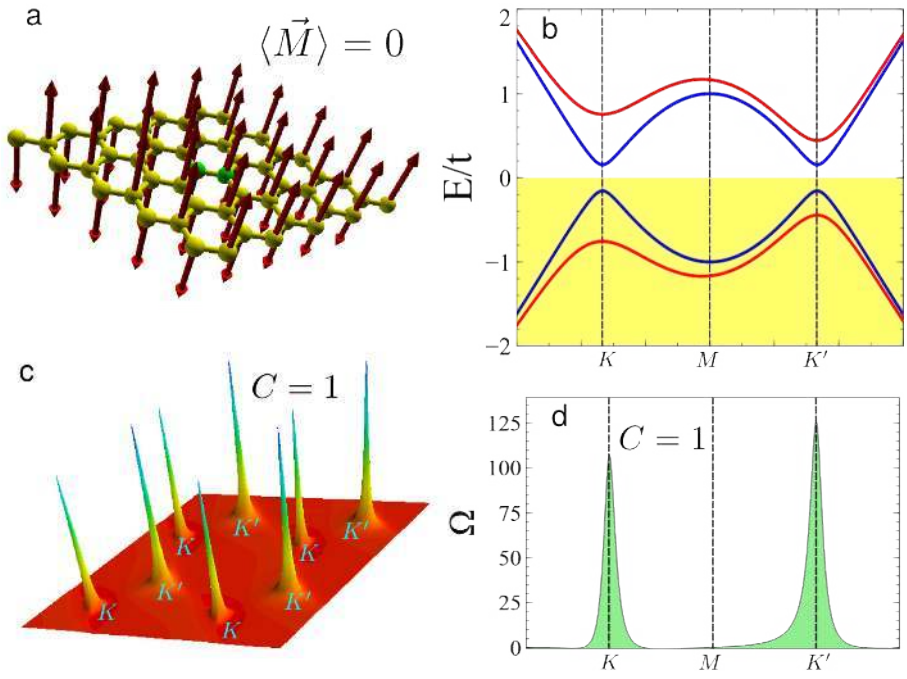

Figure 7.2: (a) Scheme of the antiferromagnetic order in the honeycomb lattice, and (b) band structure in the presence of AF order, sublattice imbalance and intrinsic SOC. (c) Berry curvature in the full Brillouin zone and (c) along the band structure path, showing total $C = 1$ Chern number. The parameters are $m_{AF} = m_{AB} = 0.3t$ and $\lambda_{SOC} = 0.03t$

reversal. For the monolayer system, H_V takes the form of sublattice imbalance

$$H_V^{\text{mono}} = m_{AB} \sum_i \sigma_z c_i^\dagger c_i \tag{7.5}$$

where σ_z is the sublattice Pauli matrix.

For bilayer and trilayer graphene an analogous term comes from a combination of interlayer coupling and perpendicular electric field

$$H_V^{\text{bi/tri}} = t_{IL} \sum_{\text{NN layer}} c_{j,l}^\dagger c_{i,l'} + E \sum_i \langle z \rangle c_i^\dagger c_i \tag{7.6}$$

where t_{IL} is the interlayer hopping, E is the applied electric field and $\langle z \rangle$ the z-position of the localized orbital.

The role of the different terms can be understood by their respective symmetry. H_{SOC} respects both time reversal and inversion symmetry, but breaks spin symmetry. H_V respects time reversal and spin symmetry, but breaks inversion symmetry.

H_{AF} breaks time reversal and inversion symmetry, but respects their simultaneous application. With this in mind, the necessity of the different terms can be anticipated from the symmetry properties of the Chern number. For a Hamiltonian with time reversal, inversion symmetry or conjugation, the Berry curvature is odd under time reversal symmetry, odd under conjugation and even under inversion symmetry.

$$\Theta : \Omega(k) \rightarrow -\Omega(-k) \tag{7.7}$$

$$K : \Omega(k) \rightarrow -\Omega(-k) \tag{7.8}$$

$$P : \Omega(k) \rightarrow \Omega(-k) \tag{7.9}$$

Finally, it is convenient to define a symmetry operator specific of this system

$$D = s_x PK \tag{7.10}$$

which leaves invariant both the antiferromagnetic term and the Kane-Mele term, and that acts on the Berry curvature as

$$D : \Omega(k) \rightarrow -\Omega(k) \tag{7.11}$$

where Θ, K, P are the time reversal, conjugation and parity operators.

In the case H_V and H_{SOC} are non-zero, the Hamiltonian has time reversal symmetry, so that the Chern number is automatically zero. If only H_V and H_{AF} are non zero, the system has conjugation symmetry, so that the Chern number is also zero. If only H_{AF} and H_{SOC} are non-zero, the Berry curvature is identically zero according to Eq. 7.11.

Therefore, in order to get a non-zero Chern number, the three terms H_V, H_{SOC} and H_{AF} have to be different from zero. In the following we will see that if the three terms are present, a quantum anomalous state can arise in monolayer, bilayer and trilayer graphene. Specifically, we will focus on bilayer AB and trilayer ABC.

7.3 QAH state in different layer numbers

In the following we show how the combination of spin-orbit coupling, antiferromagnetism and perpendicular electric field is able to drive the quantum anomalous Hall state.

7.3.1 QAH in monolayer

The full Hamiltonian to model the monolayer system reads as

$$H = \sum_{\text{NN}} t c^\dagger_{j,l} c_{i,l} + m_{AF} \sum_i \sigma_z s_z c^\dagger_i c_i + m_{AB} \sum_i \sigma_z c^\dagger_i c_i + \\ + \lambda_{SOC} \sum_{\text{NNN}} s_z \hat{z} \cdot (\vec{r}_{ik} \times \vec{r}_{kj}) c^\dagger_{j,s} c_{i,s} \quad (7.12)$$

The monolayer antiferromagnetic system can be easily rationalized in terms of two decoupled Haldane models. Since z_z commutes with the hamiltonian, each spin channel has an spin dependent mass in each valley given by

$$m(\kappa, s_z) = s_z \kappa m_{SOC} + s_z m_{AF} + m_{AB} \quad (7.13)$$

The Chern number for a spin flavor in certain valley is given by $C = \frac{1}{2}\kappa \text{sign}(m_{\kappa,s_z})$, and thus the total Chern number is

$$C = \frac{1}{2} \sum_{\kappa,s_z} m_{\kappa,s_z} \quad (7.14)$$

It be easily seen that the previous topological invariant can be non-zero. By taking $m_{AB} = m_{AF} = m_0$, the total Chern number turns out to be $C = \text{sign}(m_{SO}) = \pm 1$. Thus, in this regime, the system develops a quantum anomalous Hall state (see Fig. 7.2). The previous regime can be rationalized as a topological Haldane model for one of the spin channels, and a trivial insulating state for the other channel.

7.3.2 QAH in bilayer

The full Hamiltonian to model the bilayer system reads as

$$H = \sum_{\text{NN}} t c^\dagger_{j,l} c_{i,l} + m_{AF} \sum_i \sigma_z s_z c^\dagger_i c_i + t_{IL} \sum_{\text{NN layer}} c^\dagger_{j,l} c_{i,l'} \\ + E \sum_i \langle z \rangle c^\dagger_i c_i + \lambda_{SOC} \sum_{\text{NNN}} s_z \hat{z} \cdot (\vec{r}_{ik} \times \vec{r}_{kj}) c^\dagger_{j,s} c_{i,s} \quad (7.15)$$

where we choose the coordinates of the bilayer honeycomb in the AB stacking.

Due to the larger density of states near the Fermi level, bilayer systems are known to develop magnetic order. For instance, bilayer graphene is know to develop an insulating state even at zero magnetic field, which is believed to be an antiferromagnetic state, very much like trilayer systems. For other bilayer systems as bilayer silicene or germanene, a reduced bandwidth is expected to enhance the

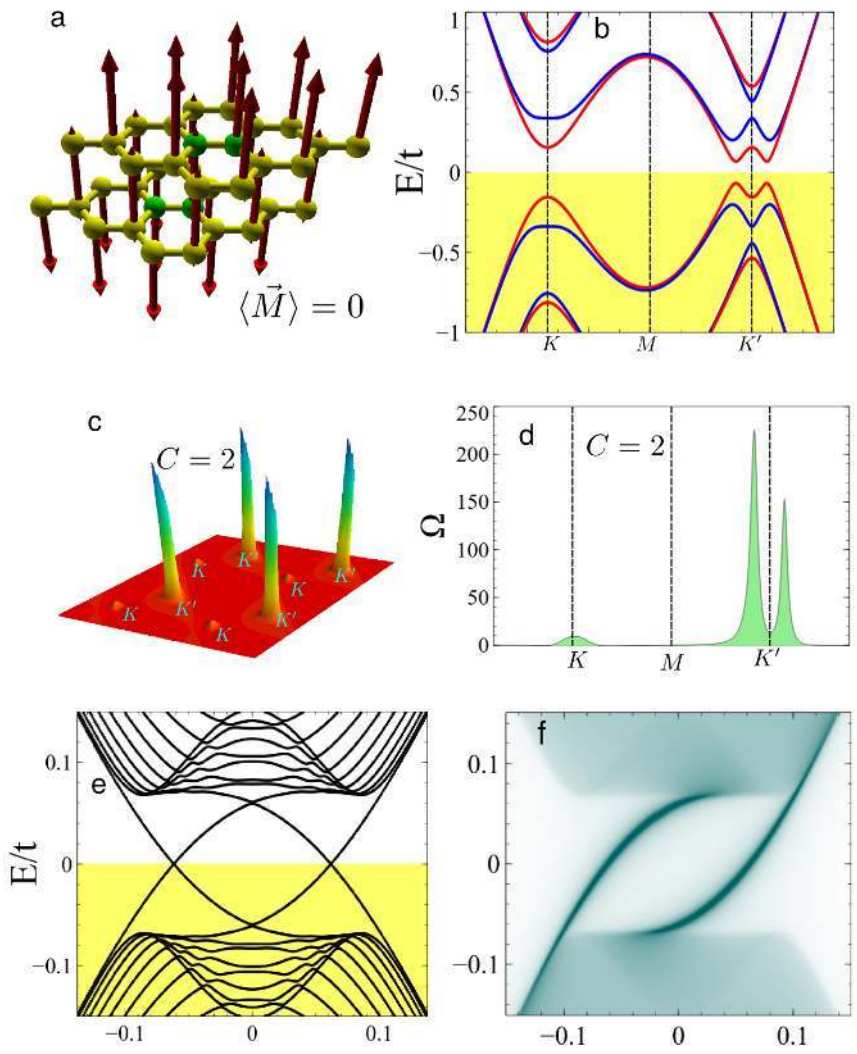

Figure 7.3: (a) Scheme of the antiferromagnetic order in the bilayer honeycomb lattice, and (b) band structure in the presence of AF order, perpendicular electric field and intrinsic SOC. (c) Berry curvature in the full Brillouin zone and (c) along the band structure path, showing total $C = 1$ Chern number. The parameters are $m_{AF} = m_{AB} = 0.3t$ and $\lambda_{SOC} = 0.03t$

trend towards developing magnetic order. Thus, magnetic order in multilayered systems is an easy to achieve state, which in combination of externally broken inversion symmetry and intrinsic SOC, can yield a quantum anomalous Hall state.

We show that a similar mechanism can be used in a bilayer honeycomb lattice

to induce a tunable quantum anomalous Hall state by an off-plane electric field (see Fig. 7.3). In this system, the off-plane takes the role of the sublattice imbalance in the monolayer case.

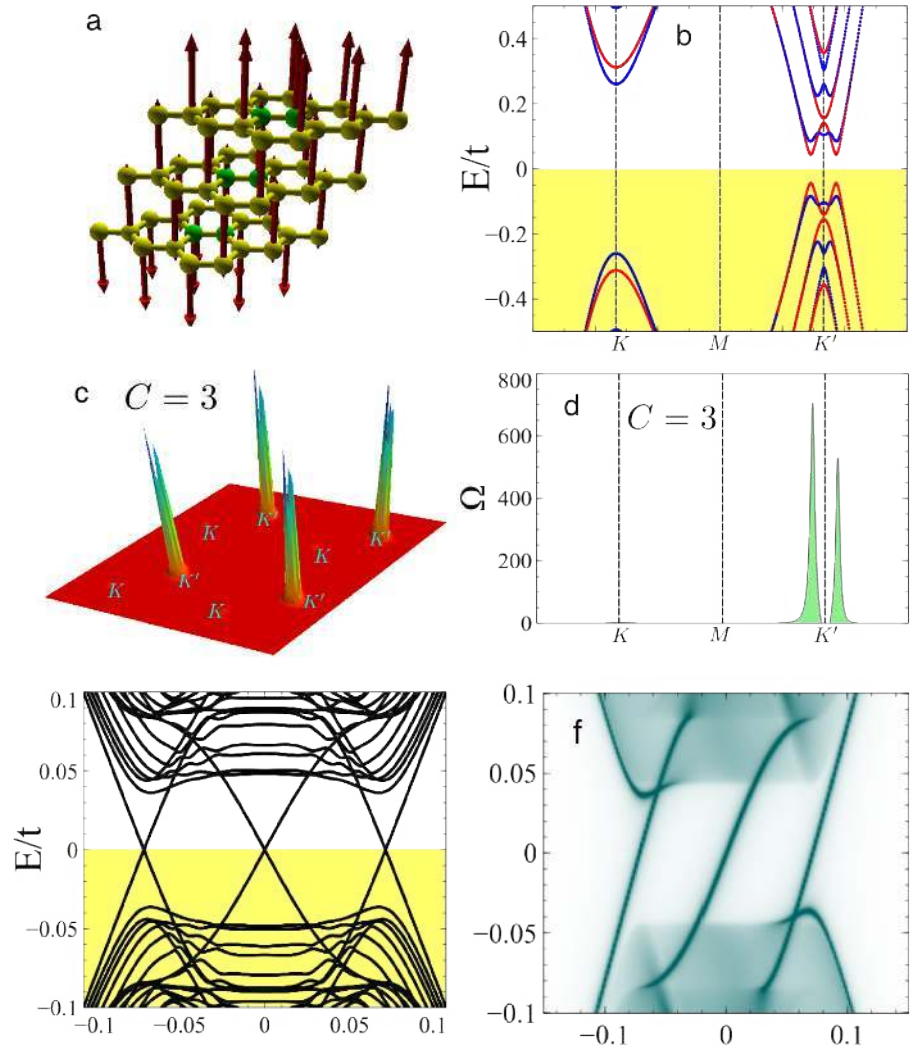

Figure 7.4: Magnetic structure (a) of ABC antiferromagnetic trilayer graphene and its band structure (b). Calculation of the Berry curvature (c) gives a net contribution, localized in the valleys (d). In a finite geometry the system develops edge states (e), which propagate in the same direction for a given edge (f).

7.3.3 QAH in trilayer

The last system that we will consider is an ABC trilayer stacked honeycomb lattice. In this case, in the absence of antiferromagnetism and SOC, an off-plane electric field opens up a gap very much like in the case of bilayer graphene. When magnetism and SOC are turned on, the gap closes and reopens, giving rise to a Chern insulator with $C = 3$.

The model for the trilayer system is analogous to the bilayer one.

$$H = \sum_{\text{NN}} t c^\dagger_{j,l} c_{i,l} + m_{AF} \sum_i \sigma_z s_z c^\dagger_i c_i + t_{IL} \sum_{\text{NN layer}} c^\dagger_{j,l} c_{i,l'} + E \sum_i \langle z \rangle c^\dagger_i c_i + \lambda_{SOC} \sum_{\text{NNN}} s_z \hat{z} \cdot (\vec{r}_{ik} \times \vec{r}_{kj}) c^\dagger_{j,s} c_{i,s} \quad (7.16)$$

where we choose the coordinates of the trilayer honeycomb in the ABC stacking.

As shown in Fig.7.4bcd, the Berry curvature concentrates in one of the valleys, the one corresponding to the low energy excitations. The effect of the non-topologically trivial band structure is directly observed in a ribbon geometry Fig.7.4e, where several gapless bands are observed. Calculation of the momentum resolved spectral function (Fig.7.4) yields that every edge host three co-propagating modes, in agreement with the bulk Chern number (see Fig. 7.4).

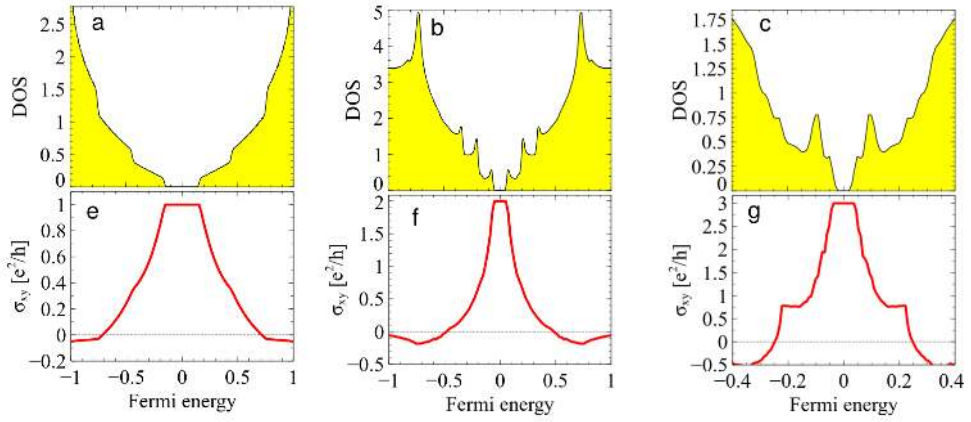

Figure 7.5: Density of states (a,b,c) and Hall conductivity (d,e,f) as a function of the chemical potential for the monolayer (a,d), bilayer (b,e) and trilayer (c,f) anomalous antiferromagnets. For energies inside the gap, the Hall conductance shows the quantized value $\sigma_{xy} = Ce^2/h$. As the chemical potential enters the valence (conduction) band, σ_{xy} becomes smaller, even changing its sign.

7.4 Anomalous Hall effect away from half filling

The Hall conductance is quantized as long as the Fermi level lies in between the gap. In this section, we will study the behavior of σ_{xy} when the Fermi energy lies in the conduction or valence band. In this regime, an intrinsic unquantized anomalous Hall effect remains[64], due to the sum over the bands of their Chern number weighted by their occupation. At zero temperature, we have

$$\sigma_{xy}(E_F) = \int_{BZ} d^2k \sum_n \Omega_{n,k}\Theta(\epsilon_{n,k} - E_F) \tag{7.17}$$

where $\Theta(x)$ is the step function $\Theta(x < 0) = 1$ and $\Theta(x > 0) = 0$

As shown in Fig. 7.5, the Hall conductance is maximum when the Fermi energy lies in the gap, being equal to the Chern number $\sigma_{xy} = Ce^2/h$. For doped systems, the Hall conductance becomes smaller as the chemical potential goes deeper in the valence (conduction) band. Eventually, a energy where the response vanishes is reached, and from that point, the response changes sign. Thus, the sign of the intrinsic contribution of the Hall conductance is not constant, but depends on the chemical potential of the system.

Importantly, the previous study shows that even though the system is not at half filling, the anomalous response can be observed for metallic systems. We empathize that in comparison with usual ferromagnets where the anomalous response is studied, in this antiferromagnets no net magnetic field is present, therefore allowing to a pure anomalous Hall signal.

Nevertheless, it is expected that doping on the system might change its magnetic state. The critical doping at which this systems develop an antiferromagnetic state have to be taken into account.

7.5 Summary

We have shown that the quantum anomalous Hall state can arise in different honeycomb antiferromagnets. Our findings suggest that different systems can be turned into a pure Quantum anomalous Hall state without net magnetic moment. In comparison with ferromagnetic anomalous states, the vanishing magnetic moment allows to identify the anomalous Hall signal without having to remove a trivial Hall signal that would arise due to the finite magnetic field of the system. Furthermore, our mechanism relies on gate controlled symmetry braking of the lattices, allowing to have a gate control of the topological state of the system.

The exact value of the gap opening will depend strongly on the particular system. For graphene multilayers, the gap would have a rather too small magnitude for

practical applications, however for heavier multilayers as stanene[340] trilayer, the gap could widely exceed room temperature.

Chapter 8

Unconventional Shiba states in hydrogenated graphene[1]

Conventional in-gap Shiba states require two ingredients: magnetic atoms and a superconducting host that, in the normal phase, has a finite density of states at the Fermi energy. Here we show that hydrogenated graphene can host Shiba states without any of those two ingredients. Atomic hydrogen chemisorbed in graphene is known to act as paramagnetic center with a weakly localized magnetic moment. Our calculations for hydrogenated graphene in proximity to a superconductor show that individual adatoms induce in-gap Shiba states with an exotic spectrum whereas chains of adatoms result in a gapless Shiba band. Our predictions can be tested using state of the art techniques, combining recent progress of atomic manipulation of atomic hydrogen on graphene together with the well tested proximity effect in graphene.

8.1 Introduction

Magnetic moments have long been known[341, 342] to deplete the superconducting order, hindering the coexistence of ferromagnetism and superconductivity. At the atomic scale, a single magnetic atom can locally modify the superconducting order parameter, binding in-gap Shiba states[342, 343]. Using scanning tunneling spectroscopy (STS), these in-gap states have been observed in a variety of systems[344, 345, 346, 347, 348], all of them involving transition metal or rare earth local moments. In presence of either spin-orbit coupling or non-collinear magnetic order, chains of Shiba impurities[349] have been predicted to result in topological superconductivity, whose fingerprint would be the emergence of zero energy Majorana[80] edge states. The recent observation[318] of zero energy end states by means of STS

[1]some parts of this chapter are taken from 2D Materials 3 (2), 025001 (2015)

in atomic chains of Fe atoms on the surface of superconducting Pb has been interpreted along this line and has triggered and enormous interest in the engineering of Shiba states[349, 350, 351].

In conventional superconductors, the parameter that controls the energetics of Shiba states is ρJ where ρ is the density of states (DOS) at the Fermi surface in the normal phase and J is strength of the Kondo exchange between the local moment with spin S and the conduction electrons. When ρ is a slowly varying function of energy, the binding energy of Shiba states for a classical spin in a superconductor, is given by[342, 352]

$$E_S = \Delta \frac{1 - (\pi \frac{S}{2} J\rho)^2}{1 + (\pi \frac{S}{2} J\rho)^2} \tag{8.1}$$

where Δ is the superconducting energy gap. Thus, according to this classical result, a finite ρ is needed in order to have in-gap Shiba states. We now address the question of how could graphene change this state of affairs.

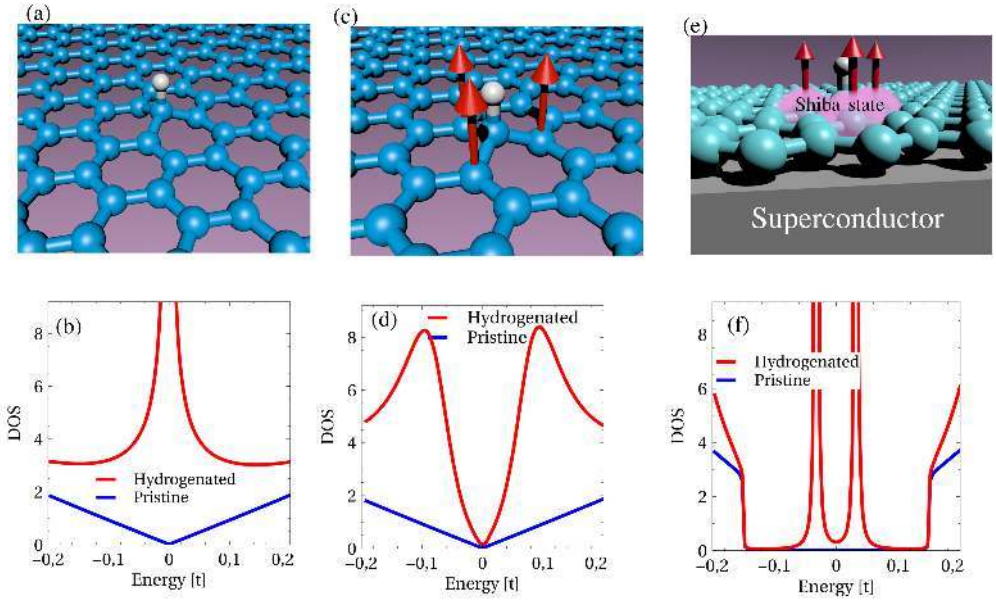

Figure 8.1: (a) Sketch of hydrogenated graphene (b) and DOS in the carbons close to the hydrogen. Upon introduction of interactions a local magnetic moment is developed (c), changing dramatically the associated DOS (d). When the system is placed on top of a superconductor (e), Shiba excitations arise below the superconducting gap (f).

Graphene can be made superconductor via proximity effect using several complementary strategies. On one hand superconductivity can be induced in lateral

graphene/superconductor heterostructures[353, 66, 354] and on the other hand taking advantage of its two dimensional character, graphene can be deposited on top of a superconductor[355, 356]. The recent reports of fabrication of vertical Van der Waals structures combining[357, 358, 71] graphene with superconducting $NbSe_2$ also present a promising venue in this regard. Moreover, a carbon layer of intercalated graphite C_6Ca,[359, 360, 361] could be considered as superconducting graphene, although in the former case the Fermi level is away from half filling.

Local magnetic moments can be induced in graphene without using transition metals via chemisorption of atomic hydrogen[362, 149, 363] as well as many other covalent functionalizations[364]. Within a one-body picture, the chemisorption of atomic hydrogen in graphene creates a zero energy state[365, 366], which greatly enhances the local DOS close to the Fermi energy. Electron-electron interactions result[362, 367, 149, 365] in the formation of a local moment associated to chemisorbed hydrogen. When two hydrogen atoms are chemisorbed on the same sub lattice, ferromagnetic couplings are expected[149, 365]. These theoretical results are in line with recent experiments[368] where both individual chemisorbed hydrogen, as well as dimers and trimers, have been probed using STS. In these experiments atomic manipulation of individual hydrogen atoms has been demonstrated, showing the potential for atomic scale engineering of magnetism in graphene. In addition, this magnetism can be turned on and off when the density of carriers is changed [368], in line with the experimentally demonstrated electrical control of paramagnetism in the case of fluorinated graphene [369] and as expected from theoretical calculations[370].

8.2 Methods

We now model hydrogenated graphene on top of a superconductor using a one orbital tight-binding model with pairing and exchange fields. Within the one-orbital model, the effect of hydrogenation and other covalent functionalizations[364] are equivalent to the removal of a site in the lattice[365]. At the non-interacting level, this results in an in-gap $E = 0$ state in the case of gapped graphene nanostructures, and a resonance in the case of 2D graphene [371].

In most instances, interactions have been included at a mean field level using supercells[362], that invariably result in spin-split solutions with a sublattice polarized magnetization cloud in the neighborhood of the hydrogen atom and total spin $S = 1/2$. Our Hamiltonian includes the spin-dependent potential in the three closest carbon atoms to the one underneath the chemisorbed hydrogen. This minimal model mimics a self-consistently calculated exchange field that breaks time reversal symmetry that implies a local magnetization induced by the chemisorbed hydrogen. Finally, in order to account for the proximity induced superconducting gap Δ , we include a pairing term[372] in the theory. Thus, the complete Bogoliubov-De Gennes

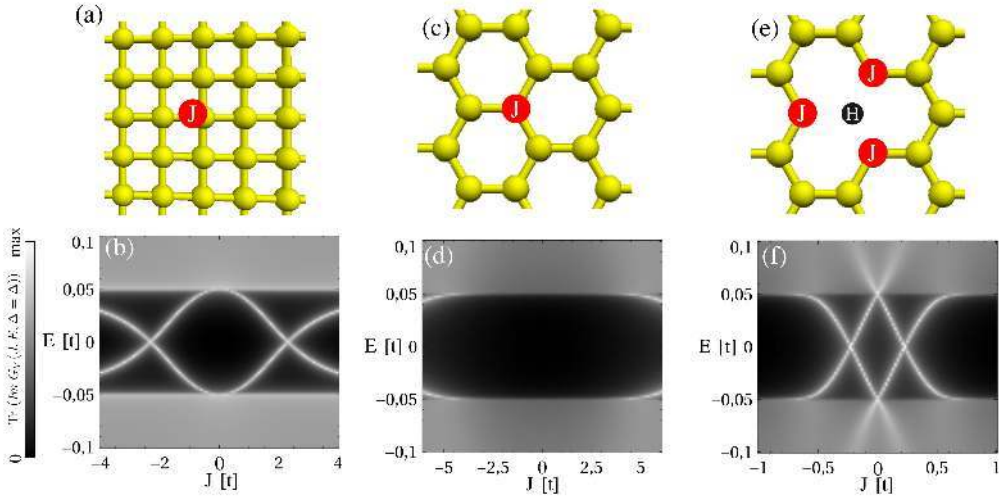

Figure 8.2: Single magnetic impurity in an infinite square lattice (a), showing in-gap states described by Eq.8.1. The same impurity in the honeycomb lattice (c) does not show Shiba states at weak coupling (d). For the single hydrogenated graphene (e), a new and qualitatively different branch of in-gap state arises (f).

(BdG) Hamiltonian reads:

$$H = H_{kin} + H_W + H_J + H_{SC} \tag{8.2}$$

where H_{kin} describes hopping, H_W an onsite potential term, H_J is the exchange term and H_{SC} the superconducting pairing. The hopping term is the standard nearest neighbor (NN) hopping:

$$H_{kin} = t \sum_s \sum_{(i,j)\in NN} c^\dagger_{j\sigma} c_{i\sigma} \tag{8.3}$$

In the case of the hydrogenated system, the effect of hydrogenation is captured by adding an infinite onsite energy W to functionalized carbon site

$$H_W = \lim_{W\to\infty} W \sum_s c^\dagger_{0,s} c_{0,s} \tag{8.4}$$

The exchange term can be written down as:

$$H_J = \sum_i j(i) c^\dagger_{i\sigma} \frac{\sigma_z}{2} c_{i\sigma} \tag{8.5}$$

When we model the a conventional Shiba state in the square and honeycomb lattice, we take $W = 0$ and $j(i)$ takes a non-zero value J in just one site, marked

in red in figures 2(a,c). In contrast, when we model hydrogenated graphene we take $W = \infty$ and $j(i)$ takes a non zero value J in the three first neighbors[363] of the functionalized carbon site (see figure 8.2(e)). We treat J as a free parameter, to account for variations of the local magnetization coming from temperature or doping[369, 370].

Finally, the superconducting proximity effect is introduced as an effective conventional s-wave pairing term

$$H_{SC} = \Delta \sum_i \left[c_{i,\uparrow} c_{i,\downarrow} + c^\dagger_{i,\downarrow} c^\dagger_{i,\uparrow} \right] \tag{8.6}$$

Here Δ is taken as an input parameter in the calculation, and no attempt to compute it self-consistently is done. Since we are considering a single impurity in an infinite pristine system, we have to deal with a problem with infinite size and no translational invariance. We tackle the problem using Green functions and a partition method, valid for any dimension. To do so, we divide the problem in a core region that contains the impurity site(s) and an outer region[373]. This division is performed by creating a graphene supercell as the new unit cell C, where the central supercell host the hydrogenated site and the sites with exchange coupling

$$h_V = h_{kin} + h_W + h_J + h_{SC} \tag{8.7}$$

with h_{kin}, h_W, h_J and h_{SC} are the projection of Eq. 8.2 in the central defective supercell. The rest of the system is formed of pristine supercells coupled to each other and to the defective one. To calculate the full Green function of the defective supercell, we write down the Dyson equation of defective supercell coupled to the infinite graphene.

$$G_V = (E - h_V - \Sigma(E))^{-1} \tag{8.8}$$

where $\Sigma(E)$ is the selfenergy induced over the defective supercell by the rest of pristine system. The calculation of $\Sigma(E)$ is done noting that, for a pristine supercell, an analogous Dyson equation can be written up:

$$G_0(E) = (E - h_0 - \Sigma(E))^{-1} \tag{8.9}$$

However, in the case of pristine graphene the Green function G_0 of the supercell C can also be calculated by summing up the Green functions of the Bloch Hamiltonian H_k as

$$G_0(E) = \frac{1}{(2\pi)^2} \int (E - H_k)^{-1} d^2k \tag{8.10}$$

with H_k the usual Bloch Hamiltonian

$$H_k = h_0 + \sum_{\vec{r}} t_{\vec{r}} e^{i\vec{k}\cdot\vec{r}} \tag{8.11}$$

where h_0 is the pristine intracell hopping matrix, $t_{\vec{r}}$ are the intercell hopping matrices and $\vec{r}$ are real space vector connecting supercells. Coming back to Eq. 8.9, the self energy that pristine graphene induces on a central supercell can be calculated combining Eq. 8.9 and 8.10 as

$$\Sigma(E) = E - h_0 - \left(\frac{1}{(2\pi)^2} \int (E - H_k)^{-1} d^2k \right)^{-1} \tag{8.12}$$

Finally, with the previous self energy the full Green function of the defective supercell G_V can be calculated with Eq. 8.8. From the Green function, the spectral function can easily be obtained as $\rho = -\frac{1}{\pi}\text{Im}G_V(E)$ introducing a small but finite imaginary part in the energy $E \to E + i\delta$. We stress that this method is specially well suited to capture single impurities in infinite systems, not relying on periodic boundary conditions and avoiding undesired interference effects between different impurities.

8.3 Results

It is instructive to analyze the density of states of the single hydrogenated graphene in three stages. First, with $J = \Delta = 0$, we see in figure 8.1(b) how the density of states diverges for $E = 0$, in line with analytic results [57]. Second, when the effect of the mean field exchange is added ($J \neq 0$ in our Hamiltonian), the $E = 0$ peak spin splits, and results in a vanishing DOS at $E = 0$ (see fig. 8.1(d)). The resulting DOS calculated using the embedding method shows a phenomenology analogous to a toy model, a zero energy level, spin splitted by an exchange J and coupled to a bath with the graphene density of states $\rho_0 = \lambda|E|$. In this toy model, the Dyson equation gives the spectral function $\rho_\pm(E, J) = \frac{\lambda|E|+0^+}{(J\pm E)^2+(\lambda|E|+0^+)^2}$. The dramatic difference between the results with $J = 0$ (fig. 8.1a) and $J \neq 0$ (fig. 8.1b) are analogous to the pathological behavior of the function $\rho(E, J)$. In particular, ρ can not be Taylor expanded for $E = 0$, because the small J and E limits can not be exchanged. This prevents the use of ρJ as a well defined function and invalidates the use of Eq.8.1 to model Shiba states in hydrogenated graphene.

Finally, in the third stage, we study the effect of the superconducting proximity effect on graphene. A proximity gap opens in the DOS of pristine graphene (blue line in Fig. 8.1(f)). In contrast, the calculated DOS close to a chemisorbed hydrogen atom shows an intra-gap Shiba state (red line in Fig. 8.1(f))

8.3.1 Shiba states for individual magnetic centers

The in-gap excitation energy is governed by the strength of the exchange coupling. Using our methodology for a magnetic impurity embedded in square lattice (Fig.

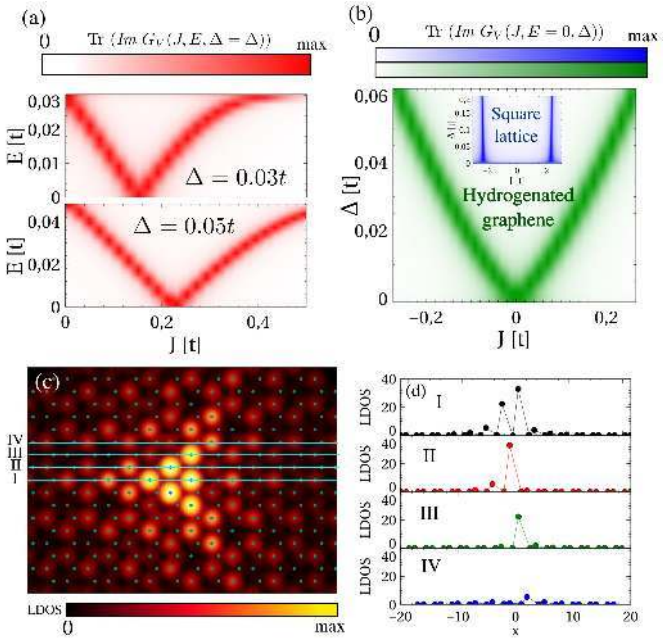

Figure 8.3: (a) Low energy spectral function of the Shiba states for single hydrogenated graphene, for different paring couplings, showing an anomalous displacement of the pairing switching point. (b) $E = 0$ spectral function as a function of superconducting paring and exchange coupling for hydrogenated graphene (green), showing a non linear dependence of the switching point. The inset (blue) shows the result for the usual parabolic band which yields a Δ independent transition point. (c) Spatially resolved DOS at $E = 0$ for the parity switching point $J = 0.22t$, $\Delta = 0.05t$. Panel (d) shows the amplitude of the DOS along different lines, marked in panel (c), showing a strong localization of the Shiba state close to the hydrogenated site.

8.2a) , with conventional parabolic bands, the evolution of the in-gap Shiba state as a function of J is shown in Fig. 8.2b, with $\Delta = 0.05t$ taking chemical potential $E_F = -2t$. Our results follow Eq. 8.1. In particular, in the low J limit the in-gap energies E_S follow a quadratic law $\Delta - E_S \propto J^2$.

In contrast, a single magnetic impurity (Fig. 8.2c) in the honeycomb lattice at half filling yields no in-gap state unless the exchange interaction J takes unrealistically large values $J >> t$ (Fig. 8.2d), in line with a previous result[374]. This can be understood within the standard model as a straightforward consequence of the vanishing DOS at $E = 0$. The situation is radically different when we consider the model for hydrogenated graphene (Fig. 8.2e). In this case, in-gap Shiba states appear at weak coupling that, in contrast with conventional Shiba states, follow a linear evolution with J at low coupling, and therefore are not described by Eq. 8.1.

This is the main result of this paper.

On top of their linear dependence on J, the hydrogenated graphene Shiba states have another unconventional property. Let us define J_c as the point that satisfies $E_S(J_c) = 0$, which marks a parity switching of the ground state between a singlet state for $J < J_c$ to a doublet state for $J > J_c$.[352] For the conventional case, equation (1) shows how J_c is independent from the superconducting pairing Δ, depending solely on the density of states at Fermi energy $\pi \frac{S}{2} \rho J_c = 1$. In comparison, for hydrogenated graphene the parity switching point is Δ dependent, as can be observed in Fig.8.3(a). In fig. 8.3(b) we plot a contour map of the BdG spectral function evaluated at $E = 0$ as a function of J and Δ, showing a clear linear dependence of J_c on Δ. In contrast, in the case of a square lattice, the same procedure yields a J_c that is independent of Δ (inset of Fig.8.3(b)).

Thus, from an experimental point of view, the parity switching point could be observed by controlling either the superconducting gap Δ, that depends strongly on temperature, as well as tuning the hydrogen magnetic moment by controlling the doping level of graphene with a gate[369]. Given that $E_S \simeq \Delta - J/6$, the critical J_c is in the range of the 6Δ, ie, in the range of 10 meV[375, 376]. Another prediction for experiments is shown in figures 8.3(c) and 8.3(d), where we show the spectral function of the Shiba states, as it would be measured with an STM. This hydrogenated-graphene Shiba wave function inherits both the extension and the C_3 symmetry of the impurity resonance of the normal phase[362] (Fig. 8.3(c)). In particular, the Shiba state peaks on the first neighbors of the hydrogen atom (Fig. 8.3(d)).

8.3.2 Shiba states for superlattices

We now consider Shiba state superlattices formed by several hydrogen atoms chemisorbed in the same sublattice. This secures a ferromagnetic coupling between them[149, 365]. We first consider the case of a dimer (Fig. 8.4a) which is expected[149] to have $S = 1$. The resulting density of states with $\Delta = 0$ and $J \neq 0$ shows two peaks (Fig. 8.4b), rather than only one (Fig. 8.1d) for the single hydrogen case. When the superconducting pairing is switched on, the Shiba spectrum also acquires an extra line, compared to the single hydrogen case. The evolution of the two Shiba states is still linear with J, as in the single hydrogen case. Thus, there are as many bound Shiba states as hydrogen atoms. We now extend this notion to the case of a one dimensional periodic array of hydrogen atoms (Fig. 8.4d). For this one dimensional Shiba crystal we obtain a single Shiba band that corresponds to a gapless 1D superconductor, reminiscent of the one recently found at the interface of a magnetically ordered graphene edge and a superconductor[377]. The map of density of states at $E = 0$ for the one dimensional array is shown in (Fig.8.4f), whose spatial profile resembles the single hydrogen Shiba state.

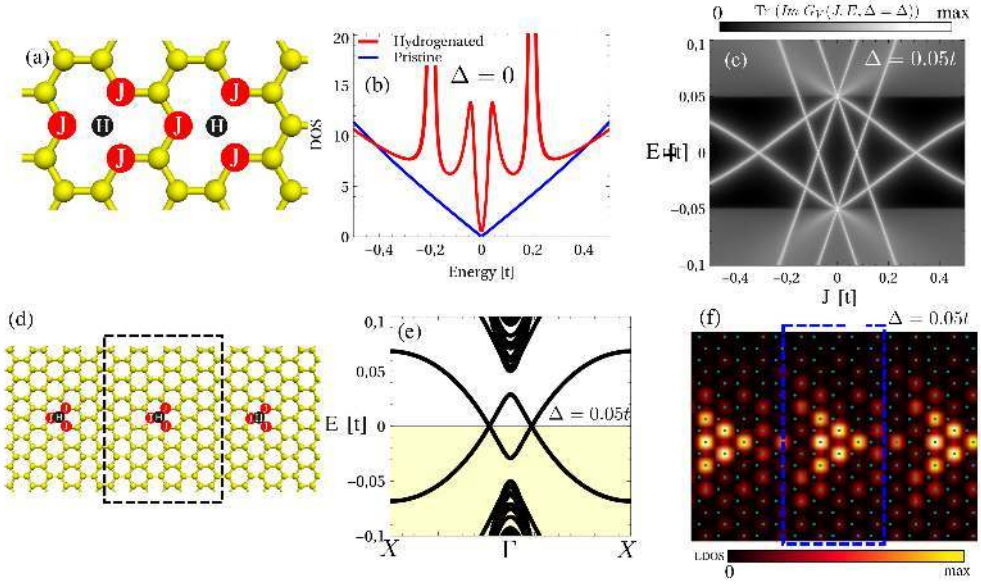

Figure 8.4: (a) Central cell with two hydrogen atoms, and (b) density of states before the superconducting proximity is considered. (c) Evolution of the Shiba spectrum for case (a), resembling the same linear evolution as Fig. 8.2f. (d) Sketch of the unit cell for a periodic array of hydrogenated sites. Panel (e) shows the BdG band structure of the periodic array, showing a gapless Shiba band. Panel (f) shows the spatial resolved DOS for the periodic array (d) at $E = 0$.

So far we assumed that resonant magnetism behaves as a classical magnetic moment. It must be noted that quantum fluctuation scale as $\frac{1}{S}$ and are thus expected to have an important role both in conventional Shiba states[378] as well as in the case of hydrogenated graphene[379, 380]. Such fluctuations are not captured within the present theoretical framework. However, our approach becomes more accurate for the larger structures considered in figure 8.4, that have a larger spin, and thereby smaller quantum fluctuations.

8.4 Further properties of Shiba states in graphene

8.4.1 Effect of doping in conventional Shiba states

For pristine graphene, electronic doping increases the density of states at the Fermi energy. Electronic doping naturally occurs due to chemical unintentional doping[381] (different types of impurities), by field effect[382], or by charge transfer with a substrate[383]. In any of those situations, conventional Shiba states could be observed. Assuming that for a finite density of states the usual theory works, the parity switch-

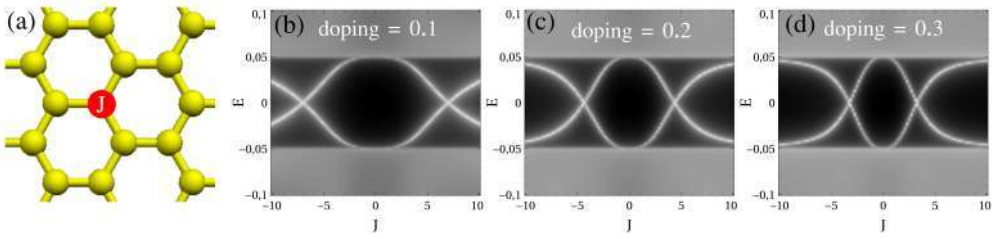

Figure 8.5: (a) Sketch of the central cell for a magnetic impurity in pristine graphene. In panels (b,c,d) it is shown the evolution of the spectrum as the system is doped (in units of the hopping). It is observed that as J becomes larger, the Shiba band that appeared at large J moves towards the low J region.

ing exchange would be

$$\rho J_c = 1 \tag{8.13}$$

and due to the linear density of states in graphene, the dependence with the Fermi energy, measures with respect to the charge neutrality point will be

$$J_c \propto \frac{1}{E_F} \tag{8.14}$$

therefore, as E_F increases, the switching point comes closer to $J = 0$ At very small doping the previous equation is obviously not valid, as proven by the Shiba states that appeared a very high exchange ($J = 10t$). In Fig. we show the evolution of the Shiba spectrum for pristine as the doping is increased, which clear shows the movement of the Shiba band towards $J = 0$ as the Fermi energy (and thus the DOS) becomes larger.

8.4.2 Effect of doping in unconventional Shiba states

As stated previously, the exchange effect can be tuned by means of electrical doping in graphene. Electrical doping will also create at finite density of states at the Fermi level, raising the question of whether conventional Shiba states are going to blur the unconventional ones presented so far.

As shown in Fig. 8.4, the unconventional Shiba states (white lines in panel b close to $J = 0$) survive even in the case of a finite density of states at the Fermi energy. This has important consequences: it implies that a finite density of states of conduction electrons do not alter the picture we assumed so far. When graphene is put on top of a superconductor, it is expected a certain amount of electronic doping, arising from charge transfer from the metal into the carbon atoms. The robustness

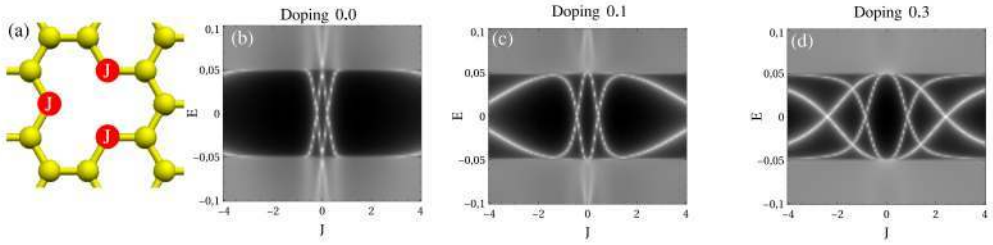

Figure 8.6: (a) Sketch of the central cell for the hydrogenated graphene. In panels (b,c,d) it is shown the evolution of the spectrum as the system is doped (in units of the hopping). It is observed that at low J the unconventional Shiba states survive, and at large doping a Shiba band from high energy comes to the small J region.

of Shiba states that guarantee that they will observed even when graphene is slightly away from half filling.

8.5 Majorana bound states from hydrogen Shiba states

A issue not addressed yet is whether this Shiba states arising from carbon magnetism are able to yield a one dimensional topological superconductor. Chains of Shiba states are known to be potentials sources of topologically gapped one dimensional superconductors, as shown in 9.1.2. Importantly, this possibility increases its interest by the possibility of manipulating single hydrogen ad atoms. In this fashion, Majorana circuits could be imprinted in a graphene monolayer by selectively depositing hydrogen adatoms.

In order to get a 1d topological superconductor from a chain of hydrogen adatoms, it will be necessary to introduce spin orbit coupling, in the form of Rashba coupling. The term introduced is

$$H_R = \lambda_R \sum_{\langle i,j \rangle} \hat{z} \cdot (\vec{d}_{ij} \times \vec{s}) \tag{8.15}$$

which is the usual Rashba term that arises when mirror symmetry along the z-axis is broken. This term naturally arises due to the superconductor lying underneath graphene, and its strength will depend on the details of the material and its hybridization with graphene.

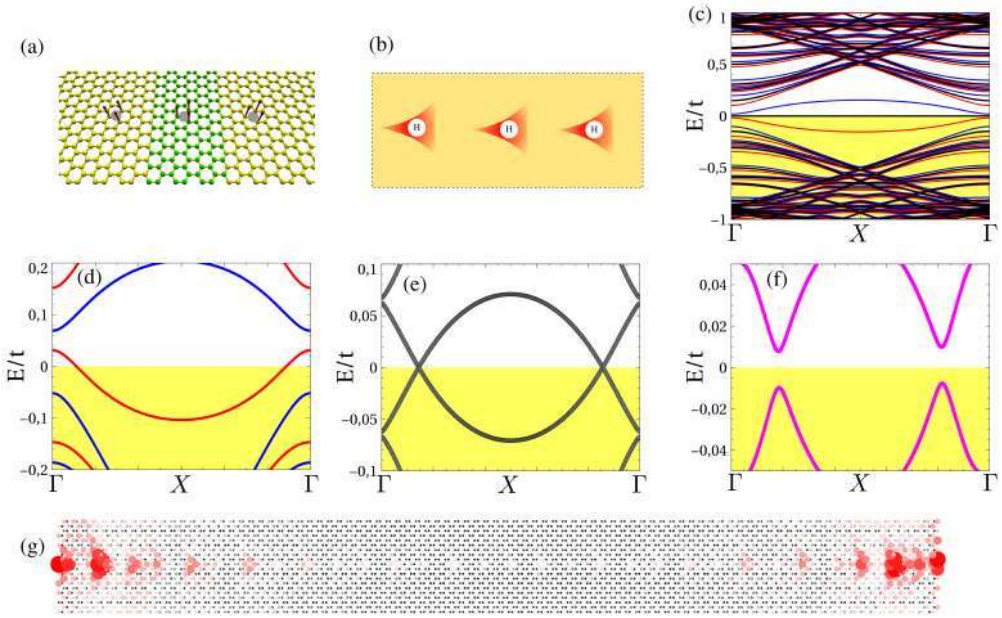

Figure 8.7: (a) Sketch of the chain of hydrogenated, highlighting the localized magnetic moments (b). In panel (c) it is shown that upon inclusion of local exchange arising from interactions, the original spinless bands (black) spin split into up and down (red and blue). We will focus in the impurity band below the Fermi energy as shown in panel (d), moving the chemical potential to the middle of that band. Upon introduction of superconducting pairing (e) the system becomes a gapless superconductor. Finally, inclusion of the Rashba term opens up a gap (f). The previous gap is topological, whose typical signature is the appearance of localized bound states at the corners of a ribbon at $\omega = 0$ (g)

8.6 Summary

We have shown that a single chemisorbed hydrogen in superconducting graphene creates a Shiba bound state, in spite of the vanishing density of states of pristine graphene. These Shiba states have properties very different from conventional Shiba states, such as a linear dependence of the binding energy E_S with exchange, and a parity switching point J_c that depends on the superconducting pairing energy, and can thereby be modulated with temperature. Motivated by recent experiments that demonstrate the atomic manipulation of individual hydrogen atoms on graphene[368], we have also explored the properties of Shiba super-structures. Furthermore, these results also apply for a much wider class of covalent functionalizations in graphene[364]. Combined with the electric control of magnetism, this class of systems offers a unique platform to engineer exotic superconducting states

at the nanoscale.

Chapter 9

Majorana modes in quantum Hall graphene[1]

A clear demonstration of topological superconductivity[384] (TS) and Majorana zero modes[80] remains one of the major pending goal in the field of topological materials. One common strategy to generate TS is through the coupling of an s-wave superconductor to a helical half-metallic system. Numerous proposals for the latter have been put forward in the literature, most of them based on semiconductors or topological insulators with strong spin-orbit coupling. Here we demonstrate an alternative approach for the creation of TS in graphene/superconductor junctions without the need of spin-orbit coupling. Our prediction stems from the helicity of graphene's zero Landau level edge states in the presence of interactions (see Chapter 5), and on the possibility, experimentally demonstrated[385], to tune their magnetic properties with in-plane magnetic fields. We show[386] how canted antiferromagnetic ordering in the graphene bulk close to neutrality induces TS along the junction, and gives rise to isolated, topologically protected Majorana bound states at either end. We also discuss possible strategies to detect their presence in graphene Josephson junctions through Fraunhofer pattern anomalies and Andreev spectroscopy. The latter in particular exhibits strong unambiguous signatures of the presence of the Majorana states in the form of universal zero bias anomalies. Remarkable progress has recently been reported[387, 354] in the fabrication of the proposed type of junctions, which offers a promising outlook for Majorana physics in graphene systems.

Before entering in the current graphene Majorana proposal, we will do a brief introduction of Majorana bound states in condensed matter systems. We will show some of the simplest toy models that develop topological superconductivity, and we will try to give an intuition about the basic ingredients that topological superconductivity demands. The underlying mathematical models that lead to topological

[1]some parts of this chapter are taken from Physical Review X 5 (4), 041042 (2015)

superconductivity are analogous to those of topological electronic states: a Hamiltonian that has a non-trivial topology on its spectrum gives rise to protected zero energy modes, states that cross the gap. In the present situation, we will deal with one dimensional superconductivity, so that the signature of non-trivial topology will be simply a zero mode.

9.1 p-wave superconductor from chiral channels

The ultimate ingredient needed to obtain Majorana bound states is to have a topological superconductor. In one dimension, this is realized by a p-wave superconducting order parameter $\Delta(-k) = -\Delta(k)$. In this section we will start introducing some well known examples for getting such emerging superconducting state.

9.1.1 The Kitaev chain

The simplest model that yields Majorana bound states is the so called Kitaev chain[388]. The Hamiltonian of the system involves spinless fermions and has the form

$$H = \sum_n t c_{n+1}^\dagger c_n + \Delta c_n c_{n+1} + c.c. \tag{9.1}$$

where $c_i, c_i^\dagger$ are the annihilation/creation operators in a linear chain, t is the nearest neighbor hopping and Δ the superconducting pairing.

By defining the Bloch operators

$$c_k = \sum_n e^{ikn} c_n \tag{9.2}$$

Eq. 9.1 turns

$$H = \sum_k \epsilon_k c_k^\dagger c_k + \Delta \left[e^{ik} c_{-k} c_k + e^{-ik} c_{-k}^\dagger c_k^\dagger \right] \tag{9.3}$$

It is worth to note that the second term in Eq. 9.3 gives rise to similar terms for $k > 0$ and $k < 0$ but with opposite real part due to anticommutation relation. Therefore by applying

$$\sum_k e^{-ik} c_{-k} c_k = \sum_{k>0} \left[e^{-ik} c_{-k} c_k - e^{ik} c_{-k} c_k \right] = \sum_{k>0} -2ic_{-k} c_k \sin k \tag{9.4}$$

$$\sum_{k>0} -2ic_{-k} c_k \sin k = \sum_k -ic_{-k} c_k \sin k \tag{9.5}$$

the Hamiltonian can be rewritten as

$$H = \sum_k \epsilon_k c_k^\dagger c_k + i\Delta \left[c_{-k} c_k \sin k - c_{-k}^\dagger c_k^\dagger \sin k \right] \tag{9.6}$$

The previous Hamiltonian is easily solved by defining the Nambu spinor

$$\Psi = \begin{pmatrix} c_k \\ c_{-k}^\dagger \end{pmatrix} \tag{9.7}$$

In this basis, the Hamiltonian takes the form

$$H = \begin{pmatrix} 2t\cos k & i\Delta \sin k \\ -i\Delta \sin k & -2t\cos k \end{pmatrix} \tag{9.8}$$

whose spectrum is

$$\epsilon = \sqrt{[2t\cos k]^2 + [\Delta \sin k]^2} \tag{9.9}$$

The previous spectrum shows a gap in the whole Brillouin zone. However, when the same Hamiltonian is applied to a finite system, the spectrum shows a zero energy mode in the edge, whereas the rest of the spectrum remains gapped. The mathematical reason to such zero energy mode is analogous to the protected edge states in topological insulators: an interface between two topologically different vacuums host zero energy modes. In this case the topological invariant that characterizes the different phases is not the Chern number, but the Majorana invariant $\mathcal{M}$

To get some insight in the mathematical structure of the previous Hamiltonian, it is useful to perform a change of basis into the Majorana representation

$$\gamma_{i,1} = c_i + c_i^\dagger \tag{9.10}$$

$$\gamma_{i,2} = i\left(c_i^\dagger - c_i\right) \tag{9.11}$$

where γ are Majorana field operators that follow the anticommutation relation

$$\{\gamma_{i,\alpha}, \gamma_{j,\beta}\} = 2\delta_{ij}\delta_{\alpha,\beta} \tag{9.12}$$

that can be easily seen that follows from the anticommutation fermion anticommutation relations. It be checked that this Majorana operators obey

$$\gamma_{i,\alpha} = \gamma_{i,\alpha}^\dagger \tag{9.13}$$

which the definition of Majorana fermion, a particle which is its own antiparticle. With those operators, we can rewrite the Hamiltonian 9.1 in the case $\Delta = t$ as

$$H = it \sum_j \gamma_{j,2}\gamma_{j+1,1} \tag{9.14}$$

In the very specific case of a finite system (open boundary conditions), the above sum runs between 1 and N

$$H = it \sum_{j=1}^{N} \gamma_{j,2}\gamma_{j+1,1} \tag{9.15}$$

The previous Hamiltonian is easily diagonalized with the change of basis

$$a_j = \frac{1}{2}\left(\gamma_{j,2} + i\gamma_{j+1,1}\right) \tag{9.16}$$

$$a_j^\dagger = \frac{1}{2}\left(\gamma_{j,2} - i\gamma_{j+1,1}\right) \tag{9.17}$$

transforming Eq. 9.15 into

$$H = 2t \sum_{j=1}^{N} \left(a_j^\dagger a_j - \frac{1}{2}\right) \tag{9.18}$$

In the previous equation it crucial to note that the operators $\gamma_{1,1}$ and $\gamma_{N,2}$ do not appear at any point. Therefore, any combination of $\gamma_{1,1}$ and $\gamma_{N,2}$ leads to an eigenvalue of zero energy. In particular, they encode the wavefunction of an electron whose wavefunction is localized in the two corners of the chain. If the state is chosen to be localized just in one corner, the state is a pure Majorana operator. This localized edge mode formed by a single Majorana operator is what will be called a Majorana zero energy mode. The zero energy modes can be expressed explicitly in the Hamiltonian as

$$H = 2t \sum_{j=1}^{N} \left(a_j^\dagger a_j - \frac{1}{2}\right) + 0\left(\gamma_{1,1}\gamma_{2,N}\right) \tag{9.19}$$

where the zero energy mode is seen. The goal of the upcoming sections is to show how an analogous mathematical model arises by other mechanisms. Any mechanism that leads to an Hamiltonian in the same topological class as Eq.9.1, will lead to a one-dimensional topological superconductor, and Majorana modes located in the corners of a finite geometry.

Finally, it is worth to remark that a chemical potential can be introduced in the previous models by means of

$$H_\mu = \mu \sum_i c_i^\dagger c_i \tag{9.20}$$

and in several upcoming models, its value will determine whether the system lies in a topological superconducting state or not. The addition of this term makes it possible to have either the topological phase, described above, or a trivial phase without Majorana modes

9.1.2 Emergent Kitaev chains using s-wave pairing

The very limitations to realize a 1D topological superconductor is that p-wave pairing is needed. Conventional superconductor shows a superconducting order with s-wave symmetry. This limitation motivates the following question: can an effective p-wave pairing be engineered, just by using s-wave pairing and spin-related phenomena. The answer is yes, and many of the proposals for Majorana bound state rely on this.

The usual recipe to get p-wave superconducting order consists on three ingredients, s-wave superconductivity, spin symmetry breaking and spin mixing. S-wave pairing is usually induced by means of proximity effect to a conventional superconductor. Spin symmetry-breaking by either chiral channels or magnetism. Finally, spin mixing is realized by either spin spiral[389, 390, 391] textures or spin orbit coupling.

In the following we will present several models that realize such recipe.

Chiral 1D by Rashba coupling

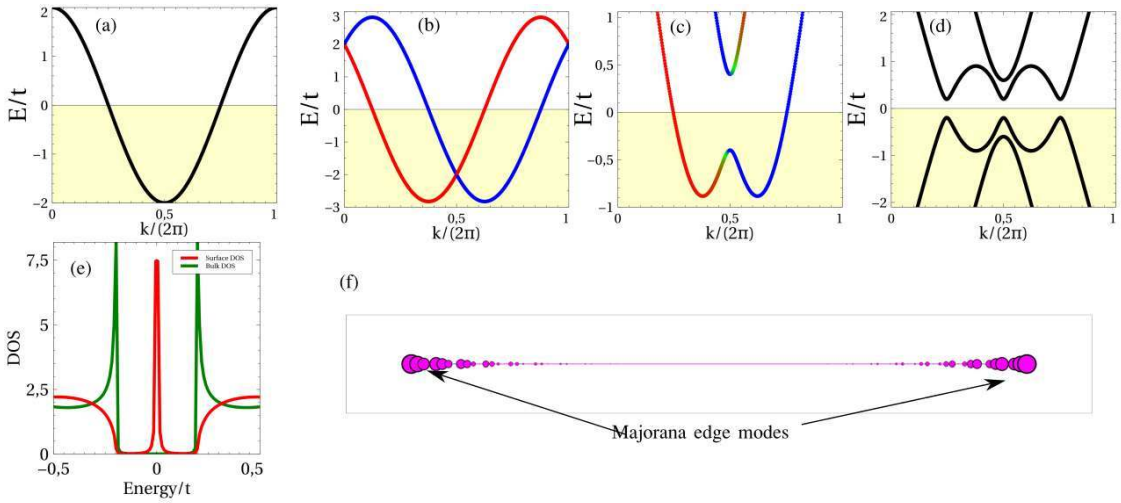

Figure 9.1: Band structure of a one-dimensional chain (a). When Rashba coupling is turned on (b), bands split. Upon introduction of perpendicular magnetization (c) a gap in Gamma opens up. Introduction of s-wave superconductivity opens up a topological gap (d). In a finite geometry, the non-trivial nature of the gap leads to zero modes as shown in spectral function (e), which are located at the edges in the corner of a long chain (f). The color in (b,c) is the s_y projection of the state, and (f) is the spatial spectral function at $\omega = 0$.

The first example that we will consider is built by a combination of Rashba cou-

pling, ferromagnetism and s-wave pairing[392]. Let us assume we have a parabolic band. Upon introduction of Rashba coupling the band becomes spin split in the reciprocal space, so that up and down cut each other at Γ. Upon introduction of ferromagnetism, the crossing point becomes spin split (see Fig. 9.1). When the chemical potential is put in the middle of that splitting, the Fermi level crosses the up channel in +k and the down channel in -k. When the superconducting pairing is introduced a topological gap opens up. This whole process is shown in Fig. 9.1

The real space model is the following

$$H = t[c_{i+1}^{\dagger}c_i + c_i^{\dagger}c_{i+1}] + m_x s_x c_{i,s}^{\dagger}c_{i,s'} + \lambda_R \hat{z}\cdot(\vec{r}\times\vec{s}) + \Delta[c_{i\uparrow}c_{i\downarrow} + c_{i\downarrow}^{\dagger}c_{i\uparrow}^{\dagger}] \qquad (9.21)$$

In a real experiment, a realization of the previous model will involve for example magnetic atoms on the surface of a conventional superconductor, or semiconducting nanowires with an applied magnetic field. The exchange coupling will come from the intrinsic magnetism in the first, or from Zeeman splitting in the second, and the Rashba coupling is induced by the mirror symmetry induced by the surface. Another realization could be an array of hydrogen adatoms in graphene. In this last case the magnetism would arise due to the missing site in the honeycomb lattice, which will create a resonant level at the Fermi level that can become magnetized.

The previous mechanism can also be realized by having a spin spiral magnetic texture instead of Rashba coupling. This is easily understood by performing a spin rotation in the Hamiltonian of a chiral magnetic texture. Upon rotation to a local spin frame where all the magnetic moments are collinear, a term in the kinetic energy shows up, whose form is precisely the one of the Rashba coupling. It is worth to note that in one dimension, the perfect nesting of the bands will allow the chiral order to appear spontaneously from electronic interactions. This can be specially important for engineering Majorana bound states in light elements, where the Rashba coupling is expected to be rather weak.

Chiral 1D gas in the surface of a quantum spin Hall insulator

A very important property of the model in Fig.9.1 is the chiral nature of the electron in panel 9.1c. The chiral state which gives rise to counter propagating spin modes can also be found in a very popular class of systems: two dimensional topological insulators (TI) with time reversal symmetry. In particular, in the following we will focus on TI with a non-vanishing spin Chern number C_S, those who realize the quantum spin Hall effect.

In the quantum spin Hall effect, the electronic structure is characterized by a gap in the bulk, and gapless states on the surface. These gapless states are also counter propagating for different spin components, and therefore can be an analogous system that shows the same behavior as Fig. 9.1c. Kramer's theorem guarantees that for a

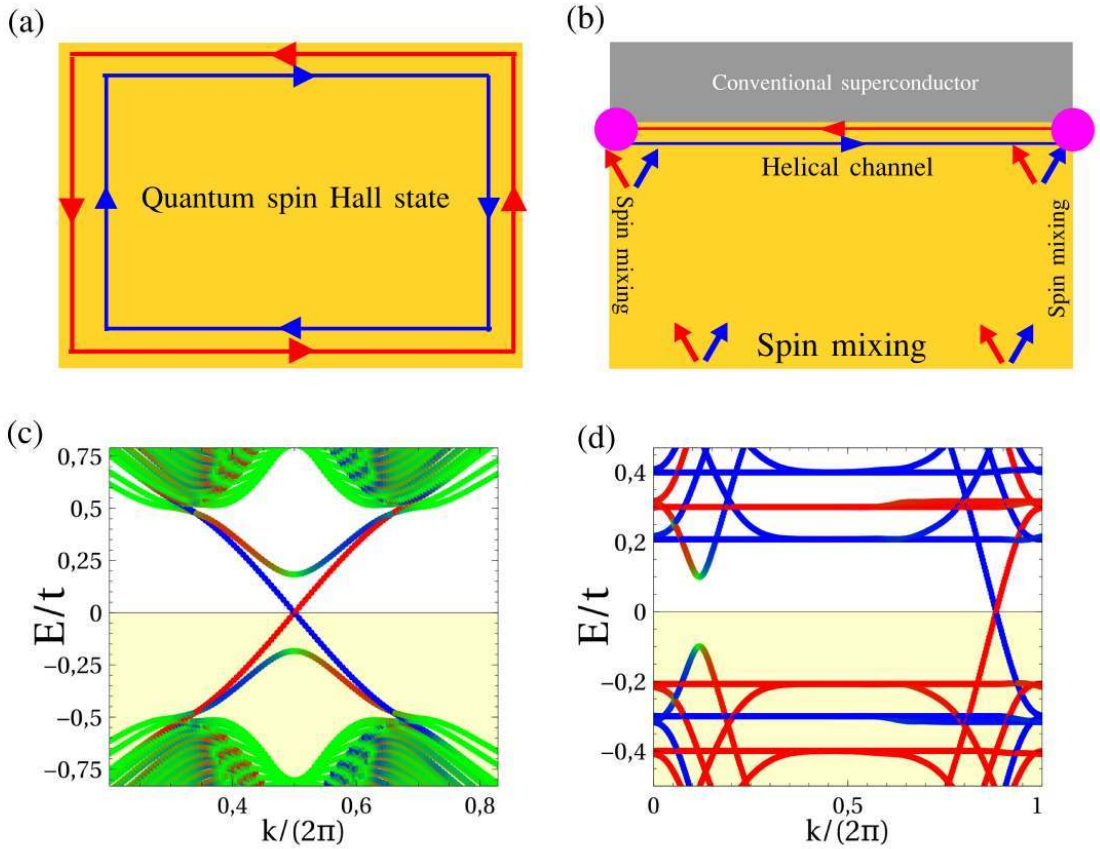

Figure 9.2: (a) Sketch of the quantum spin Hall effect and (b) scheme on how it can be used to get a 1D chiral channel. Panels (c,d) are the band structure of a ribbon in the QSH state, with spin mixing in one of the edges. In graphene, two realizations of the quantum spin Hall effect are possible. The first one involves SOC (c), whereas the second only magnetic fields (d).

state in $+k$ with spin up, there is a state in $-k$ with spin down, and therefore they will become coupled by an s-wave pairing[393]. The previous discussion will apply to any topological insulator. Importantly, the edges which are not in contact with the superconductor have to be gapped out by time reversal breaking, otherwise the corner Majorana modes could delocalize. A simple example of this state is graphene with SOC, shown in Fig. 9.2c

Furthermore, in graphene there is another mechanism able to trigger a quantum spin Hall phase. The mechanism is based on the unconventional spectrum of Landau Levels of the Dirac equation, that was discussed in chapter 5. The difference with previous mechanism is that, in the present one time reversal symmetry is broken

from the beginning. Gapping out undesired edge states is realized by spin mixing as canted magnetism. Importantly, the counter propagating edge modes are time reversal partners, so that the induced pairing effect do not couple them at first order, in comparison the become gapped out by through contributions involving high energy states.

Superconductivity in spinless channel

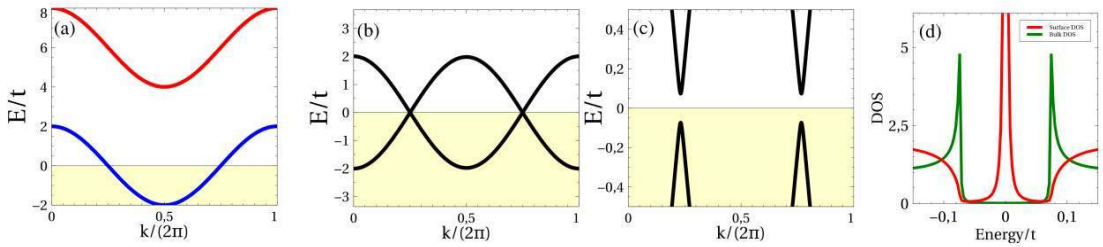

Figure 9.3: Band structure of a one-dimensional chain in the large exchange limit (a), realizing a half metal phase. When superconductivity is turned on (b), the system remains gapless because s-wave pairing couples opposite spins. Only upon introduction of Rashba coupling (c), the system develops a gap, due to the spin mixing of the bands that the Rashba term produces. The previous gap turns out to be topological, as proven by the gapless mode obtained in the surface DOS (d). The color in (a) is the s_z projection of the state.

One of the key points to get a 1D topological superconductor is to break time reversal and spin symmetry. In this fashion, it is attractive to think that there are more general situations where topological superconductivity arises.

Another limit of the model Eq. 9.21 would be to start in the large exchange limit. In this situation, when the chemical potential is in the middle of a band, the system is effectively spinless. When superconductivity is turned one, the system remains gapless, which is straightforward due to the perfect polarization of the conducting channels. This situation realizes a spinless gapless superconductor. In order to create any kind of spin splitting, a spin mixing term has to be introduced. The later, is the final role of the Rashba coupling. This whole process can be followed in Fig. 9.3

Gapping out an interfacial gapless superconductor

Previously we have shown that not only chiral spin states are able to yield a topological superconductor, but also gapping out of gapless superconductors fulfill that task. A very special case of one dimensional gapless topological superconductor is

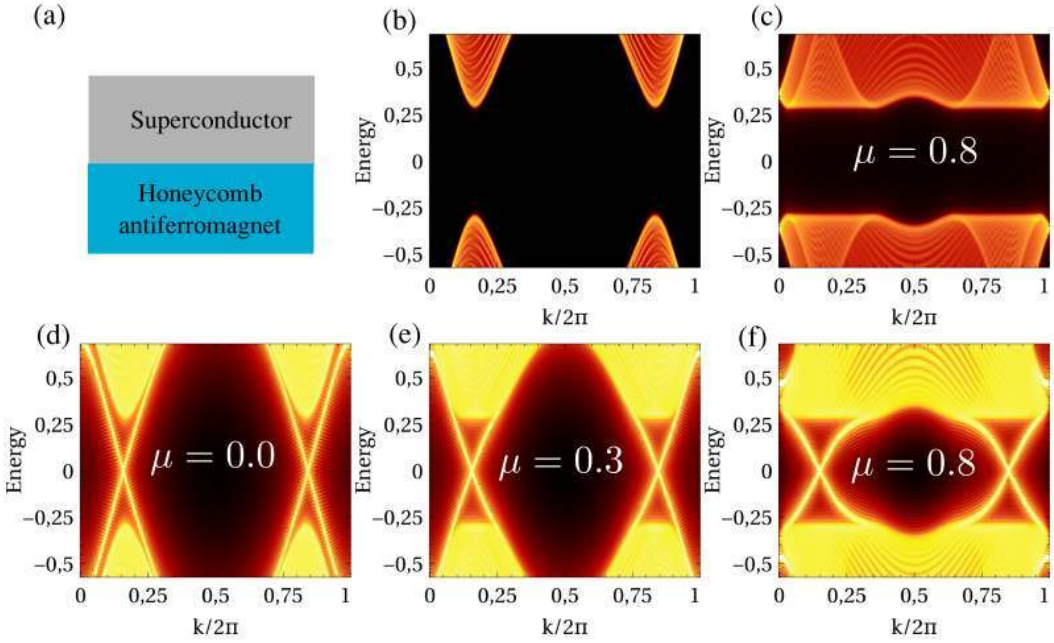

Figure 9.4: (a) Sketch of a hybrid ribbon, with the upper half superconducting and the lower half a honeycomb antiferromagnet. The spectral function (calculated with the KPM) in the bulk of the system shows that both the antiferromagnet (b) and the superconductor (c) have a gap. In comparison, when an interface between both phases is created, two branches of gapless interface modes show up (d,e,f), even when the honeycomb superconductor is doped (e,f). These gapless branches, when they become non-trivially gapped, will give rise to a 1d topological superconductor.

the interface state between a honeycomb antiferromagnet and a conventional superconductor. Skipping complex details, this interfacial states can be understood as the result of a weak topological state of the antiferromagnetic order in the honeycomb lattice. Details of the origin of this states will be discussed afterwards in section 9.6.

The basic idea behind the mechanism to get Majoranas from an antiferromagnetic state is the following. First, an interface between a honeycomb antiferromagnet and a superconductor is created. Each of the bulks is gapped, nevertheless the interface holds a channel of bound states, as shown in Fig. 9.4 . These interfacial bound states will have a small gap depending on details of the interface and smoothness of the order parameters. With this (gapless) 1d superconductor, a topological gap opening is forced by breaking all the remaining symmetries of the system, spin rotation and conjugation. The first way is by a small canting angle and spin orbit coupling. This mechanism can also be realized in some types of oxides, as discussed in section 10.3.1. The second mechanism involves a canting of the magnetic mo-

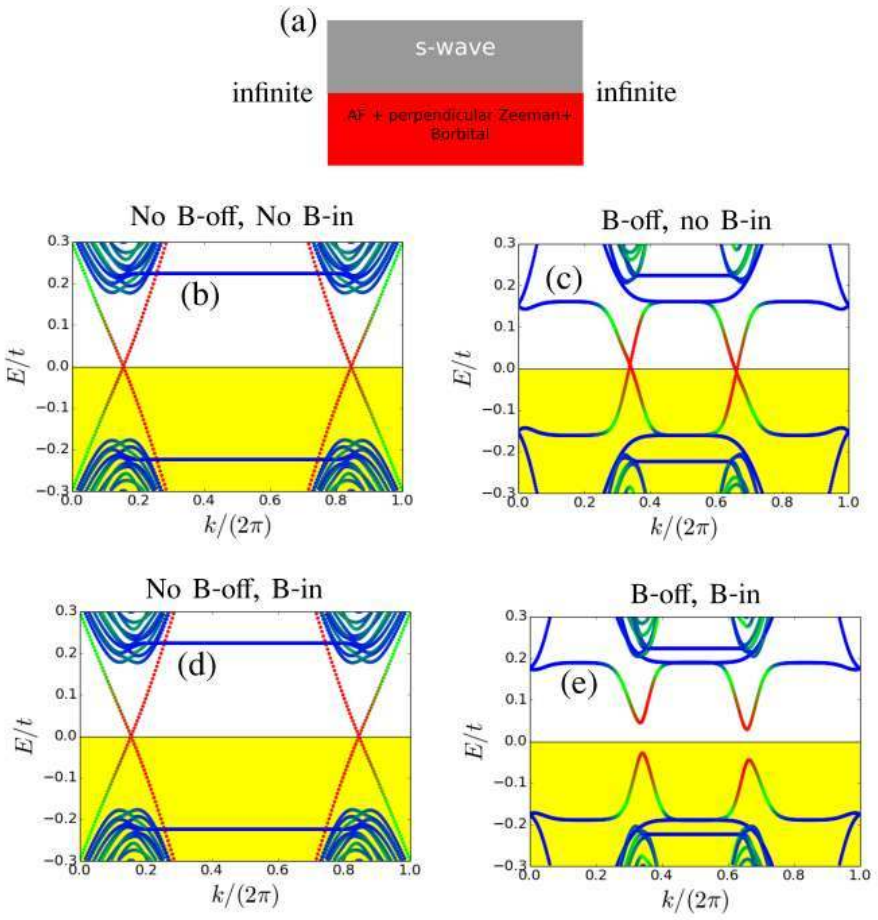

Figure 9.5: (a) Sketch of a hybrid ribbon, with the upper half superconducting and the lower half graphene with magnetic fields. In the absence of any field (b), the interface states are gapless for a zigzag interface. If only the orbital or zeeman fields are turned on (c,d), the interface remains gapless. Only when both fields are present (e), the gaps open up a topological gap

ments, and an orbital magnetic field. This last one is the one realized in graphene in the quantum Hall regime, as we discuss now.

9.2 Majorana modes in quantum Hall graphene

The realization of topological superconductivity (TS), a novel electronic phase characterized by Majorana excitations, has become a major goal in modern condensed

matter research. Despite promising experimental progress[394, 395, 396, 397, 398, 399, 400, 401, 402, 403, 404, 405, 406] on a number of appealing implementations[407, 408, 409, 410], a conclusive proof of TS remains an open challenge. We here report on a new approach to obtain TS and Majorana states in graphene/superconductor junctions. Key to our proposal is the interaction-induced magnetic ordering of graphene's zero Landau level (ZLL). Coupling this unique state to a conventional superconductor gives rise to novel edge states whose properties depend on the type of magnetic order. In particular, the canted antiferromagnetic phase is a natural host for Majorana bound states. Our proposal combines effects that were recently demonstrated experimentally (tunable spin ordering of the ZLL [411, 385] and ballistic [412, 387] graphene/superconductor junctions of high-transparency[387] operating in the Quantum Hall regime [412]), and is thus ready to be tested.

While intrinsic TS is rare, it can be synthesis ed effectively through the coupling of a conventional s-wave superconductor (SC) and tailored electronic gases with spin-momentum locking. Using this recipe, it has been predicted that Majorana excitations should emerge when one induces superconductivity onto topological insulators [407] or semiconductors with strong spin-orbit coupling [408]. Particularly attractive are implementations of one-dimensional TS using either semiconducting nanowires [409, 410] or edge states in two-dimensional Quantum Spin Hall (QSH) insulators, since the main ingredients are already in hand. These ideas have spurred a great deal of experimental activity [394, 395, 396, 397, 398, 399, 400, 401, 402, 403, 404, 405, 406]. Despite this progress, however, an unambiguous demonstration of TS is, arguably, still missing. Important limitations of these systems include disorder, bulk leakage, or imperfect proximity effect (the so-called soft gap problem). Thus, it is worthwhile to explore alternative materials.

One particularly interesting option is graphene [413], which exhibits very large mobilities even in ambient conditions, and where a ballistic proximity effect has been recently demonstrated [387]. Graphene was the first material where a topological insulating phase was proposed [414] in the presence of a finite intrinsic spin-orbit coupling. Kane and Mele showed that graphene then becomes gapped around neutrality, and a single helical edge mode with spin locked to propagation direction develops at each edge. In such QSH regime, gapping the edge states through proximity to a conventional superconductor gives rise to a one-dimensional TS along the interface [407]. Graphene's negligible spin-orbit coupling, however, has proved to be a fundamental roadblock in this program.

In this work we present a simple mechanism to realize the above situation in graphene without recourse to spin-orbit coupling. We consider a graphene ribbon in the Quantum Hall (QH) regime, in which, unlike in the QSH case, time-reversal symmetry is broken by a strong magnetic flux (section 9.2.1). In contrast to conventional two-dimensional electron gases, graphene develops a zero-Landau level at

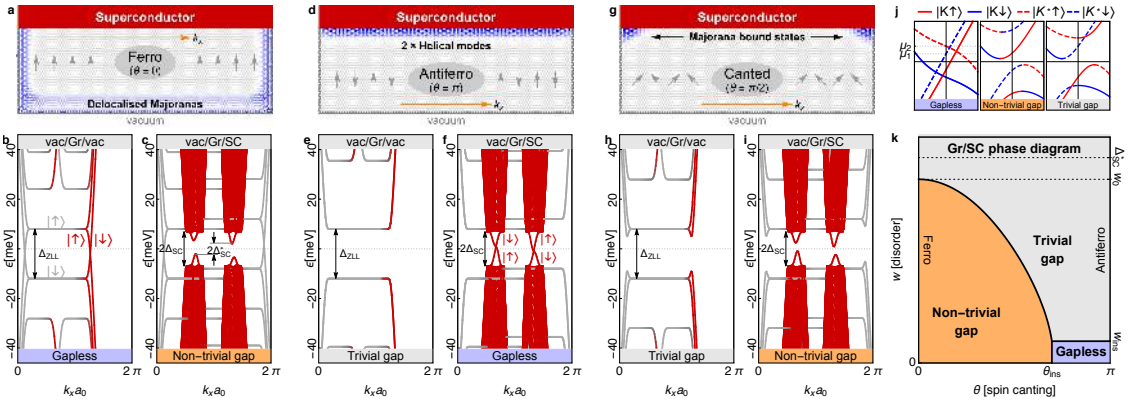

Figure 9.6: Sketch, band structure and phase diagram of a 350 nm-wide graphene sample (Fermi velocity $v_F = 10^6\, m/s$) in the Quantum Hall regime (out of plane field $B_z = 1$ T) in various configurations. The chemical potential (dotted line) is tuned within the gap $\Delta_{\rm ZLL} \approx 20$meV of the zero Landau level, which has ferromagnetic (a-c), antiferromagnetic (d-f) or canted antiferromagnetic ordering (g-i) due to electronic interactions. The band structures under each sketch correspond to an infinite graphene ribbon surrounded by vacuum (vac/Gr/vac panels) or coupled to a superconductor of gap $\Delta_{\rm SC}$ (chosen large ~ 7 meV for visibility) along the top edge as in the sketches (vac/Gr/SC panels, Nambu bands). Bands in red correspond to eigenstates localized at the top edge of the ribbon. The zero-energy local density of states is shown in blue in each sketch. (j) Low energy band structure of states along a graphene/superconductor interface folded onto the Γ point, in the gapless (left panel, zoom of panel f), non-trivially gapped (middle panel, canted order) and trivially gapped (right panel, with strong intervalley scattering) phases. (k) Phase diagram of said interface, computed from its low energy effective Hamiltonian (see text), as a function of magnetic angle θ and intervalley coupling w. The three possible phases are shown, bounded by threshold values w_0, $w_{\rm ins}$ and $\theta_{\rm ins}$

the Dirac point, which has been shown in pristine samples to become split due to electronic interactions [415, 416, 417, 418, 419, 420]. Experimental evidence [385] points towards spontaneous antiferromagnetic ordering [421, 422], although other broken symmetries have been discussed [411]. In this work we consider all possible magnetic orders. Fig. 9.6 summarizes the different possibilities, ranging from ferromagnetic (F) to antiferromagnetic (AF) ordering [2], including canted AF which may be controlled by an external in plane Zeeman field as argued in Ref. [385]. The different orders are parametrized by the angle θ between the spin orientation of the ZLL in the two graphene sublattices, so that $\theta = 0$ for F and $\theta = \pi$ for AF.

[2]Recently, schemes to experimentally probe the AF phase through spin excitations have been proposed [423].

While θ is considered in our model as an externally tunable parameter as in Ref. [385], we have checked that a mean-field calculation in a honeycomb Hubbard model under an in-plane Zeeman field (section 9.2.1) yields the same bulk and edge phenomenology presented in this work [422]. Corrections beyond mean field and the Hubbard model have been explored theoretically in the past, and have predicted the formation of a Luttinger liquid domain on an infinite vacuum edge [424]. The corresponding excitation density resembles the non-interacting edge for F order, rather than the AF case. The interacting problem at a highly transparent superconducting contact remains an open problem. We conjecture that, given their robust topological origin, the Majorana phenomena described here at a mean field level would survive in the Luttinger regime, at least within a limited range of parameters, and with power-law corrections to the transport results. These issues, however, remain beyond the scope of this work.

9.2.1 Modeling of G/SC systems

In this section we present the system models employed in this work. A non-interacting graphene flake may be modeled by a nearest-neighbor tight-binding Hamiltonian in an honeycomb lattice, with lattice constant a_0

$$H_0 \;=\; -\sum_{\langle i,j\rangle,s} te^{i\phi_{ij}} c^\dagger_{js} c_{is} + \sum_{is} \mu_N n_{is} \tag{9.22}$$

where $n_{is} = c^\dagger_{is} c_{is}$, i is the site index, s is spin, and $\phi_{ij} = -\frac{e}{\hbar}\int_{\vec{r}_i}^{\vec{r}_j} d\vec{r}\cdot\vec{A}(\vec{r})$ is the Peierls phase due to the magnetic flux $\mathcal{B}_z = \hat{z}\cdot(\vec{\nabla}\times\vec{A})$. We consider a perturbation $\sum_i \vec{B}\cdot\vec{S}_i$ arising from an external Zeeman field $\vec{B}$, where $\vec{S}_i = \sum_{ss'} c^\dagger_{is}\vec{\sigma}_{ss'}c_{is'}$ is the spin at site i. Intrinsic electron-electron interactions is furthermore included in the local Hartree-Fock approximation [422], which then take the form of a self-consistent Zeeman-like field $\vec{B}_U(\vec{r}_i)$ that is different in the two honeycomb sublattices. The total Zeeman-like perturbation H_Z thus reads

$$H_Z = \sum_i \left[\vec{B} + \vec{B}_U(\vec{r}_i)\right]\cdot\vec{S}_i \tag{9.23}$$

While $\vec{B}$ is uniform, favoring ferromagnetic (F) ordering, the self-consistent $\vec{B}_U(\vec{r}_i)$ is generally opposite for nearest neighbors, favoring antiferromagnetic ordering of the bulk. The combination of the two leads to a $\vec{B}$-tunable, spin-ordered ZLL that can be tuned from AF to F. Further details on the mean field numeric and results can be found in Ref. [422].

The hybrid graphene/superconductor (SC) system is described by the Hamiltonian

$$H \;=\; H_0 + H_Z + \sum_{\vec{r}_i\in\mathrm{SC}} \left[\Delta_{\mathrm{SC}} c^\dagger_{i\uparrow} c^\dagger_{i\downarrow} + \mathrm{h.c}\right] \tag{9.24}$$

The Fermi energy in H_0 above is μ_N for $\vec{r}_i \notin$ SC in graphene and μ_S for $\vec{r}_i \in$ SC at the superconductor (also a honeycomb lattice here, although this is not essential, see section 9.6.6). Similarly B, $\vec{B}_U$ and $\mathcal{B}_z$ are zero in the superconductor. However, gauge invariance demands that for a finite magnetic flux in graphene, $\Delta_{SC}(\vec{r}) = \Delta_{SC} \exp\left[-\frac{2e}{\hbar}\int^{\vec{r}} d\vec{r}\cdot\vec{A}(\vec{r})\right]$, where Δ_{SC} is the pairing for zero flux at a given superconductor.

The critical currents for the Fraunhofer patterns have been calculated in a wide and short graphene Josephson junction, described by a discretized H using an upscaled a_0 for numerical efficiency, following the ideas of Ref. [425]. The critical current for each magnetic flux is calculated as $I_c = 2e/\hbar \times \max_\phi(dF/d\phi)$, where ϕ is the superconducting phase difference and $F(\phi)$ is the free energy of the junction. [426] Exact diagonalization of the Hamiltonian is used to evaluate $F(\phi)$ at zero temperature.

9.2.2 Topological superconductivity in Quantum Hall graphene

An infinite ferromagnetically ordered ($\theta = 0$) ribbon in vacuum has a QH mean-field band structure [427] as shown in Fig. 9.6b. (Details on the modeling are given in section 9.2.1). The ZLL is spin-split into the two spin sectors in the direction of the ferromagnetic order, denoted by $|\uparrow\rangle, |\downarrow\rangle$ at energies $\pm\Delta_{\rm ZLL}/2$ respect to the Dirac point. For energies within this gap, a single pair of gapless counter propagating spin-polarized edge states develop, shown in red for states at the upper vacuum edge of the sample. Note the peculiar situation created in this energy window: edge states are not chiral like in the conventional QH regime, but may rather propagate in both directions with opposite spins, like in the QSH regime. Also, valley degeneracy is lifted at any given edge, which hosts a single state per propagating direction. Upon contacting one edge to a conventional superconductor of gap $\Delta_{\rm SC}$ (as in the sketch of Fig. 9.6a), while keeping the chemical potential (dotted line) within the ZLL gap, the edge states along the interface develop an induced gap $\Delta^*_{\rm SC}$ (see the corresponding Nambu band structure of Fig. 9.6c – red lines, once more, indicate states localized at the upper edge of the graphene ribbon, including now the dense quasi particle spectrum of the superconductor). The gap $\Delta^*_{\rm SC}$ is an important scale in this problem, since it turns out to be a topologically non-trivial gap. This is confirmed by computing the band structure's $\mathcal{Z}_2$ topological invariant, Eq. (9.32), relevant for quasi-one dimensional D-class systems [428]. Unlike in a conventional QSH system, where time-reversal symmetry is required, the vacuum edge states do not immediately develop a topological gap when contacted to the superconductor, but requires a reasonably good contact instead. On the other hand, while the conventional QSH metal becomes destroyed by any time-reversal-breaking perturbation (such as inelastic scattering or magnetic impurities), which in turn spoil the nontrivial superconducting gap, this is not the case of the the present implementation,

which has a broken time-reversal symmetry from the start. Moreover, we emphasize once more that no spin-orbit coupling at all is necessary for $\Delta^*_{\rm SC}$ to develop.

The immediate consequence of a non-trivial gap topology is the appearance of zero energy Majorana bound states (MBSs) at an interface with a trivial insulator, following the bulk-boundary correspondence principle. In this case, however, both ends of the topologically gapped superconducting interface are coupled to a *gapless* vacuum edge, so that the zero modes become dellocalized into the continuum away from the interface (see the zero energy local density of states [LDOS] in blue in Fig. 9.6a). This situation is similar to the fate of MBSs at the ends of a topological proximized semiconductor nanowires when strongly coupled to a metallic environment. [429]

The electronic structure associated to an antiferromagnetic ribbon ($\theta = \pi$, Fig. 9.6d) is the opposite. The states along a vacuum edge are now (trivially) gapped [422] like the ZLL itself (Fig. 9.6e). Surprisingly, when contacting the edge to a conventional superconductor *two* pairs of gapless helical edge modes emerge with spin-momentum locking around conjugate momenta K and K^* (Fig. 9.6f). These unexpected states, spatially spread along the interface (see the blue LDOS in Fig. 9.6d), are decoupled electron-hole (e-h) superpositions with orthogonal and well defined spin orientation along the AF axis, $|K^{(*)}\uparrow\rangle = a|\phi_{e\uparrow}\rangle + b|\phi_{h\downarrow}\rangle$ and $|K^{(*)}\downarrow\rangle = a'|\phi_{e\downarrow}\rangle + b'|\phi_{h\uparrow}\rangle$. A full discussion of these states is presented in section 9.6. The two helical edge modes remain gapless as long as no AF canting is present in graphene ($\theta = \pi$) and intervalley scattering is zero at the interface. We next consider deviations from these two assumptions.

9.2.3 Close look to interfacial states

It is interesting to note that the gapless edge states existed even before the magnetic field was introduced. Actually, in a zigzag ribbon such interfacial edge states are gapless due to the absence of intervalley mixing. In the situation without magnetic field and zigzag interface, the gap opening takes place once both in-plane and off-plane field are turned on. As can be observed in Fig. 9.5, only the combination of orbital and exchange fields are able to open up a topological gap. This can be easily understood taking into account that, in order to get a topological superconductor in graphene, all the degeneracies have to be broken.

In the case of an armchair interface between graphene and the honeycomb superconductor, a small gap exist without exchange splitting due to intervalley mixing, in comparison with the gapless zigzag interface. We will start with a non-zero orbital field, so the system is in the quantum Hall regime.

As the field increases, the interface gap closes and opens up as shown in Fig. 9.7. Therefore, for armchair interfaces there is a critical exchange in order to enter the topological non-trivial phase. This critical field depends on details of the interface,

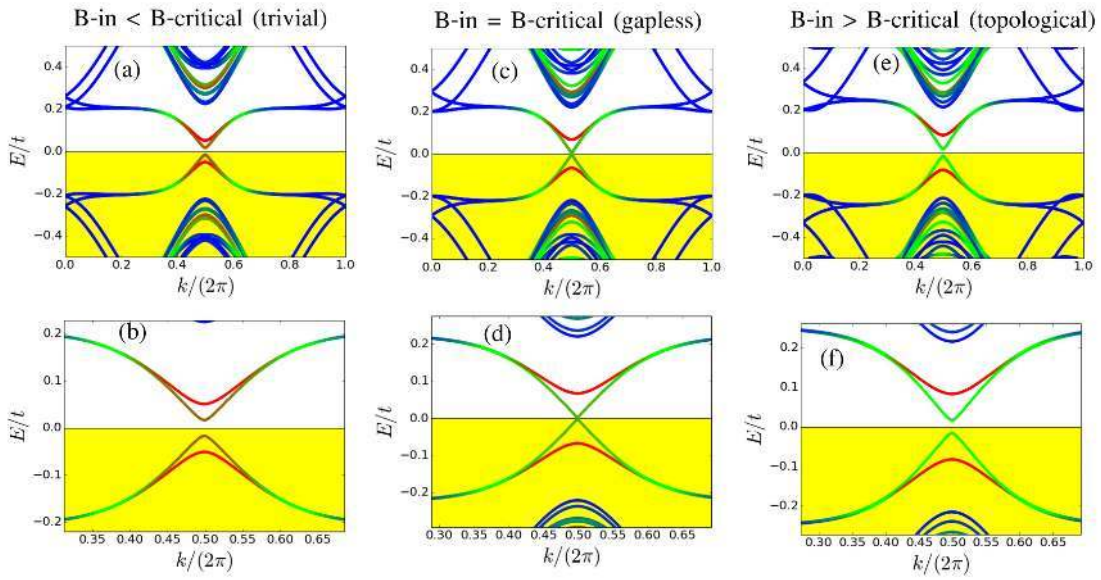

Figure 9.7: Band structure of a hybrid ribbon of superconductor and Quantum Hall antiferromagnet in the trivial state (a,b), critical (c,d) and topological (e,f). Without exchange field, intervalley mixing creates a small gap (b). As the exchange is increases, the interfacial gap closes (d) and topologically opens up (f).

mainly those defects that create intervalley mixing. In particular, it was checked that smooth interfaces turn the trivial gap smaller, so are mainly the sharp transitions are the responsible of trivial gap opening.

Canting of the AF order may be induced by means of a large enough in-plane Zeeman field, and is thus to some extent externally tunable. This idea was employed in Ref. [385] to tune a graphene QH bar in vacuum between the AF and F regimes, leading to a insulator-to-helical metal transition in edge transport (evolution from Figs. 9.6e to 9.6b). A typical canted AF band structure ($\theta = \pi/2$) is shown in Fig. 9.6h. The vacuum edge states exhibit a topologically trivial and θ-dependent gap, smaller than the bulk Δ_{ZLL}. Along a superconductor interface, the canted AF helical states are also gapped, Fig. 9.6i. Like in the ferromagnetic case, this gap is topologically non-trivial. This situation allows for the emergence of true localized zero-energy MBSs at the ends of the superconductor interface, where the edge gap changes topology, see Fig. 9.6g. The MBSs are topologically protected, and are not destroyed by any small perturbations, or even by modifying the crystal structure of the superconductor (section 9.6.6).

The emergence of the bound states are easily seen when a finite ribbon is calculated as shown in Fig. 9.8. Whereas the system is fully gapped, a zero energy excitation appears at the end of the interface, when three different vacuums coex-

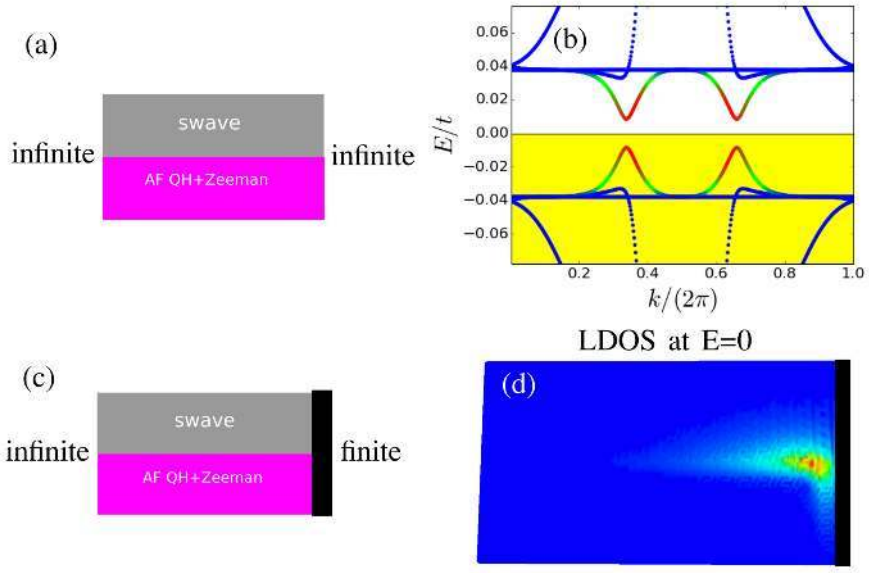

Figure 9.8: Sketch (a) and band structure of an hybrid ribbon (b), showing a gapless spectrum. When the geometry considered is a semi-infinite ribbon (c), the system sustains a zero energy mode in the corner. This can be easily seen by calculated the spatial resolved density of states at zero energy as shown in (d), which develops a peak at the end of the interface, where coexist the superconductor, the quantum Hall antiferromagnet and vacuum.

ist: the superconductor, the quantum Hall antiferromagnet and the normal vacuum. This behavior is completely analogous to a semiinfinite Kitaev chain, with its zero mode arising at the end. But in this case, the one-dimensional Kitaev chain emerges as the interface between the superconductor and the antiferromagnet.

9.2.4 Effective model

To understand the full phase diagram of the graphene/superconductor interface quantitatively, it is useful to employ a simplified description in terms of an effective low-energy Hamiltonian for the edge states (see section 9.5). The model is valid for a chemical potential tuned to the ZLL gap, and has the advantage of allowing us to incorporate the effects of atomic disorder along the junction (encoded in an inter-valley coupling w, where 'valley' here refers to the conjugate K and K^* momenta) and arbitrary spin canting (encoded in an intra valley splitting $b_\theta = \Delta^*_{\rm SC}\cos[\theta/2]$). It correctly describes the three possible phases for low-energy interface modes: gapless, trivially gapped and non-trivially gapped. The corresponding phase diagram is shown in Fig. 9.6k. Typical edge-mode dispersions within each phase (with K and

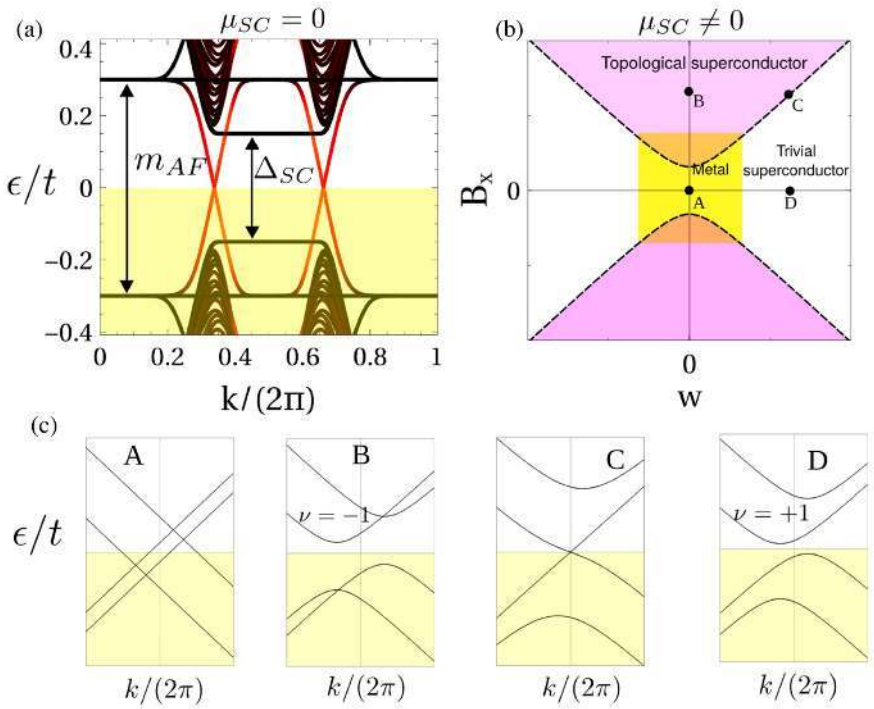

Figure 9.9: Band structure of the hybrid system (a), highlighting the two different gaps that can be observed. In the presence of orbital field, the topological state depends on the relative strength of the exchange and valley mixing couplings (b). the previous phenomenology can be captured in an effective model for the interfacial states, as shown in (c). The gapless region in (c) depends on the detail of the superconductor.

K^* points folded onto the Γ point) are shown in Fig. 9.6j, and are characterized by their energies $\mu_{1,2} < \Delta^*_{\rm SC}$ at $k_x = 0$ for $\theta = \pi$ [AF], $w = 0$, and their corresponding velocities $v_{1,2} > 0$ (left panel).

The gapless interface regime (light blue in Fig. 9.6k) is achieved for $|w| < w_{\rm ins} \equiv \frac{1}{2}|\mu_1\sqrt{v_2/v_1} - \mu_2\sqrt{v_1/v_2}|$ and $\theta > \theta_{\rm ins}$, where $b_{\theta_{\rm ins}} = \Delta^*_{\rm SC}\cos(\theta_{\rm ins}/2) \equiv \frac{1}{2}|\mu_1\sqrt{v_2/v_1} + \mu_2\sqrt{v_1/v_2}|$. The gapped regimes are characterized by the $\mathcal{Z}_2$ topological invariant of the system, which reads $\nu = \text{sign}\,(w^2 + \mu_1\mu_2 - b_\theta^2)$ (see section 9.5). A trivially gapped phase $\nu = +1$ is reached for strong intervalley coupling w at the interface, while for intervalley scattering below a threshold $w < \sqrt{b_\theta^2 - \mu_1\mu_2}$, the interface is one-dimensional TS with invariant $\nu = -1$. The non-trivially gapped regime is most robust against disorder for F order, for which the threshold w reaches its maximum $w_0 = \sqrt{(\Delta^*_{\rm SC})^2 - \mu_1\mu_2}$. Note that to achieve a non-trivial TS interface, the intervalley coupling w should therefore never exceed the induced gap $\Delta^*_{\rm SC}$ (this

is always the case for sufficiently transparent junctions).

This effective model can be straightforward connected to the tight binding calculations, by choosing a supercell which allows spin mixing, as 3 times the unit cell of a zigzag ribbon. In this situation the interfacial bands obtained by numerical calculations resemble the ones obtained by the effective model as shown in Fig. 9.9.

9.3 Signatures of graphene Majoranas

In the following we will focus on what are the experimental features that can be observed, based on a Josephson junction, and spot the existence of this Majorana bound state. First, we will present the computational method, and toy model where the difference between conventional bound state and Majorana is clearly seen. Afterwards, we will apply the same methodology to tackle our proposal of graphene Majoranas.

9.3.1 Andreev bound states in graphene Josephson junctions

Before moving to the experimental signature that will be the Fraunhofer pattern, we will briefly study the Andreev spectrum of a Josephson junction.

The setup is the following. The central part consists on graphene, with a presence of an off-plane and in-plane magnetic fields. On two opposite side, two semiinfinite superconducting leads are placed. The electronic transport takes places from the first lead to the second lead, passing through the graphene sample. The interface between each superconductor and graphene hosts the 1d topological superconductor, with the Majorana bound states located on the corner.

To start with, we will focus on the spectra projected onto the graphene sample, taking into account the superconducting leads. This is done by solving the Dyson equation in the Nambu space

$$G_G(\omega) = (\omega - H_G^0 - \Sigma_R - \Sigma_L)^{-1} \tag{9.25}$$

where Σ_R and Σ_L are the self energies of the right and left leads. The effective Hamiltonian of graphene is

$$H_{eff}(\omega) = \omega - G_G(\omega)^{-1} \tag{9.26}$$

This effective Hamiltonian is in general non-Hermitian, due to the imaginary part of the selfenergies Σ_R, Σ_L. The eigenvalues of H_{eff} have thus real and imaginary part, where the imaginary part is related with probability of the state to escape the graphene sample. Nevertheless, for $\omega < \Delta$, the selfenergies are purely real, so that

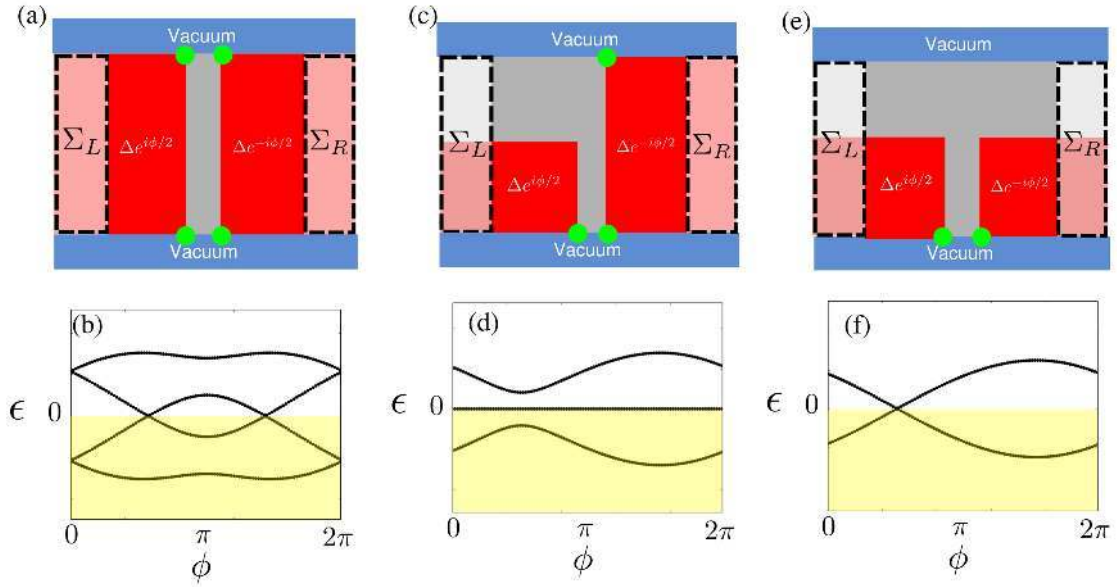

Figure 9.10: Sketch of a Josephson junction with four (a), three (c) and two (e) Majorana bound states. The junctions are not wide enough to have all the states decoupled, so they have a finite overlap both along as well as across. The overlap will be controlled by the superconducting phase difference. With four Majoranas, two zero crossing points take place (b). With three Majoranas, an anti crossing in developed, but also a zero bias resonance is always present (d). Finally, we just two Majoranas are present (e), a single topologically protected crossing point takes place (f).

the eigenvalues within the gap are also purely real. As first approximation, we study the spectrum by numerically diagonalizing.

$$H_{eff} = -G_G(\omega = 0)^{-1} \tag{9.27}$$

The eigenvalues of the previous matrix will give an approximate energy for the states of the junction. It is worth to note that the previous approximation is valid as long as the energy of the state is close to $\omega = 0$.

9.3.2 Toy model: Fraunhofer pattern

The first setup that we will study consists on two Kitaev chains, which are weakly coupled between them and to two semiinfinite superconductors. In each corner of each Kitaev chain there is an initial Majorana bound state. When two Majoranas are coupled, the bound states spin splitting depending on their overlap. By controlling

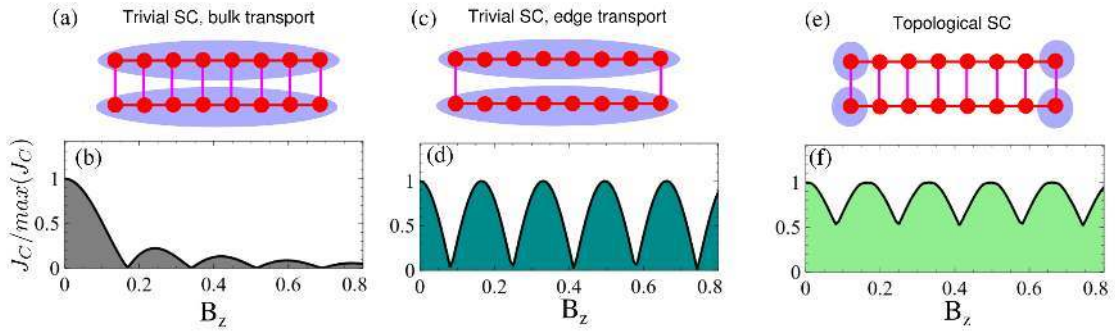

Figure 9.11: Toy model of two weakly coupled conventional superconducting chains (a) and their Fraunhofer pattern resembling a wide slit (b). Toy model of two superconducting chains, only coupled by their corners (c) and their Fraunhofer pattern resembling a double slit (d). Two weakly coupled topological Kitaev chains (e), with their unconventional Fraunhofer pattern (f). The absence of zeros in the pattern (f) is a signature of Majorana bound states.

the superconducting paring phase and a perpendicular magnetic phase the overlap can tuned, and there their splitting.

Each superconductor holds a superconducting pairing with different phase, namely ϕ_R and ϕ_L. The eigenvalues of the Nambu Hamiltonian of the whole system are therefore a function of the phase difference $\phi = \phi_R - \phi_L$

$$\epsilon = \epsilon(\phi_R, \phi_L) = \epsilon(\phi_R - \phi_L) = \epsilon(\phi) \tag{9.28}$$

The critical current of the heterojunction can be calculated as

$$J_c = \frac{2\pi}{\Phi_0} \max_{\phi} \left(\sum_{\epsilon<0} \frac{d\epsilon}{d\phi} \right) \tag{9.29}$$

We will focus first on two trivial superconductor, which in our case is represented by two weakly coupled superconducting chains as shown in Fig. 9.11a,c. The Fraunhofer pattern obtained by applying Eq. 9.29 depends on the coupling between the superconductors. For uniform coupling Fig. 9.11a, the pattern shown an oscillating and decaying behavior (Fig. 9.11b). In comparison, for only edge coupling Fig. 9.11c, the patter Fig. 9.11d shows a uniform oscillation without decaying as the magnetic field increases. Therefore, the study of the Fraunhofer pattern allows to know from which parts of the sample the transport takes place, i.e. allows to do a real space image of the current. Mathematically, in this cases the Fraunhofer pattern represents the Fourier transform of the real space current. This last relation allows to relate the result obtained for Fig. 9.11a as the diffraction of a wide slit, and the result of Fig. 9.11c with the diffraction of the double slit.

We will move to the case of two coupled topological superconductors. The Majorana bound states cross zero energy as the phase difference changes, and as we will see this will have a critical effect on the Fraunhofer pattern. In this case, every pair of Majorana bound states are splitted due to their overlap. As the phase between them changes, there is an odd number of zero energy crossing. This constrain over the number of crossings imposes that the critical current is non-zero for any magnetic field.

It is important to note that a non-zero critical current is not a proof of Majorana bound states, it is just a mandatory condition to have Majorana bound states. The other mechanisms that can give rise to a non-vanishing signal are contributions from low energy bound states, so that if the junction shows multiple interference channels, the critical current will have multiple contribution from different transport paths. This will the case when for example, the transport is not purely edge, but has bulk and edge contributions.

9.3.3 Graphene Majoranas setup

We finally consider measurable signatures of the MBSs in the system. A powerful probe whose feasibility has been recently demonstrated experimentally [412, 387] involves interferometry of critical currents in Josephson junctions, and Fraunhofer pattern anomalies in particular [430, 405, 402]. Lee *et al.* predicted [431] that topological superconductivity in a short and wide Josephson junction could be directly detected in its Fraunhofer pattern, in the form of non-vanishing minima of the critical current for arbitrary magnetic flux through the junction. Such Fraunhofer anomaly was recently observed in a three-dimensional topological insulator, and was interpreted as possible evidence of MBSs [405].

Fig. 9.12 shows the Fraunhofer pattern in a short and wide (10nm $\times$ 3μm) graphene Josephson junction in various regimes. The black (bottom) curve corresponds to the non-interacting case (no magnetic ordering, $\Delta_{\mathrm{ZLL}} = 0$), which exhibits the conventional $I_c(\Phi) = I_c^0|\sin(\pi\Phi/\Phi_0)|/(\pi\Phi/\Phi_0)$ critical current that decays as the inverse magnetic flux Φ through the junction $I_c \sim 1/\Phi$ and vanishes at multiples of the flux quantum $\Phi_0 = h/2e$. A similar behavior is obtained in the gapless regime $\theta > \theta_{\mathrm{ins}}, w < w_{\mathrm{ins}}$ (purple curve, with $\theta = \pi$ [AF] and $w = 0$). In both cases, the junction is host to a narrow quasi-continuum of Andreev bound states around the Fermi energy for any value of the superconducting phase difference ϕ. The corresponding spectra are shown in the top row of inset *a* (for $\Phi = 15.5\Phi_0$). States in red and blue are localized at the top and bottom edges of the junction (inset *b*), respectively, with gray denoting states spread across the junction (inset *c*). The case with trivially gapped interfaces (strong intervalley scattering) also exhibits a generic Fraunhofer pattern with vanishing minima (light gray curve, $\theta = 0$ [F] and $w > w_0$). The minima, however, occur at fluxes that are shifted away from integer

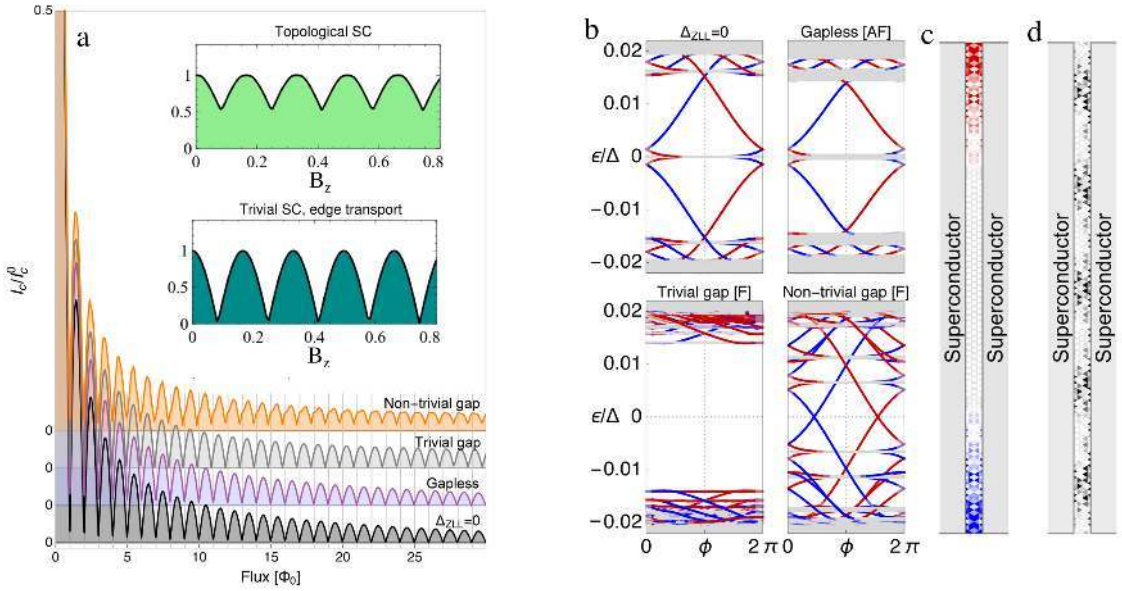

Figure 9.12: Normalized critical current (a) I_c/I_c^0 as a function of magnetic flux through a Josephson junction. The inset shows the behavior expected for an edge trivial superconductor and a topological superconductor, as shown previously in Fig. 9.11. Curves from bottom to top in (a) (shifted for better visibility) correspond to the non-interacting case (black), gapless AF phase (purple), a trivially gapped AF phase (light gray) and a ferromagnetic phase with a topologically non-trivial gap (orange). Only the latter shows non-decaying non-zero minima in I_c, a consequence of an Andreev spectrum (b) with an odd number (one) of edge-resolved zero energy crossings . States colored in red and blue are located at the top and bottom edges, respectively (c), while states in gray are spread across the width of the junction (d).

Φ/Φ_0 at high Φ, while the maxima do not decay like the conventional $I_c \sim 1/\Phi$ pattern, which is connected to non-uniform currents across the junction[430]. The Andreev spectrum of the trivially gapped phase is qualitatively different from the gapless spectra, and generally shows a distinct gap devoid of any edge states (inset a, bottom left). For certain values of parameters, it may exhibit zero-energy crossings inside the gap, but in such cases these crossings are accidental (not topologically protected) and there is always an even number of them at a given edge.

The Josephson junction with a non-trivial gap along the contacts is distinctly different from all previous cases. This phase develops two MBSs at each edge (top and bottom) which hybridize to carry a finite supercurrent that never vanishes as the flux increases. The corresponding Fraunhofer pattern thus exhibits a finite background with a superimposed non-decaying oscillation (orange curve in Fig. 9.12), as described in Ref. [431]. The finite minima are roughly one half of the maxima at

large flux, and occur away from integer Φ/Φ_0, at values very close to the zeroes of the trivially gapped phase. (Note, however, that such distinctive pattern develops only in junctions shorter than the Majorana localization length and pierced by a large number of flux quanta, so that the Majoranas are well developed and opposite edges are decoupled). These Fraunhofer anomalies, although not completely unambiguous, thus constitute a measurable hint of the presence of MBSs at the end of a graphene/superconductor interface. Unfortunately, fabricating a very short junction is challenging, in particular due to charge-transfer effects from the superconductors which were neglected here, and which will dope graphene away from neutrality within a few nanometers of the contacts. It is thus important to explore other less stringent experimental schemes that are at the same time not ambiguous. The key is to probe the Andreev spectrum directly for signatures of Majoranas and non-trivial topology.

The presence of the two hybridized Majoranas per vacuum edge (see Fig. 9.10) in the non-trivial phase manifests in the Andreev spectrum as a single topologically protected zero energy crossing at each edge as ϕ is increased by 2π (one red and one blue crossing, see bottom-right inset a in Fig. 9.12). An odd number of such zero energy crossings has been shown [432] to be an direct manifestation of non-trivial topological order $\nu = -1$, and is the underlying reason for the anomalous Fraunhofer pattern of the junction. A completely non-ambiguous demonstration of the presence of MBSs is also thus possible in principle, by directly counting edge-resolved zero-energy crossings using Andreev spectroscopy [433] in a phase-controlled Josephson junction. This may be achieved by measuring differential conductance dI/dV through a normal point contact attached to one edge of the junction.

9.4 Discussion

Our results show that the spontaneous magnetic ordering of the ZLL in graphene enables the creation of topological superconductivity and Majorana states at an interface with a conventional superconductor, even in the absence of spin-orbit coupling in the system. The key is to tune the Fermi energy in the contact into the ZLL gap, and to achieve a good proximity effect therein. The recently characterized samples of Ref. [412] are good candidates to realize our proposal. Impressive progress in controlling graphene filling into proximity gaps has also been reported [434]. We furthermore showed that non-vanishing and non-decaying supercurrent minima in the Fraunhofer pattern across a depleted graphene Josephson junction constitute a characteristic signal of topological order and the presence of Majorana bound states in the junction [431]. Fraunhofer patterns of extraordinary quality have been recently reported in high-transparency ballistic graphene Josephson junctions [387]. We predict even stronger observable signatures of non-trivial topology in Andreev

transport spectroscopy, both in the form of an odd number of $4e^2/h$ edge-resolved zero-bias crossings versus junction phase difference ϕ or out of plane magnetic field B, and extended $2e^2/h$ zero bias anomalies versus canting angle θ. These experimental probes and the required device parameters are within reach in top laboratories today. We thus expect that the possibility of tuning graphene/superconducting interfaces into a topological phase hosting Majorana bound states could be tested soon.

9.5 Low-energy description of a G/SC junction

Here we derive a simplified effective Hamiltonian H_{eff} for the two helical edge modes below the superconducting gap Δ_{SC} that arise in a generic Quantum Hall graphene ribbon and a superconductor. We also characterize its topology by deriving expressions for the relevant topological invariant as a function of model parameters.

We assume the chemical potential lies within the gap Δ_{ZLL} induced by interactions in the zero Landau Level (ZLL). The gap is associated to a bulk spin ordering described by a canting angle θ between the two sublattice. The effective model incorporates an arbitrary value for θ in graphene and also intervalley coupling due to atomic disorder along the interface. Formally, H_{eff} is a projection of the microscopic Hamiltonian on the basis $\{|K\uparrow\rangle, |K\downarrow\rangle, |K^*\uparrow\rangle, |K^*\downarrow\rangle\}$ of the four AF helical edge states along the junction. We furthermore consider a linearization of their dispersion in the AF case around 'valleys' K and K^* points. These two valleys are folded onto the Γ point by appropriately expanding the ribbon unit cell. Such folding allows us to include intervalley scattering into H_{eff} in a simple way. H_{eff} then takes the form ($\hbar = 1$)

$$H_{\text{eff}} \approx \begin{pmatrix} \mu_1 + v_1 k_x & b_\theta & w & 0 \\ b_\theta & \mu_2 - v_2 k_x & 0 & w \\ w & 0 & -\mu_2 - v_2 k_x & b_\theta \\ 0 & w & b_\theta & -\mu_1 + v_1 k_x \end{pmatrix} \tag{9.30}$$

Here, the intravalley coupling $b_\theta = \Delta^*_{\text{SC}} \cos(\theta/2)$ implements AF canting, and couples opposite spins within the same valley. The intervalley coupling w is spin-independent, and corresponds to the harmonic of wavenumber $\Delta K = (\vec{K}^* - \vec{K}) \cdot \hat{x}$ of any disorder term W close to the interface, $w = \langle \phi_{\uparrow K^*} | W(\Delta K) | \phi_{\uparrow K} \rangle$. Both b_θ and w can be chosen real without loss of generality. $v_{1,2} > 0$ are the velocities of the counter-propagating helical states, and $\mu_{1,2} < \Delta^*_{\text{SC}}$ are their energy, relative to the Fermi energy, at the Γ point. The overall structure apparent in H_{eff} is fully determined by the particle-hole symmetry of the underlying Nambu description. Note that H_{eff} only retains terms linear in momentum k_x along the interface.

We finally sketch the derivation of the insulating thresholds $w_{\rm ins}$ and $\theta_{\rm ins}$. These are extracted by computing the solutions for the wavenumber k_x of $H_{\rm eff}$ modes at zero energy. Since $H_{\rm eff}(k_x)$ is linear in k_x, said k_x solutions at $\epsilon = 0$ can be obtained as eigenvalues of a matrix $-(\partial_{k_x} H_{\rm eff}(0))^{-1} H_{\rm eff}(0)$. These can be worked out analytically, and turn out to be all complex (i.e. the interface becomes gapped, see e.g. Fig. 9.14f) if $w > w_{\rm ins}$ or $\theta < \theta_{\rm ins}$ with the expressions

$$\begin{aligned} w_{\rm ins} &= \frac{1}{2}\left|\mu_1\sqrt{v_2/v_1} - \mu_2\sqrt{v_1/v_2}\right| \\ b_{\theta_{\rm ins}} &= \Delta^*_{\rm SC}\cos(\theta_{\rm ins}/2) \equiv \frac{1}{2}\left|\mu_1\sqrt{v_2/v_1} + \mu_2\sqrt{v_1/v_2}\right| \end{aligned} \tag{9.31}$$

9.5.1 Topological invariant of edge Hamiltonian

In symmetry class D (superconductors without time reversal symmetry), the one-dimensional topological invariant is $\mathcal{Z}_2$. It is conventionally defined, for periodic systems, as [435]

$$\nu = \text{sign}\left(\frac{\text{Pf}[H(0)\tau_x]}{\text{Pf}[H(\pi)\tau_x]}\right) = \frac{s_0}{s_\pi} \tag{9.32}$$

where $s_\alpha = \text{sign}\,\text{Pf}[H(\alpha)\tau_x]$, $H(k_x a_0)$ is the 1D Bloch Hamiltonian for momentum k_x, a_0 is the lattice constant of the ribbon lattice, τ_x is the first Pauli matrix in the electron-hole sector, and Pf is the Pfaffian. It can be shown in general that $H\tau_x$ is antisymmetric at the high-symmetry points $k_x a_0 = 0, \pi$. The invariant ν is thus fully determined by the structure of H at these two points. The effective Hamiltonian $H_{\rm eff}$, Eq. (9.30), only gives a faithful representation of the full microscopic Hamiltonian H around one of them, the folded Γ point $k_x = 0$. To extract analytic results for ν for the full H using $H_{\rm eff}$, we must ensure that at the π-point s_π does not change when sweeping the parameter space (since this sector of states is not described by $H_{\rm eff}$). This is indeed the case in our system for the chosen basis, for which $s_\pi = 1$. The changes in topology stem from the reconnections of the low-energy edge states that are concentrated around Γ, and are well described by $H_{\rm eff}$. Higher excited states not included in $H_{\rm eff}$ never cross zero energy, and therefore cannot affect the sign of the Pfaffian of $H(0)\tau_x$. One can thus write

$$\nu = \text{sign}\,\text{Pf}[H_{\rm eff}(0)\tau_x] = \text{sign}(w^2 + \mu_1\mu_2 - b^2) \tag{9.33}$$

We have numerically verified the above result by evaluating the $\mathcal{Z}_2$ invariant exactly from the microscopic Hamiltonian H.

9.5.2 Estimates for canting angles $\theta_{L,W}$

The canting angle θ_L is defined as the θ such that the corresponding decay length of edge states along a *vacuum* edge equals the length L of the Josephson junction.

Likewise, θ_W is defined as the θ such that the corresponding decay length of edge states along a *superconducting* edge equals the width W (hence $\theta_W \leq \theta_{\rm ins}$).

The evaluation of θ_W can be made by extracting the decay length $1/{\rm Im}k_x$ of gap states at zero energy from the effective Hamiltonian of Eq. (9.30) without disorder ($w = 0$), and equating that to W. The result comes out simply as

$$\cos\theta_W \approx \cos\theta_{\rm ins} + \frac{2v_1v_2}{W^2\Delta_{\rm SC}^{*2}}$$

where, recall, $\hbar = 1$ and

$$\cos(\theta_{\rm ins}/2) = \frac{1}{2}\left|\mu_1\sqrt{v_2/v_1} + \mu_2\sqrt{v_1/v_2}\right|/\Delta_{\rm SC}^*$$

Note that in the limit $W \to \infty$, $\theta_W = \theta_{\rm ins}$, as expected.

An analogous calculation can be done for the vacuum edge along the y direction, whose effective (normal) Hamiltonian can be written in analogy to Eq. (9.30) as

$$H_{\rm eff}^{\rm vac} \approx \begin{pmatrix} \mu_N + v_F k_y & \frac{1}{2}\Delta_{\rm ZLL}\sin(\theta/2) \\ \frac{1}{2}\Delta_{\rm ZLL}\sin(\theta/2) & \mu_N - v_F k_y \end{pmatrix} \tag{9.34}$$

This leads to the estimate

$$\sin^2\frac{\theta_L}{2} \approx \left(2\frac{\mu_N}{\Delta_{\rm ZLL}}\right)^2 + \left(\frac{2v_F}{L\Delta_{\rm ZLL}}\right)^2$$

Note that as $L \to \infty$, θ_L reaches a minimum value that corresponds to the threshold where the vacuum edge becomes gapped (non-zero for $\mu_N \neq 0$).

Mean field results within the Hubbard model (see9.2.1 and Ref. [422]) yield a dependence of canting angle θ with in-plane magnetic field $B_\parallel$ of the form $\sin(\theta/2) \approx \sqrt{1-(B_\parallel/B_0)^2}$, where B_0 is the in-plane field that achieves complete Ferromagnetic polarization.

9.6 Helical edge states in an AF graphene-SC interface

9.6.1 Interface states without Landau levels

The interface states between a superconductor and an antiferromagnetic honeycomb lattice are not related to the Landau level structure. In the particular case of graphene, the magnetic field is the key ingredient to develop magnetic order (due to the large kinetic energy of electrons), which is developed when the kinetic energy is

quenched by the magnetic field. However, in a general honeycomb lattice, provided the interactions are large enough at $B = 0$, electrons might be able to develop AF order, and thus create interface states between a SC even at $B = 0$. This behavior might be relevant for other honeycomb systems with smaller hopping strengths than graphene, as silicene, germanene, stanene or honeycomb oxides.

We show in Fig. 9.13, that such interface sustains the same kind of states as in the case of the antiferromagnetic quantum Hall state. In the case of zigzag interfaces (9.13c,9.13d), each valley supports its own set of interface states, whereas for an armchair interface (9.13b), the two valley are folded and interface states between different valleys can couple. In the former case, if the interface is abrupt enough, a small gap opens up due to intervalley mixing.

If a canting in the magnetic moments is introduced, the zigzag interphase remains gapless. The same happens when only a orbital magnetic field is introduced. Only when both perturbations are present simultaneously, the system is able to enter into the topological superconducting state. Thus, an off-plane magnetic field is mandatory to observe the Majorana bound states. The previous phenomenology, suggests that in order to develop a topological gap, both the spin rotation symmetry and the spatial gauge symmetries have to be broken.

9.6.2 Helical edge states from wavematching

The interface states between a honeycomb antiferromagnet and a superconductor are not intrinsically related to the Landau level spectrum. Although in graphene, the antiferromagnetic state is only expected to arise when the system enters in the quantum Hall regime, a general antiferromagnetic honeycomb lattice might also sustain interface states when attached to a superconductor without a magnetic flux.

In this section, we will show how that interface states naturally arise by an analytic argument in the absence of magnetic field. In particular, a simple wavematching between a $E = 0$ energy state shows that the boundary between an antiferromagnet and an swave superconductor is able to sustain such state.

To proceed, we will look for bounded solutions such that $H|\phi\rangle = 0$ with

$$\phi(x) = \begin{pmatrix} c_1 \\ c_2 \\ c_3 \\ c_4 \end{pmatrix} r(x) = \begin{pmatrix} c_1 \\ c_2 \\ c_3 \\ c_4 \end{pmatrix} e^{-\lambda(x)x} \tag{9.35}$$

$$\lambda(x) = \begin{cases} -\Delta_{SC} & \text{if } x < 0 \\ m & \text{if } x > 0 \end{cases} \tag{9.36}$$

In the following we will focus in one of the four decoupled sectors, in particular the $|e, \uparrow K\rangle$ with $|h, \downarrow K'\rangle$ sector

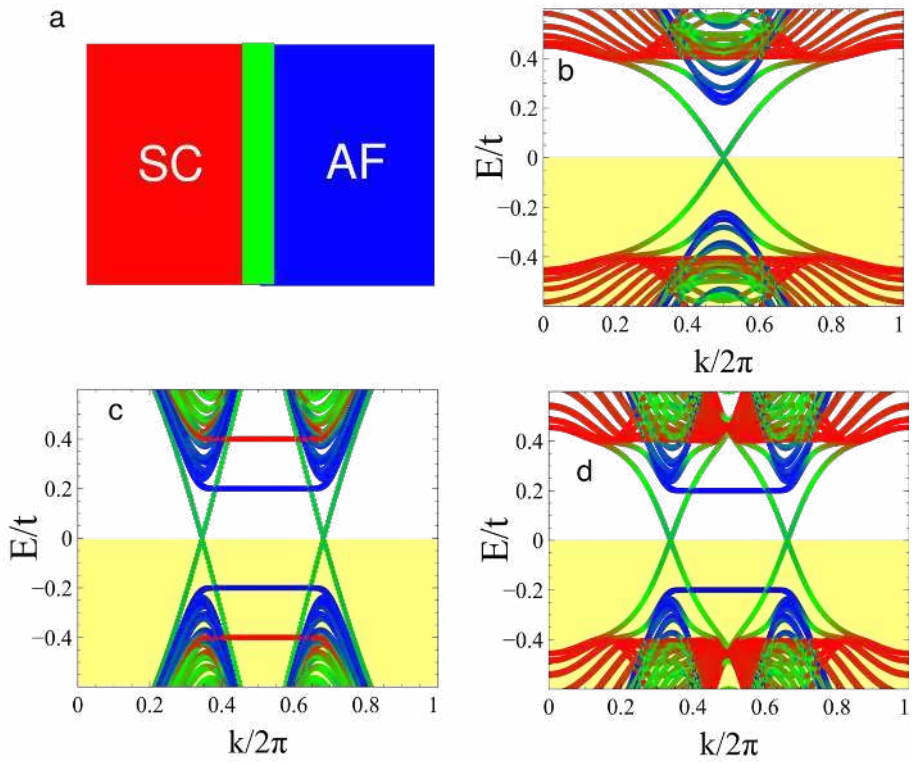

Figure 9.13: (a) Scheme of a ribbon hybrid ribbon AF-SC, with the color code of the band structure. (b) Band structure of a hybrid ribbon with doped SC and armchair interface. Band structure of a hybrid ribbon with un-doped (c) and doped (d) SC with zigzag interface, which shows the different interface states in each valley.

For the antiferromagnet the Hamiltonian reads

$$H_{SC} = \begin{pmatrix} m & p & 0 & 0 \\ p & -m & 0 & 0 \\ 0 & 0 & m & -p \\ 0 & 0 & -p & -m \end{pmatrix} \tag{9.37}$$

whose $E = 0$ solutions are

$$\Phi_1 = \frac{1}{\sqrt{2}} \begin{pmatrix} 1 \\ i \\ 0 \\ 0 \end{pmatrix} \qquad \Phi_2 = \frac{1}{\sqrt{2}} \begin{pmatrix} 0 \\ 0 \\ 1 \\ -i \end{pmatrix} \tag{9.38}$$

On the other hand, for the superconductor the Hamiltonian reads

$$H_{SC} = \begin{pmatrix} 0 & p & \Delta_{SC} & 0 \\ p & 0 & 0 & \Delta_{SC} \\ \Delta_{SC} & 0 & 0 & -p \\ 0 & \Delta_{SC} & -p & 0 \end{pmatrix} \tag{9.39}$$

with $E = 0$ solutions

$$\Psi_1 = \frac{1}{\sqrt{2}} \begin{pmatrix} 0 \\ 1 \\ i \\ 0 \end{pmatrix} \qquad \Psi_2 = \frac{1}{\sqrt{2}} \begin{pmatrix} 1 \\ 0 \\ 0 \\ i \end{pmatrix} \tag{9.40}$$

Imposing continuity at the interface $x = 0$, the full $E = 0$ solution reads

$$\phi(x) = \frac{1}{2} \begin{pmatrix} 1 \\ i \\ -1 \\ i \end{pmatrix} r(x) \tag{9.41}$$

$$r(x) = \begin{cases} e^{\Delta_{SC} x} & \text{if } x < 0 \\ e^{-mx} & \text{if } x > 0 \end{cases} \tag{9.42}$$

so that a normalizable $E = 0$ exist for an interface between a trivial antiferromagnet and a trivial Dirac superconductor.

9.6.3 Helical modes from explicit integration

In previous section, we build the $E = 0$ by wavematching across a sharp interface. However, it is is possible to give a general solution for the interface state between the antiferromagnet and the superconductor. Without loss of generality, in the following we will assume $m > 0$ and $\Delta_{SC} > 0$. The Hamiltonian for an arbitrary antiferromagnet and pairing profile for $k_y = 0$ reads

$$H = \gamma_1 m(x) + \gamma_2 p + \gamma_3 \Delta_{SC}(x) \tag{9.43}$$

with $\gamma_1, \gamma_2, \gamma_3$ defined by

$$\gamma_1 = \begin{pmatrix} 1 & 0 & 0 & 0 \\ 0 & -1 & 0 & 0 \\ 0 & 0 & 1 & 0 \\ 0 & 0 & 0 & -1 \end{pmatrix} \tag{9.44}$$

$$\gamma_2 = \begin{pmatrix} 0 & 1 & 0 & 0 \\ 1 & 0 & 0 & 0 \\ 0 & 0 & 0 & -1 \\ 0 & 0 & -1 & 0 \end{pmatrix} \tag{9.45}$$

$$\gamma_3 = \begin{pmatrix} 0 & 0 & 1 & 0 \\ 0 & 0 & 0 & 1 \\ 1 & 0 & 0 & 0 \\ 0 & 1 & 0 & 0 \end{pmatrix} \tag{9.46}$$

Defining $\gamma_4 = -i\gamma_2\gamma_1$ and $\gamma_5 = i\gamma_2\gamma_3$, the zero energy equation reads

$$(p + i\gamma_4 m(x) - i\gamma_5 \Delta_{SC}(x))\phi = 0 \tag{9.47}$$

The spinor wavefunction

$$\phi_0 = \frac{1}{2}\begin{pmatrix} 1 \\ i \\ -1 \\ i \end{pmatrix} \tag{9.48}$$

verifies $\gamma_4\phi_0 = \gamma_5\phi_0 = \phi_0$, which allows to build the $E = 0$ solution

$$\phi(x) = Ne^{-\int_0^x (m(x') - \Delta_{SC}(x'))dx'}\phi_0 \tag{9.49}$$

which is normalizable provided that $m(+\infty) > \Delta_{SC}(+\infty)$ and $\Delta_{SC}(-\infty) > m(-\infty)$, which is the condition of domain wall between superconductor and antiferromagnet. For the case of step profiles, the solution obtained by wavematching is recovered.

9.6.4 Influence of μ_{SC} in the critical Zeeman coupling

In the idealized situation in which the superconductor is described as a single-orbital honeycomb lattice at half filling, a arbitrary small Zeeman field is capable of opening the interface topological gap. However, charge transfer processes are expected to shift the chemical potential of the proximized graphene (SC region in Fig. 9.6). In this situation, band bending of the interfacial states leads to a one dimensional gapless state (see Fig. 9.14c). In order to reach the interfacial topological superconducting state, the bended bands (Fig. 9.14c) have to be moved up in energy. This can achieved by increasing the in-plane field, so that $\theta < \theta_{\text{ins}}$. The critical in-plane field B_x as a function of doping, which separates the gapless and topologically gapped states is shown in Figs. 9.14e,f. For small μ_{SC}, the critical field increases linearly, leading to small critical fields at small doping in the SC, whereas for large doping the critical field saturates.

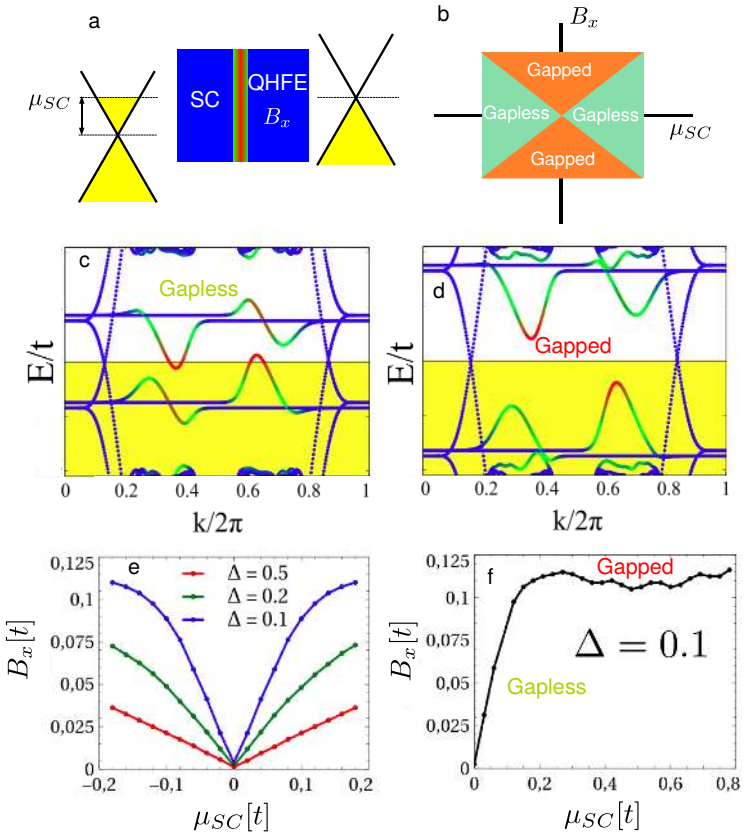

Figure 9.14: Scheme of the effect of chemical doping in the Dirac spectrum of proximized graphene (a). Schematic phase diagram (b) of the interface electronic spectrum between the SC and the QH ferromagnet, as function of the in-plane field and the chemical doping of the SC. Quasi particle energies for a gapless (c) and gapped (d) interface. Phase boundary obtained by numerical calculation at low doping (e) and at large doping (f). The green and red colored states of the band structures correspond to the states localized at the interface, where the topological superconducting gap is calculated between the red states shown in (c,d). The blue gapless states correspond to the chiral states between the QH and vacuum.

9.6.5 Emergence of AF helical states from a topological point of view

An analysis of the emergent AF helical edge modes in terms of topology can be made, but it is less rigorous mathematically than the topological superconductor order in the canted AF phase. As shown in Fig. 9.6k, there is a finite volume in parameter space for which the SC contacts are helical metals. The relevant

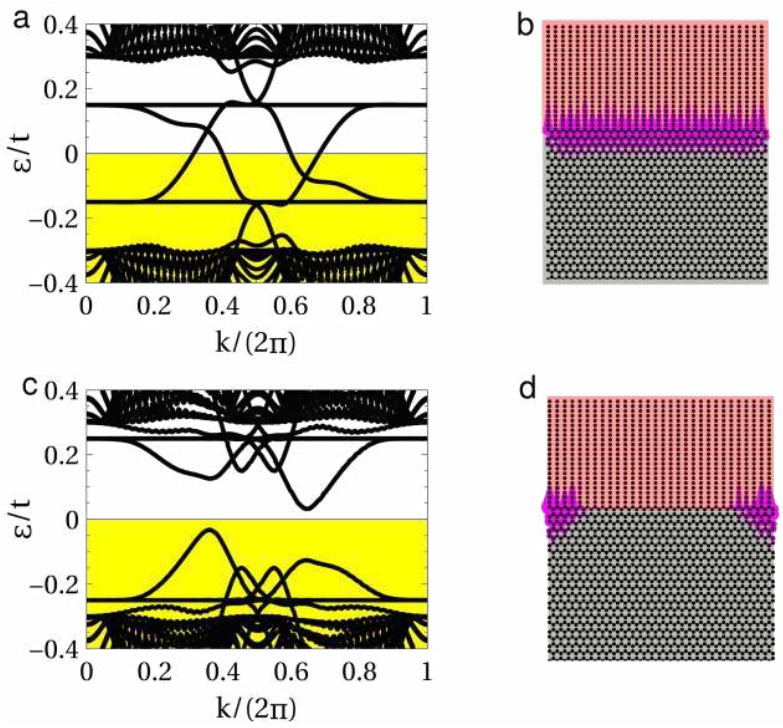

Figure 9.15: Band structure of the an interface between a square superconductor and an antiferromagnet (a) or canted antiferromagnet (c) honeycomb lattice. Figures (b) and (d) show the local density of states in a finite system, which correspond to gapless interface channels (without canting) (b) and Majorana states (with canting) (d)

symmetry class within the ten-fold way[436] for the infinite system is the 2D class D, and its topological invariant is $\mathcal{Z}$, which corresponds to the number of *chiral* edge states at a surface [437]. Within this language the helical SC contact has a trivial (zero) $\mathcal{Z}$ invariant, since the number of right minus left propagating modes is zero. This is actually the reason why crossing the $\theta = \theta_{\text{ins}}$ destroys the helical edge states without an intervening bulk-gap inversion. Therefore, the reason for the existence of helical states for $\theta > \theta_{\text{ins}}$ cannot be found in the standard homotopy classification. It is rather an instance of non-trivial *valley* Chern number.

If one computes the $\mathcal{Z}$ invariant in 2D of our system, both in the graphene side and on the superconductor side, one needs to integrate the Berry curvature of the Nambu bands. For the superconductor one obtains negligible Berry curvature for all momenta. However on the graphene side (and choosing the magnetic unit cell to compute the bands), one finds that while the integrated curvature is zero (hence $\mathcal{Z}$ is zero), it is the sum of two integer and opposite contributions from different valleys. For a specific spin sector (e.g. $|e\uparrow\rangle, |h\downarrow\rangle$), one valley has partial

integral 1 and the other -1. Therefore, assuming valley symmetry is preserved at the graphene/SC interface (that is $w = 0$ in the phase diagram of Fig. 9.6k, i.e. the contact is transparent), one can invoke a bulk-boundary correspondence principle for each of the two valleys and spin sectors independently, which yields two pairs of counter propagating (helical) states (one per valley and spin). If the contact is not transparent ($w > 0$) but intervalley scattering is below the threshold $w < w_{\rm ins}$, the helical states will split, but the contact will still be metallic (since the splitting is smaller than the energy where they cross). Hence the AF helical states are an instance of weak topology from the two valleys, just like e.g. the helical modes in works like Refs. [438, 439]. Note, however, that the mathematical standing of these arguments are less sound than the conventional ones from full-Brillouin-zone invariants, since to our knowledge there is no rigorous theorem that guarantees the existence of surface states from partially integrated (valley) Chern numbers.

9.6.6 Square-lattice superconductor

In section 9.6 we have considered the superconductor arising from electrons hopping in a honeycomb lattice and subjected to pairing potential. Nevertheless, the fact that the interface states persist even upon doping of the superconductor, suggests that their existence goes far beyond what our analytic argument might suggest. Actually, we here show that a honeycomb superconducting lattice is not mandatory, so that even an interface between a square superconductor will give rise to localized Majorana states.

To illustrate this, we show in Fig. 9.15 the band structure of an interface between the canted Quantum Hall antiferromagnet, and the local density of states for a finite system. In the case of fully collinear antiferromagnetism, the interface sustains a gapless channel. When the moments are canted, a topological gap in the inter-facial bands opens up and localized Majorana modes show up.

9.7 Majoranas in multilayer graphene

Previously, we have seen how Majorana bound states can appear at the interface between antiferromagnetic graphene and a superconductor. Pristine graphene is not antiferromagnet, only when the kinetic energy is quenched interactions overcome hopping and the system opens a gap. However, bilayer and trilayer graphene are able to become insulating in the absence of magnetic field. In the particular case of bilayer graphene in the AB configuration, the low energy electronic structure is not longer linear the momentum, but becomes quadratic. In the later, the interlayer hopping increases the density of states at the Fermi level, increasing the vulnerability of the system towards electronic order[328, 440]. The effect is even stronger in trilayer

graphene ABC, where the dispersion becomes cubic in the momentum, increasing even further the DOS at the Fermi energy[334, 332]. Signatures of such electronic order in multilayer graphene have been observed[332], and which has also been confirmed by first principles calculations[441].

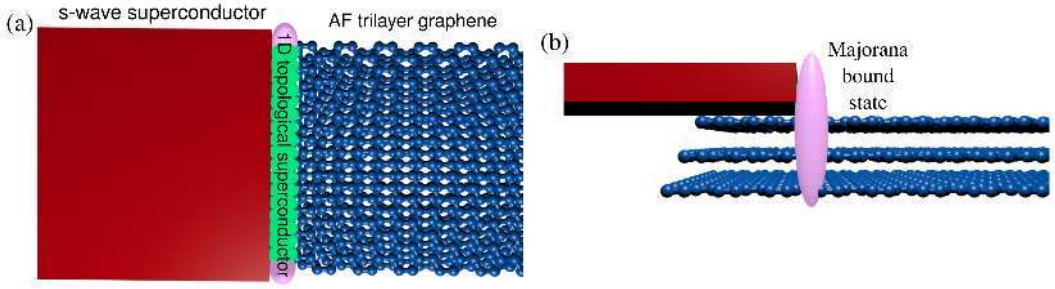

Figure 9.16: (a,b) Schemes of the heterostructure of trilayer graphene and conventional superconductor which gives rise to 1D interfacial topological superconductor.

The unconventional interfacial states between the honeycomb antiferromagnet and a superconductor also show up for the case of multilayer graphene as shown in Fig. 9.17, where it can be seen that there is small qualitative change between monolayer, bilayer and trilayer antiferromagnet. These interfacial states will be source of topological superconductivity in trilayer graphene. Trilayer graphene offers a very important advantage in comparison with the monolayer proposal: trilayer graphene is already antiferromagnetic, so that no magnetic field has to be applied to see interfacial states between the antiferromagnet and a superconductor. This is specially important due to the vulnerability of conventional superconductors to strong magnetic fields.

In the antiferromagnetic state, valley symmetry is broken by a magnetic flux, which can be tuned by a perpendicular magnetic field. The spin rotation symmetry left in the antiferromagnetic state is broken by magnetic canting of the moments in the two sublattices, which can be tuned by an in-plane field. Thus, all the remaining symmetries of the gapless interface branches are broken just by applying different magnetic fields off-plane and in-plane. In the case of monolayer graphene, the antiferromagnetic state only appears when the kinetic energy is quenched by a magnetic flux, however, bilayer and trilayer systems have been shown to develop an antiferromagnetic state even at zero field[328, 332].

The question of whether bilayer and trilayer systems will also be able to sustain Majorana modes can be answer in terms of an adiabatic argument. An antiferromagnetic monolayer sustain those modes, and thus has a non-trivial topological invariant $\nu = -1$ in the $\mathcal{Z}_2$ classification of 1D superconductors. An AF bilayer and trilayer systems can be built up by staking two and three AF monolayers, and turn-

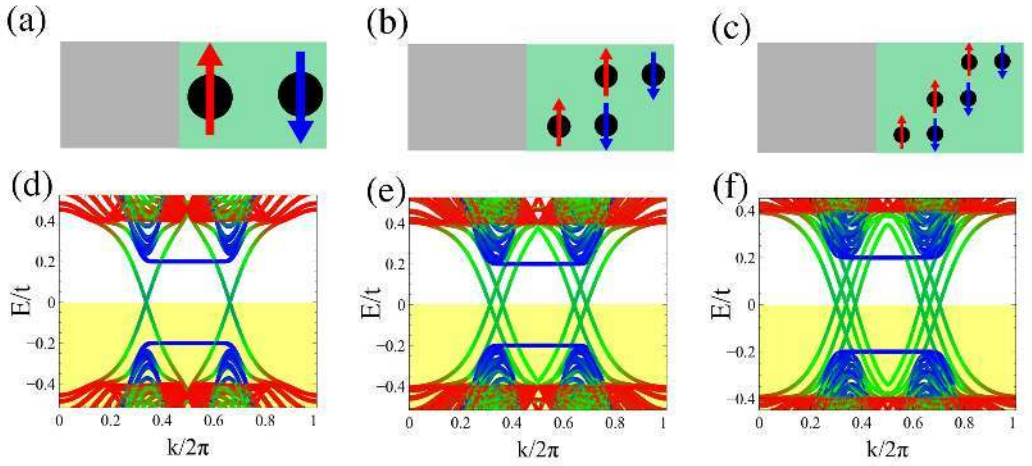

Figure 9.17: Sketch of hybrid ribbons of monolayer (a), bilayer (b) and trilayer (c) graphene. The interface between between the antiferromagnetic part and the superconducting part gives rise to gapless interfacial modes (d,e,f). Gapping out those modes opens up a topological gap for monolayer (d) and trilayer (f).

ing on interlayer interactions slowly until the true ground state is reached. Provided both the multilayer and interface gaps are not closed in the path, the topological invariant on the 1D superconductor will be $(-1)^n$, with n the number of layers. Thus trilayer graphene will sustain Majorana modes, whereas the bilayer will show a trivial gap. This automatically follows from the evolution shown in Fig. 9.18 and Fig. 9.19, and is the focus of the next section.

9.7.1 Adiabatic connection of bilayer and trilayer

Effect of interlayer coupling

As shown in Fig.9.17, the interlayer coupling does not destroy the interfacial states. Actually, when off-plane and inplane magnetic fields are turned on, the interfacial band become gapped (Fig. 9.18cde), which in the monolayer case is known to give rise to a 1d topological superconductor. In the case of multilayer systems, it observed that the gap remains open even when the interlayer coupling goes to zero Fig.9.18ab, and automatically proves that a N-layer is adiabatically connected to N decoupled monolayers. Therefore, trilayer graphene will also sustain an interfacial 1d topological superconductor, whereas bilayer will be trivial.

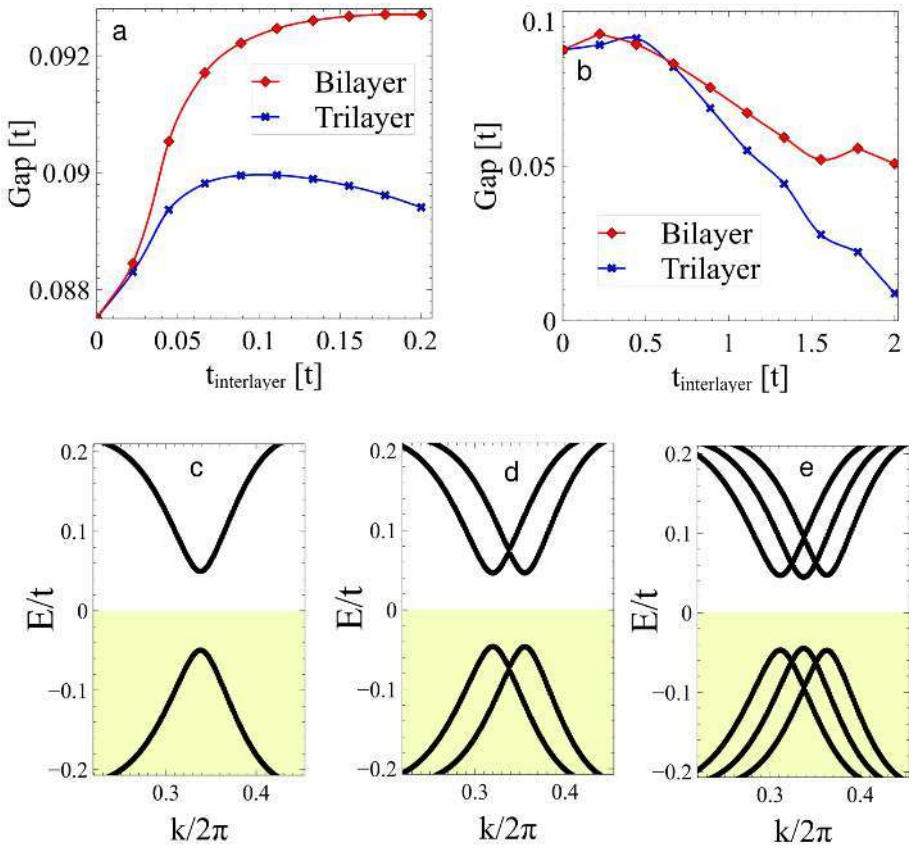

Figure 9.18: Evolution of the topological interfacial gap in bilayer and trilayer graphene as a function of the interlayer coupling, for small (a) and large (b) coupling. The topological gap is opened by the simultaneous application of off-plane and in-plane magnetic fields. The fact that the gap remains open as the interlayer coupling is switched on yields that the topological invariant can be calculated as $(-1)^n$, giving a trivial interface for bilayer and topological for trilayer. Band structures, zoomed on the interface states, for monolayer (c), bilayer (d) and trilayer (e), for $t_{interlayer} = 0.2$, showing a nearly equal interface gap

From bare AF to real multilayer moments

As a rough toy model, the antiferromagnetic state in the interlayer system was modeled as of uniform strength in analogy with the monolayer system, even when interlayer coupling was increased. nevertheless, interlayer coupling between atoms stacked one over others, magnetic moments are not expected to be uniform. To show that the actual magnitude of the magnetic moments is not critical, we show in Fig. 9.19 the evolution of the interfacial gap a function of the magnetic moment asymmetry. It is observed that the gap does not close, proving the adiabatic connection

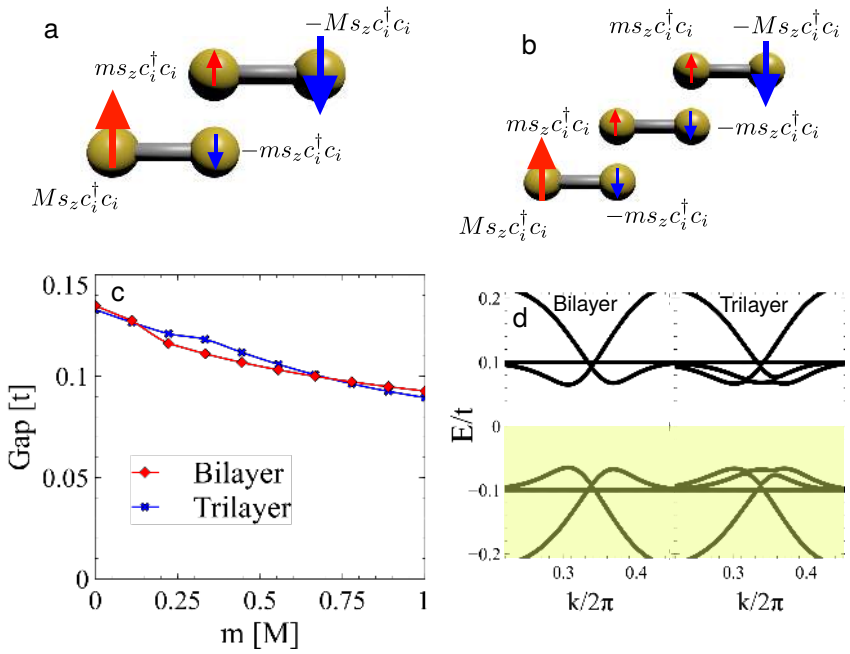

Figure 9.19: Scheme of the non-uniform magnetization in bilayer (a) and a toy trilayer (b) graphene due to interlayer coupling. (c) Evolution of the interfacial topological gap as the magnetization stagger magnetization in the coupled atoms increases from 0 to the decoupled limit. Band structures zoomed on the interface states for $m = 0$.

between uniform and non-uniform magnetic structures. Therefore, the topological character of the interface correspond to the one obtained with toy model, and does not rely on the specific details of the non-uniform magnetization.

9.7.2 Signature of Majorana states

Previously, we showed that monolayer and trilayer graphene would sustain Majorana bound states. In particular for trilayer, the AF state naturally shows up, and upon an application of a tilted magnetic field, which would break valley and spin rotation symmetry, will open up a topological gap. Therefore, Majorana states are expected to appear at the boundary between the AF, superconductor and vacuum.

Apart from usual spectroscopic techniques to observe the expected zero energy states, transport measurements also will give signatures of topological zero modes. Here we will consider two different situations. The first setup corresponds a setup in which there are present 2n Majorana modes, by connecting the AF to two hybrid leads. In the other setup, 3n modes appear, by connecting the AF to a SC lead and

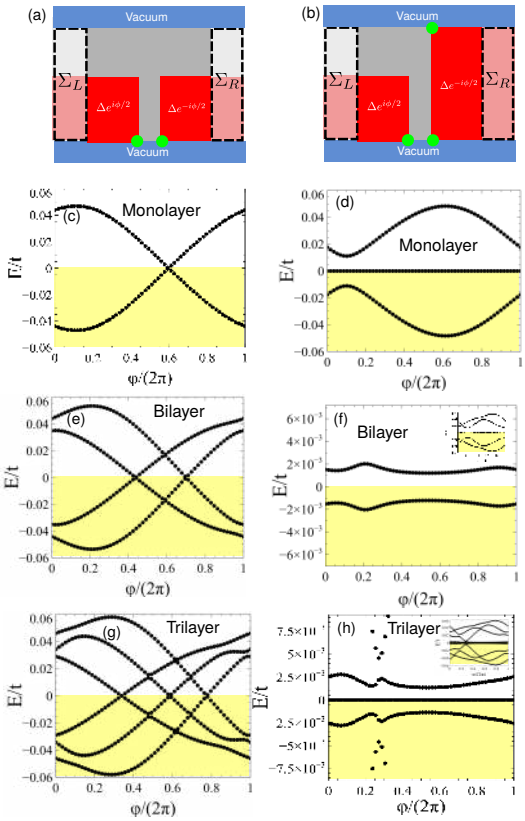

Figure 9.20: Scheme of an heterostructure sustaining $2 \times n$ (a) and $3 \times n$ Majorana bound states, where n is the number of graphene layers. The evolution of the eigenvalues of the central hamiltonian for the setup (a) are shown in (c,e,g) and for (b) in (d,f,h) for monolayer (c,d), bilayer (e,f) and trilayer (h,i) graphene. In the setup (a), all the evolution seem to show eigenvalue crossing. However setup (b) highlights that the monolayer (d) and trilayer (h) have protected zero energy modes, whereas for the bilayer (f) a small gap opens up. For the bilayer and trilayer systems, also a small electric field ($0.1t$) was included to break accidental degeneracies.

a hybrid AF-SC lead.

We calculate the spectrum of the central part by diagonalizing the low energy effective Hamiltonian of central device coupled to the two infinite leads

$$H_{eff} = H_C + \Sigma_R(E=0) + \Sigma_L(E=0) \tag{9.50}$$

where H_C is the Hamiltonian of the central device, and Σ_R, Σ_L the selfenergies induced by the right and left leads. It is important to note, that the previous Hamiltonian is not Hermitic, and therefore its eigenvalues are not guaranteed to

be real. However, for states within the lead gap, and provided the central part is long enough, the selfenergies are purely real yielding a Hermitic Hamiltonian. The low energy eigenvalues are therefore the Majorana energy modes bounded to the AF-SC-V interface.

We show in Fig.9.20 the evolution of the eigenvalues corresponding to the (splitted) Majorana modes as a function of the superconducting phase difference between the right and left leads. The simplest case is the monolayer, where when two Majorana are present Fig.9.20c a 4π effect arises, and when three are present (Fig.9.20 two of the hybridize whereas the other remains at zero energy. In the geometry with 2n Majorana modes, even in the case of bilayer, which is supposed to be trivial, the Majorana modes cut the zero energy, giving rise to a 4π effect, although not topologically protected. Moving to the setup with 3n states, in general, for an odd number of modes Figs.9.20g,h), states become splitted in pairs, leaving an unpaired state at exactly $E = 0$. In comparison, for the bilayer an even number of modes is present (Fig.9.20g), end they become splitted due to the of interlayer mixing.

9.7.3 Experimental realization in trilayer graphene

We move to the conditions which would lead to the experimental observation of Majorana bound states in trilayer graphene. As stated previously, trilayer graphene becomes an antiferromagnetic insulator in ultra clean samples. Emergence of gapless interfacial states between trilayer graphene and a superconductor will be immediate provided the contact is transparent enough. This compares with the case of monolayer graphene, where a strong off-plane field had to be introduced in the system.

On the other hand, the topological gap opening in the interfacial superconductor relies on the application of a magnetic field, also in trilayer graphene. Due to the large antiferromagnetic gap, the in-plane fields needed to tilt the magnetic moments might seem a bottle neck due to the vulnerability of superconductivity. However, since the magnetic field can be applied in-plane, two dimensional superconductors as $NbSe_2$ are the perfect candidates to act as superconductivity source, due to their resilience towards in-plane magnetic field due to spin momentum locking in the Fermi surface.

Moreover, the antiferromagnetic state of the trilayer is expected to be locally depleted due to charge transfer effects. Therefore, the decreasing of the order parameter will allow to tilt the weaker magnetic moments by applying smaller fields. In addition, if the superconductor is deposited on top of the trilayer, the charge transfer will also create an layer imbalance, which also depletes the magnetic moment. This last feature can be tuned by means of a gate voltage on the superconducting dichalcogenides, yielding a powerful tunability of the local order parameter.

9.8 Summary

Majorana bound states require that the superconducting electronic state looses all the possible degeneracies, in particular spin symmetry. For the case of graphene, the addition valley degeneracy might seem that the task of getting Majorana bound states is even tougher. Here we have shown that actually this is not the case, and that the electronic structure of graphene is actually an advantage.

On one hand, we have shown that the very peculiar Landau level structure of graphene allows to create a quantum spin Hall state without any kind of spin orbit coupling. The helical edge states associated with this phase allow to create an effective one dimensional topological superconductor when superconducting pairing is induced by a neighboring superconductor. Experimentally, the quantum spin Hall state is associated with a ferromagnetic order, which has been realized by application of an additional in-plane fields.

On the other hand, we showed that a different mechanism based on solitonic electron-hole states between a honeycomb antiferromagnet and a superconductor can be exploited. Those interfacial states, when gapped out by magnetic tilting and orbital field also give rise to a one dimensional topological superconductor, with the associated Majorana bound states. The previous model is exactly realized in graphene over magnetic field, where the orbital field quenches angular momentum and induces an anti-ferromagnetically ordered quantum Hall state. Importantly, the ways to get Majorana bound states are adiabatically connected, giving rise to a whole family of intermediate state realizing 1D topological superconductivity.

The topological honeycomb antiferromagnet-superconductor interfacial states can be also further to give rise to 1D topological superconductors. Those states are not unique of the monolayer honeycomb, but also arise in bilayer and trilayer systems, enlarging the zoo of possibilities. In particular, trilayer graphene is an antiferromagnet at zero field, with an order tunable by a perpendicular electric field, which upon magnetic field would also sustain Majorana bound states when interfaced with a superconductor. Moreover, honeycomb antiferromagnetic structures are realized also in several oxides, allowing to use this interfacial states to create Majorana bound states in heterostructures.

Chapter 10

Beyond graphene

Graphene is a very appealing material from the theoretical point of view: it can be treated with a simple model and shows very unconventional electronic properties. In this chapter we will use a combination of density functional theory methods, Wannierization and tight binding calculations. By doing so, we will explore the electronic properties for materials with complex electronic structure, in the same fashion as we did for graphene. This method will be specially useful when the low energy model for the material is unknown, giving us a systematic methodology to study complex materials.

10.1 Introduction

Graphene has been the main character of our story so far. The Dirac-like spectrum has been one of the main responsible of the unconventional electronic properties shown. An interesting feature is that systems with honeycomb-like lattices present electronic properties that can be understood with modified versions of the graphene Hamiltonian: either adding more orbitals or including spin-orbit coupling. The simplest example is boron nitride, whose low energy model can be understood as two massive Dirac equations[442], which naturally arise in a tight binding model with sublattice imbalance.

The first group of materials consist on the different two dimensional materials[443, 444, 75, 445, 446, 447, 448, 449, 450, 451, 452, 453], whose bulk structures consist on layers bonded by van der Waals interactions. Among these systems are found the different types of dichalcogenides [75, 445], black phosphorus[446] or boron nitride[454].

The second type of systems, whose relation at first seems less trivial, consist on oxide multilayers. These systems are based on bulk structures made of transition metal atoms surrounded by an oxygen environment. The active orbitals at low

energies are usually hybrids between the d-orbitals of the transition metal atom and the oxygen p-orbitals. Close to the Fermi energy, the electronic structure can be understood in terms of these orbitals, siting in a lattice defined by the positions of the transition metal atoms. The clear advantage of these systems is that provided the transition metal atoms can be heavy elements, the spin orbit coupling effect can be much stronger than in graphene based materials.

10.2 Computational methods to describe 2D materials

The study of general two dimensional materials usually requires ab initio method due to the complex electronic structure that they develop. In comparison with graphene where the effective orbitals are simple p_z orbitals, systems like MoS_2 posses a low energy structure which involves combinations of orbitals from Mo and S in a rather non-trivial way[455]. Therefore, ab initio calculations are the most suitable way to get insight on the low energy properties of these systems.

Bulk properties of two dimensional materials are successfully described by density functional theory methods. However, when dealing with finite size effects DFT encounters a barrier. Ab initio modeling usually scales cubic with the number of atoms, and although pseudopotential codes allow to study systems up to 100 atoms in a normal computational cluster, this number is too small for actual systems. An even worse situation is for the study of quantum Hall effect, where the gauge potential forbids to use periodic boundary conditions for an arbitrary magnetic field. In this last situation, tight binding modeling is way more convenient tool, but with it has the obstacle that the electronic structure is too complex to have a simple tight binding Hamiltonian.

However, a tight binding model can be obtained systematically from a DFT calculation[456]. The method is known as Wannierization, and it relies on gauge transformation of the Bloch wavefunctions, to go from a dellocalized basis into a local basis, suitable for tight binding modeling. In the Wannier basis, the Hamiltonian is local, i.e. presents only hopping to closest neighbors in the following way

$$H = \sum_{ij} t_{ij} c_j^\dagger c_i \tag{10.1}$$

where t_{ij} is the hopping from the orbital i to the orbital j and c_i destroys an electron in the site i. In the following, our workflow will consist on calculating the electronic structure of the desired material using the open source Quantum Espresso package[240], together with the also open source Wannier90 package [457] to perform the Wannierization procedure. In addition, we will compare the results obtained by

adding atomic spin-orbit coupling to the tight binding models with the ab initio results got with the open source all-electron code Elk [241, 458].

With the previous Hamiltonian obtained from the DFT electronic structure, orbital magnetic fields can be introduced by means of the Peierls substitution

$$t_{ij} \to t_{ij} e^{i\phi_{ij}} \tag{10.2}$$

where ϕ_{ij} is the Peierls phase between the Wannier centers of the Wannier functions i and j

$$\phi_{ij} = B \frac{e(x_i - x_j)(y_i + y_j)}{2\hbar} \tag{10.3}$$

With the previous formalism, quantum Hall effect can be systematically studied in any two dimensional system, provided the Wannier Hamiltonian is obtained from the electronic structure of the density functional calculation.

Finally, it is worth to note that the Wannier basis also allows to introduce spin-orbit coupling effects[459]. Close to the core, usually the Wannier functions are atomic-like. It is precisely in the cores where the spin-orbit coupling is maximal. Therefore, by identifying which Wannier functions are located in which atom, the SOC can be introduced as

$$H_{SOC} = \lambda_{SOC} \sum \vec{l} \cdot \vec{s} c^{\dagger}_{j,s} c_{i,s'} \tag{10.4}$$

where the sum runs over pairs of orbitals located in the same atom, and $\vec{l}$ is the atomic angular momentum operator.

10.2.1 Wannier modeling for MoS_2

The first system that we will study is MoS_2. This monolayer was first obtained by mechanical exfoliation[460], has three atoms per unit cell, with an underlying triangular lattice. Large scale synthesis has been achieved[445], and it has shown a powerful potential in electronic and spintronics applications.[75] Its electronic structure has also been widely studied [455, 461, 462, 463]. It shows a similar electronic structure as the isostructural XY_2, where X can be Mo,W and Y S,Se,Te[464, 465]. Several effective model have been suggested for this system [466, 467, 468, 469] . Here we will show how the systematic Wannier procedure allows to reproduce many of the well known results of MoS_2.

The calculation is performed by projecting the electronic wavefunction onto 11 Wannier states, the 3 p orbitals of S, and the 5 d orbitals of Mo.

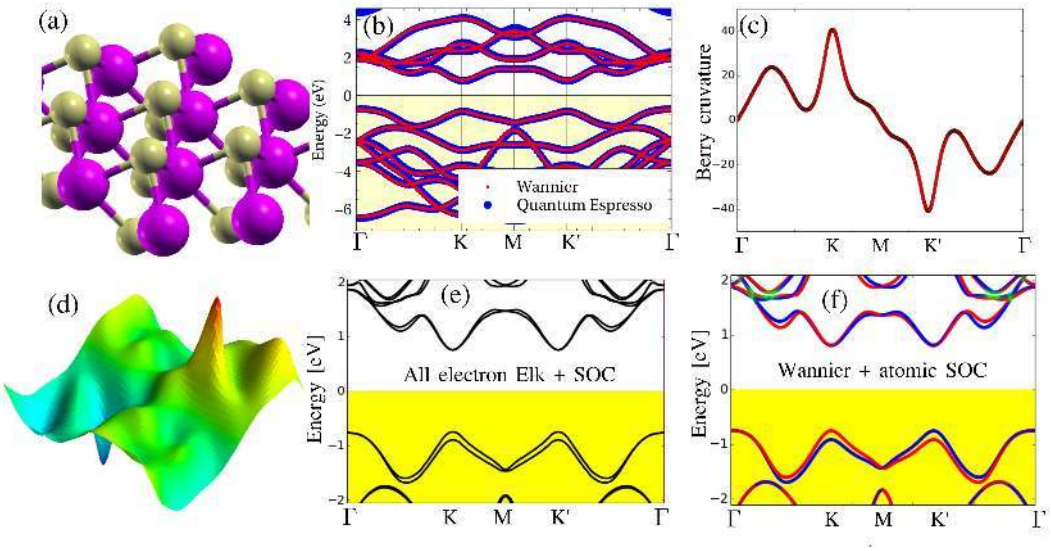

Figure 10.1: Structure of MoS_2. Comparison of the band structure of MoS_2 between DFT and Wannier (b). Berry curvature (c) along the reciprocal space path, showing a large contribution in the two valleys. Plot of the Berry curvature in the 2D Brillouin zone (d). The Berry curvature is calculated taking into account the contribution of all the occupied bands. Band structure with spin-orbit coupling calculated with Elk (e), and Wannier band structure adding atomic SOC (f) to the Mo d orbitals (100 meV).

Bulk electronic structure

MoS_2 is a semiconductor, with a gap located in the K and K' points of the Brillouin zone. The low energy properties of the system are governed by electrons located in K and K'. In Fig. 10.1 we show the comparison between ab initio band electronic structure calculations and the Wannier results. The Wannier Hamiltonian gives a good fit in comparison with Quantum Espresso PAW calculations. With the tight binding Hamiltonian, the Berry curvature is easily calculated, giving a large contribution in the two valleys. Introducing atomic spin orbit coupling in the Wannier Hamiltonian leads to a band structure developing the well know spin-valley splitting, and resembles the ab initio result obtained with all-electron Elk calculations with SOC.

Quantum Hall effect

In the presence of magnetic field, MoS_2 develops a set of Landau level. In the following we will ignore the spin degree of freedom and we will focus our discussion on the conduction band. Although the parabolic dispersion in the conduction might

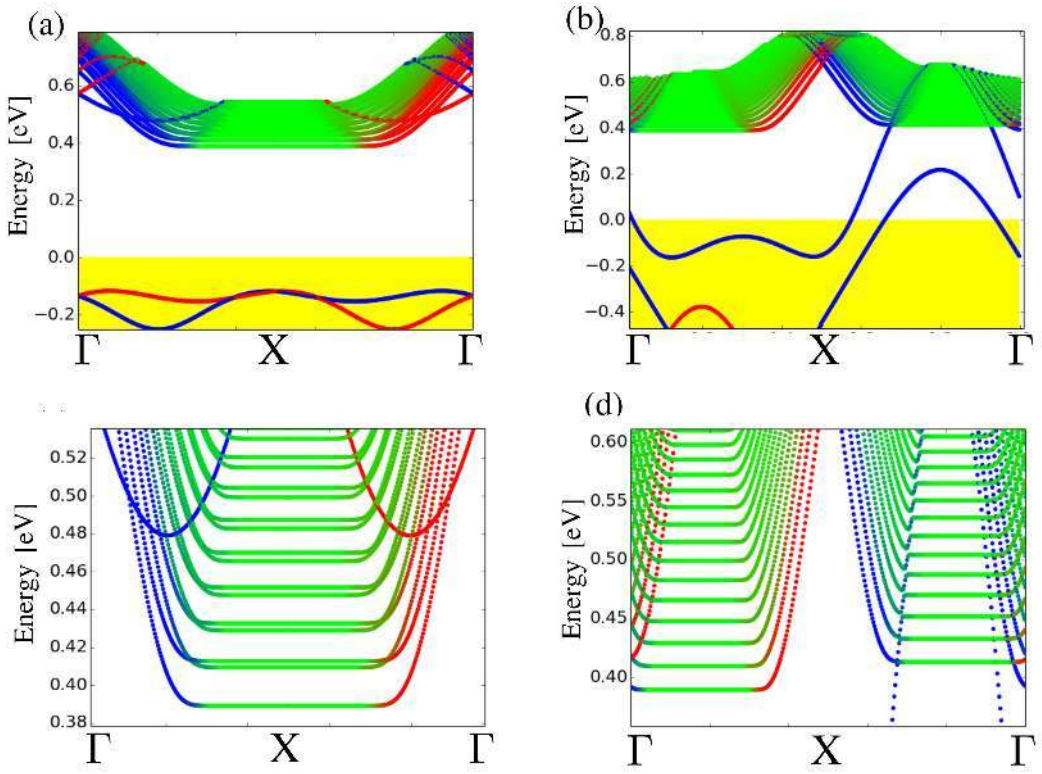

Figure 10.2: Band structure of an armchair (a,c) and zigzag (b,d) quantum Hall bar of MoS_2. Panels (a,b) show a wide window of the spectrum, whereas (c,d) show a zoom into the valence band. As shown in panel (c), the Landau level spectra is no longer degenerate for $n > 1$. The valley character of each LL can be seen in the zigzag ribbon (d). The color of the eigenvalues represent the position of the wavefunction: red for upper edge, blue for lower edge and green for bulk.

suggest a conventional Landau spectra, the quantum Hall effect in MoS_2 is far from a conventional 2D gas. In particular, only one valley has a lowest LL similar as would be in boron nitride and follows from a massive Dirac equation.

In the case of massive honeycomb lattice the LL have double degeneracy for $n > 0$, which can be understood as a perfect compensation between the valley dependent orbital angular momentum and an increasing on the Landau index. However, such compensation no longer holds for the extended Berry curvature of MoS_2, so that the LL which where degenerate in the massive honeycomb lattice, are no longer degenerate in MoS_2 [470, 471, 472]. This can be easily observed by calculating the band structure of a quantum Hall bar using the Wannier Hamiltonian as shown in Fig.10.2. Finally is worth to note that by considering SOC, additional spin splitting will take place. The spin splitting will be most important in the valence band, where

a spin polarized quantum Hall state appears at low hole filling.

10.2.2 Wannier modeling of black phosphorus

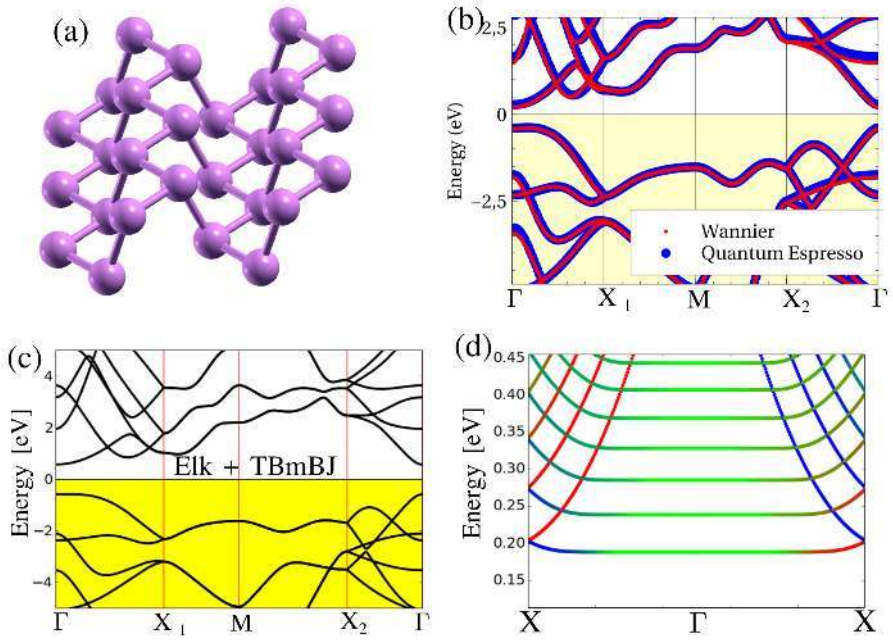

Figure 10.3: Crystal structure of black phosphorus (a) and comparison of the band structures obtained with DFT and Wannier (b). Band structure obtained with the Tran Blaha potential (c), showing a similar band dispersion but greater band gap. Landau levels in the conduction band, obtained by creating a quantum Hall bar with the Wannier Hamiltonian.

Monolayer black phosphorus[446] is another 2d material. It is a semiconductor with a band gap on the order of 1.5 eV[473, 474] and a structure that resembles a distorted honeycomb lattice. The band gap of black phosphorus is largely underestimated by conventional DFT methods, but the band dispersion is well captures when compared with the results obtained with the Tran-Blaha meta-GGA potential[475] (Fig. 10.3b,c). Black phosphorus has a highly anisotropic electronic structure due to the nearly one dimensional arrangement of the P atoms. This highly anisotropic behavior is easily seen in the top of the valences band, where the dispersion along $\Gamma - X_1$ is completely different and nearly flat compared with $\Gamma - X_2$.

In the presence of magnetic field, the Landau level spectra resembles the one of a conventional 2D electron gas [476, 477]. Using the Wannier Hamiltonian obtained

from the DFT calculation, a quantum Hall bar can easily be created, whose band structure in shown in 10.3d

10.2.3 Wannier modeling of bismuth

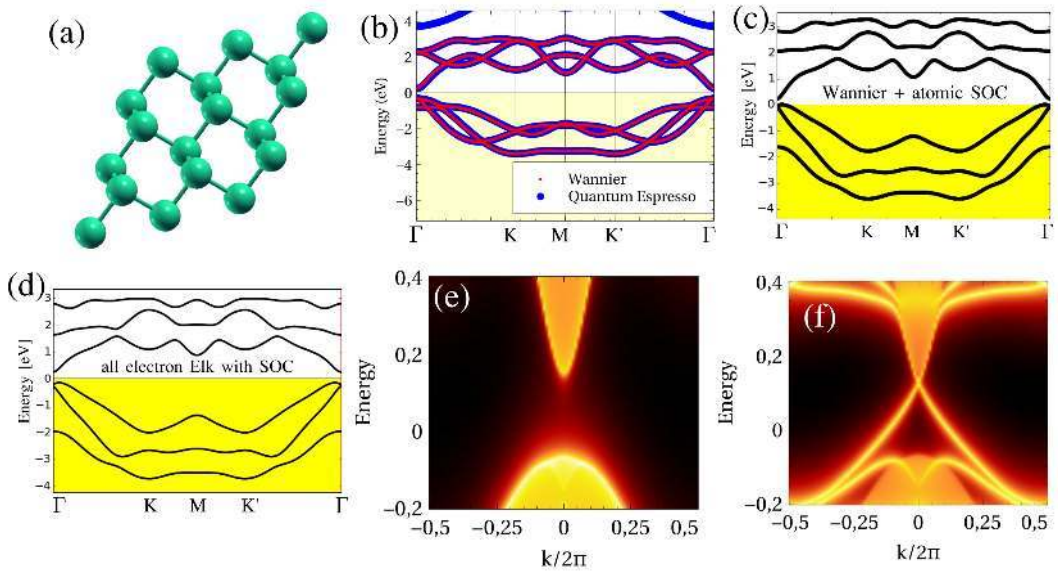

Figure 10.4: Structure of hexagonal bismuth (a), forming a buckled honeycomb lattice. Comparison of the band structure obtained with Quantum Espresso and Wannier (b). Panel (c) Shows the Wannier band structure after introduction of SOC, and (d) the band structure obtained from an SCF calculation with Elk with SOC. The introduction of SOC creates a band inversion, driving the system into a topologically insulating phase with a bulk gap (e) and gapless edge states (f).

The next two dimensional material that we will study is a monolayer of hexagonal bismuth. Bismuth (111) thin films is known for being a topological insulator[478, 479], opening a large band gap. The structure of bismuth is an hexagonal buckled honeycomb lattice, similar to silicene and germanene.

To model the effect of SOC in bismuth, we will obtain a Wannier tight binding model from a non-magnetic calculation without SOC. Afterwards, SOC will be included in the Wannier Hamiltonian, and we compare the results with a selfconsistent DFT calculation with SOC using Elk. In the absence of spin orbit coupling (Fig. 10.4b), bismuth has a bulk gap. When spin orbit coupling is included, the bulk gap closes and reopens, yielding a topological insulating state (Fig.10.4c,d,e,f).

10.3 Oxide multilayers

The other type of systems that we will deal with are oxide multilayers. Although they might seem physically very different, band engineering in this systems allows to easily create topological insulating phases. In systems based on the perovskite structure, transition metal atoms are surrounded by an octahedral crystal environment, that splits the d levels into e_g and t_{2g} manifolds. In this situation, depending on the filling, crystal field and strength of spin orbit coupling, different topological phases can arise.

Here we will focus in a particular unexplored structure, whose parent compound is $InCu_{2/3}V_{1/3}O_3$[480, 481]. This compound show a low energy electronic structures dominated by the dz^2 orbitals of Cu. Furthermore, the Cu atoms form two coupled honeycomb lattices, and its band structure resembles the one of AA graphene. The system shows an antiferromagnetic electronic order [481] due to the small bandwidth and strong interactions in Cu.

In the following, we will focus on an heterostructure of this crystal, where one Cu layer is substituted by Zn, becoming that layer insulating. In this situation, the low energy structure will be dominated by the d_z^2 orbitals of Cu. The combination of antiferromagnetism and SOC will be then used to engineer a 1D topological superconductor in a fashion similar to the Quantum Hall graphene. Finally, upon substitution of Cu by Ag, the system will become non magnetic, and it will be shown that it develops a topological gap.

10.3.1 Majorana bound states in oxides

As shown in the graphene Majoranas section, an interface between a honeycomb antiferromagnet with a conventional superconductor gives rise to an interfacial gapless superconductor. Such gapless superconductor can be topologically gapped by introducing certain perturbation. In the case of graphene, these perturbation was the orbital magnetic field and the canted order.

Here will focus on the structure derived from $In_6Cu_4V_2O_6$, where one Cu atom is substituted by Zn yielding $In_6Cu_2Zn_2V_2O_6$ (Fig. 10.5a), whose low energy properties are dominated by dz^2 orbitals forming a slightly distorted honeycomb lattice. The low energy band structure resembles the one of graphene (Fig. 10.5c), and in the low energy dz^2 manifold, spin orbit coupling can be modeled by the Kane Mele model. In the following, we will assume that the electronic structure of these compound can be modeled by the Hubbard-Kane Mele model. Interactions will turn the system honeycomb antiferromagnetic, so that if it is interfaced with another oxide which is superconducting, a one dimensional gapless superconductor will appear at the boundary.

In the hybrid AF-SC system, spin-orbit coupling will have two effects. The first

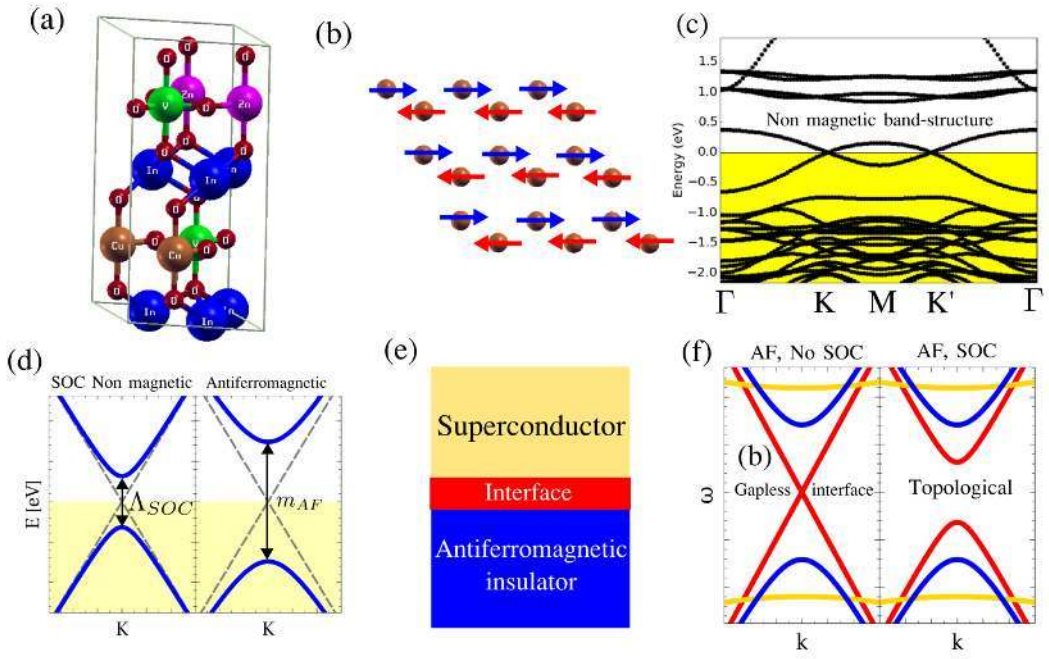

Figure 10.5: Unit cell of $In_6Cu_2Zn_2V_2O_6$ (a), where the Cu atoms form a honeycomb lattice with antiferromagnetic order (b). The ab initio non-magnetic band structure resembles the one of graphene (c). Sketch showing the interplay between SOC and AF, that opens two different gaps in the bulk band structure (d). Such interplay yields that when the honeycomb lattice in the in-plane AF state is interfaced with a superconductor (e), a topological gap can open up (f).

one is to give a preferential axis for the magnetic moment, which for the Kane-Mele-Hubbard model is in-plane. The second effect is that SOC will create spin mixing of interfacial gapless superconducting states, opening up a gap. The previous gap turns out to be topological (Fig. 10.5d), giving rise to localized Majorana bound states.

The previous argument can be easily checked by building a ribbon, where the upper half is a doped superconducting honeycomb lattice, whereas the lower part is an in-plane antiferromagnetic honeycomb lattice with Kane-Mele spin-orbit coupling. In the case of vanishing SOC, the interfacial states are gapless provided intervalley mixing is negligible (Fig. 10.6a). When SOC is turned on, a gap opens up (Fig. 10.6b). Calculation of the surface Green function shows that a pinned zero energy resonance appears (Fig. 10.6c) located in the surface of the flake (Fig.10.6d).

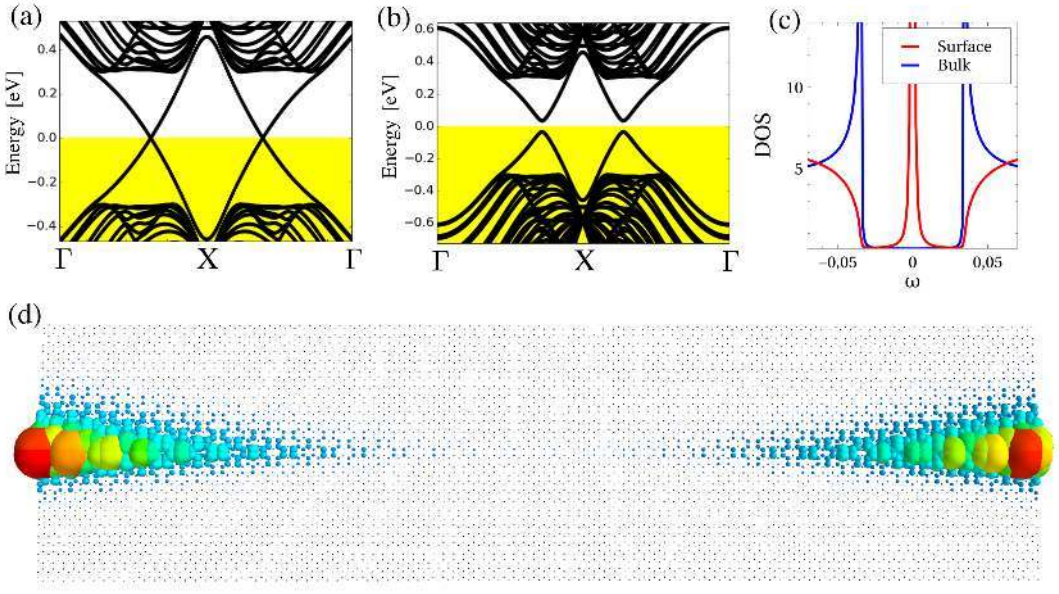

Figure 10.6: BdG band structure of an interface of an AF honeycomb ribbon and a doped superconducting honeycomb (a), and bands when SOC is introduced (b) opening up a topological gap. Spectral function in the bulk and surface (c), showing a zero energy peak in the surface. The spatial resolved spectral function for $\omega = 0$ shows that the zero energy peak is located certainly in the boundaries in the case o finite rectangular flake (d).

10.3.2 Quantum spin Hall effect in oxides

A more straightforward example of graphene like behavior in this system would be in the non-magnetic state, where spin orbit coupling is expected to open up a topological gap. In order to turn the system non-magnetic, we substitute in the previous multilayered Cu by Ag, yielding $In_6Ag_2Zn_2V_2O_6$. Such substitution, gives a bigger bandwidth and SOC while maintaining the electronic filling, turning the system non-magnetic according to our DFT calculations (Fig. 10.7b).

If the Kane-Mele model holds for this compound, this system will automatically be a topological insulator. To prove so, we follow the workflow of DFT calculation, then Wannierization and calculation of edge states, projecting onto the d orbitals of Ag (Fig. 10.7c). These will yield a 10x10 non-magnetic Hamiltonian, which is doubled after the introduction of SOC. The low energy Wannier bands correspond to the dz^2 Wannier orbitals, whereas the other states lie deep in energy. It is worth to note that the deep energy states are strongly mixed with other bands. The role of the deep energy states on the low energy structure is to induce an effective spin orbit coupling. Therefore, not capturing the exact deep energy dispersion is not a

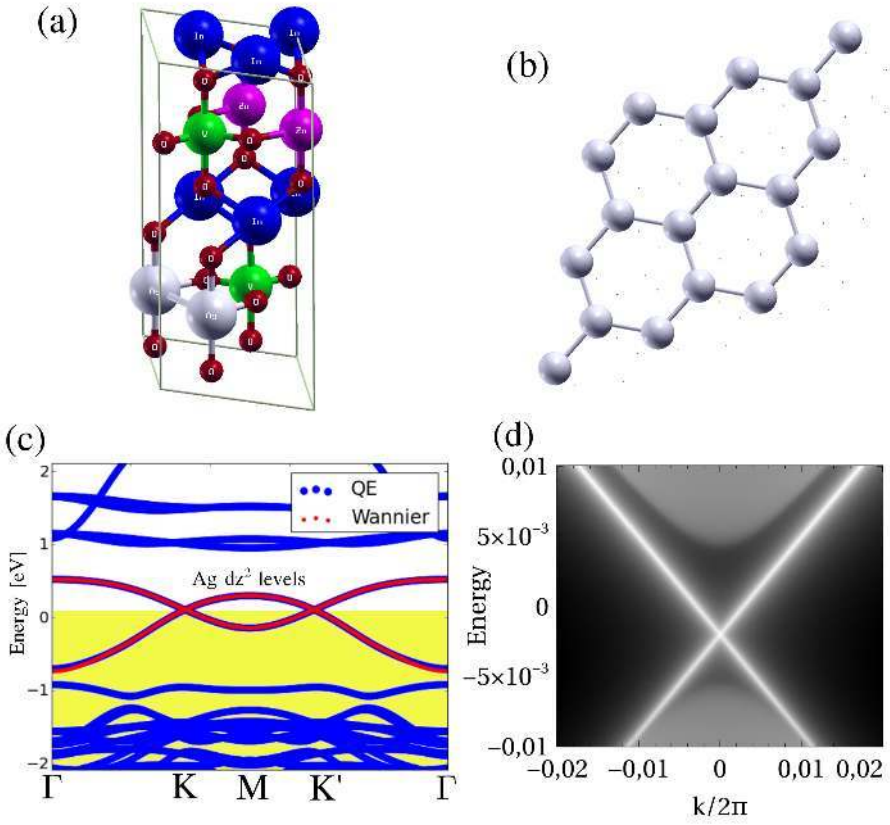

Figure 10.7: Unit cell of $In_6Ag_2Zn_2V_2O_6$ (a), where the Ag atoms form a honeycomb lattice (b). The low energy band structure is well captured with the Wannier Hamiltonian using d orbitals in Ag, where the one that crosses the Fermi energy has dz^2 character (c). Introduction of SOC opens up a topological gap, that gives rise to gapless edge states as calculated in a semiinfinite geometry with the Wannier Hamiltonian (d), following the recursive method of Section 11.4.

concern as long as the induced spin orbit coupling in the dz^2 is properly captured . With that in mind, the spinful Wannier Hamiltonian allows to calculate the Z_2 invariant[482] yields that the system is topological, which is confirmed by the surface spectral function in a semiinfinite geometry Fig 10.7d

The appearance of a topological insulating phase in a honeycomb oxide has been addressed in many other systems[483, 484, 485, 486, 487]. However, the present case differs in that the environment of the transition metal is not octahedral, and the low energy band structure is unexpectedly clean at low energy.

10.4 Summary

The success of graphene can be understood as the combination of unconventional electronic properties, and the ease to be synthesized and manipulated. Focusing on the electronic properties, another different materials where predicted to show Dirac fermions. On the side of versatility and ease, new families of two dimensional materials are showing up, boosting the potential interplay that could give rise to.

In this chapter we applied the Wannierization technique to connect between the first principles electronic structure of these materials and the tight binding models that allow to study mesoscopic systems. We have shown the electronic spectra of dichalcogenides in the quantum Hall regime, edge states of topological insulators with complex electronic structure and even Majorana bound states in oxides.

The powerful multi-scale playground of Wannierization builds a bridge between the mesoscopic techniques that allow to predict topological states of matter, with the powerful ab initio techniques that successfully predict the properties of complex materials.

Chapter 11

The embedding method

In principle, solving the Schrodinger equation would allow to know all the electronic properties of any system. While the solution for a single atom can be performed either analytically, (for the hydrogen atom) or numerically (for any atom), the task becomes more and more complex as the number of atoms considered increases. But real systems usually have a really large amount of atoms. Lets assume that we would like to perform a calculation in a normal laptop. Using tight binding models we would be able to study between 1000 and 10000 atoms in some minutes. If we move on to complex system with complicated electronic structure, we could treat between 10 and 40 atoms in some minutes, depending on the formalism. But real systems are way larger that those numbers, if we want to see a meaningful result in an acceptable amount of time, brute force calculation is out of the game. And even more, if we want to know about the bulk properties of the system, the size needed can be even worse than unacceptable to work with.

Bloch's theorem provided an elegant solution to this big system size problem. It is simple application of a basic mathematical relationship in linear algebra that tells you that if you have an operator that commutes with your Hamiltonian, you can arrange the eigenstates in a set of wavefunctions which are simultaneously eigenstates of the Hamiltonian and of the symmetry. In particular, for periodic systems, it translates into the fact that you only have to consider the basic unit cell, and the different eigenstates are generated by changing the Bloch phase. This basic mathematical fact was one of the cornerstones of any calculation in infinitely large systems, as long as they were perfect.

But what happens if your system is incredibly large, and in has some finite region which has some defects. You cannot do brute force calculations, they are too expensive. You cannot also apply Bloch's theorem either, since there is no translational invariance. The problem looks frustrating, and maybe complex, but it analogous to having a delta potential in an infinite space: this is a problem we can solve trivially, analytically. By scattering theory the local spectra can be

easily calculated. But it seems that those tricks are hard to implement numerically. However, there is a way to study individual impurities in infinite pristine systems, which is the actual topic of these chapter. And by impurities it doesn't mean that it has to be a single atom, it means that the region of the space where the the perturbation exists is bounded. The main advantage of this technique is that it allows to get the properties of a system with an infinite amount of atoms, without translational invariant, at the prize that grows as the third power of the number of states in the defective region.

In the following we present an efficient method to calculate the electronic properties of a defective region inside an otherwise perfect two dimensional crystal. The method relies on the partition of the system in two parts, a central region that hosts the defect, and the infinite crystal with a missing patch that accommodates the central region. The effect of the infinite crystal on the central region can is expressed in terms of a self-energy. We present a straightforward expression of this self-energy and, more important, a very efficient numerical method to to compute it. The method can be applied to any material, regardless of the geometry or chemical composition, provided that a tight-binding representation of the Hamiltonian is available. We apply the method to a variety of defects in two dimensional materials and models, such as vacancies in the honeycomb lattice and the Kane Mele model, chemisorbed hydrogen in graphene described with a 4 orbital tight-binding model, a missing skyrmion in a skyrmion lattice coupled to graphene, a vacancy in graphene in the Quantum Hall regime, etc.

11.1 Motivation

Atomic scale defects are unavoidably present in crystals. They affect both the mechanical and electronic properties of materials, to the point that it is often said that crystals are like people: it is their defects that makes them interesting. The entire field of semiconductor electronics is based on the concept of doping, the controlled introduction of defects in otherwise pure crystals. In addition, the amazing progress in atomic scale engineering permits to use individual point defects in solids to achieve functionality[488]. This is the case of NV centers in diamond[489], acting as magnetic sensors, and phosphorous donor in Silicon[490], acting as a spin qbits. Two dimensional materials are not different, they host point defects[491] that also determine their properties, and given their surface nature, they can also be functionalized with atoms and molecules[492] some case, such as chemisorbed atomic hydrogen in graphene, have spin properties analogous to single-dopant spin qubits in silicon.

Numerical solution of the Schrodinger equation, at the independent electron level, is routinely done in finite size systems, such as atoms or molecules, or in

infinite systems such as crystals, where symmetry permits to block-diagonalize the problem. In contrast, the solution of the Schrodinger equation for defects in crystals, or atoms and molecules deposited at the surface of crystals, requires some additional ingenuity. Very often, the problem is tackled by brute force, computing a supercell that contains a single defect/atom/molecule. However, unless a very large cell can be simulated, finite size effects can lead to incorrect results.

It would be therefore desirable to have a method to address the single defect problem embedded in a crystal, rather than the alternative problem of a super crystal of defects. Formally, given a small system A coupled to an infinite system B, it is always possible to write down the Green function $\mathcal{G}_A$ where the effect of B is included as a self-energy Σ_B , where both $\mathcal{G}_A$ and Σ_B are matrices of the same dimension than the Hilbert space describing A, and are thereby suitable for numerical computations.

There is a general class of problems in which the calculation of Σ_B is routinely done. Whenever whenever the system B is the surface of a semi-infinite crystal and A is only coupled to the surface. In that case it is possible to obtain the self energy matrix as $\Sigma_B(A, A') = V_{AB} g_{B,B'} V_{B',A'}$ where V is the matrix that describes the coupling between the system A and $g_{B,B'}$ is the surface green function of B. Since the computation of surface green functions of semi-infinite crystals can be efficiently done using recursive methods, this makes it possible to obtain the self energy and the Green function of the small system[493].. This approach is the basis for an astonishingly large number of problems in condensed matter, including quantum transport through quantum dots, molecules and nanocontacts. Essential in this approach is the fact that the Hamiltonian of B has to be written down as a tridiagonal matrix that permits the evaluation of the surface Green function $g_{B,B'}$.

The problem comes when the local system A is embedded in a crystal, rather than lying on a surface. Typical examples of this would be a vacancy or a substitutional defect, but many other possibilities will be considered as well below. In those instances the geometry of B lacks of an obvious translational symmetry that permits to implement the recursion method.

Here we propose a method that permits to compute the self-energy of system B in the general class of situations depicted in the figure 11.1b. Whereas we focus on 2D materials, it must be said that the approach described here could be also applied for 3D materials as well. The rest of the chapter is organized as follows. First we present the simple theory that permits to compute the self-energy Σ_B for the Green function G_A. Afterwards, we discuss efficient numerical approach to dramatically speed up the computation of Σ_B. Finally we apply the method to a variety of point defects in two dimensional crystals, reproducing well known existing results in the literature and to producing new ones.

11.2 Green function approach and self-energy

11.2.1 Statement of the problem

The system of interest is a tight-binding model that describes two regions, A and B. The region A has a finite number of sites, N_A, and the region B is infinite and has the following property: is two dimensional crystal that embeds region A. In the following we assume that the system A is described by single-particle basis i that labels a given site in the lattice, and in the case of multi-orbital tigth-binding model, it also encodes the atomic orbital. Spin indexes are omitted. If there is no spin-orbit coupling and no spin-dependent potentials, the spin is a dummy variable. Otherwise, we assume that i also encodes the spin degree of freedom.

The goal is to compute the Green function associated to the central region A. For that matter, our starting point is the standard equation

$$G_0 = (E - h_0 - \Sigma)^{-1} \tag{11.1}$$

where h_0 is the Hamiltonian of region A, and Σ is the self-energy associated to the coupling of A to B.

11.2.2 The self-energy trick

The critical remark lies on the fact that *, the self-energy Σ_B does not depend on whatever lies in the central region A*. We take advantage of this to obtain an expression in the simplest case where A is not an impurity and, taken altogether with B, form an ideal crystal, whose electronic structure can be readily computed, taking advantage of crystal symmetry and Bloch theorem. In this particular instance we can denote the Green function, projected in the central region, as $\mathcal{G}_A^0$, and write it down as:

$$G_0 = \frac{1}{(2\pi)^2} \int (E - H(k))^{-1} d^2k \tag{11.2}$$

where $H(k)$ is the Bloch Hamiltonian

$$H(k) = h_0 + \sum e^{i\vec{k}\cdot\vec{R}} t_{\vec{R}} \tag{11.3}$$

with h_0 the intracell matrix in the region A and $t_{\vec{R}}$ the hopping to the unit cell in the direction $\vec{R}$

From equations eq. (11.1) we write obtain a closed expression for $\Sigma_B(i,j)$:

$$\Sigma = E - h_0 - \left(\frac{1}{(2\pi)^2} \int (E - H(k))^{-1} d^2k \right)^{-1} \tag{11.4}$$

In this simplest case equation (11.4) can be readily computed because G_0 can be obtained by from eq. (11.2) by numerical integration over the Brillouin zone, and efficient methods to do so are presented below. Once we are done with the calculation of $\Sigma_B(i,j)$ in the trivial case where A and B form an ideal crystal, *we can use* Σ *as a self-energy for any other Hamiltonian* $\mathcal{H}_A$ *that describes a defect, as given in equation (11.1).*

11.3 Efficient computational approach to compute the self-energy

The most computationally demanding part of the calculation is the is the integration over k for the calculation of G_0. Although for small unit cells the integration can be performed, for bigger Hamiltonians the integration can be beyond an acceptable computation time. The main reason is that the mesh used has to be very dense, on the order of 500x500 k-points for a normal 2D system. In the following, we propose an efficient method to accelerate dramatically the calculation of eq. (11.2). It must be noted that for a system A with a Hilbert space of dimension $\mathcal{N}_A$, the Green function G_A has $\mathcal{N}_A^2$ entries for every value of the argument ω. Whenever we are interested in computing integrated quantities, such as the charge in a given atom or orbital, we need to integrate over ω. Thus, numerical efficiency is essential for the success of the embedding approach.

11.4 Calculation of G_P

The calculation of G_D can be performed by brute force by summing over the different k's.

$$G_P = \sum_k (E - h_k)^{-1} \tag{11.5}$$

The brute force approach has the problem that a super fine mesh in reciprocal space has to performed in order to achieve a good convergence, on the order of 300x300 kpoints. This is particularly important in cases of pathological Fermi surfaces as semimetals.

However, for a two dimensional system, a much more efficient technique can be used to calculate this Green function. The key point is to remind that in a two dimensional Brillouin zone, a line in reciprocal space can be understood as a one dimensional k-dependent system.

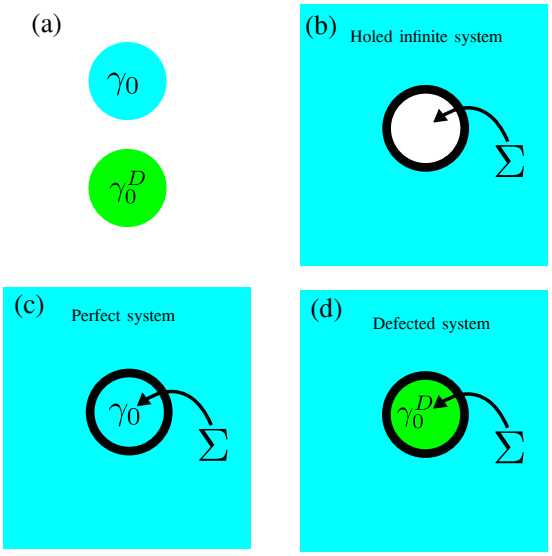

Figure 11.1: (a) Sketch of the two different central cells, pristine (blue) and defected (green). (b) Sketch of an infinite system with hole and the selfenergy that will be induced in the hole considered the coupling (black). Sketch of a perfect (c) and defected (d) system and the selfenergies induced to a central by the rest infinite system

We separate the summation over k in the two different components

$$G_P = \sum_{k_y} \sum_{k_y} (E - h_{(k_x,k_y)})^{-1} = \sum_{k_x} g(k_x) \tag{11.6}$$

where $g_(k_x)$ is the Green function of the k-dependent 1d system (Fig. 2c) obtained for a given k_x, whose hopping parameters are defined by

$$\gamma_0(k_x) = \gamma_0 + e^{ik_x}\gamma_{1,0} + c.c. \tag{11.7}$$

$$\gamma(k_x) = \gamma_{0,1} + e^{ik_x}\gamma_{1,1} + e^{-ik_x}\gamma_{-1,1} + c.c. \tag{11.8}$$

defining a Bloch hamiltonian in the y direction of the form

$$\hat{h}(k_x, k_y) = \gamma_0(k_x) + e^{ik_y}\gamma(k_x) + c.c. \tag{11.9}$$

whose Green function could be calculated as

$$g(k_x) = \sum_{k_y} (E - \hat{h}(k_x, k_y))^{-1} \tag{11.10}$$

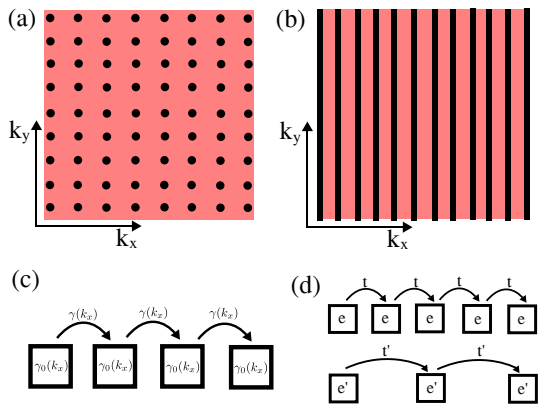

Figure 11.2: (a) Uniform mesh in a two dimensional Brillouin zone, corresponding to the simplest scheme to calculate G_D. (b) Equivalent mesh in the optimized approach, which consists on exactly integrate different lines. Each line in the reciprocal space corresponds to the calculation of a k-dependent one dimensional system as shown in (c). The integration of each 1d system is performed by evaluating the Green function using a renormalization technique.

The previous integral can be performed very efficiently for each 1d system by using a renormalization technique[493] of the coupling in real space. The idea is redefine equivalent intracell and intercell matrices between the cells with even index as depicted in Fig. 2d.

For a 1d hamiltonian with intracell matrix e and intercell matrix t, the renormalized matrices which yield the bulk Green functions are obtained by the following iterative procedure

$$e' = e - te^{-1}t^{\dagger} - t^{\dagger}e^{-1}t \tag{11.11}$$

$$t' = te^{-1}t \tag{11.12}$$

$$e' \to e \qquad t' \to t \tag{11.13}$$

until t' is small enough. Once that point is reached, the bulk Green function is simply

$$g = e'^{-1} \tag{11.14}$$

The previous algorithm can be easily obtained by considering different product

of Green function with the bulk Hamiltonian

$$H = \begin{pmatrix} & & & \vdots & & & \\ \dots & t^\dagger & e & t & 0 & \dots & \\ \dots & 0 & t^\dagger & e & t & 0 & \dots \\ \dots & & 0 & t^\dagger & e & t & \dots \\ & & & \vdots & & & \end{pmatrix} \tag{11.15}$$

$$G = \begin{pmatrix} & & & \vdots & & & \\ \dots & g_{0,1} & g_{0,0} & g_{1,0} & g_{2,0} & \dots & \\ \dots & g_{0,2} & g_{0,1} & g_{0,0} & g_{1,0} & g_{2,0} & \dots \\ \dots & & g_{0,2} & g_{0,1} & g_{0,0} & g_{0,1} & \dots \\ & & & \vdots & & & \end{pmatrix} \tag{11.16}$$

where by definition $GH = I$
Taking diagonal and off diagonal products we obtain

$$g_{0,0}e + g_{0,1}t + g_{1,0}t^\dagger = I \tag{11.17}$$

$$g_{0,0}t + g_{1,0}e + g_{2,0}t^\dagger = 0 \tag{11.18}$$

$$g_{1,0}t + g_{2,0}e + g_{3,0}t^\dagger = 0 \tag{11.19}$$

$$g_{2,0}t + g_{3,0}e + g_{4,0}t^\dagger = 0 \tag{11.20}$$

extracting $g_{1,0}$ from Eq. 11.22, inserting in 11.17 and rearranging one obtains

$$g_{0,0}[e - te^{-1}t^\dagger - t^\dagger e^{-1}t] + g_{0,2}te^{-1}t + g_{2,0}t^\dagger e^{-1}t^\dagger = I \tag{11.21}$$

and analogously

$$g_{0,0}te^{-1}t + g_{2,0}[e - te^{-1}t^\dagger - t^\dagger e^{-1}t] + g_{4,0}t^\dagger e^{-1}t^\dagger = 0 \tag{11.22}$$

where redefining

$$e' \to e - te^{-1}t^\dagger - t^\dagger e^{-1}t \tag{11.23}$$

$$t' \to te^{-1}t \tag{11.24}$$

$$g_{2,0} \to g_{1,0} \tag{11.25}$$

leads again to Eqs. 11.22,11.17. Since $g_{0,\infty} = 0$, the previous re-definitions will eventually yield a vanishing t, and therefore the bulk Green function will be simply

$$g_{0,0} = e'^{-1} \tag{11.26}$$

with the redefined e' given by the iterative method

11.5 Examples

In the following we will apply the embedding method to calculate the spectral function of single impurities in different systems. We will deal with several two dimensional systems. In particular, we will calculate vacancies in monolayer, bilayer honeycomb, Kagome lattice, quantum anomalous states and quantum Hall states.

11.5.1 Vacancy in honeycomb and Kagome lattice

As stated before, the embedding method is specially suitable to metallic and semimetallic systems, where the superlattice approach is not able to capture asymptotic limits. The simplest example is the single vacancy in graphene, which is know by analytic solution that develops a divergent density of states for $E = 0$ close to the vacancy. The origin of such state comes directly from the imbalance between the number of sites in the bipartite honeycomb lattice, which in an island creates a zero mode while in a sheet turns into a resonance. The density of states obtained with the embedding method is shown in Fig. 11.3ac.

A more interesting example[is realized by the Kagome lattice. The Kagome lattice consist in a unit cell of three sites, with hoppings that create antiferromagnetic frustration, which comes from its non-bipartite nature. Although different from the honeycomb lattice, its electronic spectrum shows a very similar structure. In particular, two Dirac cones appear in the K and K' points, yielding a band structure similar to graphene. The band counting is completed by a flat band at the bottom of the valence band. Although the lattice is no longer bipartite, a single vacancy also creates a resonant state close to the Dirac point, but with a large electron-hole asymmetry as shown in Fig.11.3bd.

11.5.2 Vacancy in Quantum Hall for honeycomb lattice

Another class of situations where the embedding approach shows its usefulness is the Quantum Hall state. The magnetic field in a tight binding model is usually included by the minimal coupling Peierls substitution

$$B : t_{ij} \to t e^{i\phi_{ij}} \quad \text{with} \quad \phi_{ij} = \int_i^j \vec{A} \cdot d\vec{l} \tag{11.27}$$

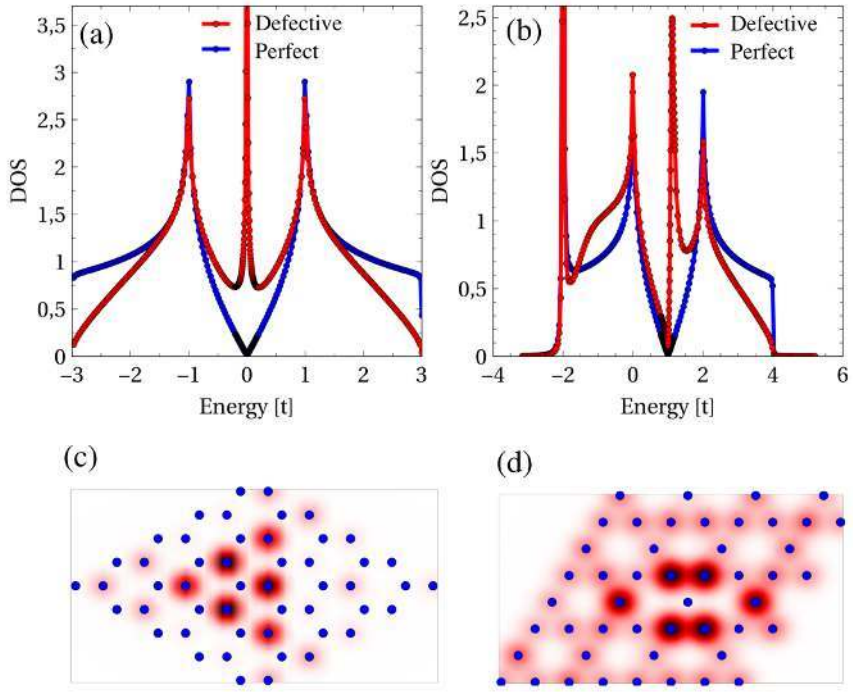

Figure 11.3: (a) Comparison of the DOS the atom close to a single vacancy (red) with the pristine case (blue) for (a) honeycomb and (c) Kagome lattices. Local density of states for the defective honeycomb at $E = 0.0$ (b) and for the defective Kagome for $E = 1.0$ (d)

with a simple gauge choice $\vec{A} = (By, 0, 0)$. The previous gauge preserves translational symmetry in the x direction, but apparently breaks it on the y direction, and therefore Bloch factorization can be done only in x. However, a convenient choice $BL = 2\pi$, with L the y dimension of the unit cell, recovers the translational symmetry in y, and a 2D system with magnetic field can be numerically considered.

Therefore we can also study single vacancies in a Quantum Hall bulk by embedding technique. The spectrum of a QH bulk is a set of peaks associated with the different Landau levels. When a single vacancy is added, inter Landau levels are expected to show up due to the topological nature of the inter-Landau gap. where the DOS is expected to develop isolated peaks in the

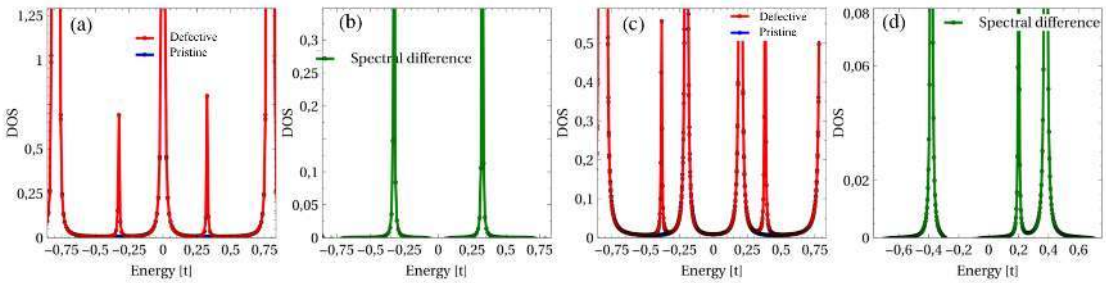

Figure 11.4: Comparison of the DOS in the quantum Hall regime for half filled graphene, in the massless (a) and massive(c). Figures (b,d) are the difference in DOS between the defect and pristine cell, showing the DOS of the induced in-gap state.

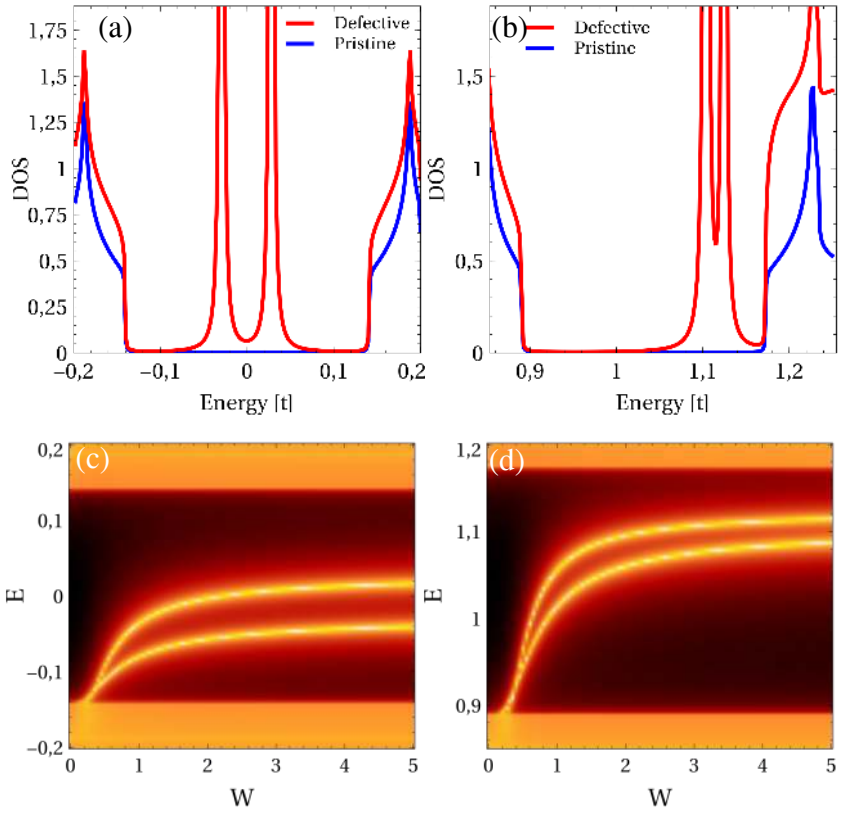

Figure 11.5: Comparison of the DOS in the quantum anomalous Hall regime for a lattice with Rashba and exchange, (a) honeycomb at half filling (b) and Kagome at filling 2/3.

11.5.3 Vacancy in Quantum anomalous Hall

In the QAH state, a vacancy can be understood as a limiting case of a boundary. Due to the topological nature of the ground state, edge states show up at boundaries of the system. In the particular case of the point defect, an in-gap state is expected to appear, which can be understood as a a survivor of the previous edge states. In Fig 11.5 we show two cases of single vacancy in QAH. To interpolate between the pristine anomalous state and the vacancy, we add to the central unit cell a local potential as

$$H_V = W c_0^\dagger c_0 \tag{11.28}$$

so that in the limit $W \to \infty$ we recover the vacancy solution. The evolution of the spectra for the anomalous Hall state in the honeycomb and Kagome lattices is shown in Fig.11.5. In is observed that the in-gap state enters the gap already at couplings of the order $W = t$, showing even a faster appearance in the Kagome lattice.

The appearance of in-gap states in the quantum anomalous Hall states in the presence of defects is not an specific feature of the previous two models, but a general one from non-trivial topological states. In this fashion, impurities in in quantum anomalous Hall insulators like those involving oxides are also expected to show this behavior. In particular, certain atomic substitutions can emulate the role of the vacancy in an effective tight binding model, bringing in-gap states. This last feature implies that quantum anomalous Hall insulators are way more resilient towards Anderson disorder that to atomic substitution, since the later one at high enough concentrations can create impurity bands, allowing percolation of edge states from one site of the sample to the other one.

11.5.4 Vacancy in Quantum Spin Hall

Spin orbit coupling drives the honeycomb lattice into the quantum spin Hall state, generating the Kane-Mele model. In that situation, a vacancy on the system can trap an in-gap state, very much like the quantum anomalous Hall state shown before. In the following, we will see how we can interpolate between the situation of perfect quantum spin Hall, to a single vacancy in quantum Spin Hall by switching on a local potential in the lattice.

A vacancy in the honeycomb lattice can be easily modeled by switching on a infinite local potential in the site that wants to be removed. We will consider two different perturbations, an spinless onsite potential

$$H_V = W c_0^\dagger c_0 \tag{11.29}$$

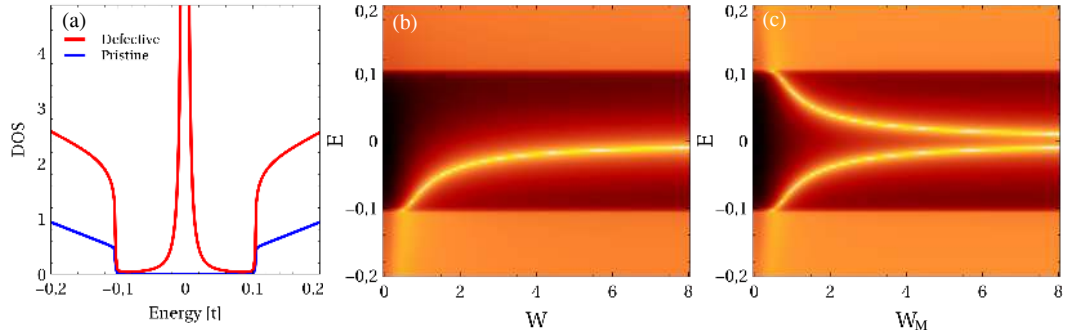

Figure 11.6: (a) DOS for a single vacancy in graphene on the Quantum spin Hall state. Evolution of the DOS as an nonmagnetic (b) and in-plane magnetic (c) impurity is turned on in one site.

and a local exchange

$$H_V = M c_0^\dagger s_x c_0 \tag{11.30}$$

with s_x the spin Pauli matrix.

It can analytically obtained that for a vacancy, a zero energy mode arises, even in the presence of spin orbit coupling gap. This is properly captured by the embedding technique, as shown in Fig.11.6a. With the embedding technique we can easily calculate the density of states close to the perturbation at intermediate values. In Fig.11.6 we show the evolution of the spectra as W (Fig.11.6b) or M (Fig.11.6c) are ramped up. The former evolution shows that as the onsite potential is turned of, an localized states moves towards the gap. It is interesting to note that an impurity of the order of $W = t$ already creates a bound state in the system. This latter phenomena can have important consequences for the effective gap in a topological insulator. If the has a concentration impurities, the bound states created around those impurities can create an impurity band greatly reducing the gap.

11.5.5 Shiba state in the square lattice

An interesting case is the effect of a magnetic impurity in a superconductor, which creates the so called Shiba states. Superconductivity is introduced by the conventional swave pairing term

$$H_{SC} = \Delta c_{i\uparrow} c_{i\downarrow} + c.c. \tag{11.31}$$

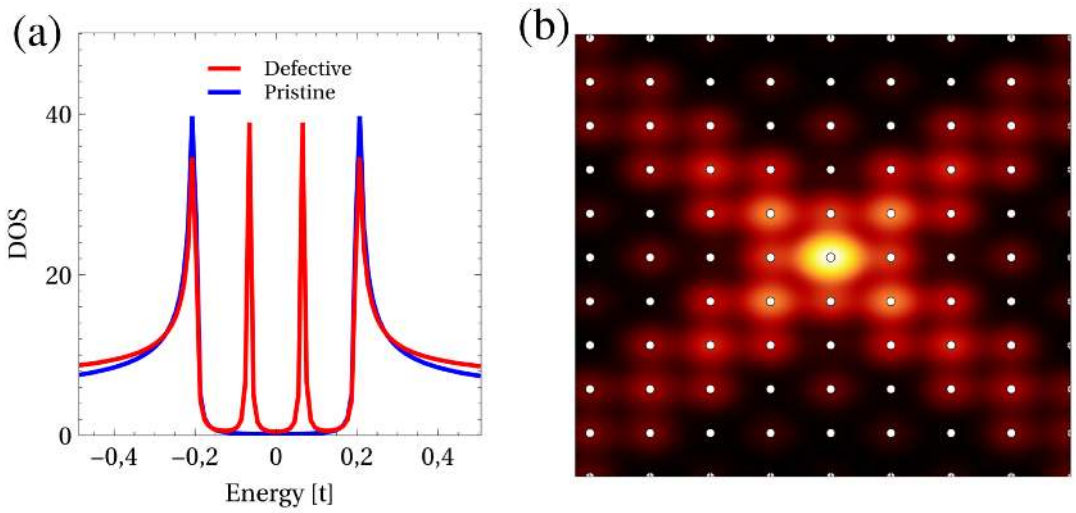

Figure 11.7: (a) DOS for a exchange impurity in a conventional superconductor and (b) spatial distribution of such state. The superconductor is taken as a square lattice, and the in-gap state shows the C_4 symmetry of the underlying lattice.

and the exchange term as

$$H_J = J c_0^\dagger s_z c_0 \tag{11.32}$$

with s_z the spin Pauli matrix.

The local exchange term traps part of the Cooper pairs in the electronic bath, and lowers the energy to break a pair, creating an in-gap state. The in-gap state appears as a peak in the spectral function as shown in Fig.11.7a. The spatial distribution of the in-gap state can be easily calculated by projecting the Spectral function onto each site of the lattice, shown in Fig.11.7b

11.5.6 Bilayer graphene

An application in line with the ones shown so far is bilayer graphene, in particular single hydrogenated sites[494, 495]. This gives rise to another example of in-gap state, which can be interpreted as a vacancy in a so called quantum valley Hall insulator. Although this is not a true topological insulating phase and therefore in gap states can be gapped out by intervalley mixing, some of the features of true TI can still be observed. The Hamiltonian has usual interlayer coupling, and a term which makes the two layer inequivalent, tuned by a perpendicular electric field.

$$H_L = V z \tag{11.33}$$

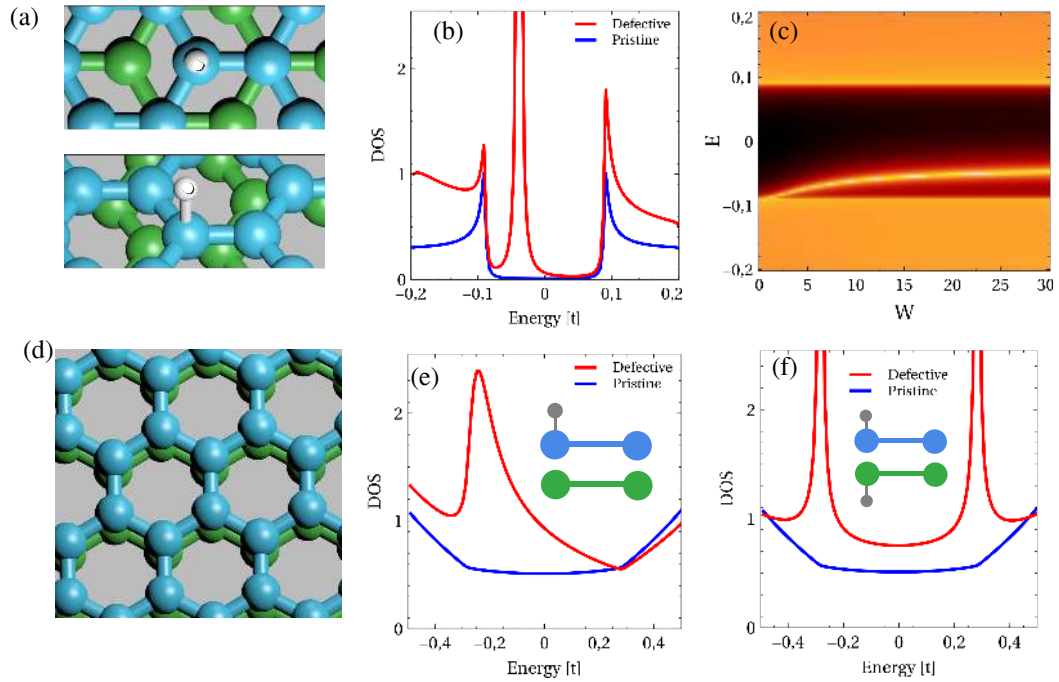

Figure 11.8: (a) Sketch of AB graphene bilayer with a hydrogenated site. (b) Density of states for a single hydrogenated site. Panel (b) is the limiting case of an infinite onsite energy W in an atom, whose spectrum as a function of W is shown in (c)

where z is the position of the atom, and V is the potential imbalance. between layers.

The effect on the electronic structure is pretty different for the two different stacking AB and AA. For AB stacking, the previous term opens up a gap in the band structure by breaking inversion symmetry, which gives rise to the valley Hall state. In this situation, a single hydrogenated site gives rise to an in-gap state. In comparison, in the AA stacking, electric field does not open a gap, so that the systems remains metallic. Nevertheless, the missing site still creates a localized resonance, that shifts with the electric field.

11.6 Summary

Study of individual impurities always represented a problem in numerical models. Whereas analytic calculations provide a natural methodology based on poles of Green functions or S-matrix, the complexity of the Hamiltonians for certain systems turns the problem not solvable analytically. Conventionally, numerical techniques

relied on taking bigger and bigger systems with a single impurity, but this approach has the drawback that it becomes computationally demanding and, sometimes, the desired limit beyond computational capabilities. In this chapter we presented a way around, providing a technique to exactly treat systems with an infinite amount of atoms and no translational invariance.

We have shown a methodology to study single defects in a pristine system, by means of a Green function embedding technique. The single defective unit cell can host different types of perturbations depending on the Hamiltonian considered. For honeycomb lattice, the missing site reproduces the well know zero energy mode, whereas when the systems enters into the Quantum Hall regime, additional in-gap states show up. Similar phenomenology show up for quantum anomalous Hall, quantum spin Hall and quantum valley Hall. Finally, it is worth to remark that the workflow presented is valid for any kind of real space Hamiltonian, and any kind of impurity, allowing to study even atomic substitution even in complex systems by taking advantage of the Wannier technique.

Chapter 12

Quantum Honeycomp, a user-friendly computational code

In this chapter I introduce a suite of computer codes with a graphical interface that allow non-experts to carry out most of the calculations presented here. The development of this code, named Quantum Honeycomp, has been a part of my research project

12.1 Motivation

A major barrier between theorist and experimentalist, is that the tools used by each one of them become increasingly sophisticated. This makes a though task the possibility of interchanging tools between them. Usually, this ends up in the undesirable situation that theorist do not know what are the different techniques that experimentalist can do and their limitations. In the same way, simple mathematical or computational tools that theorist use are rather unknown for experimental people. Focusing on electronic properties of graphene, the possibility of a portable "graphene lab" that you can use at your home is yet a fantasy; however, a portable simulation center that you can have in your laptop is not. Importantly, the success and usefulness of these tools rely on the free and open use of them, so that a key factor that motivated their development is to provide a tool that anyone can use for free, with an open source code.

Specialization and training in advance techniques are unavoidable skills that different scientist have to develop in order to advance science. However, communication and interactivity are also key factors to foster the discovery of new phenomena. Bridging the gap between different approaches is though task, but the revenues are way bigger that they may look. With that motivation, our goal is to provide with simple but yet powerful tool to understand electronic properties in graphene sys-

tems. The objective is that, without the need of any background in programming skills or complex mathematical tools, anyone can be able to explore the different electronic properties of graphene.

Following the previous fashion, we present a computational code called Quantum Honeycomp[89, 88]. The code allows the user to study different electronic properties of graphene systems and other 2D lattices. It uses a friendly user interface [496, 497, 498, 499] , so that the different characteristics of the systems can be chosen. Different parameters of the system as magnetic fields, substrate effects or defects can be introduced in different boxes in the user interface. The results are shown using different visualization programs. As a first try I developed a much more simple code that allowed to study nanoribbons[500] (not updated anymore), whereas Quantum Honeycomp yields a more wider flexibility to study systems of any dimensionality.

12.2 Inside the code

In the following we will detail the different part of the inner code, how they are organized and how they communicate with each other.

12.2.1 Requirements

Quantum Honeycomp[89, 88] is a free and open source software, and it is also based on free software. The different packages and tools that Quantum Honeycomp uses are the following

- gfortran
- lapack and blas FORTRAN libraries
- Python-numpy
- Python-scipy
- Python-matplotlib
- Python-visual
- Python-mayavi
- gtk3 library

The program has been developed to run on Linux machines. Specifically, it comes with scripts that will install all the needed dependencies on Debian based distributions.

For non Linux operating systems, the simplest solution is to install Linux in a virtual machine and execute the program there.

12.2.2 Organization

The code is arranged in the following main parts

- Fortran program (f90src folder)
- Python library (pysrc folder)
- User interface scripts (systems folder)

Fortran library

The FORTRAN library creates a FORTRAN executable, tb90.x, which is able to calculate many of the different properties for the different systems. It has specialized routines for 0d, 1d and 2d Hamiltonian. It has two main input files: tb90.in and Hamiltonian.in. On one hand tb90.in, the different options for the calculation are written according to the namelist FORTRAN syntax. On the other hand, Hamiltonian.in gives the different hopping parameters for the system that will be analyzed. In the case of selfconsistent calculations, the free Hamiltonian is read from hamiltonian_0.in, while the final mean field Hamiltonian is written in hamiltonian.in. In addition, other input files can be read from depending on the different parameters in tb90.in. Some examples are

- mean_field.in : rerun a mean field calculation with a custom initial guess
- mean_field_operators.in : perform a mean field calculation using interaction operators provided on input

This FORTRAN program has been implemented with open-mp parallelization, which makes it suitable to be used in parallel machines to calculate large systems. By default the the open-mp parallelization is switched off, but it can be turned on by modifying the compilation script.

Quantum Honeycomp calls the tb90.x executable, so that it will have to be in the PATH bash variable.

Python library

The main Python library in which Quantum Honeycomp relies is located in the folder pysrc. This is a multipurpose library developed from the start of this thesis and it is able to perform many more tasks than the ones shown in the user interface. The basic use of the library relies on two different objects: the geometry object and the hamiltonian object.

The geometry object creates a certain lattice, that can be 0d, 1d or 2d. The geometry can be modified by creating supercells calling the supercell method, and

calling different function from the sculpt module. The geometry object basically stores the different positions of the lattice, the dimensional and the cell vectors.

The hamiltonian object can be created from the geometry object by calling the get_hamiltonian method. The hamiltonian object stores the different hopping matrices. Different terms to the Hamiltonian can be added calling different methods:

- add_sublattice : adds sublattice imbalance (only bipartite systems)
- add_zeeman : adds a zeeman field
- add_antiferromagnetism : adds antiferromagnetic order (only bipartite systems)
- add_rashba : adds rashba spin orbit coupling
- add_peierls : adds orbital magnetic field (only 0d and 1d systems)

These methods accept both numbers of functions that have as input coordinates and as output a certain number. This is specially suitable to create Hamiltonian whose parameters depend on the space, as for example skyrmions.

This Python library is also released as an independent library to be used simply within a Python script[501, 502].

Connection between Fortran program and Python library

Those calculations that require calling the FORTRAN program make use of the input_tb90 module. Inside that module, the object tb90in stores the different possible options in their attributes. Its method in90.write() will write the tb90.in file. In addition, the Hamiltonian is written to the file hamiltonian.in that tb90.x by calling the method hamiltonian.write()

User interface scripts

The different user interfaces are located in the folder **systems**. Each folder located in **systems** corresponds to a different setup.

Each folder consists on a .py file and an .xml file. The xml describes the different objects of the user interface, and can easily be edited with Glade. The Python file connects the different signals created by the gtk interface to different Python functions that perform the different tasks. I also used a similar philosophy, combining Python and gtk3 with Glade, to develop a code to study transition metal atoms on surfaces[503], but using C++ instead of FORTRAN.

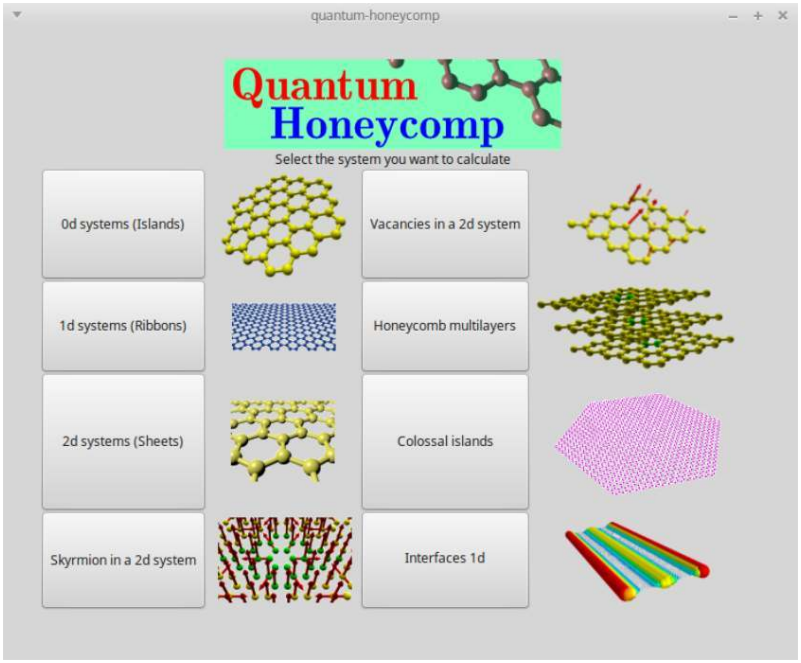

Figure 12.1: Main window of Quantum Honeycomp, with the different modules implemented.

12.3 Modules of Quantum Honeycomp

The user interface of Quantum Honeycomp is arranged in different modules. Every module is specialized in different types of calculations. Currently, the different modules implemented in the interface

- Islands : Zero dimensional systems
- Ribbons : One dimensional systems
- Sheets : Two dimensional systems
- Vacancies in 2D : Special modulo for vacancies in 2d systems
- Skyrmions in 2D : Special module for skyrmions in 2d systems
- Multilayers : Special module for multilayered systems
- Colossal islands: Special module for huge 0d systems, using the Kernel polynomial method
- Interfaces in 1D: Special module to study interfaces in 1d

Every module allows to change the different terms in Hamiltonian that the system can have, as orbital magnetic field, exchange fields, spin orbit coupling. In addition, different lattices can be chosen, the graphene honeycomb lattice, the more conventional square lattice, Kagome and Lieb lattices. Furthermore, all the modules except the *Colossal islands* module allow also to perform selfconsistent Hubbard calculations.

In the following, we will shows several examples on how the different modules can be used to obtain different non-trivial properties of graphene and related materials.

12.3.1 Islands module

The first module (Fig. 12.2a) allows to calculate properties of systems with 0d geometry, as graphene dots. In this mode, the eigenvalues are presented by their index, in comparison with the modules that have some periodic boundary condition.

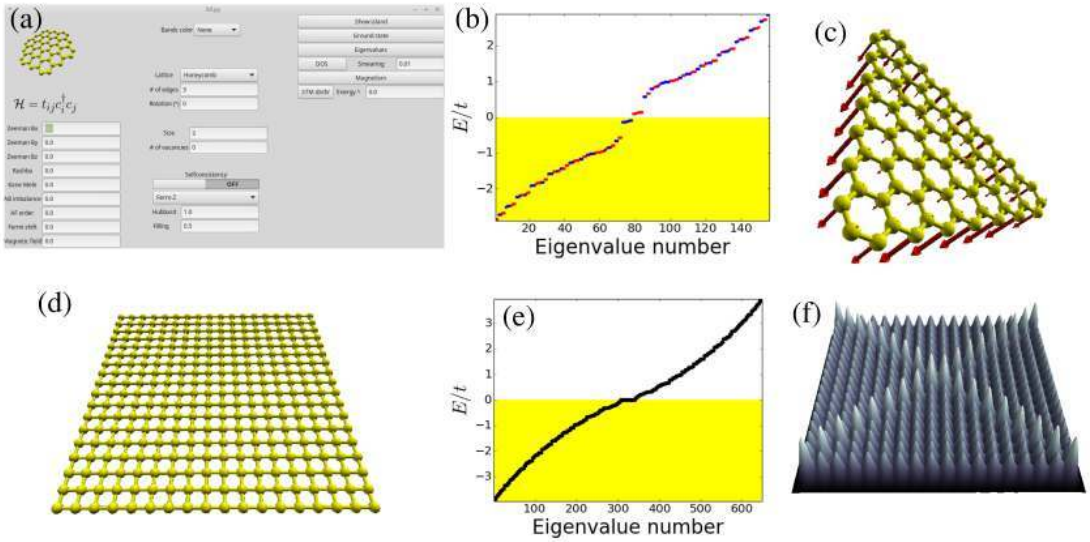

Figure 12.2: Main window for the islands module (a). The first example corresponds to a triangular zigzag island, where after electronic interactions the systems develops a spin splitting in the spectrum (b), and local magnetic moments (c). In the second example, a square island is created (d), that shows several states pinned at zero energy (e), some of them strongly located on the diagonals of the island (f).

Graphene islands

In the case of a graphene island, if the edges of the system are zigzag there can be a total sublattice imbalance. In the case of the graphene zigzag island, this sublattice

imbalance leads to zero energy states. Such states become magnetically order[120, 504] when interactions are taken into account as seen in Figs. 12.2b,c.

Square islands

The case of square islands is rather unconventional. In principle there is no simple system that shows a pure square lattice. However, many oxides as perovskites show cubic lattices[505]. The oxygen environment creates an effective cubic lattice for the d-orbitals of transition metal atom. In that situation, nano-fabrication techniques might be able to create confined thin films, that realize an effective square lattice. A very particular example is cuprate like compounds[506], that their layered structure naturally creates effective square lattices. Another examples are atomically engineered atoms deposited on surfaces[507, 508, 509, 510, 511, 512].

The example that we will try below consists on a finite square island as shown in Fig. 12.2d. It is well know that the square island has a van Hove singularity at $E = 0$, so that the DOS is expected to diverge. Something less obvious is that the DOS along the diagonals of the island is largely increased respect to the other points. This phenomena can be understood in terms of the local sublattice imbalance of the corner atoms, that create additional states that propagate on the diagonal (Figs 12.2e,f).

12.3.2 Ribbons module

The ribbons module deals with systems that are periodic in one direction. It is the ideal module to look for edge states in topological insulators.

Magnetism in zigzag ribbons

In a zigzag ribbon, the local sublattice imbalance creates localized states on the edges. Those states can become magnetic when interactions are introduced (Figs. 12.3). In the case of a ribbon with finite width, the relative orientation of the magnetic moments between the two edges creates an energy splitting. The lowest energy configuration corresponds to the antiferromagnetic one. While in the antiferromagnetic configuration the system is insulating, the ferromagnetic one gives a metallic state.

Quantum anomalous Hall effect in graphene

A simple example to show the quantum anomalous Hall effect is a graphene sample where both Rashba SOC and off-plane exchange have been introduced. In that situation, the system opens up a gap, at the same time it sustains gapless channels.

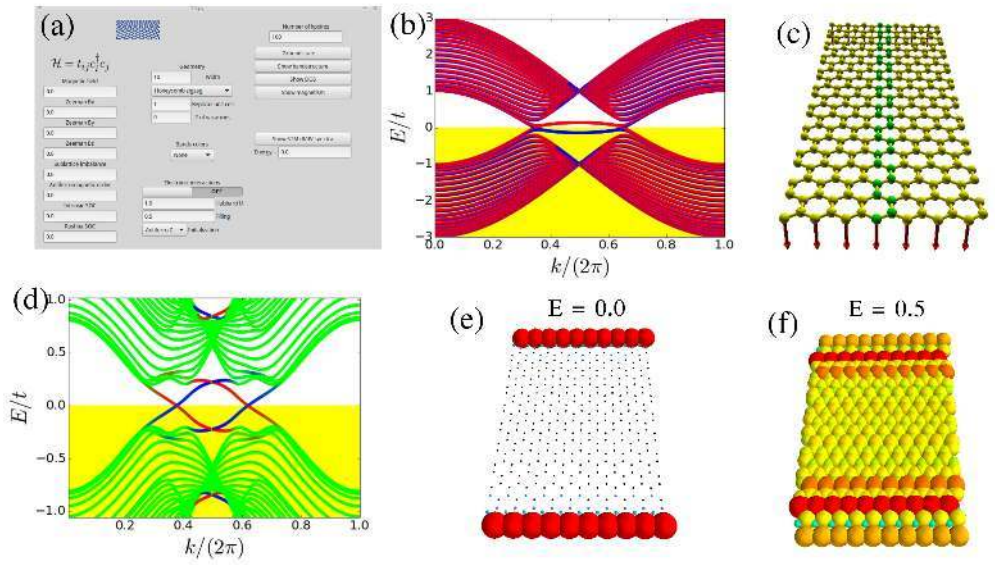

Figure 12.3: Main window for the ribbons module (a). The first example corresponds to a zigzag ribbon, where after electronic interactions the systems develops a spin splitting in the spectrum (b), and local magnetic moments (c). In the second example, Rashba SOC and off-plane exchange are introduced turning the system into a quantum anomalous Hall insulator (d). In the bulk gap only edge states show up (e), whereas at other energies the states live in the whole ribbon (f)

In this precise example, the Chern number of the system is $C = 2$, so that there will be two edge channels.

12.3.3 Sheets module

The sheets module deals with systems that are periodic in two directions. It is the ideal module to study bulk properties of different lattices. In particular, it allows to calculate Chern invariants, which reflect the topological state of systems with broken time reversal symmetry. Importantly, the two dimensional geometry can not include general magnetic fields due to the mistmatch of the Peierls phase.

Quantum anomalous Hall state in Kagome lattice

The quantum anomalous Hall sate in graphene was shown previously. However, there is a special lattice that has many common properties with graphene, which is the Kagome lattice. In particular, it develops a Dirac like spectrum close to the K-point.

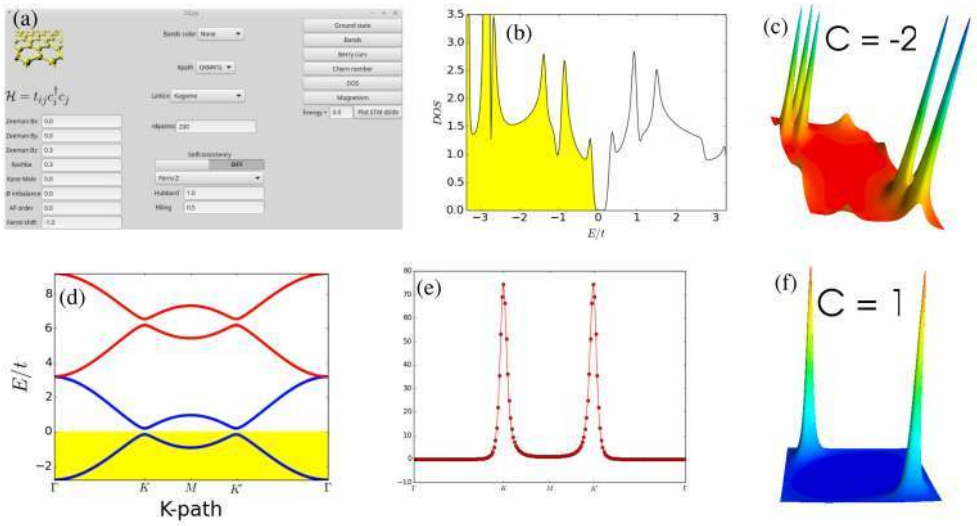

Figure 12.4: Main window for the sheets module (a). A simple example corresponds to the Kagome lattice with off-plane exchange and Rashba SOC (b), which shows a Chern number $C = 2$ (c) and therefore develops the quantum anomalous Hall effect. In the large exchange limit, the honeycomb lattice is effectively spinless (d) and upon application of Rashba SOC develops Berry curvature in the Dirac points (e). The Berry curvature sums up to $C = 1$, yielding a realization of the Haldane model.

An interesting question is if this system is able to show quantum anomalous Hall state[513, 514, 515], in the same fashion the honeycomb lattice can. It turns out that upon the introduction of off-plane exchange and Rashba coupling the system opens up a gap in the Dirac points. Calculation of the Chern number yields a value of $C = 2$, predicting two edge states per edge, as shown in Fig. 12.4c,d.

Realization of Haldane model in honeycomb lattice

Although the honeycomb lattice has a simple situation that sustains the quantum anomalous Hall effect, such realization has not been observed yet. That model is know as the Haldane model, and it requires a system with spinless fermions and second neighbor hoppings. Importantly, although no system realizes purely this celebrated model, there exist a very simple realization of it. If a large exchange is introduced in a honeycomb lattice and the filling is set to 1/4, the systems becomes effectively spinless. If in addition, spin orbit coupling is present, transitions from the low energy manifold to the high energy manifold will open up a gap in the Dirac points. Due to the real space structure of the Rashba coupling, it is directly seen that the effect of the Rashba perturbation is to create a second neighbor hopping,

linking states with the same spin at low energy. Therefore, the Haldane model can be easily realized is a ferromagnetic honeycomb with off-plane electric field as shown in Figs. 12.4 d,e,f

12.3.4 Skyrmions module

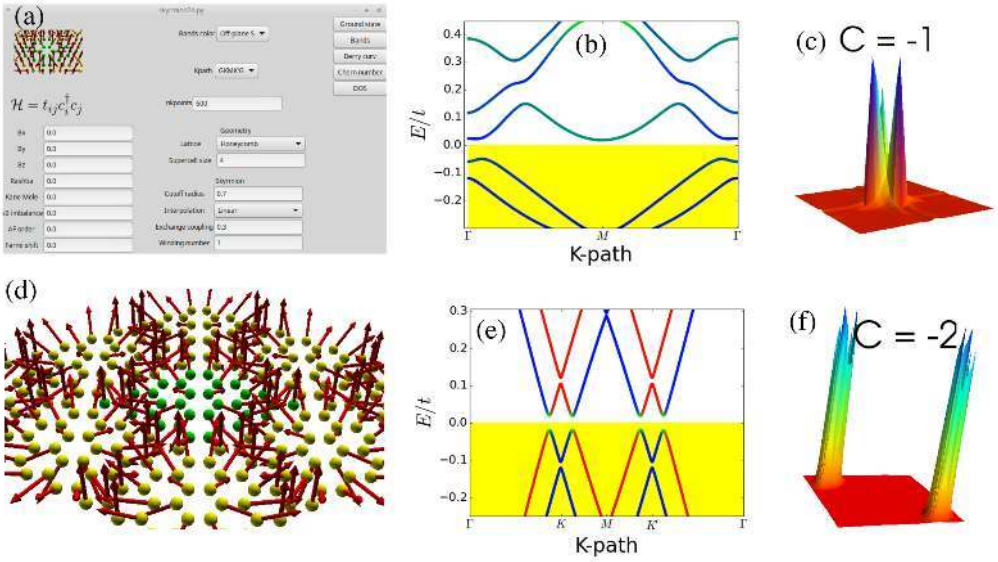

Figure 12.5: Main window for the skyrmions module (a). Band structure (b) of a square lattice in the large exchange coupling at low filling showing a gap. Calculation of the Chern number (c) yields $C = 1$, thus realizing the QAH without SOC. Unit cell (d), band structure (e) and Berry curvature of the honeycomb lattice at weak coupling, realizing also the QAH state.

The skyrmions module allows to calculate 2D properties of lattices couples to a skyrmion background. This is accomplished by including a space dependent exchange field, whose dependence can be changed in the interface. Skyrmions are a simple way to induce quantum anomalous Hall state in systems that do not have spin orbit coupling

QAH effect driven by skyrmions in square lattice

In the large exchange limit of skyrmion coupling, a square lattice is able to sustain the quantum anomalous Hall state. Mathematically, this is understood in terms of the effective magnetic field that arises in the system. The effective magnetic field can be obtained by performing a spin rotation in each point of the space along the

axis of the local exchange. Such rotation creates a new term in the kinetic energy, equivalent to a gauge field.

Is is shown in Fig. 12.5 the band structure and Berry curvature of a $4x4$ square lattice under the influence of a strong skyrmion exchange. At low filling, the system opens up a gap, and calculation of the Chern number identifies it as a topological gap.

QAH effect driven by skyrmions in graphene

Another example of quantum anomalous Hall state driven by skyrmions is the honeycomb lattice at half filling. In comparison with the square lattice, the honeycomb lattice sustains the QAH even in the low coupling limit. Mathematically, the model resembles the QAH state driven by exchange and SOC. Finally, as shown before, graphene is also capable of showing the QAH state in the large exchange limit.

12.3.5 Vacancies module

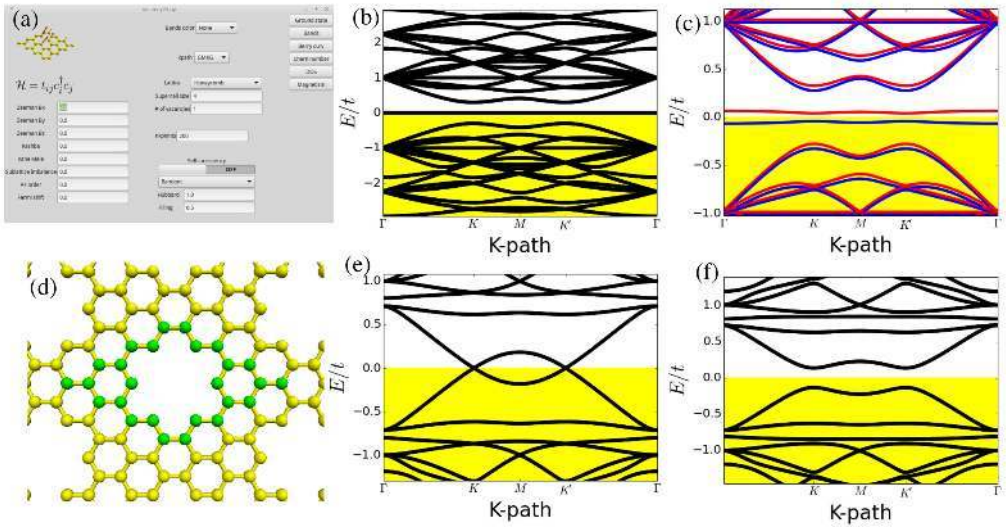

Figure 12.6: Main window for the vacancies module (a). Band structure of a honeycomb supercell with one vacancy, before (b) and after (c) interactions are turned on. Unit cell (d) and band structure (e) of a graphene supercell with six vacancies, showing a Dirac like spectrum in the K point. When interactions are turned on, the system becomes antiferromagnetic (f) below the critical value for graphene.

An interesting case is when a two-dimensional lattice has certain defects that create a new emergent superlattice. The present module is specially suited for that

goal, allowing to create an amount of vacancies in different types of lattices. By default, the vacancies are put to get the maximum symmetry for the new lattice. The default window in shown in Fig. 12.6a

Magnetism induced by vacancies

The simplest example to consider is the emergence of magnetism[516, 517, 518, 519, 520, 521] when a hydrogen atom is deposited on graphene. A hydrogen atom bonds covalent to the lattice, effectively removing the p_z orbital of the atom sited underneath. In a one orbital model, the effect of a hydrogen atom is included by simply removing a site in the lattice[522, 523, 524, 525, 526].

In Fig. 12.6b,c it is shown the band structure of a graphene superlattice with a single defect. In the non-interacting case, the sublattice imbalance creates flat band at the Fermi energy. When interactions are turned on, the flat band becomes spin-splitted and the system becomes ferromagnetic.

Fermi velocity renormalization

A certain set of vacancies it is also able to create an emergent honeycomb lattice, but with a renormalized Fermi velocity. A simple case of that behavior consists on a $4x4$ unit cell, with six hydrogen adatoms sitting on an hexagon (Fig. 12.6d,e,f). In that situation, the electronic spectra of the new lattice resembles the one of graphene, showing Dirac bands crossing at the K point. However, the slope of the bands is smaller than the original graphene ones, which translates into a smaller Fermi velocity.

In graphene, under the mean field Hubbard model the antiferromagnetic transition takes place around $U = 2.2$[527, 528, 529]. In the case of the emergent lattice stated before, since the Fermi velocity is smaller than in pristine graphene, the antiferromagnetic transition will take place at smaller values of U. In particular, we show in Fig. 12.6f the band structure for $U = 2$, which shows a gap due to the antiferromagnetic order developed.

12.3.6 Multilayers module

In the case of graphene, Van der Waals multilayers are known for showing many unconventional properties. The present module was designed to address the study of different bulk properties in honeycomb multilayers. In particular, it allows to tune the interlayer coupling and perpendicular electric field.

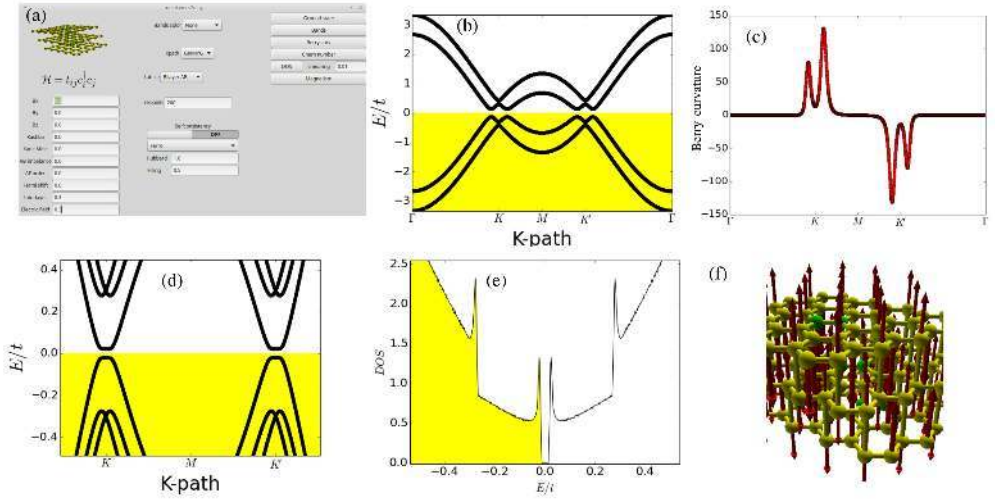

Figure 12.7: Main window for the multilayers module (a). Band structure of gated bilayer graphene (b), showing a non zero anomalous velocity in the different valleys (c). Band structure of trilayer graphene after electronic interactions are considered (d), opening up a gap in the DOS (e). The gap is opened by the antiferromagnetic order that appears (f).

Valley Hall in bilayer graphene

The effect of the Berry curvature in the propagation of electrons is to creates an anomalous term in their velocity, adding like a momentum dependent magnetic field. In system with inversion and time reversal symmetry, the Berry curvature is identically zero at every point. However, if inversion symmetry is broken, the Berry curvature can be non-zero, even though time reversal still ensures that the net value vanishes.

Bilayer graphene in the presence of a perpendicular electric field opens up a gap at the Fermi energy[494]. Importantly, the Berry curvature of electrons close to the K point is very large, and change sign between different valleys. Therefore, a slightly doped bilayer graphene sample is expected to show a valley current, since electrons feel an anomalous velocity in one direction and in K' in the opposite, as shown in Fig. 12.7b,c

Magnetism in trilayer graphene

Monolayer graphene is known to be non magnetic, However, multilayered systems[530, 531, 532] can have a way larger density of states at the Fermi energy, which might drive them magnetic due to interactions. The ultimate case is trilayer graphene, whose dispersion relation is cubic in momentum close to the Fermi energy, and

therefore has a divergent DOS. When interactions are turned on, trilayer graphene opens up a gap (Fig. 12.7d,e,f) by developing an antiferromagnetic order.

The antiferromagnetic order[533] in trilayer graphene[334] can have important consequences. In particular, trilayer graphene can be a interesting host for interfacial bound states between superconductor and antiferromagnet as shown previously.

12.3.7 Colossal islands module

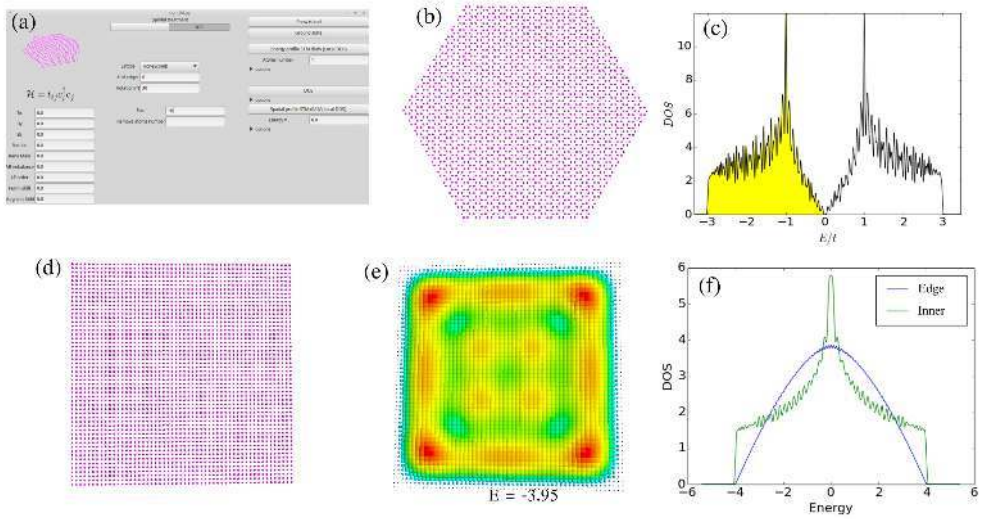

Figure 12.8: Main window for the colossal module (a). Structure of a hexagonal graphene island (b), and total DOS (c) resembling pristine graphene. Structure of a square island made of a square lattice (d), and its spatial resolved DOS at a deep energy (e). Deep energy states avoid the edges, as can be seen by comparing the local DOS in a bulk and an edge site (f)

A conventional limitation of any other module is that the computational cost of the calculation increases cubic with the number of atoms. In the case of zero dimensional systems, it can be possible that a very large amount of atoms is needed to obtain a certain behavior, as can be to recover a continuous density of states. The present module implements the Kernel polynomial method, which is specially suitable to deal with a very large amount of atoms. In particular, it can handle in seconds systems with tens of thousands of atoms, and calculate local or global spectral properties as shown in Fig. 12.8a.

Graphene dots

The *Colossal islands* module allows to create different types of dots, starting from a certain lattice and requesting a dot with a certain number of edges. Additional, an initial rotation of the primitive cell can be introduced to change between armchair-like to zigzag or even chiral edges.

A simple and instructive example is to build a graphene dot. In order to get armchair edges, an initial rotation of 30 degrees is introduced. To select an hexagonal island (Fig. 12.8b), six sides are requested. In this case, it is observed that total density of states of the island (Fig. 12.8c) resembles the one of graphene, showing peaks due to finite size effects.

Edge and bulk properties in the square lattice

A interesting use of this module is to study edge effects on the electronic structure. In other words, to understand how the electronic DOS rearranges on edges with respect to bulk, to understand if electronic interactions are going to have a bigger or smaller effect on the edge electronic structure.

In particular, we show in Figs. 12.8 a square island made from a square lattice. In the local DOS, it is observed that electronic states at deep energies avoid the edges of the system. This can be further seen by comparing the local DOS at all the energies in an atom located in the bulk with one located in the edge. For the bulk site, the DOS resembles the bulk result, whereas for the edge site, the DOS goes to zero at the bottom of the valence states.

12.3.8 Interfacial module

So far, all the modules dealt with system rather homogeneous. The only in-homogeneity considered has been finite size effects. However, several types of electronic orders show unexpected behavior when they coexist. To deal with this kind of systems, the module interfaces was developed. It allows to study infinite one dimensional interfaces between two systems with different electronic orders. In this module each half of the ribbon has its own parameters, allowing create interfaces between many different electronic orders.

Jackiw-Rebbi states in boron nitride

A simple example of interfacial states is the interface between a hexagonal lattice with masses with different signs[534]. In particular, such interface is directly related with the Jackiw-Rebbi soliton in the Dirac equation. Actually, the interfacial states[535] can be understood as a set of solitonic bands for each valley.

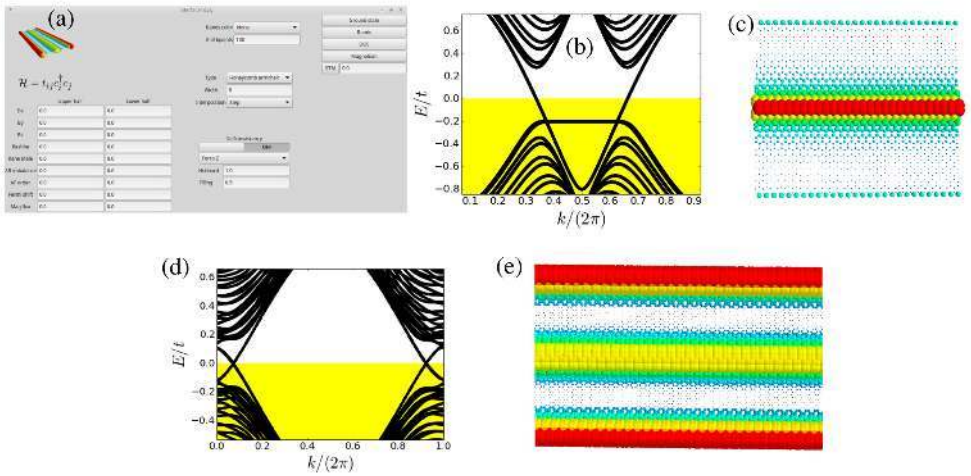

Figure 12.9: Main window for the interface module (a). Band structure (b) of a ribbon whose upper part has positive sublattice imbalance whereas the lower negative. At the interface, gapless modes appear (c) corresponding to solitonic solutions. For the case of two different Chern insulators (d), with opposite Chern numbers $C = \pm 2$, the system develops states both in the edges and at the interface (e).

In the case of a zigzag interface (Fig. 12.1b,c) valleys do not get mixed and the states remain gapless. In the case of armchair interfaces, the valley mixing opens up a small gap, which closes down as the interface becomes smoother. A similar behavior happens in bilayer graphene with opposite electric fields[536, 537, 538, 539]. Remarkably, these interface states resemble the phenomenology of the antiferromagnet superconducting states that lead to an interfacial gapless superconductor.

Interface between opposite QAH

Interfacial states naturally arise at the boundary of two different Chern insulators. In particular, for the QAH state of the honeycomb lattice driven by exchange coupling and Rashba field, the Chern number depends on the relative sign of the exchange coupling. Therefore, if the graphene sample gets its exchange by proximity to a ferromagnet that has a domain boundary, gapless edge states will appear as the exchange coupling changes its sign. In Fig. 12.1d,e we show the case of a ribbon whose upper part has positive off-plane exchange whereas the lower part has negative exchange. In total there are 6 edge channels that overlap in the reciprocal space: two in the upper edge, two in the lower edge, and four in the interface.

12.4 Summary

We have presented the Quantum Honeycomp package, a computational tool that allows to study electronic properties of systems with different dimensionality, including spin orbit effect as well as Hubbard interaction at a mean field level. The software is free and open source, which allows everyone to use it. Its easy use, together with its versatility and computational power makes it an interesting tools to explore qualitatively many different electronic phenomena. Specially, it is well suited as a simple computational lab to understand basic electronic properties in materials, and hopefully will be an useful tool for teaching purposes at the advanced undergrad and graduate school level in materials science and solid state physics classes.

Chapter 13

Methods

In this chapter we will detail different methodologies used along this thesis. In particular, we will show how to calculate Berry curvature for entangled bands, how to perform collinear and non-collinear mean field calculations for arbitary operators and the formalism behind the kernel polynomial method.

13.1 Berry curvature

In this section we present an efficient and numerically stable method to calculate the Berry curvature. The method is based on the definition of Berry phase ϕ for a closed path, and its formulation in terms of the Berry curvature

$$\phi = \int \Omega dS = \oint \vec{A} \cdot d\vec{l} \tag{13.1}$$

for a very small surface (i.e. short closed path), the Berry curvature Ω is constant in the surface enclosed so

$$\Omega = \frac{\phi}{S} \tag{13.2}$$

where S in the surface enclosed. The goal of the method is to calculate efficiently the previous Berry phase.

The Berry phase in a closed path is calculated by

$$\phi = \oint \vec{A} \cdot d\vec{l} \tag{13.3}$$

where $\vec{A}$ is the Berry connection, which for a non degenerate band is

$$\vec{A} = i\langle \Phi | \partial_{k_i} | \Phi \rangle \tag{13.4}$$

The Berry connection is not uniquely define, given that the wavefunctions in the Brillouin zone have a local gauge freedom

$$\Psi(k) \to e^{i\alpha(k)}\Psi(k) \tag{13.5}$$

which turns into a variation on the Berry connection

$$\vec{A} \to \vec{A} + i\partial_{k_i}\alpha \tag{13.6}$$

The previous equation suggest that, given an arbitrary gauge with a certain Berry connection, there is always a gauge transformation which makes the Berry connection 0 due to new term which arises after the gauge transformation. Lets call this choice of gauge the "parallel gauge" However, although such transformation exists, which is not straightforward is that given an arbitrary closed path, the initial and final phases of the gauge transformation are going to be the same. Actually, they are not the same, and the Berry phase it is precisely the de-phasing of the wavefunction gets after a cyclic evolution. To summarize, the Berry phase is the de-phasing that a wavefunction gets after a cyclic parallel transport. It is interesting to note that this deviation of phase is analogous to the definition of Riemann curvature in differential geometry.

These gauge choice seems to be pathological, given that the wavefunctions are no longer continuous in the beginning/end points, making the Berry connection ill defined

$$\langle\Phi|\partial_{k_i}|\Phi\rangle =? \quad \text{(beginning/end point)} \tag{13.7}$$

$$\langle\Phi|\partial_{k_i}|\Phi\rangle = 0 \quad \text{(any intermediate point)} \tag{13.8}$$

In comparison, a gauge transformation (not parallel) whose phase at the beginning and the end is the same, give a well defined connection, and more importantly, gauge invariant.

$$\phi[\alpha] = \oint \vec{A}[\alpha]\cdot d\vec{l} = \oint \vec{A}\cdot d\vec{l} + \alpha(2\pi) - \alpha(0) = \phi \tag{13.9}$$

Is the parallel gauge going to give the same answer as a smooth gauge, after a suitable regularization? The answer is yes, as we will see shortly.

Lets assume that we do know the wavefunctions in the parallel gauge. In that gauge, we called Berry curvature the phase shift between the initial and the final wavefunctions

$$e^{i\phi} = \langle\Psi(2\pi)|\Psi(0)\rangle \tag{13.10}$$

where $\Psi(k)$ is the wavefunction evaluated in a closed path of kpoints in the interval $[0, 2\pi]$. For any intermediate kpoint, the quantity

$$U(k, k + dk) = \langle \Psi(k) | \Psi(k + dk) \rangle = 1 \tag{13.11}$$

is unity, so we can substitute Eq.13.10 by

$$e^{i\phi} = \prod_j \langle \Psi(k^j) | \Psi(k^{j+1}) \rangle \tag{13.12}$$

where k^j are the points in the path. In this form, it is clearly seen that a gauge transformation leaves the overall product invariant. This simply follows for the fact that for every kpoint, a term of the form $|\Psi(k^j)\rangle\langle\Psi(k^j)|$ appears, so that a local phase shift vanishes. Therefore, the previous expression allows to calculate the Berry phase for an isolated band, independently on the gauge of the wavefunctions.

For two bands disentangled, an analogous procedure can be followed. In that case, lets define the net Berry phase $\phi = \phi_1 + \phi_2$ as

$$e^{i\phi} = e^{i\phi_1} e^{i\phi_2} = \prod_j \langle \Psi_1(k^j) | \Psi_1(k^{j+1}) \rangle \prod_j \langle \Psi_2(k^j) | \Psi_2(k^{j+1}) \rangle \tag{13.13}$$

where Ψ_1 and Ψ_2 are the wavefunctions of the first and second band respectively. The previous form is valid as long as the two band are not degenerate. Now lets write down Eq. 13.13 in a more suggestive form by defining a k-dependent density matrix

$$U_{lm}(k^j) = \langle \Psi_l(k^j) | \Psi_m(k^{j+1}) \rangle \tag{13.14}$$

where l, m run over the band indexes (in our case 1,2). For disentangled bands $U_{l,m} = 0$ for $i \neq j$ so that U is a diagonal square matrix. With the previous definition, Eq. 13.13 can be trivially rewritten as

$$e^{i\phi} = \det \left(\prod_j U(k^j) \right) \tag{13.15}$$

The previous expression in invariant upon band mixing. A local gauge rotation is a transformation of the form

$$\Psi \rightarrow R\Psi \tag{13.16}$$

where R is a matrix and Ψ a spinor wavefunction. In Eq. 13.15, the previous transformation will appear twice (once for the bra and once for the ket),so that the term of the product

$$U(k^j) R R^\dagger U(k^{j+1}) = U(k^j) U(k^{j+1}) \tag{13.17}$$

remains invariant for any band mixing.

To summarize, a gauge and mixing invariant form of the Berry curvature is given by

$$e^{i\phi} = \det\left(\prod_j U(k^j)\right) \tag{13.18}$$

Finally, once the Berry phase in the small path is known, the Berry curvature is calculated by.

$$\Omega = \frac{\phi}{S} \tag{13.19}$$

13.2 Mean field calculations

In this section we will briefly describe the mean field approach to solve electronic interactions by means of a selfconsistent one electron solution.

Lets assume the Hamiltonian has the form

$$H = H_0 + V \tag{13.20}$$

where H_0 is a free particle Hamiltonian and V is the interaction part. In the problems encountered, H_0 has a form

$$H_0 = t_{ij} c_j^\dagger c_i \tag{13.21}$$

where t_{ij} are the hopping amplitudes. The interaction part V is in the simplest case a density-density operator as given in the Hubbard model

$$V = U n_{i,\uparrow} n_{i,\downarrow} \tag{13.22}$$

We will assume that the interaction part is quadratic in two fermion operators

$$V = AB \tag{13.23}$$

where A and B are operators of the form $A = a_{ij} c_j^\dagger c_i$. In the case of the Hubbard model shown above, the operators read

$$A = c_{i\uparrow}^\dagger c_{i\uparrow} \tag{13.24}$$

$$B = c_{i\downarrow}^\dagger c_{i\downarrow} \tag{13.25}$$

In the following, we will look for solution where the fermions have vanishing fluctuations of the two operators A, B, with respect to their expectation value. Mathematically this is represented as

$$\langle (A - \langle A \rangle)(B - \langle B \rangle) \rangle = 0 \tag{13.26}$$

expanding the previous equation

$$AB = \langle A \rangle B + \langle B \rangle A - \langle A \rangle \langle B \rangle \tag{13.27}$$

Using Eq. 13.27 we can substitute the terms involving two operators in the interaction Hamiltonian by terms that only involve a single operator. Since terms with a single A, B operators are quadratic in the fermionic operators, this last step will transform the whole Hamiltonian into a quadratic fermion operator.

Therefore, the mean field antsaz gives the following substitution

$$H = H_0 + AB = H_0 + \langle A \rangle B + \langle B \rangle A - \langle A \rangle \langle B \rangle \tag{13.28}$$

The previous Hamiltonian involves the expectation value of the operators, which need the ground state wavefunction to be calculated. But to calculate the ground state we need the Hamiltonian, so that to get the solution we need the solution itself. To solve this problem a selfconsistent approach is taken. We start with an initial guess for the ground state wavefunction Ψ_0 and we plug it in Eq. 13.28. We calculate the expectation value of the operators A, B to get the full Hamiltonian H, and from there we calculate the new ground state solution Ψ_1. This procedure goes on until the solution Ψ_n and Ψ_{n-1} have a distance small enough. It is important to note that all the information is encoded in the mean field values $\langle A \rangle, \langle B \rangle$, so that from one iteration to next the one only those values have to be tracked.

Specifically, in each iteration the expectation values are calculated as

$$\langle A \rangle = \sum_{\text{occ}} = \langle \phi_i | A | \phi_i \rangle \tag{13.29}$$

where ϕ_i are the eigenfunctions of H. The previous sum runs over the occupied states, so that the number of electrons in the systems enters in how many waves are summed up. To look for the ground state, the states are filled from lower to bigger energy.

Usually oscillations between two solutions might arise. To quench such solutions a mixing between ground states is used. This mixing yields a new mean field values which are combination of the last iteration and the previous one.

$$\langle A \rangle^{\text{mixed}} = \nu \langle A \rangle_n + (1 - \nu) \langle A \rangle_{n-1} \tag{13.30}$$

where ν is the mixing parameter. In general, the bigger the value of ν the faster the convergence, but also the more unstable. Systems with a smooth convergence will reach the ground state independently on the value of ν, however systems with unstable convergence will need small values of ν (around 0.1) to reach a selfconsistent solution.

Finally, we will move to the case of the actual interaction Hamiltonians we used. The Hubbard model reads

$$V = \sum_i U n_{i,\uparrow} n_{i,\downarrow} \tag{13.31}$$

where i runs over the different sites of the lattice. The mean field antsaz has to be applied to the operators in every site of the lattice. Therefore, the Hamiltonian consists on n pairs of density operators, where n is the number of sites. It is important to note that this antsaz creates a preferred direction for the magnetization. This is easily seen by considering the difference in energy between a solution with in-plane magnetization and off-plane. For the off-plane one, the interacting energy is

$$E_V^{\text{off}} = U \sum_i \langle n_{i\uparrow} \rangle \langle n_{i\downarrow} \rangle \tag{13.32}$$

where E_V can be non zero because the expectation values are also non zero. In comparison, for an in-plane solution the interacting energy is zero because the expectation value of the spin in an axis perpendicular to the actual magnetism is zero.

$$E_V^{in} = 0 \tag{13.33}$$

This anomaly in the mean field antsaz does not give absurd results as long as all the solution considered show off-plane magnetization. The mean field antsaz shows broken spin symmetry, which is the reason why off-plane and in-plane solutions are not equivalent. To track down this flaw in the theory we should come back to the original Hubbard Hamiltonian written in terms of the fermionic operators

$$V = U c_{i\uparrow}^\dagger c_{i,\uparrow} c_{i\downarrow}^\dagger c_{i,\downarrow} \tag{13.34}$$

The energy of the systems will be the expectation value of the four operators

$$\langle V \rangle = U \langle c_{i\uparrow}^\dagger c_{i,\uparrow} c_{i\downarrow}^\dagger c_{i,\downarrow} \rangle \tag{13.35}$$

The four field operators expectation value can be transformed into the product of two operators by means of Wick's theorem

$$\langle V \rangle = U \left[\langle c_{i\uparrow}^\dagger c_{i,\uparrow} \rangle \langle c_{i\downarrow}^\dagger c_{i,\downarrow} \rangle - \langle c_{i\uparrow}^\dagger c_{i,\downarrow} \rangle \langle c_{i\downarrow}^\dagger c_{i,\uparrow} \rangle \right] \tag{13.36}$$

The first term in the previous equation is the density density operator expectation value as in Eq. 13.32. The second term is the exchange term, which vanishes provided the magnetism lies off-plane. This last feature is the explanation why the original mean field antsaz was valid only for off-plane magnetism. The mean field operators for the second term in Eq. 13.36 are

$$A = c^{\dagger}_{i\uparrow} c_{i,\downarrow} \tag{13.37}$$

$$B = c^{\dagger}_{i\downarrow} c_{i,\uparrow} \tag{13.38}$$

In the general case of a non-collinear magnetic structure, both the density-density terms and the exchange terms have to be included in the selfconsistent calculation to have a mean field antsaz that does not break spin rotation symmetry.

13.3 The kernel polynomial method

One of the computational limitations of the calculations presented in this thesis is their computational cost. In particular, the diagonalization of a general Hamiltonian scales cubic with the number of atoms, so that making the system twice as big turns the calculation 8 times slower. Even in the case of sparse matrices, such as tight binding Hamiltonians, the calculations become way slower as the system size increases. Iteration diagonalization methods, such as Arnoldi or Lanczos can provide a temporal improvement of the properties that we want to study rely on few states that are located close in energy. However, when the properties that we are interested in are located in large spectral window, as in the case of the density of states, Arnoldi or Lanczos are no longer a good solution. To tackle that kind of problems, it is convenient to use the so called kernel polynomial method (KPM) [540].

The method consists on calculating the polynomial expansion of the desired quantity in terms of Chebyshev polynomials. Chebyshev polynomials require that the function to be expanded is bounded to the interval (-1,1), so that usually a scaling of the function is needed to fit in that interval. The function is expanded as

$$f(x) = \frac{1}{\pi\sqrt{1-x^2}}\left[\mu_0 + 2\sum_n \mu_n T_n(x)\right] \tag{13.39}$$

where T_n are the Chebyshev polynomials defined by the recursion relations

$$T_0(x) = 1 \tag{13.40}$$

$$T_1(x) = x \tag{13.41}$$

$$T_{m+1}(x) = 2xT_m(x) - T_{m-1}(x) \tag{13.42}$$

and μ_n are the moments of the function that is expanded

$$\mu_n = \int_{-1}^{1} f(x)T_n(x)dx \tag{13.43}$$

Therefore, once the moments μ_n are calculated, the function can be reconstructed.

In the situation that we are interested in, the variable x will be the energy, and our goal is to expand the local density of states of the system. The integral that we have to calculate is thus

$$\mu_n = \sum_k \int_{-1}^{1} |\langle i|k\rangle|^2 \delta(E_k - E)T_n(E) = \sum_k |\langle i|k\rangle|^2 T_n(E_k) = \langle i|T_n(H)|i\rangle \tag{13.44}$$

where H is the Hamiltonian of the system. It is important to note that the last term in the previous equation is calculated iterative by using the recursion relation

$$T_{m+1}(H)|i\rangle = 2HT_m(H)|i\rangle - T_{m-1}(H)|i\rangle \tag{13.45}$$

Initially, a vector localized in a site is created. Then Eq. 13.45 is applied to obtain the set of vectors that will allow to calculate the moments μ_n. The projection of all those vectors over the first one are precisely the moments μ_n. It is worth to remark that for a sparse Hamiltonian the previous workflow scales linear with n, where n is the dimension of the Hamiltonian.

In the numerical implementation, a finite amount of polynomials is used. The truncation of the series creates un-physical oscillations in the spectra, so called Gibbs oscillations[541]. To heal such anomalous behavior, the terms of the series are redefined according to a certain scheme.

$$\mu_n \to g_n(N)\mu_n \tag{13.46}$$

such redefinition is equivalent to convolve the function $f(x)$ with a Kernel function $K(x, y)$ so that

$$f(x) \to \int K(x, y)f(y) \tag{13.47}$$

The redefinition of the coefficients depends on the number of coefficients. In particular, for the calculation of the density of states, a suitable Kernel to use is the so called Jackson kernel[542].

$$g_n = \frac{1}{N+1}\left[(N - n + 1)\cos\frac{\pi n}{N+1} + \sin\frac{\pi n}{N+1}\cot\frac{\pi}{N+1}\right] \tag{13.48}$$

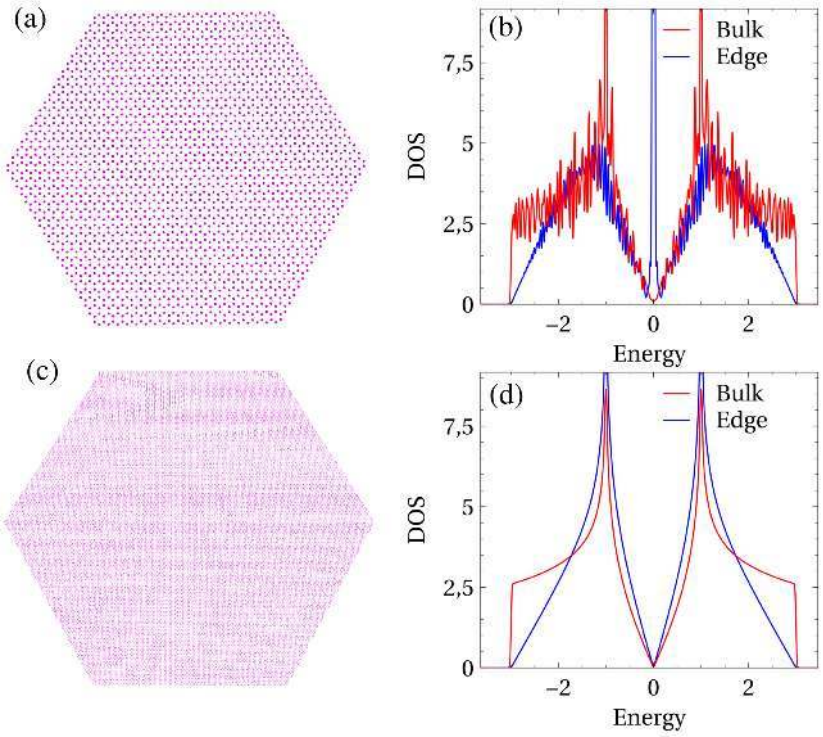

Figure 13.1: (a) Island with 2400 atoms and DOS (b) in the bulk and in the zigzag edge of the island. (c) Island with 60000 atoms, showing the DOS (d) in the center and in the armchair edge.

which can be obtained by requiring that the Kernel minimizes the quantity Q, which is basically the width of the peak of $K(x, y)$ at $x = y$

$$Q = \int (x - y)^2 K(x, y) dx dy \tag{13.49}$$

The local density of states takes the form

$$D_i(E) = \frac{1}{\pi\sqrt{1 - E^2}} \left[\mu_0 + 2 \sum_n \mu_n T_n(E) \right] \tag{13.50}$$

There are two ways to calculate the total density of states. The first one consists on calculate the local density of states for every site and sum everything, which yields a quadratic scaling with the size of the system. The alternative way consists on calculating the DOS starting with random vectors, instead of localized vectors. This is equivalent to approximate the trace of the Chebyshev expansion by a random

average

$$\mu_n = \frac{1}{N}\sum_i \langle i|T_n(H)|i\rangle \approx \langle\langle v|T_n(H)|v\rangle\rangle_v \tag{13.51}$$

where v are vectors chosen randomly.

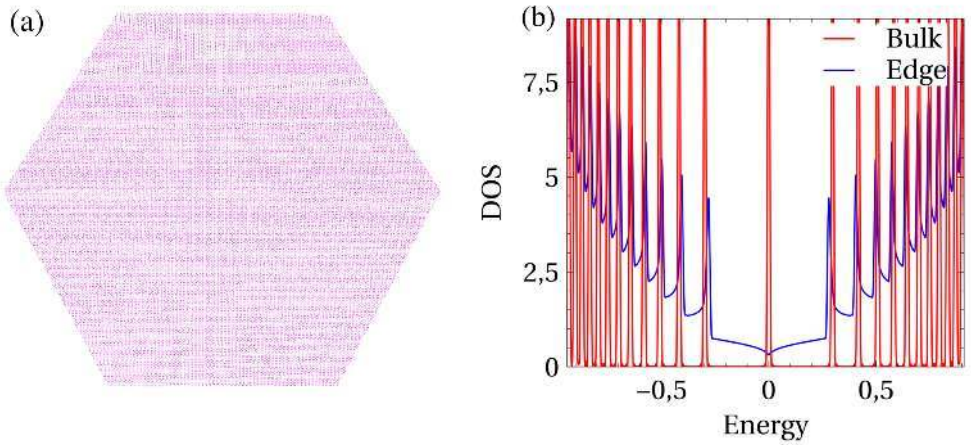

Figure 13.2: (a) Sketch of a graphene armchair island with 60000 atoms. Upon application of a perpendicular magnetic field, the spectrum of the system dramatically changes (b). The bulk becomes completely insulating, whereas the edge sustains gapless edge states. The DOS in the bulk accumulates at certain energies, forming Landau levels.

In the following we will present typical examples where the power of the Kernel polynomial method becomes apparent. The first system that we will consider is rather big graphene island. We show in Fig. 13.1 the structure of two graphene islands and their density of states (DOS), in the bulk and on the edge. For the island with zigzag edges, the DOS in the edge shows a peak corresponding to the edge states. For the island with armchair edges, the edge has a depletion of states at high energies, and zero DOS at zero energy. It is worth to note that for the bigger island, the bulk DOS resembles the one of bulk graphene, whereas the small one shows oscillation due to finite size effects.

A way more interesting case is a graphene island in the presence of magnetic field as shown in Fig. 13.2. In this situation, the linear density of states of pristine graphene disappears, giving rise to a bulk DOS concentrated in Landau levels. At the same time, the edge shows DOS when the bulk is insulating, corresponding to the edge states of the quantum Hall regime.

Chapter 14

Conclusions

Graphene proved to be one of the most remarkable materials discovered in the last years, both for its potential in electronics, as well as its simplicity to be synthesized. In this thesis we have presented different mechanisms to drive graphene systems into topological states. In addition, we showed how the different topological states can break down, and their resilience towards perturbations.

Regarding quantum spin Hall states, we discussed the two different mechanism by which they can arise in graphene, intrinsic spin orbit coupling and ferromagnetic quantum Hall effect. We showed that in the intrinsic quantum spin Hall effect, direction of the magnetization totally changed the transport properties, with a very small energy cost. For the ferromagnetic Hall state, we unveiled how the different electronic orders determined the topological state of the system, crucial to the proposal for Majorana bound states. Furthermore, we showed how inhomogeneous magnetism lead to backscattering channels, and how different spin waves emerge from such inhomogeneities. Therefore, magnetism opens different backscattering channels in both mechanisms, which suggests that transport measurements in those systems can act as detectors of local magnetic moments.

Later we moved to mechanism driving graphene into a quantum anomalous Hall insulator. We showed how topological magnetic textures called skyrmions imprint their topological number into the graphene electronic structure. Remarkably, we show that this effect happened at arbitrary low coupling, in comparison with any other proposal. These phenomena suggested that graphene can be used as probe of non-trivial magnetic textures, by measuring anomalous transport signals. We also showed how the quantum anomalous Hall effect can arise in antiferromagnetic honeycomb lattices, for several multilayered states. This last proposal would be specially appealing to be realized in honeycomb oxides, where the interplay between correlations and spin orbit coupling could lead to anomalous Hall effect without net magnetization.

After exploring the single electron topological states, we entered the land where

magnetism encountered superconductivity. We showed that conventional magnetic impurities do not create bound states in graphene with proximized to superconductors, whereas single hydrogen deposition created a magnetic moments that binds very special superconducting Shiba in-gap states. We showed that such states break the conventional Shiba theory, and in particular allow to tune the in-gap energy by means of temperature. Furthermore, we showed that such in-gap states could be used as building blocks to create a one-dimensional topological superconductor. Finally, we moved to our proposal of Majorana bound states without any kind of spin orbit coupling, exploiting the topological non-trivial properties of the quantum Hall effect and symmetry broken Dirac equation. We showed how the unique quantum spin Hall effect in graphene driven by magnetic field created the chiral channel that upon superconducting pairing creates a p-wave superconductor. And more importantly, we showed that a similar mechanism could be used in the antiferromagnetic state, generating interface states with valley nature, that could also find a similar realization in antiferromagnetic oxides.

Finally, we showed how the tight binding methods techniques used could also be applied to other 2D material, taking advantage of powerful density functional techniques, and the Wannierization procedure. We showed how MoS_2 shows unconventional quantum Hall effect due to valley orbital fields, and how topological insulator and topological superconductors can be engineered in complex oxides.

We have also presented a computational tool that allows non experts to reproduce many of the calculations presented in this thesis. The computational package Quantum Honeycomp, it is based fully on free software and is totally open, free and publicly available under the GPL public license. The program was intended to be as simple as possible, providing powerful numerical techniques and with a user friendly plug and play interface.

Acknowledgements

I thank Joaquin for all the scientific guidance and strong motivation given during these years. I specially appreciate having learned the importance of having fun when working, and of recognizing the importance of team work and communication. I thank all my collaborators for the fruitful results we got, and specially Victor Pardo for his help. I also thank SPINOGRAPH for this opportunity, Pablo San Jose for his suggestion of the kernel polynomial method, David Jacob for showing the embedding method, Vitor Oliveira for the amazing setup of the cluster and CSIC for the hospitality during the secondment.

I thank all my colleagues for all the nice experiences we shared, both during these rainy years in Braga as well as the sunny months in Alicante. Among them, I specially thank Noel and Teresa.

Finally, I thank my parents for the motivation they have always given to me.

Bibliography

[1] Lilienfeld Julius Edgar. *Method and apparatus for controlling electric currents*. US Patent 1,745,175. 1930.

[2] Michio Kaku. *Physics of the future: How science will shape human destiny and our daily lives by the year 2100*. Anchor, 2012.

[3] Grant Heiken, David Vaniman, and Bevan M French. *Lunar sourcebook: A user's guide to the Moon*. CUP Archive, 1991.

[4] Zang-Hee Cho. *Foundations of medical imaging*. Wiley-Interscience, 1993.

[5] Nick Couldry. *Media, society, world: Social theory and digital media practice*. Polity, 2012.

[6] Saw-Wai Hia. "Review Article-Scanning tunneling microscopy single atom/molecule manipulation and its application to nanoscience and technology". In: *Journal of Vacuum Science and Technology-Section B* 23.4 (2005), pp. 1351–1360.

[7] I PRESENT. "Cramming more components onto integrated circuits". In: *Readings in computer architecture* 56 (2000).

[8] John Bardeen, Leon N Cooper, and J Robert Schrieffer. "Theory of superconductivity". In: *Physical Review* 108.5 (1957), p. 1175.

[9] Marvin E Cage, Kv Klitzing, AM Chang, F Duncan, M Haldane, RB Laughlin, AMM Pruisken, DJ Thouless, Richard E Prange, and Steven M Girvin. *The quantum Hall effect*. Springer Science & Business Media, 2012.

[10] Philip W Anderson. "Plasmons, gauge invariance, and mass". In: *Physical Review* 130.1 (1963), p. 439.

[11] Peter W Higgs. "Broken symmetries and the masses of gauge bosons". In: *Physical Review Letters* 13.16 (1964), p. 508.

[12] Cristina Buzea and Tsutomu Yamashita. "Review of the superconducting properties of MgB2". In: *Superconductor Science and Technology* 14.11 (2001), R115.

[13] P Dai, BC Chakoumakos, GF Sun, KW Wong, Y Xin, and DF Lu. "Synthesis and neutron powder diffraction study of the superconductor HgBa 2 Ca 2 Cu 3 O 8+ δ by Tl substitution". In: *Physica C: Superconductivity* 243.3 (1995), pp. 201–206.

[14] J Weis and K Von Klitzing. "Metrology and microscopic picture of the integer quantum Hall effect". In: *Philosophical Transactions of the Royal Society of London A: Mathematical, Physical and Engineering Sciences* 369.1953 (2011), pp. 3954–3974.

[15] Beat Jeckelmann and Blaise Jeanneret. "The quantum Hall effect as an electrical resistance standard". In: *Reports on Progress in Physics* 64.12 (2001), p. 1603.

[16] F Guinea, AH Castro Neto, and NMR Peres. "Electronic states and Landau levels in graphene stacks". In: *Physical Review B* 73.24 (2006), p. 245426.

[17] Konstantin S Novoselov, Z Jiang, Y Zhang, SV Morozov, HL Stormer, U Zeitler, JC Maan, GS Boebinger, P Kim, and AK Geim. "Room-temperature quantum Hall effect in graphene". In: *Science* 315.5817 (2007), pp. 1379–1379.

[18] Jean-Claude Tolédano and Pierre Tolédano. *The Landau theory of phase transitions*. World Scientific, 1987.

[19] M Zahid Hasan and Charles L Kane. "Colloquium: topological insulators". In: *Reviews of Modern Physics* 82.4 (2010), p. 3045.

[20] DJ Thouless, M Kohmoto, MP Nightingale, and M Den Nijs. "Quantized Hall conductance in a two-dimensional periodic potential". In: *Physical Review Letters* 49.6 (1982), p. 405.

[21] David J Thouless. *Topological quantum numbers in nonrelativistic physics*. World Scientific Singapore, 1998.

[22] Cui-Zu Chang, Weiwei Zhao, Duk Y Kim, Haijun Zhang, Badih A Assaf, Don Heiman, Shou-Cheng Zhang, Chaoxing Liu, Moses HW Chan, and Jagadeesh S Moodera. "High-precision realization of robust quantum anomalous Hall state in a hard ferromagnetic topological insulator". In: *Nature materials* 14.5 (2015), pp. 473–477.

[23] Pablo San-Jose, Elsa Prada, Edward McCann, and Henning Schomerus. "Pseudospin valve in bilayer graphene: towards graphene-based pseudospintronics". In: *Physical review letters* 102.24 (2009), p. 247204.

[24] A Rycerz, J Tworzydło, and CWJ Beenakker. "Valley filter and valley valve in graphene". In: *Nature Physics* 3.3 (2007), pp. 172–175.

[25] Jairo Sinova and Igor Žutić. "New moves of the spintronics tango". In: *Nature materials* 11.5 (2012), pp. 368–371.

[26] H Kurebayashi, Jairo Sinova, D Fang, AC Irvine, TD Skinner, J Wunderlich, V Novák, RP Campion, BL Gallagher, EK Vehstedt, et al. "An antidamping spin-orbit torque originating from the Berry curvature". In: *Nature nanotechnology* 9.3 (2014), pp. 211–217.

[27] Igor Žutić, Jaroslav Fabian, and S Das Sarma. "Spintronics: Fundamentals and applications". In: *Reviews of modern physics* 76.2 (2004), p. 323.

[28] David D Awschalom and Michael E Flatté. "Challenges for semiconductor spintronics". In: *Nature Physics* 3.3 (2007), pp. 153–159.

[29] Jaroslav Fabian and S Das Sarma. "Spin relaxation of conduction electrons". In: *Journal of Vacuum Science & Technology B* 17.4 (1999), pp. 1708–1715.

[30] Wei Han, Roland K Kawakami, Martin Gmitra, and Jaroslav Fabian. "Graphene spintronics". In: *Nature nanotechnology* 9.10 (2014), pp. 794–807.

[31] Mario Norberto Baibich, Jean Marc Broto, Albert Fert, F Nguyen Van Dau, Frédéric Petroff, P Etienne, G Creuzet, A Friederich, and J Chazelas. "Giant magnetoresistance of (001) Fe/(001) Cr magnetic superlattices". In: *Physical review letters* 61.21 (1988), p. 2472.

[32] Di Xiao, Ming-Che Chang, and Qian Niu. "Berry phase effects on electronic properties". In: *Reviews of modern physics* 82.3 (2010), p. 1959.

[33] Naoto Nagaosa and Yoshinori Tokura. "Topological properties and dynamics of magnetic skyrmions". In: *Nature nanotechnology* 8.12 (2013), pp. 899–911.

[34] S Das Sarma, Jaroslav Fabian, Xuedong Hu, and Igor Zutić. "Spin electronics and spin computation". In: *Solid State Communications* 119.4 (2001), pp. 207–215.

[35] Markus König, Hartmut Buhmann, Laurens W. Molenkamp, Taylor Hughes, Chao-Xing Liu, Xiao-Liang Qi, and Shou-Cheng Zhang. "The quantum spin Hall effect: theory and experiment". In: *Journal of the Physical Society of Japan* 77.3 (2008), p. 031007.

[36] Charles L Kane and Eugene J Mele. "Quantum spin Hall effect in graphene". In: *Physical review letters* 95.22 (2005), p. 226801.

[37] David Hsieh, Dong Qian, Lewis Wray, YuQi Xia, Yew San Hor, RJ Cava, and M Zahid Hasan. "A topological Dirac insulator in a quantum spin Hall phase". In: *Nature* 452.7190 (2008), pp. 970–974.

[38] MP Kostylev, AA Serga, T Schneider, B Leven, and B Hillebrands. "Spin-wave logical gates". In: *Applied Physics Letters* 87.15 (2005), p. 153501.

[39] Jairo Sinova, Dimitrie Culcer, Q Niu, NA Sinitsyn, T Jungwirth, and AH MacDonald. "Universal intrinsic spin Hall effect". In: *Physical Review Letters* 92.12 (2004), p. 126603.

[40] Joerg Wunderlich, Bernd Kaestner, Jairo Sinova, and Tomas Jungwirth. "Experimental observation of the spin-Hall effect in a two-dimensional spin-orbit coupled semiconductor system". In: *Physical review letters* 94.4 (2005), p. 047204.

[41] Jairo Sinova, Sergio O Valenzuela, J Wunderlich, CH Back, and T Jungwirth. "Spin Hall effects". In: *Reviews of Modern Physics* 87.4 (2015), p. 1213.

[42] Branislav K Nikolić, Satofumi Souma, Liviu P Zârbo, and Jairo Sinova. "Nonequilibrium spin Hall accumulation in ballistic semiconductor nanostructures". In: *Physical review letters* 95.4 (2005), p. 046601.

[43] Dimitrie Culcer, Jairo Sinova, NA Sinitsyn, T Jungwirth, AH MacDonald, and Q Niu. "Semiclassical spin transport in spin-orbit-coupled bands". In: *Physical review letters* 93.4 (2004), p. 046602.

[44] AH Castro Neto, F Guinea, NMR Peres, Kostya S Novoselov, and Andre K Geim. "The electronic properties of graphene". In: *Reviews of modern physics* 81.1 (2009), p. 109.

[45] N David Mermin and Ho Wagner. "Absence of ferromagnetism or antiferromagnetism in one-or two-dimensional isotropic Heisenberg models". In: *Physical Review Letters* 17.22 (1966), p. 1133.

[46] Sidney Coleman. "There are no Goldstone bosons in two dimensions". In: *Communications in Mathematical Physics* 31.4 (1973), pp. 259–264.

[47] Khaled Parvez, Zhong-Shuai Wu, Rongjin Li, Xianjie Liu, Robert Graf, Xinliang Feng, and Klaus Mullen. "Exfoliation of graphite into graphene in aqueous solutions of inorganic salts". In: *Journal of the American Chemical Society* 136.16 (2014), pp. 6083–6091.

[48] Andre K Geim and Konstantin S Novoselov. "The rise of graphene". In: *Nature materials* 6.3 (2007), pp. 183–191.

[49] Seung Jin Chae, Fethullah Güneş, Ki Kang Kim, Eun Sung Kim, Gang Hee Han, Soo Min Kim, Hyeon-Jin Shin, Seon-Mi Yoon, Jae-Young Choi, Min Ho Park, et al. "Synthesis of large-area graphene layers on poly-nickel substrate by chemical vapor deposition: wrinkle formation". In: *Advanced Materials* 21.22 (2009), pp. 2328–2333.

[50] Timothy H Vo, Mikhail Shekhirev, Donna A Kunkel, Martha D Morton, Eric Berglund, Lingmei Kong, Peter M Wilson, Peter A Dowben, Axel Enders, and Alexander Sinitskii. "Large-scale solution synthesis of narrow graphene nanoribbons". In: *Nature communications* 5 (2014).

[51] Long Chen, Yenny Hernandez, Xinliang Feng, and Klaus Mullen. "From nanographene and graphene nanoribbons to graphene sheets: chemical synthesis". In: *Angewandte Chemie International Edition* 51.31 (2012), pp. 7640–7654.

[52] NMR Peres. "Colloquium: The transport properties of graphene: An introduction". In: *Reviews of Modern Physics* 82.3 (2010), p. 2673.

[53] T Stauber, NMR Peres, and F Guinea. "Electronic transport in graphene: A semiclassical approach including midgap states". In: *Physical Review B* 76.20 (2007), p. 205423.

[54] Vitor M Pereira, F Guinea, JMB Lopes Dos Santos, NMR Peres, and AH Castro Neto. "Disorder induced localized states in graphene". In: *Physical review letters* 96.3 (2006), p. 036801.

[55] NMR Peres, AH Castro Neto, and F Guinea. "Conductance quantization in mesoscopic graphene". In: *Physical Review B* 73.19 (2006), p. 195411.

[56] Liam Britnell, Roman V Gorbachev, Rashid Jalil, Branson D Belle, Fred Schedin, Mikhail I Katsnelson, Laurence Eaves, Sergey V Morozov, Alexander S Mayorov, Nuno MR Peres, et al. "Electron tunneling through ultrathin boron nitride crystalline barriers". In: *Nano letters* 12.3 (2012), pp. 1707–1710.

[57] NMR Peres, F Guinea, and AH Castro Neto. "Electronic properties of disordered two-dimensional carbon". In: *Physical Review B* 73.12 (2006), p. 125411.

[58] AJ Chaves, NMR Peres, and Felipe A Pinheiro. "Anderson localization of light in disordered superlattices containing graphene layers". In: *Physical Review B* 92.19 (2015), p. 195425.

[59] Federico Muñoz-Rojas, David Jacob, Joaquín Fernández-Rossier, and JJ Palacios. "Coherent transport in graphene nanoconstrictions". In: *Physical Review B* 74.19 (2006), p. 195417.

[60] JJ Palacios, AJ Pérez-Jiménez, E Louis, E SanFabián, and JA Vergés. "First-principles phase-coherent transport in metallic nanotubes with realistic contacts". In: *Physical review letters* 90.10 (2003), p. 106801.

[61] Federico Muñoz-Rojas, Joaquín Fernández-Rossier, and JJ Palacios. "Giant magnetoresistance in ultrasmall graphene based devices". In: *Physical review letters* 102.13 (2009), p. 136810.

[62] R Ahuja, S Auluck, J Trygg, JM Wills, O Eriksson, and B Johansson. "Electronic structure of graphite: Effect of hydrostatic pressure". In: *Physical Review B* 51.8 (1995), p. 4813.

[63] Sumanta Bhandary, Saurabh Ghosh, Heike Herper, Heiko Wende, Olle Eriksson, and Biplab Sanyal. "Graphene as a reversible spin manipulator of molecular magnets". In: *Physical review letters* 107.25 (2011), p. 257202.

[64] Zhiyong Wang, Chi Tang, Raymond Sachs, Yafis Barlas, and Jing Shi. "Proximity-induced ferromagnetism in graphene revealed by the anomalous hall effect". In: *Physical review letters* 114.1 (2015), p. 016603.

[65] JC Leutenantsmeyer, AA Kaverzin, M Wojtaszek, and BJ van Wees. "Proximity induced room-temperature ferromagnetism in graphene probed with spin currents". In: *arXiv preprint arXiv:1601.00995* (2016).

[66] Katsuyoshi Komatsu, Chuan Li, S Autier-Laurent, H Bouchiat, and S Guéron. "Superconducting proximity effect in long superconductor/graphene/superconductor junctions: From specular Andreev reflection at zero field to the quantum Hall regime". In: *Physical Review B* 86.11 (2012), p. 115412.

[67] Pablo San-Jose, A Gutiérrez-Rubio, Mauricio Sturla, and Francisco Guinea. "Spontaneous strains and gap in graphene on boron nitride". In: *Physical Review B* 90.7 (2014), p. 075428.

[68] Gianluca Giovannetti, Petr A Khomyakov, Geert Brocks, Paul J Kelly, and Jeroen van den Brink. "Substrate-induced band gap in graphene on hexagonal boron nitride: Ab initio density functional calculations". In: *Physical Review B* 76.7 (2007), p. 073103.

[69] Kallol Roy, Medini Padmanabhan, Srijit Goswami, T Phanindra Sai, Gopalakrishnan Ramalingam, Srinivasan Raghavan, and Arindam Ghosh. "Graphene-MoS2 hybrid structures for multifunctional photoresponsive memory devices". In: *Nature nanotechnology* 8.11 (2013), pp. 826–830.

[70] L Vicarelli, MS Vitiello, D Coquillat, A Lombardo, AC Ferrari, W Knap, M Polini, V Pellegrini, and A Tredicucci. "Graphene field-effect transistors as room-temperature terahertz detectors". In: *Nature materials* 11.10 (2012), pp. 865–871.

[71] DK Efetov, L Wang, C Handschin, KB Efetov, J Shuang, R Cava, T Taniguchi, K Watanabe, J Hone, CR Dean, et al. "Specular Interband Andreev Reflections in Graphene". In: *arXiv preprint arXiv:1505.04812* (2015).

[72] Jeil Jung, Ashley M DaSilva, Allan H MacDonald, and Shaffique Adam. "Origin of band gaps in graphene on hexagonal boron nitride". In: *Nature communications* 6 (2015).

[73] Meng-Lin Tsai, Sheng-Han Su, Jan-Kai Chang, Dung-Sheng Tsai, Chang-Hsiao Chen, Chih-I Wu, Lain-Jong Li, Lih-Juann Chen, and Jr-Hau He. "Monolayer MoS2 heterojunction solar cells". In: *Acs Nano* 8.8 (2014), pp. 8317–8322.

[74] Jelena Klinovaja and Daniel Loss. "Spintronics in MoS 2 monolayer quantum wires". In: *Physical Review B* 88.7 (2013), p. 075404.

[75] Branimir Radisavljevic, Aleksandra Radenovic, Jacopo Brivio, V Giacometti, and A Kis. "Single-layer MoS2 transistors". In: *Nature nanotechnology* 6.3 (2011), pp. 147–150.

[76] Andrew Steane. "Quantum computing". In: *Reports on Progress in Physics* 61.2 (1998), p. 117.

[77] Peter W Shor. "Polynomial-time algorithms for prime factorization and discrete logarithms on a quantum computer". In: *SIAM review* 41.2 (1999), pp. 303–332.

[78] Daniel Loss and David P DiVincenzo. "Quantum computation with quantum dots". In: *Physical Review A* 57.1 (1998), p. 120.

[79] Bruce E Kane. "A silicon-based nuclear spin quantum computer". In: *nature* 393.6681 (1998), pp. 133–137.

[80] Steven R Elliott and Marcel Franz. "Colloquium: Majorana fermions in nuclear, particle, and solid-state physics". In: *Reviews of Modern Physics* 87.1 (2015), p. 137.

[81] Meng Cheng, Roman M Lutchyn, Victor Galitski, and S Das Sarma. "Tunneling of anyonic Majorana excitations in topological superconductors". In: *Physical Review B* 82.9 (2010), p. 094504.

[82] Thaddeus D Ladd, Fedor Jelezko, Raymond Laflamme, Yasunobu Nakamura, Christopher Monroe, and Jeremy L O'Brien. "Quantum computers". In: *Nature* 464.7285 (2010), pp. 45–53.

[83] Andrea Franchini Young, JD Sanchez-Yamagishi, B Hunt, Sang Hyun Choi, K Watanabe, T Taniguchi, RC Ashoori, and Pablo Jarillo-Herrero. "Tunable symmetry breaking and helical edge transport in a graphene quantum spin Hall state". In: *Nature* 505.7484 (2014), pp. 528–532.

[84] Boris Kayser. "Are neutrinos their own antiparticles?" In: *Journal of Physics: Conference Series*. Vol. 173. 1. IOP Publishing. 2009, p. 012013.

[85] Gerd Binnig and Heinrich Rohrer. "Scanning tunneling microscopy—from birth to adolescence". In: *reviews of modern physics* 59.3 (1987), p. 615.

[86] Richard P Feynman. "There's plenty of room at the bottom". In: *Engineering and science* 23.5 (1960), pp. 22–36.

[87] URL: http://www.spinograph.org/.

[88] URL: https://github.com/joselado/quantum-honeycomp.

[89] URL: https://sourceforge.net/projects/quantum-honeycomp/.

[90] Kostya S Novoselov, Andre K Geim, SV Morozov, D Jiang, Y_ Zhang, SV Dubonos, IV Grigorieva, and AA Firsov. "Electric field effect in atomically thin carbon films". In: *science* 306.5696 (2004), pp. 666–669.

[91] KSA Novoselov, Andre K Geim, SVb Morozov, Da Jiang, MIc Katsnelson, IVa Grigorieva, SVb Dubonos, and AAb Firsov. "Two-dimensional gas of massless Dirac fermions in graphene". In: *nature* 438.7065 (2005), pp. 197–200.

[92] Yuanbo Zhang, Yan-Wen Tan, Horst L Stormer, and Philip Kim. "Experimental observation of the quantum Hall effect and Berry's phase in graphene". In: *Nature* 438.7065 (2005), pp. 201–204.

[93] Klaus von Klitzing. "The quantized Hall effect". In: *Reviews of Modern Physics* 58.3 (1986), p. 519.

[94] A. H. Castro Neto, F. Guinea, N. M. R. Peres, K. S. Novoselov, and A. K. Geim. "The electronic properties of graphene". In: *Rev. Mod. Phys.* 81 (1 2009), pp. 109–162.

[95] Mikhail I Katsnelson. "Graphene: carbon in two dimensions". In: *Materials today* 10.1 (2007), pp. 20–27.

[96] Patrick Vogt, Paola De Padova, Claudio Quaresima, Jose Avila, Emmanouil Frantzeskakis, Maria Carmen Asensio, Andrea Resta, Bénédicte Ealet, and Guy Le Lay. "Silicene: compelling experimental evidence for graphenelike two-dimensional silicon". In: *Physical review letters* 108.15 (2012), p. 155501.

[97] Cheng-Cheng Liu, Wanxiang Feng, and Yugui Yao. "Quantum spin Hall effect in silicene and two-dimensional germanium". In: *Physical review letters* 107.7 (2011), p. 076802.

[98] Yong Xu, Binghai Yan, Hai-Jun Zhang, Jing Wang, Gang Xu, Peizhe Tang, Wenhui Duan, and Shou-Cheng Zhang. "Large-gap quantum spin Hall insulators in tin films". In: *Physical review letters* 111.13 (2013), p. 136804.

[99] ZF Wang, Zheng Liu, and Feng Liu. "Organic topological insulators in organometallic lattices". In: *Nature communications* 4 (2013), p. 1471.

[100] Chengwang Niu, Gustav Bihlmayer, Hongbin Zhang, Daniel Wortmann, Stefan Blügel, and Yuriy Mokrousov. "Functionalized bismuth films: Giant gap quantum spin Hall and valley-polarized quantum anomalous Hall states". In: *Physical Review B* 91.4 (2015), p. 041303.

[101] Marco Polini, Francisco Guinea, Maciej Lewenstein, Hari C Manoharan, and Vittorio Pellegrini. "Artificial honeycomb lattices for electrons, atoms and photons". In: *Nature nanotechnology* 8.9 (2013), pp. 625–633.

[102] Shun-Qing Shen. *Topological Insulators: Dirac Equation in Condensed Matters*. Vol. 174. Springer Science & Business Media, 2013.

[103] Robert B Laughlin. "Quantized Hall conductivity in two dimensions". In: *Physical Review B* 23.10 (1981), p. 5632.

[104] Bertrand I Halperin. "Quantized Hall conductance, current-carrying edge states, and the existence of extended states in a two-dimensional disordered potential". In: *Physical Review B* 25.4 (1982), p. 2185.

[105] Charles L Kane and Eugene J Mele. "Z 2 topological order and the quantum spin Hall effect". In: *Physical review letters* 95.14 (2005), p. 146802.

[106] Charles L Kane and Eugene J Mele. "Quantum spin Hall effect in graphene". In: *Physical review letters* 95.22 (2005), p. 226801.

[107] F Duncan M Haldane. "Model for a quantum Hall effect without Landau levels: Condensed-matter realization of the" parity anomaly"". In: *Physical Review Letters* 61.18 (1988), p. 2015.

[108] Hongki Min, JE Hill, Nikolas A Sinitsyn, BR Sahu, Leonard Kleinman, and Allan H MacDonald. "Intrinsic and Rashba spin-orbit interactions in graphene sheets". In: *Physical Review B* 74.16 (2006), p. 165310.

[109] Yugui Yao, Fei Ye, Xiao-Liang Qi, Shou-Cheng Zhang, and Zhong Fang. "Spin-orbit gap of graphene: First-principles calculations". In: *Physical Review B* 75.4 (2007), p. 041401.

[110] Cheng-Cheng Liu, Hua Jiang, and Yugui Yao. "Low-energy effective Hamiltonian involving spin-orbit coupling in silicene and two-dimensional germanium and tin". In: *arXiv preprint arXiv:1108.2933* (2011).

[111] Markus König, Steffen Wiedmann, Christoph Brüne, Andreas Roth, Hartmut Buhmann, Laurens W Molenkamp, Xiao-Liang Qi, and Shou-Cheng Zhang. "Quantum spin Hall insulator state in HgTe quantum wells". In: *Science* 318.5851 (2007), pp. 766–770.

[112] Ivan Knez, Rui-Rui Du, and Gerard Sullivan. "Evidence for helical edge modes in inverted InAs/GaSb quantum wells". In: *Physical review letters* 107.13 (2011), p. 136603.

[113] B Andrei Bernevig, Taylor L Hughes, and Shou-Cheng Zhang. "Quantum spin Hall effect and topological phase transition in HgTe quantum wells". In: *Science* 314.5806 (2006), pp. 1757–1761.

[114] Chaoxing Liu, Taylor L Hughes, Xiao-Liang Qi, Kang Wang, and Shou-Cheng Zhang. "Quantum spin Hall effect in inverted type-II semiconductors". In: *Physical review letters* 100.23 (2008), p. 236601.

[115] Masanori Maruyama and Koichi Kusakabe. "Theoretical Prediction of Synthesis Methods to Create Magnetic Nanographite". In: *Journal of the Physical Society of Japan* 73.3 (2004), pp. 656–663.

[116] Katsunori Wakabayashi, Manfred Sigrist, and Mitsutaka Fujita. "Spin wave mode of edge-localized magnetic states in nanographite zigzag ribbons". In: *Journal of the Physical Society of Japan* 67.6 (1998), pp. 2089–2093.

[117] Young-Woo Son, Marvin L. Cohen, and Steven G. Louie. "Energy Gaps in Graphene Nanoribbons". In: *Phys. Rev. Lett.* 97 (21 2006), p. 216803.

[118] Eduardo V Castro, NMR Peres, and JMB Lopes dos Santos. "Localized states at zigzag edges of multilayer graphene and graphite steps". In: *EPL (Europhysics Letters)* 84.1 (2008), p. 17001.

[119] Cohen Marvin L. Louie Steven G. Son Young-Woo. "Half-metallic graphene nanoribbons". In: *Nature* 444 (7117 2006).

[120] J. Fernández-Rossier and J. J. Palacios. "Magnetism in Graphene Nanoislands". In: *Phys. Rev. Lett.* 99 (17 2007), p. 177204.

[121] Daniel Gunlycke, Denis A. Areshkin, Junwen Li, John W. Mintmire, and Carter T. White. "Graphene Nanostrip Digital Memory Device". In: *Nano Letters* 7.12 (2007), pp. 3608–3611.

[122] J. Fernández-Rossier. "Prediction of hidden multiferroic order in graphene zigzag ribbons". In: *Phys. Rev. B* 77 (7 2008), p. 075430.

[123] Woo Youn Kim and Kwang S Kim. "Prediction of very large values of magnetoresistance in a graphene nanoribbon device". In: *Nature nanotechnology* 3.7 (2008), pp. 408–412.

[124] Federico Muñoz-Rojas, Joaquín Fernández-Rossier, and JJ Palacios. "Giant magnetoresistance in ultrasmall graphene based devices". In: *Physical review letters* 102.13 (2009), p. 136810.

[125] Oleg V Yazyev. "Emergence of magnetism in graphene materials and nanostructures". In: *Reports on Progress in Physics* 73.5 (2010), p. 056501.

[126] Mahdi Zarea and Nancy Sandler. "Electron-electron and spin-orbit interactions in armchair graphene ribbons". In: *Physical review letters* 99.25 (2007), p. 256804.

[127] D Soriano and Joaquín Fernández-Rossier. "Spontaneous persistent currents in a quantum spin Hall insulator". In: *Physical Review B* 82.16 (2010), p. 161302.

[128] Daniel Gosálbez-Martínez, JJ Palacios, and Joaquín Fernández-Rossier. "Spin-orbit interaction in curved graphene ribbons". In: *Physical Review B* 83.11 (2011), p. 115436.

[129] JL Lado and J Fernández-Rossier. "Magnetic Edge Anisotropy in Graphene-like Honeycomb Crystals". In: *Physical review letters* 113.2 (2014), p. 027203.

[130] JL Lado and J Fernández-Rossier. "Noncollinear magnetic phases and edge states in graphene quantum Hall bars". In: *Physical Review B* 90.16 (2014), p. 165429.

[131] Roman Jackiw and C Rebbi. "Solitons with fermion number 1/2". In: *Physical Review D* 13.12 (1976), p. 3398.

[132] Jose L Lado, Jhon W González, and Joaquín Fernández-Rossier. "Quantum Hall effect in gapped graphene heterojunctions". In: *Physical Review B* 88.3 (2013), p. 035448.

[133] PA Maksimov, AV Rozhkov, and AO Sboychakov. "Localized electron states near the armchair edge of graphene". In: *Physical Review B* 88.24 (2013), p. 245421.

[134] Monica T Allen, Oles Shtanko, Ion Cosma Fulga, Anton Akhmerov, Kenji Watanabi, Takashi Taniguchi, Pablo Jarillo-Herrero, Leonid S Levitov, and Amir Yacoby. "Spatially resolved edge currents and guided-wave electronic states in graphene". In: *arXiv preprint arXiv:1504.07630* (2015).

[135] Pablo San-Jose Jose Lado, Ramón Aguado, Francisco Guinea, and Joaquín Fernández-Rossier. "Majorana Zero Modes in Graphene". In: *arXiv preprint arXiv:1506.04961* (2015).

[136] Ming-Hao Liu. "Gate-induced carrier density modulation in bulk graphene: theories and electrostatic simulation using Matlab pdetool". In: *Journal of Computational Electronics* 12.2 (2013), pp. 188–202.

[137] Valeri N Kotov, Bruno Uchoa, Vitor M Pereira, F Guinea, and AH Castro Neto. "Electron-electron interactions in graphene: Current status and perspectives". In: *Reviews of Modern Physics* 84.3 (2012), p. 1067.

[138] Jeil Jung, Tami Pereg-Barnea, and AH MacDonald. "Theory of interedge superexchange in zigzag edge magnetism". In: *Physical review letters* 102.22 (2009), p. 227205.

[139] Oleg V Yazyev, Rodrigo B Capaz, and Steven G Louie. "Theory of magnetic edge states in chiral graphene nanoribbons". In: *Physical Review B* 84.11 (2011), p. 115406.

[140] Kyoko Nakada, Mitsutaka Fujita, Gene Dresselhaus, and Mildred S Dresselhaus. "Edge state in graphene ribbons: Nanometer size effect and edge shape dependence". In: *Physical Review B* 54.24 (1996), p. 17954.

[141] Xiaolin Li, Xinran Wang, Li Zhang, Sangwon Lee, and Hongjie Dai. "Chemically derived, ultrasmooth graphene nanoribbon semiconductors". In: *Science* 319.5867 (2008), pp. 1229–1232.

[142] Liying Jiao, Xinran Wang, Georgi Diankov, Hailiang Wang, and Hongjie Dai. "Facile synthesis of high-quality graphene nanoribbons". In: *Nature nanotechnology* 5.5 (2010), pp. 321–325.

[143] Xinran Wang, Yijian Ouyang, Liying Jiao, Hailiang Wang, Liming Xie, Justin Wu, Jing Guo, and Hongjie Dai. "Graphene nanoribbons with smooth edges behave as quantum wires". In: *Nature nanotechnology* 6.9 (2011), pp. 563–567.

[144] Jiao Liying Yazyev Oleg V. Chen Yen-Chia Feng Juanjuan Zhang Xiaowei Capaz Rodrigo B.-Tour James M. Zettl Alex Louie Steven G. Dai Hongjie Crommie Michael F. Tao Chenggang. "Spatially resolving edge states of chiral graphene nanoribbons". In: *Nat Phys* 7 (8 2011).

[145] Gábor Zsolt Magda, Xiaozhan Jin, Imre Hagymási, Péter Vancsó, Zoltán Osváth, Péter Nemes-Incze, Chanyong Hwang, László P Biró, and Levente Tapasztó. "Room-temperature magnetic order on zigzag edges of narrow graphene nanoribbons". In: *Nature* 514.7524 (2014), pp. 608–611.

[146] Luis Brey and HA Fertig. "Electronic states of graphene nanoribbons studied with the Dirac equation". In: *Physical Review B* 73.23 (2006), p. 235411.

[147] Supriyo Datta. *Electronic transport in mesoscopic systems*. Cambridge university press, 1997.

[148] M Inui, SA Trugman, and Elihu Abrahams. "Unusual properties of midband states in systems with off-diagonal disorder". In: *Physical Review B* 49.5 (1994), p. 3190.

[149] JJ Palacios, Joaquın Fernández-Rossier, and L Brey. "Vacancy-induced magnetism in graphene and graphene ribbons". In: *Physical Review B* 77.19 (2008), p. 195428.

[150] D Soriano and Joaquín Fernández-Rossier. "Interplay between sublattice and spin symmetry breaking in graphene". In: *Physical Review B* 85.19 (2012), p. 195433.

[151] Jhon W González and Joaquín Fernández-Rossier. "Impurity states in the quantum spin Hall phase in graphene". In: *Physical Review B* 86.11 (2012), p. 115327.

[152] Mikito Koshino, Takahiro Morimoto, and Masatoshi Sato. "Topological zero modes and Dirac points protected by spatial symmetry and chiral symmetry". In: *Physical Review B* 90.11 (2014), p. 115207.

[153] P Potasz, AD Güçlü, and P Hawrylak. "Zero-energy states in triangular and trapezoidal graphene structures". In: *Physical review. B, Condensed matter and materials physics* 81.033403 (2010), pp. 1–4.

[154] Chengyong Xu, Guangfu Luo, Qihang Liu, Jiaxin Zheng, Zhimeng Zhang, Shigeru Nagase, Zhengxiang Gao, and Jing Lu. "Giant magnetoresistance in silicene nanoribbons". In: *Nanoscale* 4.10 (2012), pp. 3111–3117.

[155] J Jung and AH MacDonald. "Carrier density and magnetism in graphene zigzag nanoribbons". In: *arXiv preprint arXiv:0904.2396* (2009).

[156] S Sorella and E Tosatti. "Semi-metal-insulator transition of the Hubbard model in the honeycomb lattice". In: *EPL (Europhysics Letters)* 19.8 (1992), p. 699.

[157] Elliott H. Lieb. "Two theorems on the Hubbard model". In: *Phys. Rev. Lett.* 62 (10 1989), pp. 1201–1204. DOI: 10.1103/PhysRevLett.62.1201.

[158] Jeil Jung. "Nonlocal exchange effects in zigzag-edge magnetism of neutral graphene nanoribbons". In: *Physical Review B* 83.16 (2011), p. 165415.

[159] Oleg V. Yazyev and M. I. Katsnelson. "Magnetic Correlations at Graphene Edges: Basis for Novel Spintronics Devices". In: *Phys. Rev. Lett.* 100 (4 2008), p. 047209.

[160] HA Fertig and Luis Brey. "Luttinger liquid at the edge of undoped graphene in a strong magnetic field". In: *Physical review letters* 97.11 (2006), p. 116805.

[161] Manuel J Schmidt. "Bosonic field theory of tunable edge magnetism in graphene". In: *Physical Review B* 86.7 (2012), p. 075458.

[162] JM Luttinger and W Kohn. "Motion of electrons and holes in perturbed periodic fields". In: *Physical Review* 97.4 (1955), p. 869.

[163] Gordon W Semenoff. "Condensed-matter simulation of a three-dimensional anomaly". In: *Physical Review Letters* 53.26 (1984), p. 2449.

[164] Mikito Koshino and Tsuneya Ando. "Anomalous orbital magnetism in Dirac-electron systems: Role of pseudospin paramagnetism". In: *Physical Review B* 81.19 (2010), p. 195431.

[165] PM Krstajić and P Vasilopoulos. "Integer quantum Hall effect in gapped single-layer graphene". In: *Physical Review B* 86.11 (2012), p. 115432.

[166] Luis Brey and HA Fertig. "Edge states and the quantized Hall effect in graphene". In: *Physical Review B* 73.19 (2006), p. 195408.

[167] Yasuhiro Hatsugai. "Chern number and edge states in the integer quantum Hall effect". In: *Physical review letters* 71.22 (1993), p. 3697.

[168] Dmitry A Abanin, Patrick A Lee, and Leonid S Levitov. "Spin-filtered edge states and quantum Hall effect in graphene". In: *Physical review letters* 96.17 (2006), p. 176803.

[169] Zhenhua Qiao, Shengyuan A Yang, Wanxiang Feng, Wang-Kong Tse, Jun Ding, Yugui Yao, Jian Wang, and Qian Niu. "Quantum anomalous Hall effect in graphene from Rashba and exchange effects". In: *Physical Review B* 82.16 (2010), p. 161414.

[170] Zhenhua Qiao, Hua Jiang, Xiao Li, Yugui Yao, and Qian Niu. "Microscopic theory of quantum anomalous Hall effect in graphene". In: *Physical Review B* 85.11 (2012), p. 115439.

[171] Di Xiao, Ming-Che Chang, and Qian Niu. "Berry phase effects on electronic properties". In: *Reviews of modern physics* 82.3 (2010), p. 1959.

[172] Wang-Kong Tse, Zhenhua Qiao, Yugui Yao, AH MacDonald, and Qian Niu. "Quantum anomalous Hall effect in single-layer and bilayer graphene". In: *Physical Review B* 83.15 (2011), p. 155447.

[173] Zhiyong Wang, Chi Tang, Raymond Sachs, Yafis Barlas, and Jing Shi. "Proximity-induced ferromagnetism in graphene revealed by the anomalous hall effect". In: *Physical review letters* 114.1 (2015), p. 016603.

[174] Hongbin Zhang, Cesar Lazo, Stefan Blügel, Stefan Heinze, and Yuriy Mokrousov. "Electrically Tunable Quantum Anomalous Hall Effect in Graphene Decorated by 5 d Transition-Metal Adatoms". In: *Physical review letters* 108.5 (2012), p. 056802.

[175] Zhenhua Qiao, Wei Ren, Hua Chen, L Bellaiche, Zhenyu Zhang, AH MacDonald, and Qian Niu. "Quantum anomalous Hall effect in graphene proximity coupled to an antiferromagnetic insulator". In: *Physical review letters* 112.11 (2014), p. 116404.

[176] J. L. Lado and J. Fernández-Rossier. "Quantum anomalous Hall effect in graphene coupled to skyrmions". In: *Phys. Rev. B* 92 (2015), p. 115433.

[177] Dmytro Pesin and Allan H MacDonald. "Spintronics and pseudospintronics in graphene and topological insulators". In: *Nature materials* 11.5 (2012), pp. 409–416.

[178] Wei Han, Roland K Kawakami, Martin Gmitra, and Jaroslav Fabian. "Graphene spintronics". In: *Nature nanotechnology* 9.10 (2014), pp. 794–807.

[179] Markus König, Steffen Wiedmann, Christoph Brüne, Andreas Roth, Hartmut Buhmann, Laurens W Molenkamp, Xiao-Liang Qi, and Shou-Cheng Zhang. "Quantum spin Hall insulator state in HgTe quantum wells". In: *Science* 318.5851 (2007), pp. 766–770.

[180] Kentaro Nomura and Allan H MacDonald. "Quantum Hall ferromagnetism in graphene". In: *Physical review letters* 96.25 (2006), p. 256602.

[181] Jason Alicea and Matthew PA Fisher. "Graphene integer quantum Hall effect in the ferromagnetic and paramagnetic regimes". In: *Physical Review B* 74.7 (2006), p. 075422.

[182] Calvin J Tabert and Elisabeth J Nicol. "Valley-spin polarization in the magneto-optical response of silicene and other similar 2D crystals". In: *Physical review letters* 110.19 (2013), p. 197402.

[183] Andrea Franchini Young, JD Sanchez-Yamagishi, B Hunt, Sang Hyun Choi, K Watanabe, T Taniguchi, RC Ashoori, and Pablo Jarillo-Herrero. "Tunable symmetry breaking and helical edge transport in a graphene quantum spin Hall state". In: *Nature* 505.7484 (2014), pp. 528–532.

[184] Stephan Rachel and Karyn Le Hur. "Topological insulators and Mott physics from the Hubbard interaction". In: *Physical Review B* 82.7 (2010), p. 075106.

[185] M Hohenadler, ZY Meng, TC Lang, S Wessel, A Muramatsu, and FF Assaad. "Quantum phase transitions in the Kane-Mele-Hubbard model". In: *Physical Review B* 85.11 (2012), p. 115132.

[186] Hsiang-Hsuan Hung, Lei Wang, Zheng-Cheng Gu, and Gregory A Fiete. "Topological phase transition in a generalized Kane-Mele-Hubbard model: A combined quantum Monte Carlo and Green's function study". In: *Physical Review B* 87.12 (2013), p. 121113.

[187] Manuel Laubach, Johannes Reuther, Ronny Thomale, and Stephan Rachel. "Rashba spin-orbit coupling in the Kane-Mele-Hubbard model". In: *Physical Review B* 90.16 (2014), p. 165136.

[188] Jun Wen, Mehdi Kargarian, Abolhassan Vaezi, and Gregory A Fiete. "Doping the Kane-Mele-Hubbard model: A slave-boson approach". In: *Physical Review B* 84.23 (2011), p. 235149.

[189] Daniel Gosálbez-Martínez, D Soriano, JJ Palacios, and Joaquín Fernández-Rossier. "Spin-filtered edge states in graphene". In: *Solid State Communications* 152.15 (2012), pp. 1469–1476.

[190] Stephan Rachel and Motohiko Ezawa. "Giant magnetoresistance and perfect spin filter in silicene, germanene, and stanene". In: *Physical Review B* 89.19 (2014), p. 195303.

[191] Igor F Herbut. "SO (3) symmetry between Neel and ferromagnetic order parameters for graphene in a magnetic field". In: *Physical Review B* 76.8 (2007), p. 085432.

[192] Yousuke Kobayashi, Ken-ichi Fukui, Toshiaki Enoki, Koichi Kusakabe, and Yutaka Kaburagi. "Observation of zigzag and armchair edges of graphite using scanning tunneling microscopy and spectroscopy". In: *Physical Review B* 71.19 (2005), p. 193406.

[193] Xiaowei Zhang, Oleg V Yazyev, Juanjuan Feng, Liming Xie, Chenggang Tao, Yen-Chia Chen, Liying Jiao, Zahra Pedramrazi, Alex Zettl, Steven G Louie, et al. "Experimentally engineering the edge termination of graphene nanoribbons". In: *ACS nano* 7.1 (2012), pp. 198–202.

[194] Robert Drost, Andreas Uppstu, Fabian Schulz, Sampsa K Hamalainen, Mikko Ervasti, Ari Harju, and Peter Liljeroth. "Electronic states at the graphene–hexagonal boron nitride zigzag interface". In: *Nano letters* 14.9 (2014), pp. 5128–5132.

[195] RR Nair, M Sepioni, I-Ling Tsai, O Lehtinen, J Keinonen, AV Krasheninnikov, T Thomson, AK Geim, and IV Grigorieva. "Spin-half paramagnetism in graphene induced by point defects". In: *Nature Physics* 8.3 (2012), pp. 199–202.

[196] S. S. Rao, S. Narayana Jammalamadaka, A. Stesmans, V. V. Moshchalkov, J. van Tol, D. V. Kosynkin, A. Higginbotham-Duque, and J. M. Tour. "Ferromagnetism in Graphene Nanoribbons: Split versus Oxidative Unzipped Ribbons". In: *Nano Letters* 12.3 (2012), pp. 1210–1217.

[197] M Sepioni, RR Nair, I-Ling Tsai, AK Geim, and IV Grigorieva. "Revealing common artifacts due to ferromagnetic inclusions in highly oriented pyrolytic graphite". In: *EPL (Europhysics Letters)* 97.4 (2012), p. 47001.

[198] P Esquinazi, D Spemann, R Höhne, A Setzer, K-H Han, and T Butz. "Induced magnetic ordering by proton irradiation in graphite". In: *Physical Review Letters* 91.22 (2003), p. 227201.

[199] Roland Wiesendanger. "Spin mapping at the nanoscale and atomic scale". In: *Reviews of Modern Physics* 81.4 (2009), p. 1495.

[200] Eike Schäfer-Nolte, Lukas Schlipf, Markus Ternes, Friedemann Reinhard, Klaus Kern, and Jörg Wrachtrup. "Tracking temperature-dependent relaxation times of ferritin nanomagnets with a wideband quantum spectrometer". In: *Physical review letters* 113.21 (2014), p. 217204.

[201] Yan Li, Wei Zhang, Markus Morgenstern, and Riccardo Mazzarello. "Electronic and magnetic properties of zigzag graphene nanoribbons on the (111) surface of Cu, Ag, and Au". In: *Physical review letters* 110.21 (2013), p. 216804.

[202] Jens Baringhaus, Ming Ruan, Frederik Edler, Antonio Tejeda, Muriel Sicot, Amina Taleb-Ibrahimi, An-Ping Li, Zhigang Jiang, Edward H Conrad, Claire Berger, et al. "Exceptional ballistic transport in epitaxial graphene nanoribbons". In: *Nature* 506.7488 (2014), pp. 349–354.

[203] Pascal Ruffieux, Shiyong Wang, Bo Yang, Carlos Sanchez, Jia Liu, Thomas Dienel, Leopold Talirz, Prashant Shinde, Carlo A Pignedoli, Daniele Passerone, et al. "On-surface synthesis of graphene nanoribbons with zigzag edge topology". In: *arXiv preprint arXiv:1511.05037* (2015).

[204] Jun Inoue, Kozo Fukui, Takashi Kubo, Shigeaki Nakazawa, Kazunobu Sato, Daisuke Shiomi, Yasushi Morita, Kagetoshi Yamamoto, Takeji Takui, and Kazuhiro Nakasuji. "The first detection of a Clar's hydrocarbon, 2, 6, 10-tri-tert-butyltriangulene: A ground-state triplet of non-Kekule polynuclear benzenoid hydrocarbon". In: *Journal of the American Chemical Society* 123.50 (2001), pp. 12702–12703.

[205] JD Sanchez-Yamagishi, JY Luo, AF Young, B Hunt, K Watanabe, T Taniguchi, RC Ashoori, and P Jarillo-Herrero. "Observation of Helical Edge States and Fractional Quantum Hall Effect in a Graphene Electron-hole Bilayer". In: *arXiv preprint arXiv:1602.06815* (2016).

[206] R Ribeiro-Palau, F Lafont, J Brun-Picard, D Kazazis, A Michon, F Cheynis, O Couturaud, C Consejo, B Jouault, W Poirier, et al. "Graphene surpasses GaAs/AlGaAs for the application of the quantum Hall effect in metrology". In: *arXiv preprint arXiv:1504.06511* (2015).

[207] J M D Coey. *Magnetism and magnetic materials*. New York, NY: Cambridge Univ. Press, 2010.

[208] A. Smogunov, A. Dal Corso, A. Delin, R. Weht, and E. Tosatti. "Colossal magnetic anisotropy of monatomic free and deposited platinum nanowires". In: *Nat Nano* 3.1 (2008), pp. 22–25.

[209] AS Núñez and Joaquín Fernández-Rossier. "Colossal anisotropy in diluted magnetic topological insulators". In: *Solid State Communications* 152.5 (2012), pp. 403–406.

[210] Kyoko Nakada, Mitsutaka Fujita, Gene Dresselhaus, and Mildred S. Dresselhaus. "Edge state in graphene ribbons: Nanometer size effect and edge shape dependence". In: *Phys. Rev. B* 54 (24 1996), pp. 17954–17961.

[211] C. L. Kane and E. J. Mele. "Quantum Spin Hall Effect in Graphene". In: *Phys. Rev. Lett.* 95 (22 2005), p. 226801.

[212] Patrick Vogt, Paola De Padova, Claudio Quaresima, Jose Avila, Emmanouil Frantzeskakis, Maria Carmen Asensio, Andrea Resta, Bénédicte Ealet, and Guy Le Lay. "Silicene: Compelling Experimental Evidence for Graphenelike Two-Dimensional Silicon". In: *Phys. Rev. Lett.* 108 (15 2012), p. 155501.

[213] Antoine Fleurence, Rainer Friedlein, Taisuke Ozaki, Hiroyuki Kawai, Ying Wang, and Yukiko Yamada-Takamura. "Experimental Evidence for Epitaxial Silicene on Diboride Thin Films". In: *Phys. Rev. Lett.* 108 (24 2012), p. 245501.

[214] Chengyong Xu, Guangfu Luo, Qihang Liu, Jiaxin Zheng, Zhimeng Zhang, Shigeru Nagase, Zhengxiang Gao, and Jing Lu. "Giant magnetoresistance in silicene nanoribbons". In: *Nanoscale* 4 (10 2012), pp. 3111–3117.

[215] M. Houssa, G. Pourtois, V. V. Afanas'ev, and A. Stesmans. "Electronic properties of two-dimensional hexagonal germanium". In: *Applied Physics Letters* 96.8, 082111 (2010), pp. –.

[216] Yong Xu, Binghai Yan, Hai-Jun Zhang, Jing Wang, Gang Xu, Peizhe Tang, Wenhui Duan, and Shou-Cheng Zhang. "Large-Gap Quantum Spin Hall Insulators in Tin Films". In: *Phys. Rev. Lett.* 111 (13 2013), p. 136804.

[217] Atsuo Shitade, Hosho Katsura, Jan Kuneš, Xiao-Liang Qi, Shou-Cheng Zhang, and Naoto Nagaosa. "Quantum spin Hall effect in a transition metal oxide Na 2 IrO 3". In: *Physical review letters* 102.25 (2009), p. 256403.

[218] J. L. Lado, V. Pardo, and D. Baldomir. In: *Phys. Rev. B* 88 (15 2013), p. 155119.

[219] Z. F. Wang, Zheng Liu, and Feng Liu. "Organic topological insulators in organometallic lattices". In: *Nat Commun* 4 (2013), p. 1471.

[220] L. Brey and H. A. Fertig. "Electronic states of graphene nanoribbons studied with the Dirac equation". In: *Phys. Rev. B* 73 (23 2006), p. 235411.

[221] Kenjiro K. Gomes, Warren Mar, Wonhee Ko, Francisco Guinea, and Hari C. Manoharan. "Designer Dirac fermions and topological phases in molecular graphene". In: *Nature* 483.7389 (2012), pp. 306–310.

[222] Marco Polini, Francisco Guinea, Maciej Lewenstein, Hari C. Manoharan, and Vittorio Pellegrini. "Artificial honeycomb lattices for electrons, atoms and photons". In: *Nat Nano* 8.9 (2013). Review, pp. 625–633. ISSN: 1748-3387.

[223] Mitsutaka Fujita, Katsunori Wakabayashi, Kyoko Nakada, and Koichi Kusakabe. "Peculiar Localized State at Zigzag Graphite Edge". In: *Journal of the Physical Society of Japan* 65.7 (1996), pp. 1920–1923.

[224] Stephan Rachel and Karyn Le Hur. "Topological insulators and Mott physics from the Hubbard interaction". In: *Phys. Rev. B* 82 (7 2010), p. 075106.

[225] D. Soriano and J. Fernández-Rossier. "Spontaneous persistent currents in a quantum spin Hall insulator". In: *Phys. Rev. B* 82 (16 2010), p. 161302.

[226] F. D. M. Haldane. "Model for a Quantum Hall Effect without Landau Levels: Condensed-Matter Realization of the "Parity Anomaly"". In: *Phys. Rev. Lett.* 61 (18 1988), pp. 2015–2018.

[227] M. Laubach, J. Reuther, R. Thomale, and S. Rachel. "Rashba spin orbit coupling in the Kane-Mele-Hubbard model". In: *ArXiv e-prints* (2013). arXiv: 1312.2934 [cond-mat.str-el].

[228] F. Geissler, J. C. Budich, and B. Trauzettel. "Group theoretical and topological analysis of the quantum spin Hall effect in silicene". In: *New Journal of Physics* 15.8, 085030 (2013), p. 085030. arXiv: 1305.0766 [cond-mat.mes-hall].

[229] Cheng-Cheng Liu, Hua Jiang, and Yugui Yao. "Low-energy effective Hamiltonian involving spin-orbit coupling in silicene and two-dimensional germanium and tin". In: *Phys. Rev. B* 84 (19 2011), p. 195430.

[230] Till Burkert, Lars Nordström, Olle Eriksson, and Olle Heinonen. "Giant magnetic anisotropy in tetragonal FeCo alloys". In: *Physical review letters* 93.2 (2004), p. 027203.

[231] Chenggang Tao, Liying Jiao, Oleg V. Yazyev, Yen-Chia Chen, Juanjuan Feng, Xiaowei Zhang, Rodrigo B. Capaz, James M. Tour, Alex Zettl, Steven G. Louie, Hongjie Dai, and Michael F. Crommie. "Spatially resolving edge states of chiral graphene nanoribbons". In: *Nat Phys* 7.8 (2011), pp. 616–620. ISSN: 1745-2473. DOI: 10.1038/nphys1991.

[232] Xiaowei Zhang, Oleg V. Yazyev, Juanjuan Feng, Liming Xie, Chenggang Tao, Yen-Chia Chen, Liying Jiao, Zahra Pedramrazi, Alex Zettl, Steven G. Louie, Hongjie Dai, and Michael F. Crommie. "Experimentally Engineering the Edge Termination of Graphene Nanoribbons". In: *ACS Nano* 7.1 (2013), pp. 198–202.

[233] S. Rachel and M. Ezawa. "Perfect Spin Filter and Giant Magneto-Resistance in Silicene". In: *ArXiv e-prints* (2013). arXiv: 1312.1848 [cond-mat.mes-hall].

[234] Hongki Min, J. E. Hill, N. A. Sinitsyn, B. R. Sahu, Leonard Kleinman, and A. H. MacDonald. "Intrinsic and Rashba spin-orbit interactions in graphene sheets". In: *Phys. Rev. B* 74 (16 2006), p. 165310.

[235] Yugui Yao, Fei Ye, Xiao-Liang Qi, Shou-Cheng Zhang, and Zhong Fang. "Spin-orbit gap of graphene: First-principles calculations". In: *Phys. Rev. B* 75 (4 2007), p. 041401.

[236] Sergej Konschuh, Martin Gmitra, and Jaroslav Fabian. "Tight-binding theory of the spin-orbit coupling in graphene". In: *Phys. Rev. B* 82 (24 2010), p. 245412.

[237] Cheng-Cheng Liu, Wanxiang Feng, and Yugui Yao. "Quantum Spin Hall Effect in Silicene and Two-Dimensional Germanium". In: *Phys. Rev. Lett.* 107 (7 2011), p. 076802.

[238] Abdelkader Kara, Hanna Enriquez, Ari P Seitsonen, LC Lew Yan Voon, Sébastien Vizzini, Bernard Aufray, and Hamid Oughaddou. "A review on silicene—new candidate for electronics". In: *Surface science reports* 67.1 (2012), pp. 1–18.

[239] A Acun, L Zhang, P Bampoulis, M Farmanbar, A van Houselt, AN Rudenko, M Lingenfelder, G Brocks, B Poelsema, MI Katsnelson, et al. "Germanene: the germanium analogue of graphene". In: *Journal of Physics: Condensed Matter* 27.44 (2015), p. 443002.

[240] Paolo Giannozzi, Stefano Baroni, Nicola Bonini, Matteo Calandra, Roberto Car, Carlo Cavazzoni, Davide Ceresoli, Guido L Chiarotti, Matteo Cococcioni, Ismaila Dabo, et al. "QUANTUM ESPRESSO: a modular and open-source software project for quantum simulations of materials". In: *Journal of Physics: Condensed Matter* 21.39 (2009), p. 395502.

[241] URL: `http://elk.sourceforge.net/`.

[242] M Gmitra, S Konschuh, Ch Ertler, C Ambrosch-Draxl, and J Fabian. "Band-structure topologies of graphene: Spin-orbit coupling effects from first principles". In: *Physical Review B* 80.23 (2009), p. 235431.

[243] Yugui Yao, Fei Ye, Xiao-Liang Qi, Shou-Cheng Zhang, and Zhong Fang. "Spin-orbit gap of graphene: First-principles calculations". In: *Physical Review B* 75.4 (2007), p. 041401.

[244] Hongki Min, JE Hill, Nikolas A Sinitsyn, BR Sahu, Leonard Kleinman, and Allan H MacDonald. "Intrinsic and Rashba spin-orbit interactions in graphene sheets". In: *Physical Review B* 74.16 (2006), p. 165310.

[245] Cheng-Cheng Liu, Hua Jiang, and Yugui Yao. "Low-energy effective Hamiltonian involving spin-orbit coupling in silicene and two-dimensional germanium and tin". In: *Phys. Rev. B* 84 (19 2011), p. 195430.

[246] Martin Gmitra, Denis Kochan, and Jaroslav Fabian. "Spin-Orbit Coupling in Hydrogenated Graphene". In: *Phys. Rev. Lett.* 110 (24 2013), p. 246602.

[247] Alexandre Pachoud, Aires Ferreira, B. Özyilmaz, and A. H. Castro Neto. "Scattering theory of spin-orbit active adatoms on graphene". In: *Phys. Rev. B* 90 (3 2014), p. 035444.

[248] Balakrishnan Jayakumar, Kok Wai Koon Gavin, Jaiswal Manu, Castro Neto A. H., and Ozyilmaz Barbaros. "Colossal enhancement of spin-orbit coupling in weakly hydrogenated graphene". In: *Nat Phys* 9.5 (2013), 284–287. ISSN: 1745-2473.

[249] A. H. Castro Neto and F. Guinea. "Impurity-Induced Spin-Orbit Coupling in Graphene". In: *Phys. Rev. Lett.* 103 (2 2009), p. 026804.

[250] M. Gmitra, S. Konschuh, C. Ertler, C. Ambrosch-Draxl, and J. Fabian. "Band-structure topologies of graphene: Spin-orbit coupling effects from first principles". In: *Phys. Rev. B* 80 (23 2009), p. 235431.

[251] KSA Novoselov, Andre K Geim, SVb Morozov, Da Jiang, MIc Katsnelson, IVa Grigorieva, SVb Dubonos, and AAb Firsov. "Two-dimensional gas of massless Dirac fermions in graphene". In: *nature* 438.7065 (2005), pp. 197–200.

[252] Mikhail I. Katsnelson. *Graphene: Carbon in Two Dimensions*. Cambridge University Pres, 2012.

[253] VP Gusynin and SG Sharapov. "Unconventional integer quantum Hall effect in graphene". In: *Physical Review Letters* 95.14 (2005), p. 146801.

[254] Dmitry A. Abanin, Patrick A. Lee, and Leonid S. Levitov. In: *Phys. Rev. Lett.* 96 (17 2006), p. 176803.

[255] M. O. Goerbig, R. Moessner, and B. Dou çot. In: *Phys. Rev. B* 74 (16 2006), p. 161407.

[256] Jean-Noël Fuchs and Pascal Lederer. In: *Phys. Rev. Lett.* 98 (1 2007), p. 016803.

[257] L. Sheng, D. N. Sheng, F. D. M. Haldane, and Leon Balents. In: *Phys. Rev. Lett.* 99 (19 2007), p. 196802.

[258] Jason Alicea and Matthew P. A. Fisher. In: *Phys. Rev. B* 74 (7 2006), p. 075422.

[259] Valeri N. Kotov, Bruno Uchoa, Vitor M. Pereira, F. Guinea, and A. H. Castro Neto. In: *Rev. Mod. Phys.* 84 (3 2012), pp. 1067–1125.

[260] V. P. Gusynin, V. A. Miransky, S. G. Sharapov, and I. A. Shovkovy. In: *Phys. Rev. B* 74 (19 2006), p. 195429.

[261] HA Fertig and Luis Brey. "Luttinger liquid at the edge of undoped graphene in a strong magnetic field". In: *Physical review letters* 97.11 (2006), p. 116805.

[262] Igor F Herbut. "SO (3) symmetry between Neel and ferromagnetic order parameters for graphene in a magnetic field". In: *Physical Review B* 76.8 (2007), p. 085432.

[263] J. Jung and A. H. MacDonald. In: *Phys. Rev. B* 80 (23 2009), p. 235417.

[264] Kentaro Nomura and Allan H. MacDonald. In: *Phys. Rev. Lett.* 96 (25 2006), p. 256602.

[265] Jason Alicea and Matthew P. A. Fisher. In: *Phys. Rev. B* 74 (7 2006), p. 075422.

[266] Maxim Kharitonov. In: *Phys. Rev. B* 85 (15 2012), p. 155439.

[267] Maxim Kharitonov. In: *Phys. Rev. B* 86 (7 2012), p. 075450.

[268] Bitan Roy, Malcolm P Kennett, and S Das Sarma. "Chiral symmetry breaking and the quantum Hall effect in monolayer graphene". In: *Physical Review B* 90.20 (2014), p. 201409.

[269] Y Zhang, Z Jiang, JP Small, MS Purewal, Y-W Tan, M Fazlollahi, JD Chudow, JA Jaszczak, HL Stormer, and P Kim. "Landau-level splitting in graphene in high magnetic fields". In: *Physical review letters* 96.13 (2006), p. 136806.

[270] Zhigang Jiang, Yuanbo Zhang, HL Stormer, and Ph Kim. "Quantum Hall states near the charge-neutral Dirac point in graphene". In: *Physical review letters* 99.10 (2007), p. 106802.

[271] Young Jae Song, Alexander F Otte, Young Kuk, Yike Hu, David B Torrance, Phillip N First, Walt A de Heer, Hongki Min, Shaffique Adam, Mark D Stiles, et al. "High-resolution tunnelling spectroscopy of a graphene quartet". In: *Nature* 467.7312 (2010), pp. 185–189.

[272] A. F. Young, J. D. Sanchez-Yamagishi, B. Hunt, S. H. Choi, K. Watanabe, T. Taniguchi, R. C. Ashoori, and P. Jarillo-Herrero. In: *Nature* 505.7484 (2014). Letter, pp. 528–532.

[273] Lars Nordström and David J Singh. "Noncollinear intra-atomic magnetism". In: *Physical review letters* 76.23 (1996), p. 4420.

[274] Kohji Nakamura, Naoki Mizuno, Toru Akiyama, Tomonori Ito, and AJ Freeman. "Noncollinear magnetism, magnetocrystalline anisotropy, and spin-spiral structures in Fe/ W (110)". In: *Journal of applied physics* 101.9 (2007), 09G521.

[275] Elisabeth Sjöstedt and Lars Nordström. "Noncollinear full-potential studies of γ- Fe". In: *Physical Review B* 66.1 (2002), p. 014447.

[276] Pui-Wai Ma and SL Dudarev. "Constrained density functional for noncollinear magnetism". In: *Physical Review B* 91.5 (2015), p. 054420.

[277] S Sharma, JK Dewhurst, C Ambrosch-Draxl, S Kurth, N Helbig, S Pittalis, Sam Shallcross, Lars Nordström, and EKU Gross. "First-principles approach to noncollinear magnetism: Towards spin dynamics". In: *Physical review letters* 98.19 (2007), p. 196405.

[278] C. R. Young A. F.and Dean, L. Wang, H. Ren, P. Cadden-Zimansky, K. Watanabe, T. Taniguchi, J. Hone, K. L. Shepard, and P. Kim. In: *Nat Phys* 8.7 (2012), pp. 550–556.

[279] T. O. Wehling, E. Şaşıo ğlu, C. Friedrich, A. I. Lichtenstein, M. I. Katsnelson, and S. Blügel. In: *Phys. Rev. Lett.* 106 (23 2011), p. 236805.

[280] Luis Brey and HA Fertig. "Edge states and the quantized Hall effect in graphene". In: *Physical Review B* 73.19 (2006), p. 195408.

[281] Yoichiro Nambu. "Quasi-particles and gauge invariance in the theory of superconductivity". In: *Physical Review* 117.3 (1960), p. 648.

[282] Jeffrey Goldstone. "Field theories with Superconductor solutions". In: *Il Nuovo Cimento (1955-1965)* 19.1 (1961), pp. 154–164.

[283] MB Jungfleisch, W Zhang, J Sklenar, J Ding, W Jiang, H Chang, FY Fradin, JE Pearson, JB Ketterson, V Novosad, et al. "Large spin-wave bullet in a ferrimagnetic insulator driven by spin Hall effect". In: *arXiv preprint arXiv:1508.01427* (2015).

[284] Laura Feiler, Kathrin Sentker, Manuel Brinker, Nils Kuhlmann, Falk-Ulrich Stein, and Guido Meier. "Inverse spin-Hall effect voltage generation by nonlinear spin-wave excitation". In: *Physical Review B* 93.6 (2016), p. 064408.

[285] Neil W Ashcroft and N David Mermin. "Solid state phys". In: *Saunders, Philadelphia* 293 (1976).

[286] NMR Peres, MAN Araújo, and Daniel Bozi. "Phase diagram and magnetic collective excitations of the Hubbard model for graphene sheets and layers". In: *Physical Review B* 70.19 (2004), p. 195122.

[287] Gerald D Mahan. *Many-particle physics*. Springer Science & Business Media, 2013.

[288] Giuseppe Grosso and Giuseppe Pastori Parravicini. "Solid state physics". In: (2013).

[289] PW Anderson. "Antiferromagnetism. Theory of superexchange interaction". In: *Physical Review* 79.2 (1950), p. 350.

[290] John B Goodenough. "Theory of the Role of Covalence in the Perovskite-Type Manganites [La, M (II)] Mn O 3". In: *Physical Review* 100.2 (1955), p. 564.

[291] Anders Mathias Lunde and Gloria Platero. "Helical edge states coupled to a spin bath: Current-induced magnetization". In: *Physical Review B* 86.3 (2012), p. 035112.

[292] BL Altshuler, IL Aleiner, and VI Yudson. "Localization at the Edge of a 2D Topological Insulator by Kondo Impurities with Random Anisotropies". In: *Physical review letters* 111.8 (2013), p. 086401.

[293] Konstantin S Novoselov, Z Jiang, Y Zhang, SV Morozov, HL Stormer, U Zeitler, JC Maan, GS Boebinger, P Kim, and AK Geim. "Room-temperature quantum Hall effect in graphene". In: *Science* 315.5817 (2007), pp. 1379–1379.

[294] Patric W Anderson and H Hasegawa. "Considerations on double exchange". In: *Physical Review* 100.2 (1955), p. 675.

[295] Daniel Loss, Paul Goldbart, and AV Balatsky. "Berry's phase and persistent charge and spin currents in textured mesoscopic rings". In: *Physical review letters* 65.13 (1990), p. 1655.

[296] Daniel Loss, Paul Goldbart, and AV Balatsky. "Berry's phase and persistent charge and spin currents in textured mesoscopic rings". In: *Physical review letters* 65.13 (1990), p. 1655.

[297] Jinwu Ye, Yong Baek Kim, AJ Millis, BI Shraiman, P Majumdar, and Z Tešanović. "Berry phase theory of the anomalous Hall effect: application to colossal magnetoresistance manganites". In: *Physical review letters* 83.18 (1999), p. 3737.

[298] MJ Calderón and L Brey. "Skyrmion strings contribution to the anomalous Hall effect in double-exchange systems". In: *Physical Review B* 63.5 (2001), p. 054421.

[299] Ivar Martin and CD Batista. "Itinerant electron-driven chiral magnetic ordering and spontaneous quantum Hall effect in triangular lattice models". In: *Physical review letters* 101.15 (2008), p. 156402.

[300] LN Bulaevskii, CD Batista, MV Mostovoy, and DI Khomskii. "Electronic orbital currents and polarization in Mott insulators". In: *Physical Review B* 78.2 (2008), p. 024402.

[301] Yasuyuki Kato, Ivar Martin, and CD Batista. "Stability of the spontaneous quantum Hall state in the triangular Kondo-lattice model". In: *Physical review letters* 105.26 (2010), p. 266405.

[302] Y Taguchi, Y Oohara, H Yoshizawa, N Nagaosa, and Y Tokura. "Spin chirality, Berry phase, and anomalous Hall effect in a frustrated ferromagnet". In: *Science* 291.5513 (2001), pp. 2573–2576.

[303] Naoto Nagaosa, Jairo Sinova, Shigeki Onoda, AH MacDonald, and NP Ong. "Anomalous hall effect". In: *Reviews of modern physics* 82.2 (2010), p. 1539.

[304] Yugui Yao, Leonard Kleinman, AH MacDonald, Jairo Sinova, T Jungwirth, Ding-sheng Wang, Enge Wang, and Qian Niu. "First principles calculation of anomalous Hall conductivity in ferromagnetic bcc Fe". In: *Physical review letters* 92.3 (2004), p. 037204.

[305] Kenya Ohgushi, Shuichi Murakami, and Naoto Nagaosa. "Spin anisotropy and quantum Hall effect in the kagome lattice: chiral spin state based on a ferromagnet". In: *Physical Review B* 62.10 (2000), R6065.

[306] Jens Brede, Nicolae Atodiresei, Vasile Caciuc, Maciej Bazarnik, Ali Al-Zubi, Stefan Blügel, and Roland Wiesendanger. "Long-range magnetic coupling between nanoscale organic–metal hybrids mediated by a nanoskyrmion lattice". In: *Nature nanotechnology* (2014).

[307] Qing-Ze Wang, Xin Liu, Hai-Jun Zhang, Nitin Samarth, Shou-Cheng Zhang, and Chao-Xing Liu. "Quantum anomalous Hall effect in magnetically doped InAs/GaSb quantum wells". In: *Physical review letters* 113.14 (2014), p. 147201.

[308] Naoto Nagaosa and Yoshinori Tokura. "Topological properties and dynamics of magnetic skyrmions". In: *Nature nanotechnology* 8.12 (2013), pp. 899–911.

[309] J Sampaio, V Cros, S Rohart, A Thiaville, and A Fert. "Nucleation, stability and current-induced motion of isolated magnetic skyrmions in nanostructures". In: *Nature nanotechnology* 8.11 (2013), pp. 839–844.

[310] Stefan Heinze, Kirsten von Bergmann, Matthias Menzel, Jens Brede, André Kubetzka, Roland Wiesendanger, Gustav Bihlmayer, and Stefan Blügel. "Spontaneous atomic-scale magnetic skyrmion lattice in two dimensions". In: *Nature Physics* 7.9 (2011), pp. 713–718.

[311] Keita Hamamoto, Motohiko Ezawa, and Naoto Nagaosa. "Quantized Anomalous Hall Effects in Skyrmion Crystal". In: *arXiv preprint arXiv:1504.06024* (2015).

[312] JL Lado, N Garcia-Martinez, and J Fernandez-Rossier. "Edge states in graphene-like systems". In: *arXiv preprint arXiv:1502.07112* (2015).

[313] FDM Haldane. "Berry curvature on the fermi surface: Anomalous hall effect as a topological fermi-liquid property". In: *Physical review letters* 93.20 (2004), p. 206602.

[314] Zhiyong Wang, Chi Tang, Raymond Sachs, Yafis Barlas, and Jing Shi. "Proximity-induced ferromagnetism in graphene revealed by the anomalous hall effect". In: *Physical review letters* 114.1 (2015), p. 016603.

[315] Shinichiro Seki, XZ Yu, S Ishiwata, and Y Tokura. "Observation of skyrmions in a multiferroic material". In: *Science* 336.6078 (2012), pp. 198–201.

[316] Zhenhua Qiao, Wei Ren, Hua Chen, L Bellaiche, Zhenyu Zhang, AH MacDonald, and Qian Niu. "Quantum anomalous Hall effect in graphene proximity coupled to an antiferromagnetic insulator". In: *Physical review letters* 112.11 (2014), p. 116404.

[317] Zhenhua Qiao, Wei Ren, Hua Chen, L Bellaiche, Zhenyu Zhang, AH MacDonald, and Qian Niu. "Quantum anomalous Hall effect in graphene proximity coupled to an antiferromagnetic insulator". In: *Physical review letters* 112.11 (2014), p. 116404.

[318] Stevan Nadj-Perge, Ilya K Drozdov, Jian Li, Hua Chen, Sangjun Jeon, Jungpil Seo, Allan H MacDonald, B Andrei Bernevig, and Ali Yazdani. "Observation of Majorana fermions in ferromagnetic atomic chains on a superconductor". In: *Science* 346.6209 (2014), pp. 602–607.

[319] F Duncan M Haldane. "Model for a quantum Hall effect without Landau levels: Condensed-matter realization of the" parity anomaly"". In: *Physical Review Letters* 61.18 (1988), p. 2015.

[320] Naoto Nagaosa, Jairo Sinova, Shigeki Onoda, AH MacDonald, and NP Ong. "Anomalous hall effect". In: *Reviews of modern physics* 82.2 (2010), p. 1539.

[321] Jose L Lado and Joaquín Fernández-Rossier. "Quantum anomalous Hall effect in graphene coupled to skyrmions". In: *Physical Review B* 92.11 (2015), p. 115433.

[322] Keita Hamamoto, Motohiko Ezawa, and Naoto Nagaosa. "Quantized topological Hall effect in skyrmion crystal". In: *Physical Review B* 92.11 (2015), p. 115417.

[323] Gia-Wei Chern, Armin Rahmani, Ivar Martin, and Cristian D Batista. "Quantum Hall ice". In: *Physical Review B* 90.24 (2014), p. 241102.

[324] Zhenhua Qiao, Shengyuan A Yang, Wanxiang Feng, Wang-Kong Tse, Jun Ding, Yugui Yao, Jian Wang, and Qian Niu. "Quantum anomalous Hall effect in graphene from Rashba and exchange effects". In: *Physical Review B* 82.16 (2010), p. 161414.

[325] Peng Wei, Ferhat Katmis, Badih A Assaf, Hadar Steinberg, Pablo Jarillo-Herrero, Donald Heiman, and Jagadeesh S Moodera. "Exchange-coupling-induced symmetry breaking in topological insulators". In: *Physical review letters* 110.18 (2013), p. 186807.

[326] Jiayong Zhang, Bao Zhao, Yugui Yao, and Zhongqin Yang. "Quantum Anomalous Hall Effect in Graphene-based Heterostructure". In: *Scientific Reports* 5 (2015).

[327] Andrea F Young, Cory R Dean, Lei Wang, Hechen Ren, Paul Cadden-Zimansky, Kenji Watanabe, Takashi Taniguchi, James Hone, Kenneth L Shepard, and Philip Kim. "Spin and valley quantum Hall ferromagnetism in graphene". In: *Nature Physics* 8.7 (2012), pp. 550–556.

[328] Patrick Maher, Cory R Dean, Andrea F Young, Takashi Taniguchi, Kenji Watanabe, Kenneth L Shepard, James Hone, and Philip Kim. "Evidence for a spin phase transition at charge neutrality in bilayer graphene". In: *Nature Physics* 9.3 (2013), pp. 154–158.

[329] S Pezzini, C Cobaleda, BA Piot, V Bellani, and E Diez. "Critical point for the canted antiferromagnetic to ferromagnetic phase transition at charge neutrality in bilayer graphene". In: *Physical Review B* 90.12 (2014), p. 121404.

[330] Maxim Kharitonov. "Antiferromagnetic state in bilayer graphene". In: *Physical Review B* 86.19 (2012), p. 195435.

[331] NA García-Martínez, Jose L Lado, and Joaquín Fernández-Rossier. "Quantum spin Hall phase in multilayer graphene". In: *Physical Review B* 91.23 (2015), p. 235451.

[332] Y Lee, D Tran, K Myhro, J Velasco, N Gillgren, CN Lau, Y Barlas, JM Poumirol, D Smirnov, and F Guinea. "Competition between spontaneous symmetry breaking and single-particle gaps in trilayer graphene". In: *Nature communications* 5 (2014).

[333] Matthew Yankowitz, I Joel, Jan Wang, A Glen Birdwell, Yu-An Chen, K Watanabe, T Taniguchi, Philippe Jacquod, Pablo San-Jose, Pablo Jarillo-Herrero, et al. "Electric field control of soliton motion and stacking in trilayer graphene". In: *Nature materials* 13.8 (2014), pp. 786–789.

[334] Jeil Jung and Allan H MacDonald. "Gapped broken symmetry states in ABC-stacked trilayer graphene". In: *Physical Review B* 88.7 (2013), p. 075408.

[335] Lan Chen, Cheng-Cheng Liu, Baojie Feng, Xiaoyue He, Peng Cheng, Zijing Ding, Sheng Meng, Yugui Yao, and Kehui Wu. "Evidence for Dirac fermions in a honeycomb lattice based on silicon". In: *Physical review letters* 109.5 (2012), p. 056804.

[336] Stephan Rachel and Motohiko Ezawa. "Giant magnetoresistance and perfect spin filter in silicene, germanene, and stanene". In: *Physical Review B* 89.19 (2014), p. 195303.

[337] Cheng-Cheng Liu, Wanxiang Feng, and Yugui Yao. "Quantum spin Hall effect in silicene and two-dimensional germanium". In: *Physical review letters* 107.7 (2011), p. 076802.

[338] Yong Xu, Binghai Yan, Hai-Jun Zhang, Jing Wang, Gang Xu, Peizhe Tang, Wenhui Duan, and Shou-Cheng Zhang. "Large-gap quantum spin Hall insulators in tin films". In: *Physical review letters* 111.13 (2013), p. 136804.

[339] Chengwang Niu, Gustav Bihlmayer, Hongbin Zhang, Daniel Wortmann, Stefan Blügel, and Yuriy Mokrousov. "Functionalized bismuth films: Giant gap quantum spin Hall and valley-polarized quantum anomalous Hall states". In: *Physical Review B* 91.4 (2015), p. 041303.

[340] Yong Xu, Peizhe Tang, and Shou-Cheng Zhang. "Large-gap quantum spin Hall states in decorated stanene grown on a substrate". In: *Physical Review B* 92.8 (2015), p. 081112.

[341] H Suhl and BT Matthias. "Impurity Scattering in Superconductors". In: *Physical Review* 114.4 (1959), p. 977.

[342] Hiroyuki Shiba. "Classical spins in superconductors". In: *Progress of theoretical Physics* 40.3 (1968), pp. 435–451.

[343] Hiroyuki Shiba and Toshio Soda. "Superconducting tunneling through the barrier with paramagnetic impurities". In: *Progress of Theoretical Physics* 41.1 (1969), pp. 25–44.

[344] Ali Yazdani, BA Jones, CP Lutz, MF Crommie, and DM Eigler. "Probing the local effects of magnetic impurities on superconductivity". In: *Science* 275.5307 (1997), pp. 1767–1770.

[345] Shuai-Hua Ji, Tong Zhang, Ying-Shuang Fu, Xi Chen, Xu-Cun Ma, Jia Li, Wen-Hui Duan, Jin-Feng Jia, and Qi-Kun Xue. "High-resolution scanning tunneling spectroscopy of magnetic impurity induced bound states in the superconducting gap of Pb thin films". In: *Physical review letters* 100.22 (2008), p. 226801.

[346] Nino Hatter, Benjamin W Heinrich, Michael Ruby, Jose I Pascual, and Katharina J Franke. "Magnetic anisotropy in Shiba bound states across a quantum phase transition". In: *arXiv preprint arXiv:1509.09108* (2015).

[347] Gerbold C Ménard, Sébastien Guissart, Christophe Brun, Stéphane Pons, Vasily S Stolyarov, François Debontridder, Matthieu V Leclerc, Etienne Janod, Laurent Cario, Dimitri Roditchev, et al. "Coherent long-range magnetic bound states in a superconductor". In: *Nature Physics* (2015).

[348] Michael Ruby, Falko Pientka, Yang Peng, Felix von Oppen, Benjamin W Heinrich, and Katharina J Franke. "Tunneling processes into localized subgap states in superconductors". In: *arXiv preprint arXiv:1502.05048* (2015).

[349] Andreas Heimes, Panagiotis Kotetes, and Gerd Schön. "Majorana fermions from Shiba states in an antiferromagnetic chain on top of a superconductor". In: *Physical Review B* 90.6 (2014), p. 060507.

[350] Falko Pientka, Leonid I Glazman, and Felix von Oppen. "Topological superconducting phase in helical Shiba chains". In: *Physical Review B* 88.15 (2013), p. 155420.

[351] Kim Pöyhönen, Alex Weststrom, Joel Röntynen, and Teemu Ojanen. "Majorana states in helical Shiba chains and ladders". In: *Physical Review B* 89.11 (2014), p. 115109.

[352] AV Balatsky, I Vekhter, and Jian-Xin Zhu. "Impurity-induced states in conventional and unconventional superconductors". In: *Reviews of Modern Physics* 78.2 (2006), p. 373.

[353] Hubert B Heersche, Pablo Jarillo-Herrero, Jeroen B Oostinga, Lieven MK Vandersypen, and Alberto F Morpurgo. "Bipolar supercurrent in graphene". In: *Nature* 446.7131 (2007), pp. 56–59.

[354] Victor E Calado, Srijit Goswami, Gaurav Nanda, Mathias Diez, Anton R Akhmerov, Kenji Watanabe, Takashi Taniguchi, Teun M Klapwijk, and Lieven MK Vandersypen. "Ballistic Josephson junctions in edge-contacted graphene". In: *arXiv preprint arXiv:1501.06817* (2015).

[355] Charlène Tonnoir, Amina Kimouche, Johann Coraux, Laurence Magaud, Benjamin Delsol, Bruno Gilles, and Claude Chapelier. "Induced superconductivity in graphene grown on rhenium". In: *Physical review letters* 111.24 (2013), p. 246805.

[356] Zheng Han, Adrien Allain, Hadi Arjmandi-Tash, Konstantin Tikhonov, Mikhail Feigel'Man, Benjamin Sacépé, and Vincent Bouchiat. "Collapse of superconductivity in a hybrid tin-graphene Josephson junction array". In: *Nature Physics* 10.5 (2014), pp. 380–386.

[357] Miguel M Ugeda, Aaron J Bradley, Yi Zhang, Seita Onishi, Yi Chen, Wei Ruan, Claudia Ojeda-Aristizabal, Hyejin Ryu, Mark T Edmonds, Hsin-Zon Tsai, et al. "Characterization of collective ground states in single-layer NbSe2". In: *Nature Physics* (2015).

[358] Y. Cao, A. Mishchenko, G. L. Yu, E. Khestanova, A. P. Rooney, E. Prestat, A. V. Kretinin, P. Blake, M. B. Shalom, C. Woods, J. Chapman, G. Balakrishnan, I. V. Grigorieva, K. S. Novoselov, B. A. Piot, M. Potemski, K. Watanabe, T. Taniguchi, S. J. Haigh, A. K. Geim, and R. V. Gorbachev. "Quality Heterostructures from Two-Dimensional Crystals Unstable in Air by Their Assembly in Inert Atmosphere". In: *Nano Letters* 15.8 (2015), pp. 4914–4921. DOI: 10.1021/acs.nanolett.5b00648.

[359] S-L Yang, JA Sobota, CA Howard, CJ Pickard, Makoto Hashimoto, DH Lu, S-K Mo, PS Kirchmann, and Z-X Shen. "Superconducting graphene sheets in CaC6 enabled by phonon-mediated interband interactions". In: *Nature communications* 5 (2014).

[360] J Chapman, Y Su, CA Howard, D Kundys, A Grigorenko, F Guinea, AK Geim, IV Grigorieva, and RR Nair. "Superconductivity in Ca-doped graphene". In: *Nature Physics* 5 (2014).

[361] KC Rahnejat, CA Howard, NE Shuttleworth, SR Schofield, K Iwaya, CF Hirjibehedin, Ch Renner, G Aeppli, and M Ellerby. "Charge density waves in the graphene sheets of the superconductor CaC_6". In: *Nature communications* 2 (2011), p. 558.

[362] Oleg V Yazyev and Lothar Helm. "Defect-induced magnetism in graphene". In: *Physical Review B* 75.12 (2007), p. 125408.

[363] Luis A González-Árraga, JL Lado, and Francisco Guinea. "Topological features of hydrogenated graphene". In: *arXiv preprint arXiv:1507.07714* (2015).

[364] Elton JG Santos, Andrés Ayuela, and Daniel Sánchez-Portal. "Universal magnetic properties of sp3-type defects in covalently functionalized graphene". In: *New Journal of Physics* 14.4 (2012), p. 043022.

[365] D Soriano, Federico Muñoz-Rojas, J. Fernández-Rossier, and JJ Palacios. "Hydrogenated graphene nanoribbons for spintronics". In: *Physical Review B* 81.16 (2010), p. 165409.

[366] JJ Palacios, Joaquın Fernández-Rossier, and L Brey. "Vacancy-induced magnetism in graphene and graphene ribbons". In: *Physical Review B* 77.19 (2008), p. 195428.

[367] DW Boukhvalov, MI Katsnelson, and AI Lichtenstein. "Hydrogen on graphene: Electronic structure, total energy, structural distortions and magnetism from first-principles calculations". In: *Physical Review B* 77.3 (2008), p. 035427.

[368] Ivan Brihuega. "Atomic scale control of graphene magnetism using hydrogen atoms". In: *SPICE workshop, Magnetic adatoms as building blocks for quantum magnetism* (2015).

[369] RR Nair, I-L Tsai, M Sepioni, O Lehtinen, J Keinonen, AV Krasheninnikov, AH Castro Neto, MI Katsnelson, AK Geim, and IV Grigorieva. "Dual origin of defect magnetism in graphene and its reversible switching by molecular doping". In: *Nature communications* 4 (2013).

[370] Felix Yndurain. "Effect of hole doping on the magnetism of point defects in graphene: A theoretical study". In: *Physical Review B* 90.24 (2014), p. 245420.

[371] TO Wehling, AV Balatsky, MI Katsnelson, AI Lichtenstein, K Scharnberg, and R Wiesendanger. "Local electronic signatures of impurity states in graphene". In: *Physical Review B* 75.12 (2007), p. 125425.

[372] CWJ Beenakker. "Specular Andreev reflection in graphene". In: *Physical review letters* 97.6 (2006), p. 067007.

[373] D Jacob and G Kotliar. "Orbital selective and tunable Kondo effect of magnetic adatoms on graphene: Correlated electronic structure calculations". In: *Physical Review B* 82.8 (2010), p. 085423.

[374] TO Wehling, HP Dahal, AI Lichtenstein, and AV Balatsky. "Local impurity effects in superconducting graphene". In: *Physical Review B* 78.3 (2008), p. 035414.

[375] WL McMillan. "Tunneling model of the superconducting proximity effect". In: *Physical Review* 175.2 (1968), p. 537.

[376] A Chrestin, T Matsuyama, and U Merkt. "Evidence for a proximity-induced energy gap in Nb/InAs/Nb junctions". In: *Physical Review B* 55.13 (1997), p. 8457.

[377] P San-Jose, JL Lado, R Aguado, F Guinea, and J Fernández-Rossier. "Majorana Zero Modes in Graphene". In: *Physical Review X* 5.4 (2015), p. 041042.

[378] Jong Soo Lim, Rosa López, Ramón Aguado, et al. "Shiba states and zero-bias anomalies in the hybrid normal-superconductor Anderson model". In: *Physical Review B* 91.4 (2015), p. 045441.

[379] P Haase, S Fuchs, T Pruschke, H Ochoa, and F Guinea. "Magnetic moments and Kondo effect near vacancies and resonant scatterers in graphene". In: *Physical Review B* 83.24 (2011), p. 241408.

[380] JO Sofo, Gonzalo Usaj, PS Cornaglia, AM Suarez, AD Hernández-Nieves, and CA Balseiro. "Magnetic structure of hydrogen-induced defects on graphene". In: *Physical Review B* 85.11 (2012), p. 115405.

[381] Jaime E Santos, Nuno MR Peres, João MB Lopes dos Santos, and António H Castro Neto. "Electronic doping of graphene by deposited transition metal atoms". In: *Physical Review B* 84.8 (2011), p. 085430.

[382] Kostya S Novoselov, Andre K Geim, SV Morozov, D Jiang, Y_ Zhang, SV Dubonos, IV Grigorieva, and AA Firsov. "Electric field effect in atomically thin carbon films". In: *science* 306.5696 (2004), pp. 666–669.

[383] Qing Hua Wang, Zhong Jin, Ki Kang Kim, Andrew J Hilmer, Geraldine LC Paulus, Chih-Jen Shih, Moon-Ho Ham, Javier D Sanchez-Yamagishi, Kenji Watanabe, Takashi Taniguchi, et al. "Understanding and controlling the substrate effect on graphene electron-transfer chemistry via reactivity imprint lithography". In: *Nature chemistry* 4.9 (2012), pp. 724–732.

[384] Xiao-Liang Qi and Shou-Cheng Zhang. "Topological insulators and superconductors". In: *Reviews of Modern Physics* 83.4 (2011), p. 1057.

[385] A. F. Young, J. D. Sanchez-Yamagishi, B. Hunt, S. H. Choi, K. Watanabe, T. Taniguchi, R. C. Ashoori, and P. Jarillo-Herrero. "Tunable symmetry breaking and helical edge transport in a graphene quantum spin Hall state". In: *Nature* 505.7484 (Jan. 2014), pp. 528–532.

[386] P. San-Jose, J. L. Lado, R. Aguado, F. Guinea, and J. Fernández-Rossier. "Majorana Zero Modes in Graphene". In: *Phys. Rev. X* 5 (4 2015), p. 041042.

[387] M Ben Shalom, MJ Zhu, VI Fal'ko, A Mishchenko, AV Kretinin, KS Novoselov, CR Woods, K Watanabe, T Taniguchi, AK Geim, et al. "Quantum oscillations of the critical current and high-field superconducting proximity in ballistic graphene". In: *Nature Physics* (2015).

[388] A Yu Kitaev. "Unpaired Majorana fermions in quantum wires". In: *Physics-Uspekhi* 44.10S (2001), p. 131.

[389] Sumilan Banerjee, Onur Erten, and Mohit Randeria. "Ferromagnetic exchange, spin-orbit coupling and spiral magnetism at the LaAlO3/SrTiO3 interface". In: *Nature physics* 9.10 (2013), pp. 626–630.

[390] Luca F Tocchio, Claudius Gros, Roser Valentí, and Federico Becca. "One-dimensional spin liquid, collinear, and spiral phases from uncoupled chains to the triangular lattice". In: *Physical Review B* 89.23 (2014), p. 235107.

[391] Andreas Heimes, Daniel Mendler, and Panagiotis Kotetes. "Interplay of topological phases in magnetic adatom-chains on top of a Rashba superconducting surface". In: *New Journal of Physics* 17.2 (2015), p. 023051.

[392] Jelena Klinovaja, Peter Stano, and Daniel Loss. "Transition from fractional to Majorana fermions in Rashba nanowires". In: *Physical review letters* 109.23 (2012), p. 236801.

[393] Liang Fu and Charles L Kane. "Superconducting proximity effect and Majorana fermions at the surface of a topological insulator". In: *Physical review letters* 100.9 (2008), p. 096407.

[394] V. Mourik, K. Zuo, S. M. Frolov, S. R. Plissard, E. P. A. M. Bakkers, and L. P. Kouwenhoven. "Signatures of Majorana Fermions in Hybrid Superconductor-Semiconductor Nanowire Devices". In: *Science* 336.6084 (2012), pp. 1003–1007.

[395] M. T. Deng, C. L. Yu, G. Y. Huang, M. Larsson, P. Caroff, and H. Q. Xu. "Anomalous Zero-Bias Conductance Peak in a Nb–InSb Nanowire–Nb Hybrid Device". In: *Nano Letters* 12.12 (2012), pp. 6414–6419.

[396] Anindya Das, Yuval Ronen, Yonatan Most, Yuval Oreg, Moty Heiblum, and Hadas Shtrikman. "Zero-bias peaks and splitting in an Al-InAs nanowire topological superconductor as a signature of Majorana fermions". In: *Nat Phys* 8.12 (Dec. 2012), pp. 887–895.

[397] Leonid P. Rokhinson, Xinyu Liu, and Jacek K. Furdyna. "The fractional a.c. Josephson effect in a semiconductor-superconductor nanowire as a signature of Majorana particles". In: *Nat Phys* 8.11 (Nov. 2012), pp. 795–799.

[398] A. D. K. Finck, D. J. Van Harlingen, P. K. Mohseni, K. Jung, and X. Li. "Anomalous Modulation of a Zero-Bias Peak in a Hybrid Nanowire-Superconductor Device". In: *Phys. Rev. Lett.* 110 (12 2013), p. 126406.

[399] H. O. H. Churchill, V. Fatemi, K. Grove-Rasmussen, M. T. Deng, P. Caroff, H. Q. Xu, and C. M. Marcus. "Superconductor-nanowire devices from tunneling to the multichannel regime: Zero-bias oscillations and magnetoconductance crossover". In: *Phys. Rev. B* 87 (24 2013), p. 241401.

[400] Eduardo J. H. Lee, Xiaocheng Jiang, Manuel Houzet, Ramon Aguado, Charles M. Lieber, and Silvano De Franceschi. "Spin-resolved Andreev levels and parity crossings in hybrid superconductor-semiconductor nanostructures". In: *Nat Nano* 9.1 (Jan. 2014), pp. 79–84.

[401] Sean Hart, Hechen Ren, Timo Wagner, Philipp Leubner, Mathias Muhlbauer, Christoph Brune, Hartmut Buhmann, Laurens W. Molenkamp, and Amir Yacoby. "Induced superconductivity in the quantum spin Hall edge". In: *Nat Phys* 10.9 (Sept. 2014), pp. 638–643.

[402] Vlad S. Pribiag, BeukmanArjan J. A., Fanming Qu, Maja C. Cassidy, Christophe Charpentier, Werner Wegscheider, and Leo P. Kouwenhoven. "Edge-mode superconductivity in a two-dimensional topological insulator". In: *Nat Nano* 10.7 (July 2015), pp. 593–597.

[403] Stevan Nadj-Perge, Ilya K. Drozdov, Jian Li, Hua Chen, Sangjun Jeon, Jungpil Seo, Allan H. MacDonald, B. Andrei Bernevig, and Ali Yazdani. "Observation of Majorana fermions in ferromagnetic atomic chains on a superconductor". In: *Science* 346.6209 (2014), pp. 602–607.

[404] Remy Pawlak, Marcin Kisiel, Jelena Klinovaja, Tobias Meier, Shigeki Kawai, Thilo Glatzel, Daniel Loss, and Ernst Meyer. "Probing Atomic Structure and Majorana Wavefunctions in Mono-Atomic Fe-chains on Superconducting Pb-Surface". In: (May 2015).

[405] C. Kurter, A. D. K. Finck, Y. S. Hor, and D. J. Van Harlingen. "Evidence for an anomalous current-phase relation in topological insulator Josephson junctions". In: *Nat Commun* 6 (June 2015).

[406] Jonas Wiedenmann, Erwann Bocquillon, Russell S. Deacon, Simon Hartinger, Teun M. Klapwijk, Luis Maier, Christopher Ames, Christoph Brüne, Koji Ishibashi, Seigo Tarucha, Hartmut Buhmann, and Laurens W. Molenkamp. "Zero-energy Andreev bound states in a HgTe-based topological Josephson junction". In: (Mar. 2015).

[407] Liang Fu and C. L. Kane. "Superconducting Proximity Effect and Majorana Fermions at the Surface of a Topological Insulator". In: *Phys. Rev. Lett.* 100 (9 2008), p. 096407.

[408] Jay D. Sau, Roman M. Lutchyn, Sumanta Tewari, and S. Das Sarma. "Generic New Platform for Topological Quantum Computation Using Semiconductor Heterostructures". In: *Phys. Rev. Lett.* 104 (4 2010), p. 040502.

[409] Roman M. Lutchyn, Jay D. Sau, and S. Das Sarma. "Majorana Fermions and a Topological Phase Transition in Semiconductor-Superconductor Heterostructures". In: *Phys. Rev. Lett.* 105.7 (2010), p. 077001.

[410] Yuval Oreg, Gil Refael, and Felix von Oppen. "Helical Liquids and Majorana Bound States in Quantum Wires". In: *Phys. Rev. Lett.* 105 (17 2010), p. 177002.

[411] A. F. Young, C. R. Dean, L. Wang, H. Ren, P. Cadden-Zimansky, K. Watanabe, T. Taniguchi, J. Hone, K. L. Shepard, and P. Kim. "Spin and valley quantum Hall ferromagnetism in graphene". In: *Nat Phys* 8.7 (July 2012), pp. 550–556.

[412] Victor E. Calado, Srijit Goswami, Gaurav Nanda, Mathias Diez, Anton R. Akhmerov, Kenji Watanabe, Takashi Taniguchi, Teun M. Klapwijk, and Lieven M. K. Vandersypen. "Ballistic Josephson junctions in edge-contacted graphene". In: (Jan. 2015).

[413] A. H Castro Neto, F Guinea, N. M. R Peres, K. S Novoselov, and A. K Geim. "The electronic properties of graphene". In: *Rev. Mod. Phys.* 81.1 (2009), pp. 109–162.

[414] C.L. Kane and E.J. Mele. "Quantum spin Hall effect in graphene". In: *Phys. Rev. Lett.* 95.22 (2005), p. 226801.

[415] Y. Zhang, Z. Jiang, J. P. Small, M. S. Purewal, Y.-W. Tan, M. Fazlollahi, J. D. Chudow, J. A. Jaszczak, H. L. Stormer, and P. Kim. "Landau-Level Splitting in Graphene in High Magnetic Fields". In: *Phys. Rev. Lett.* 96 (13 2006), p. 136806.

[416] Kirill Bolotin, Fereshte Ghahari, Michael Shulman, Horst Stormer, and Philip Kim. "Observation of the fractional quantum Hall effect in graphene". In: *Nature* 462.7270 (2009), pp. 196–199. ISSN: 0028-0836.

[417] David L. Miller, Kevin D. Kubista, Gregory M. Rutter, Ming Ruan, Walt A. de Heer, Phillip N. First, and Joseph A. Stroscio. "Observing the Quantization of Zero Mass Carriers in Graphene". In: *Science* 324.5929 (2009), pp. 924–927.

[418] Benjamin E. Feldman, Benjamin Krauss, Jurgen H. Smet, and Amir Yacoby. "Unconventional Sequence of Fractional Quantum Hall States in Suspended Graphene". In: *Science* 337.6099 (2012), pp. 1196–1199.

[419] A. Kou, B. E. Feldman, A. J. Levin, B. I. Halperin, K. Watanabe, T. Taniguchi, and A. Yacoby. "Electron-hole asymmetric integer and fractional quantum Hall effect in bilayer graphene". In: *Science* 345.6192 (2014), pp. 55–57.

[420] G. L. Yu, R. V. Gorbachev, J. S. Tu, A. V. Kretinin, Y. Cao, R. Jalil, F. Withers, L. A. Ponomarenko, B. A. Piot, M. Potemski, D. C. Elias, X. Chen, K. Watanabe, T. Taniguchi, I. V. Grigorieva, K. S. Novoselov, V. I. Fal/'ko, A. K. Geim, and A. Mishchenko. "Hierarchy of Hofstadter states and replica quantum Hall ferromagnetism in graphene superlattices". In: *Nat Phys* advance online publication (June 2014), pp. –.

[421] Igor F. Herbut. "Theory of integer quantum Hall effect in graphene". In: *Phys. Rev. B* 75 (16 2007), p. 165411.

[422] J. L. Lado and J. Fernández-Rossier. "Noncollinear magnetic phases and edge states in graphene quantum Hall bars". In: *Phys. Rev. B* 90 (16 2014), p. 165429.

[423] So Takei, Amir Yacoby, Bertrand I. Halperin, and Yaroslav Tserkovnyak. "Spin Superfluidity in the $v = 0$ Quantum Hall State of Graphene". In: (June 2015).

[424] H. A. Fertig and L. Brey. "Luttinger Liquid at the Edge of Undoped Graphene in a Strong Magnetic Field". In: *Phys. Rev. Lett.* 97 (11 2006), p. 116805.

[425] Ming-Hao Liu, Peter Rickhaus, Péter Makk, Endre Tóvári, Romain Maurand, Fedor Tkatschenko, Markus Weiss, Christian Schönenberger, and Klaus Richter. "Scalable Tight-Binding Model for Graphene". In: *Phys. Rev. Lett.* 114 (3 2015), p. 036601.

[426] CWJ Beenakker. "Three" Universal" Mesoscopic Josephson Effects". In: *Transport phenomena in mesoscopic systems: proceedings of the 14th Taniguchi symposium, Shima, Japan, November 10-14, 1991*. Springer-Verlag. 1992. ISBN: 3540557946.

[427] Dmitry A. Abanin, Patrick A. Lee, and Leonid S. Levitov. "Spin-Filtered Edge States and Quantum Hall Effect in Graphene". In: *Phys. Rev. Lett.* 96 (17 2006), p. 176803.

[428] Xiao-Liang Qi and Shou-Cheng Zhang. "Topological insulators and superconductors". In: *Rev. Mod. Phys.* 83 (4 2011), pp. 1057–1110.

[429] M Wimmer, A R Akhmerov, J P Dahlhaus, and C W J Beenakker. "Quantum point contact as a probe of a topological superconductor". In: *New J. Phys.* 13.5 (2011), p. 053016.

[430] Monica T. Allen, Oles Shtanko, Ion Cosma Fulga, Anton Akhmerov, Kenji Watanabi, Takashi Taniguchi, Pablo Jarillo-Herrero, Leonid S. Levitov, and Amir Yacoby. "Spatially resolved edge currents and guided-wave electronic states in graphene". In: (Apr. 2015).

[431] Shu-Ping Lee, Karen Michaeli, Jason Alicea, and Amir Yacoby. "Revealing Topological Superconductivity in Extended Quantum Spin Hall Josephson Junctions". In: *Phys. Rev. Lett.* 113 (19 2014), p. 197001.

[432] A Yu Kitaev. "Unpaired Majorana fermions in quantum wires". In: *Phys. Usp.* 44.10S (2001), p. 131.

[433] Travis Dirks, Taylor L. Hughes, Siddhartha Lal, Bruno Uchoa, Yung-Fu Chen, Cesar Chialvo, Paul M. Goldbart, and Nadya Mason. "Transport through Andreev bound states in a graphene quantum dot". In: *Nat Phys* 7.5 (May 2011), pp. 386–390.

[434] D. K. Efetov, L. Wang, C. Handschin, K. B. Efetov, J. Shuang, R. Cava, T. Taniguchi, K. Watanabe, J. Hone, C. R. Dean, and P. Kim. "Specular Interband Andreev Reflections in Graphene". In: (May 2015).

[435] Sumanta Tewari and Jay D. Sau. "Topological Invariants for Spin-Orbit Coupled Superconductor Nanowires". In: *Phys. Rev. Lett.* 109 (15 2012), p. 150408.

[436] Alexander Altland and Martin R. Zirnbauer. "Nonstandard symmetry classes in mesoscopic normal-superconducting hybrid structures". In: *Phys. Rev. B* 55 (2 1997), pp. 1142–1161.

[437] Andreas P. Schnyder, Shinsei Ryu, Akira Furusaki, and Andreas W. W. Ludwig. "Classification of topological insulators and superconductors in three spatial dimensions". In: *Phys. Rev. B* 78 (19 2008), p. 195125.

[438] I. Martin, Y. M. Blanter, and A. F. Morpurgo. "Topological confinement in bilayer graphene". In: *Phys. Rev. Lett.* 100.3 (2008), p. 036804.

[439] Pablo San-Jose and Elsa Prada. "Helical networks in twisted bilayer graphene under interlayer bias". In: *Phys. Rev. B* 88 (12 2013), p. 121408.

[440] Y Lemonik, I Aleiner, and VI Fal'ko. "Competing nematic, antiferromagnetic, and spin-flux orders in the ground state of bilayer graphene". In: *Physical review b* 85.24 (2012), p. 245451.

[441] Yong Wang, Hao Wang, Jin-Hua Gao, and Fu-Chun Zhang. "Layer antiferromagnetic state in bilayer graphene: A first-principles investigation". In: *Physical Review B* 87.19 (2013), p. 195413.

[442] Di Xiao, Wang Yao, and Qian Niu. "Valley-contrasting physics in graphene: magnetic moment and topological transport". In: *Physical Review Letters* 99.23 (2007), p. 236809.

[443] Aday J Molina-Mendoza, Jose Luis Lado, Joshua Island, Miguel Angel Niño, Lucía Aballe, Michael Foerster, Flavio Y Bruno, Herre SJ van der Zant, Gabino Rubio-Bollinger, Nicolas Agraït, et al. "Centimeter-scale synthesis of ultrathin layered MoO3 by van der Waals epitaxy". In: *arXiv preprint arXiv:1512.04355* (2015).

[444] Andre K Geim and Irina V Grigorieva. "Van der Waals heterostructures". In: *Nature* 499.7459 (2013), pp. 419–425.

[445] Dumitru Dumcenco, Dmitry Ovchinnikov, Kolyo Marinov, Predrag Lazic, Marco Gibertini, Nicola Marzari, Oriol Lopez Sanchez, Yen-Cheng Kung, Daria Krasnozhon, Ming-Wei Chen, et al. "Large-area epitaxial monolayer MoS2". In: *ACS nano* 9.4 (2015), pp. 4611–4620.

[446] Andres Castellanos-Gomez, Leonardo Vicarelli, Elsa Prada, Joshua O Island, KL Narasimha-Acharya, Sofya I Blanter, Dirk J Groenendijk, Michele Buscema, Gary A Steele, JV Alvarez, et al. "Isolation and characterization of few-layer black phosphorus". In: *2D Materials* 1.2 (2014), p. 025001.

[447] S Lebegue and O Eriksson. "Electronic structure of two-dimensional crystals from ab initio theory". In: *Physical Review B* 79.11 (2009), p. 115409.

[448] Anna Delin, P Ravindran, Olle Eriksson, and JM Wills. "Full-potential optical calculations of lead chalcogenides". In: *International journal of quantum chemistry* 69.3 (1998), pp. 349–358.

[449] S Lebègue, T Björkman, Mattias Klintenberg, Risto M Nieminen, and Olle Eriksson. "Two-dimensional materials from data filtering and ab initio calculations". In: *Physical Review X* 3.3 (2013), p. 031002.

[450] B Amorim, A Cortijo, F de Juan, AG Grushin, F Guinea, A Gutiérrez-Rubio, H Ochoa, V Parente, R Roldán, P San-José, et al. "Novel effects of strains in graphene and other two dimensional materials". In: *Physics Reports* (2015).

[451] Jorge Quereda, Pablo San-Jose, Vincenzo Parente, Luis Vaquero-Garzon, Aday Jose Molina-Mendoza, Nícolas Agraït, Gabino Rubio-Bollinger, Francisco Guinea, Rafael Roldan, and Andres Castellanos-Gomez. "Strong modulation of optical properties in black phosphorus through strain-engineered rippling". In: *Nano Letters* (2016).

[452] Mattias Klintenberg, C Ortiz, B Sanyal, J Fransson, Olle Eriksson, et al. "Evolving properties of two-dimensional materials: from graphene to graphite". In: *Journal of Physics: Condensed Matter* 21.33 (2009), p. 335502.

[453] Bruno Amorim and Francisco Guinea. "Flexural mode of graphene on a substrate". In: *Physical Review B* 88.11 (2013), p. 115418.

[454] Roman V Gorbachev, Ibtsam Riaz, Rahul R Nair, Rashid Jalil, Liam Britnell, Branson D Belle, Ernie W Hill, Kostya S Novoselov, Kenji Watanabe, Takashi Taniguchi, et al. "Hunting for monolayer boron nitride: optical and Raman signatures". In: *Small* 7.4 (2011), pp. 465–468.

[455] Eugene S Kadantsev and Pawel Hawrylak. "Electronic structure of a single MoS 2 monolayer". In: *Solid State Communications* 152.10 (2012), pp. 909–913.

[456] Arash A Mostofi, Jonathan R Yates, Giovanni Pizzi, Young-Su Lee, Ivo Souza, David Vanderbilt, and Nicola Marzari. "An updated version of wannier90: A tool for obtaining maximally-localised Wannier functions". In: *Computer Physics Communications* 185.8 (2014), pp. 2309–2310.

[457] Arash A Mostofi, Jonathan R Yates, Young-Su Lee, Ivo Souza, David Vanderbilt, and Nicola Marzari. "wannier90: A tool for obtaining maximally-localised Wannier functions". In: *Computer physics communications* 178.9 (2008), pp. 685–699.

[458] David J Singh and Lars Nordstrom. *Planewaves, Pseudopotentials, and the LAPW method*. Springer Science & Business Media, 2006.

[459] K Kośmider, JW González, and J Fernández-Rossier. "Large spin splitting in the conduction band of transition metal dichalcogenide monolayers". In: *Physical Review B* 88.24 (2013), p. 245436.

[460] KS Novoselov, D Jiang, F Schedin, TJ Booth, VV Khotkevich, SV Morozov, and AK Geim. "Two-dimensional atomic crystals". In: *Proceedings of the National Academy of Sciences of the United States of America* 102.30 (2005), pp. 10451–10453.

[461] Changgu Lee, Hugen Yan, Louis E Brus, Tony F Heinz, James Hone, and Sunmin Ryu. "Anomalous lattice vibrations of single-and few-layer MoS2". In: *ACS nano* 4.5 (2010), pp. 2695–2700.

[462] Jill A Miwa, Søren Ulstrup, Signe G Sørensen, Maciej Dendzik, Antonija Grubišić Čabo, Marco Bianchi, Jeppe Vang Lauritsen, and Philip Hofmann. "Electronic Structure of Epitaxial Single-Layer MoS 2". In: *Physical review letters* 114.4 (2015), p. 046802.

[463] Krzysztof Kośmider and Joaquín Fernández-Rossier. "Electronic properties of the MoS 2-WS 2 heterojunction". In: *Physical Review B* 87.7 (2013), p. 075451.

[464] Weijie Zhao, Zohreh Ghorannevis, Leiqiang Chu, Minglin Toh, Christian Kloc, Ping-Heng Tan, and Goki Eda. "Evolution of electronic structure in atomically thin sheets of WS2 and WSe2". In: *ACS nano* 7.1 (2012), pp. 791–797.

[465] A Kumar and PK Ahluwalia. "Electronic structure of transition metal dichalcogenides monolayers 1H-MX2 (M= Mo, W; X= S, Se, Te) from ab-initio theory: new direct band gap semiconductors". In: *The European Physical Journal B* 85.6 (2012), pp. 1–7.

[466] Habib Rostami, Reza Asgari, and Francisco Guinea. "Edge modes in zigzag and armchair ribbons of monolayer MoS _2". In: *arXiv preprint arXiv:1511.07003* (2015).

[467] Habib Rostami, Ali G Moghaddam, and Reza Asgari. "Effective lattice Hamiltonian for monolayer MoS 2: Tailoring electronic structure with perpendicular electric and magnetic fields". In: *Physical Review B* 88.8 (2013), p. 085440.

[468] Ferdows Zahid, Lei Liu, Yu Zhu, Jian Wang, and Hong Guo. "A generic tight-binding model for monolayer, bilayer and bulk MoS2". In: *AIP Advances* 3.5 (2013), p. 052111.

[469] Gui-Bin Liu, Wen-Yu Shan, Yugui Yao, Wang Yao, and Di Xiao. "Three-band tight-binding model for monolayers of group-VIB transition metal dichalcogenides". In: *Physical Review B* 88.8 (2013), p. 085433.

[470] Rui-Lin Chu, Xiao Li, Sanfeng Wu, Qian Niu, Wang Yao, Xiaodong Xu, and Chuanwei Zhang. "Valley-splitting and valley-dependent inter-Landau-level optical transitions in monolayer MoS 2 quantum Hall systems". In: *Physical Review B* 90.4 (2014), p. 045427.

[471] Habib Rostami and Reza Asgari. "Valley Zeeman effect and spin-valley polarized conductance in monolayer MoS 2 in a perpendicular magnetic field". In: *Physical Review B* 91.7 (2015), p. 075433.

[472] David MacNeill, Colin Heikes, Kin Fai Mak, Zachary Anderson, Andor Kormányos, Viktor Zólyomi, Jiwoong Park, and Daniel C Ralph. "Breaking of valley degeneracy by magnetic field in monolayer MoSe 2". In: *Physical review letters* 114.3 (2015), p. 037401.

[473] Vy Tran, Ryan Soklaski, Yufeng Liang, and Li Yang. "Layer-controlled band gap and anisotropic excitons in few-layer black phosphorus". In: *Physical Review B* 89.23 (2014), p. 235319.

[474] Jingsi Qiao, Xianghua Kong, Zhi-Xin Hu, Feng Yang, and Wei Ji. "High-mobility transport anisotropy and linear dichroism in few-layer black phosphorus". In: *Nature communications* 5 (2014).

[475] Fabien Tran and Peter Blaha. "Accurate band gaps of semiconductors and insulators with a semilocal exchange-correlation potential". In: *Physical Review Letters* 102.22 (2009), p. 226401.

[476] JM Pereira Jr and MI Katsnelson. "Landau levels of single-layer and bilayer phosphorene". In: *Physical Review B* 92.7 (2015), p. 075437.

[477] Shengjun Yuan, Mikhail I Katsnelson, and Rafael Roldán. "Quantum Hall effect in biased black phosphorus". In: *arXiv preprint arXiv:1512.06345* (2015).

[478] Ilya K Drozdov, Aris Alexandradinata, Sangjun Jeon, Stevan Nadj-Perge, Huiwen Ji, RJ Cava, B Andrei Bernevig, and Ali Yazdani. "One-dimensional topological edge states of bismuth bilayers". In: *Nature Physics* 10.9 (2014), pp. 664–669.

[479] Shuichi Murakami. "Quantum spin Hall effect and enhanced magnetic response by spin-orbit coupling". In: *Physical review letters* 97.23 (2006), p. 236805.

[480] A Möller, U Löw, T Taetz, M Kriener, G André, F Damay, O Heyer, M Braden, and JA Mydosh. "Structural domain and finite-size effects of the antiferromagnetic S= 1/2 honeycomb lattice in InCu 2/3 V 1/3 O 3". In: *Physical Review B* 78.2 (2008), p. 024420.

[481] YJ Yan, ZY Li, T Zhang, XG Luo, GJ Ye, ZJ Xiang, P Cheng, Liang-Jian Zou, and XH Chen. "Magnetic properties of the doped spin-1 2 honeycomb-lattice compound In 3 Cu 2 VO 9". In: *Physical Review B* 85.8 (2012), p. 085102.

[482] Alexey A Soluyanov and David Vanderbilt. "Computing topological invariants without inversion symmetry". In: *Physical Review B* 83.23 (2011), p. 235401.

[483] Di Xiao, Wenguang Zhu, Ying Ran, Naoto Nagaosa, and Satoshi Okamoto. "Interface engineering of quantum Hall effects in digital transition metal oxide heterostructures". In: *Nature Communications* 2 (2011), p. 596.

[484] Satoshi Okamoto, Wenguang Zhu, Yusuke Nomura, Ryotaro Arita, Di Xiao, and Naoto Nagaosa. "Correlation effects in (111) bilayers of perovskite transition-metal oxides". In: *Physical Review B* 89.19 (2014), p. 195121.

[485] Hosub Jin, Jino Im, and Arthur J Freeman. "Topological insulator phase in halide perovskite structures". In: *Physical Review B* 86.12 (2012), p. 121102.

[486] JL Lado, V Pardo, and D Baldomir. "Ab initio study of Z 2 topological phases in perovskite (111)(SrTiO 3) 7/(SrIrO 3) 2 and (KTaO 3) 7/(KPtO 3) 2 multilayers". In: *Physical Review B* 88.15 (2013), p. 155119.

[487] Juan F Afonso and Victor Pardo. "Ab initio study of nontrivial topological phases in corundum-structured (M 2 O 3)/(Al 2 O 3) 5 multilayers". In: *Physical Review B* 92.23 (2015), p. 235102.

[488] J Kobak, T Smoleński, M Goryca, M Papaj, K Gietka, A Bogucki, M Koperski, J-G Rousset, J Suffczyński, E Janik, et al. "Designing quantum dots for solotronics". In: *Nature communications* 5 (2014).

[489] Marcus W Doherty, Neil B Manson, Paul Delaney, Fedor Jelezko, Jörg Wrachtrup, and Lloyd CL Hollenberg. "The nitrogen-vacancy colour centre in diamond". In: *Physics Reports* 528.1 (2013), pp. 1–45.

[490] AM Tyryshkin, SA Lyon, AV Astashkin, and AM Raitsimring. "Electron spin relaxation times of phosphorus donors in silicon". In: *Physical Review B* 68.19 (2003), p. 193207.

[491] Zongyou Yin, Hai Li, Hong Li, Lin Jiang, Yumeng Shi, Yinghui Sun, Gang Lu, Qing Zhang, Xiaodong Chen, and Hua Zhang. "Single-layer MoS2 phototransistors". In: *ACS nano* 6.1 (2011), pp. 74–80.

[492] Tapas Kuila, Saswata Bose, Ananta Kumar Mishra, Partha Khanra, Nam Hoon Kim, and Joong Hee Lee. "Chemical functionalization of graphene and its applications". In: *Progress in Materials Science* 57.7 (2012), pp. 1061–1105.

[493] MP Lopez Sancho, JM Lopez Sancho, JM Lopez Sancho, and J Rubio. "Highly convergent schemes for the calculation of bulk and surface Green functions". In: *Journal of Physics F: Metal Physics* 15.4 (1985), p. 851.

[494] Eduardo V Castro, KS Novoselov, SV Morozov, NMR Peres, JMB Lopes Dos Santos, Johan Nilsson, F Guinea, AK Geim, and AH Castro Neto. "Biased bilayer graphene: semiconductor with a gap tunable by the electric field effect". In: *Physical Review Letters* 99.21 (2007), p. 216802.

[495] Eduardo V Castro, María P López-Sancho, and María AH Vozmediano. "New type of vacancy-induced localized states in multilayer graphene". In: *Physical review letters* 104.3 (2010), p. 036802.

[496] URL: https://www.youtube.com/watch?v=8gO1yRmwgAs.

[497] URL: https://www.youtube.com/watch?v=FQlkqAW7Nhs.

[498] URL: https://www.youtube.com/watch?v=R7Kt3_DHTtM.

[499] URL: https://www.youtube.com/watch?v=tQKG_h0FaTM.

[500] URL: https://sourceforge.net/projects/graphenelikeribbons/.

[501] URL: https://github.com/joselado/pygra.

[502] URL: https://sourceforge.net/projects/pygra/.

[503] URL: https://sourceforge.net/projects/tranci/.

[504] Shuai Cheng, Jinming Yu, Tianxing Ma, and NMR Peres. "Strain-induced edge magnetism at the zigzag edge of a graphene quantum dot". In: *Physical Review B* 91.7 (2015), p. 075410.

[505] JL Lado and V Pardo. "Noncollinear versus collinear description of the Ir-based one-t 2 g-hole perovskite-related compounds: SrIrO 3 and Sr 2 IrO 4". In: *Physical Review B* 92.15 (2015), p. 155151.

[506] CC Tsuei and JR Kirtley. "Pairing symmetry in cuprate superconductors". In: *Reviews of Modern Physics* 72.4 (2000), p. 969.

[507] E. Fahrenfort J. Girovsky R. Toskovic J. L. Lado J. Fernandez-Rossier A. F. Otte F. E. Kalff M. P. Rebergen. "A kilobyte rewritable atomic memory". In: *arXiv preprint arXiv:1604.02265* (2016).

[508] Alejandro Ferrón, Jose Luis Lado, and Joaquín Fernández-Rossier. "Electronic properties of transition metal atoms on Cu 2 N/Cu (100)". In: *Physical Review B* 92.17 (2015), p. 174407.

[509] Benjamin Bryant, Ranko Toskovic, Alejandro Ferrón, José L Lado, Anna Spinelli, Joaquín Fernández-Rossier, and Alexander F Otte. "Controlled Complete Suppression of Single-Atom Inelastic Spin and Orbital Cotunneling". In: *Nano Letters* 15.10 (2015), pp. 6542–6546.

[510] B Bryant, A Spinelli, JJT Wagenaar, M Gerrits, and AF Otte. "Local control of single atom magnetocrystalline anisotropy". In: *Physical review letters* 111.12 (2013), p. 127203.

[511] Susanne Baumann, William Paul, Taeyoung Choi, Christopher P Lutz, Arzhang Ardavan, and Andreas J Heinrich. "Electron paramagnetic resonance of individual atoms on a surface". In: *Science* 350.6259 (2015), pp. 417–420.

[512] Shichao Yan, Deung-Jang Choi, Jacob AJ Burgess, Steffen Rolf-Pissarczyk, and Sebastian Loth. "Control of quantum magnets by atomic exchange bias". In: *Nature nanotechnology* 10.1 (2015), pp. 40–45.

[513] Daniel Guterding, Harald O Jeschke, and Roser Valenti. "Prospects for topologically non-trivial electronic and magnetic states in correlated kagome lattice materials". In: *arXiv preprint arXiv:1511.05686* (2015).

[514] Gang Xu, Biao Lian, and Shou-Cheng Zhang. "Intrinsic Quantum Anomalous Hall Effect in the Kagome Lattice Cs 2 LiMn 3 F 12". In: *Physical Review Letters* 115.18 (2015), p. 186802.

[515] Hiroaki Ishizuka and Yukitoshi Motome. "Quantum anomalous Hall effect in kagome ice". In: *Physical Review B* 87.8 (2013), p. 081105.

[516] Oleg V Yazyev. "Emergence of magnetism in graphene materials and nanostructures". In: *Reports on Progress in Physics* 73.5 (2010), p. 056501.

[517] Oleg V Yazyev and MI Katsnelson. "Magnetic correlations at graphene edges: basis for novel spintronics devices". In: *Physical Review Letters* 100.4 (2008), p. 047209.

[518] Chenggang Tao, Liying Jiao, Oleg V Yazyev, Yen-Chia Chen, Juanjuan Feng, Xiaowei Zhang, Rodrigo B Capaz, James M Tour, Alex Zettl, Steven G Louie, et al. "Spatially resolving edge states of chiral graphene nanoribbons". In: *Nature Physics* 7.8 (2011), pp. 616–620.

[519] Hu Li, Lakshya Daukiya, Soumyajyoti Haldar, Andreas Lindblad, Biplab Sanyal, Olle Eriksson, Dominique Aubel, Samar Hajjar-Garreau, Laurent Simon, and Klaus Leifer. "Site-selective local fluorination of graphene induced by focused ion beam irradiation". In: *Scientific reports* 6 (2016).

[520] Eduardo V Castro, M Pilar López-Sancho, and María AH Vozmediano. "Vacancy induced zero energy modes in graphene stacks: The case of ABC trilayer". In: *Solid State Communications* 152.15 (2012), pp. 1483–1488.

[521] Jonas Fransson, Olle Eriksson, and AV Balatsky. "Theory of spin-polarized scanning tunneling microscopy applied to local spins". In: *Physical Review B* 81.11 (2010), p. 115454.

[522] MM Ugeda, D Fernández-Torre, I Brihuega, P Pou, AJ Martínez-Galera, Rubén Pérez, and JM Gómez-Rodríguez. "Point defects on graphene on metals". In: *Physical review letters* 107.11 (2011), p. 116803.

[523] Miguel M Ugeda, Iván Brihuega, Francisco Guinea, and José M Gómez-Rodríguez. "Missing atom as a source of carbon magnetism". In: *Physical Review Letters* 104.9 (2010), p. 096804.

[524] Miguel M Ugeda, Iván Brihuega, Fanny Hiebel, Pierre Mallet, Jean-Yves Veuillen, José M Gómez-Rodríguez, and Félix Ynduráin. "Electronic and structural characterization of divacancies in irradiated graphene". In: *Physical Review B* 85.12 (2012), p. 121402.

[525] Oleg V Yazyev. "Magnetism in disordered graphene and irradiated graphite". In: *Physical review letters* 101.3 (2008), p. 037203.

[526] Biplab Sanyal, Olle Eriksson, Ulf Jansson, and Helena Grennberg. "Molecular adsorption in graphene with divacancy defects". In: *Physical Review B* 79.11 (2009), p. 113409.

[527] Noel A García-Martínez, Adolfo G Grushin, Titus Neupert, Belén Valenzuela, and Eduardo V Castro. "Interaction-driven phases in the half-filled spinless honeycomb lattice from exact diagonalization". In: *Physical Review B* 88.24 (2013), p. 245123.

[528] VS Arun, R Sohal, C Hickey, and A Paramekanti. "Mean field study of the topological Haldane-Hubbard model of spin-1/2 fermions". In: *arXiv preprint arXiv:1510.08856* (2015).

[529] M Ebrahimkhas. "Exact diagonalization study of 2D Hubbard model on honeycomb lattice: Semi-metal to insulator transition". In: *Physics Letters A* 375.36 (2011), pp. 3223–3227.

[530] JMB Lopes Dos Santos, NMR Peres, and AH Castro Neto. "Graphene bilayer with a twist: Electronic structure". In: *Physical review letters* 99.25 (2007), p. 256802.

[531] Johan Nilsson, AH Castro Neto, NMR Peres, and F Guinea. "Electron-electron interactions and the phase diagram of a graphene bilayer". In: *Physical Review B* 73.21 (2006), p. 214418.

[532] Johan Nilsson, AH Castro Neto, F Guinea, and NMR Peres. "Electronic properties of bilayer and multilayer graphene". In: *Physical Review B* 78.4 (2008), p. 045405.

[533] Thomas C Lang, Zi Yang Meng, Michael M Scherer, Stefan Uebelacker, Fakher F Assaad, Alejandro Muramatsu, Carsten Honerkamp, and Stefan Wessel. "Antiferromagnetism in the Hubbard model on the Bernal-stacked honeycomb bilayer". In: *Physical review letters* 109.12 (2012), p. 126402.

[534] Roman Jackiw and Cláudio Rebbi. "Solitons with fermion number 1/2". In: *Physical Review D* 13.12 (1976), p. 3398.

[535] Yu V Bludov, Daria A Smirnova, Yu S Kivshar, Nuno MR Peres, and Mikhail I Vasilevskiy. "Discrete solitons in graphene metamaterials". In: *Physical Review B* 91.4 (2015), p. 045424.

[536] Pablo San-Jose, RV Gorbachev, AK Geim, KS Novoselov, and F Guinea. "Stacking boundaries and transport in bilayer graphene". In: *Nano letters* 14.4 (2014), pp. 2052–2057.

[537] R De Gail, MO Goerbig, F Guinea, G Montambaux, and AH Castro Neto. "Topologically protected zero modes in twisted bilayer graphene". In: *Physical Review B* 84.4 (2011), p. 045436.

[538] Pablo San-Jose, Jose Gonzalez, and Francisco Guinea. "Non-Abelian gauge potentials in graphene bilayers". In: *Physical review letters* 108.21 (2012), p. 216802.

[539] J Li, K Wang, KJ McFaul, Z Zern, YF Ren, K Watanabe, T Taniguchi, ZH Qiao, and J Zhu. "Experimental observation of edge states at the line junction of two oppositely biased bilayer graphene". In: *arXiv preprint arXiv:1509.03912* (2015).

[540] Alexander Weiße, Gerhard Wellein, Andreas Alvermann, and Holger Fehske. "The kernel polynomial method". In: *Reviews of modern physics* 78.1 (2006), p. 275.

[541] RN Silver and H Röder. "Calculation of densities of states and spectral functions by Chebyshev recursion and maximum entropy". In: *Physical Review E* 56.4 (1997), p. 4822.

[542] Dunham Jackson. "On approximation by trigonometric sums and polynomials". In: *Transactions of the American Mathematical society* 13.4 (1912), pp. 491–515.